2003

Characterisation of the structure and properties of arc welded zinc alloy coated sheet steels

Yan Wang Chen
University of Wollongong

CHARACTERISATION OF THE STRUCTURE AND PROPERTIES OF ARC WELDED ZINC ALLOY COATED SHEET STEELS

A thesis submitted in fulfillment of the requirements for the award of the degree of

DOCTOR OF PHILOSOPHY

From

THE UNIVERSITY OF WOLLONGONG

by

YAN WANG CHEN, B. Eng.,

Materials Engineering, Faculty of Engineering

2003

DECLARATION

I, Yan W. Chen, declare that this thesis, submitted in fulfillment of the requirements for the award of Doctor of Philosophy, in the Materials Engineering, Faculty of Engineering, University of Wollongong, is wholly my own work unless otherwise referenced or acknowledged. The document has not been submitted for qualifications at any other academic institution.

Yan Wang Chen, B. Eng.,

26 March 2003

ACKNOWLEDGEMENTS

The research work reported in this thesis was carried out at the Materials Engineering, Faculty of Engineering, University of Wollongong under the supervisions of Professor Druce P. Dunne and Professor John Norrish.

The author would firstly wish to express the deepest gratitude to Professor D. P. Dunne, Head of the Materials Engineering, Professor John Norrish, Head of the CRC of Materials Welding and Joining, under whose supervision this research work was performed. Their invaluable guidance, patient assistance and constant encouragement are grateful acknowledged.

Special thanks are due to BHP Research, Sheet and Coil Products Division, BHP Steel and the Co-operative Research Centre for Materials Welding and Joining for financial support that has been given to this research.

In particular thanks are also due to Mr. John Szalla for organizing the materials, the tensile test, simulation experiments and chemical composition analysis at the BHP research and Central Laboratory in the PHP steels.

The author would like to express the thanks to all technical and administration staff and colleagues in the Materials Engineering, Faculty of Engineering for their assistance with various aspects of this research.

Finally, warm appreciation and respect is due to author's most respective mother and father, Yan Hua Xu and Guo Xiang Wang, author's husband, Dr. Zhi Xin Chen and lovely daughter, Maryann Chen, for their deep understanding, strong encouragement, continuous supporting and patience throughout the period of this research work.

ABSTRACT

High strength, cold rolled, corrosion resistant ZINCALUME™ (ZA) and ZINC-HI-TEN™ (ZHT) G550 sheet steels are widely used in the construction and automotive industries. The sheet steel is commonly joined by gas metal arc welding (GMAW) because of its low cost and high productivity. However, two significant problems can occur: porosity in the weld bead and loss of strength in the heat affected zone (HAZ). As a result of the strength loss, the design strength is currently down-graded to the fully annealed yield strength (250 or 300 MPa). The full strength potential of the steels cannot be utilised unless the strength loss in the HAZ can be quantified.

In this investigation the microstructures and mechanical properties of the weld metal and HAZ of gas metal arc welding and flux cored arc welding (FCAW) welded ZA and ZHT G550 1.0 mm sheet steels have been studied and the strength loss in the HAZ has been quantified. A major aim was to correlate the mechanical properties with HAZ microstructure and to correlate microstructure with the weld thermal cycle. The effect of welding process variables on the HAZ microstructure, the structure and composition of the weld metal and on the Zn alloy coating have been investigated. HAZ thermal simulations were used to elucidate the structure evolution in the actual weld HAZ.

As expected, the reduction in HAZ mechanical properties is dependent on the heat input. After GMAW at the highest heat input of 130 J/mm the tensile strength of Zn-Al coated steel decreased to 460 MPa (with a yield strength of 400 MPa) from a pre-weld minimum specified longitudinal tensile strength of 550 MPa. However, a lower decrease in tensile strength to about 520 MPa (with a yield strength of 505 MPa) occurred at the lowest heat input of 50 J/mm. All tensile pieces were fractured in the grain refined region closed to the grain coarsened region of the HAZ.

Although the microstructure of the HAZ was successfully simulated, the simulated HAZ had a much lower tensile strength than the real welds at similar heat inputs due to the absence of the 'brazing effect' or 'two phase aggregate effect' present in the real welds.

It was found that at the same nominal heat input the strength of the welded joint is significantly affected by individual welding parameters, particularly, torch angle, shielding gas and welding consumable. At the same nominal heat input FCAW generated welds with a lower tensile strength than GMAW. GMAW using perpendicular and forehand welding techniques tended to produce welds with a higher tensile strength than the backhand technique. A higher strength loss was also evident for GMAW with pure CO_2 or a shielding gas containing helium.

No obvious macro-defects or Zn penetration cracks were found in the weld bead or HAZ. However, gas pores and aluminum rich particles were observed in the weld metal. These features did not adversely affect the overall weldment tensile properties.

A more globular weld bead with a higher surface tension, corresponding to a lower oxygen content in the weld metal, was found for GMA welds shielded by Argoshield 60 (98.5%Ar+1.5%O_2), c ompared with shielding gases with a higher oxygen potential. Flatter and smoother weld beads were observed in the FCA welds despite a significantly lower oxygen content than the GMA welds. The presence of a slag layers on the weld pool and a significantly higher nitrogen content may account for this weld profile.

The oxygen content in the GMA weld metal increased with an increase of the oxygen potential of the shielding gas. This resulted in an increase in volume fraction and mean particle size of the non-metallic inclusions, consistent with the prediction of the Franklin equation. A high volume fraction and large mean particle size were also found in the FCA welds even though the FCA welds contained significantly lower oxygen and higher nitrogen and aluminum contents. The inclusions in this case were predominantly AlN, not oxides, and therefore the 'Franklin' equation is inappropriate for the prediction of inclusion volume fractions of self shielded FCA welds.

Damage to the coating by the welding thermal process has also been characterised and it is concluded that some form of surface coating remains after welding even in close proximity to the weld fusion boundary. A white layer with a composition close to Fe_3Al was formed adjacent to the weld bead for the Zn-Al coated steel and the Fe-Zn alloy phase Γ was detected in the high peak temperature region for the Zn coated steel.

However, the changes to the coating had little effect on the soundness and mechanical properties on the joints.

The investigation confirms the feasibility of arc welding of high strength Zn alloy coated sheet steels using GMAW and FCAW. The strength loss has been quantified, the processing factors exerting the most significant effect on strength loss have been identified, and the mechanisms of strength loss have been established.

The research provides guidelines for the optimum welding process and welding conditions to minimise the strength loss during arc welding of cold rolled sheet steel. The quantification of the strength loss for GMA and FCA welding high strength sheet steel should be of a considerable value in structural design and the results have the potential for incorporation into appropriate Australian Standards.

TABLE OF CONTENTS

CHAPER 1

INTRODUCTION

It is well known that a substantial strengthening of low carbon sheet steel can be obtained either by the combination of microalloying with thermomechanical controlled processing or by cold rolling. In microalloyed steels, the conventional steel chemistry is modified by single or combined additions of less than 0.1wt.% of the strong carbide-nitride forming elements: niobium, titanium and vanadium; and the hot rolling process is modified to enhance the effect of the small change in steel composition. Increases in yield strength up to 300 MPa over typical strength levels of 250 MPa in non-microalloyed steels are readily obtained, enabling considerable mass and construction savings in fabricated steel structures in, for example, the building, transportation and pipeline industries. Apart from this attractive route to higher strength, a considerable volume of sheet steel production involves less expensive non-microalloyed C-Mn structural steel grades, subject to strengthening by cold rolling. The strength is controlled both by the degree of cold rolling reduction and extent of restoration of the deformed structure by the use of a subsequent controlled annealing treatment and/or by hot dip zinc or zinc-alloy coating for corrosion protection. So-called "recovery annealed" sheet steels and "cold rolled" sheet steels constitute a significant tonnage of the output of the BHP Flat Products Division (BHP-FPD) plants at Port Kembla and Westernport. Applications for these steels include roofing, cladding, automotive body parts and structural members for building frames.

Recovery annealed Zn-Al coated ZINCALUME^{TM} and Zn coated ZINC-HI-TEN^{TM} G550 sheet steels produced by the BHP-FPD with a specified tensile strength not less than 550 MPa are widely used in the construction and automotive industries because of their high strength, low cost and corrosion resistance. Fusion joining process, such as spot welding and arc welding, are frequently employed in joining these steels in structural members of building frames, roofing, cladding and automotive body parts. After fusion joining weld metal porosity can be present due to Zn vapour in the weld pool and substantial local softening can occur in the heat affected zone because of the weld thermal cycle [Moro and Dunne 1990].

Zinc and zinc alloy coating can lead to rapid degradation of spot welding electrodes in the fabrication of steel sheet by resistance spot welding [Finlay et al. 1997]. The Zn-Al coating can result in weld metal porosity in laser welding [Frewin 1997] and both arc

instability and porosity, in the form of pits and blow holes in arc welding [Suga 1994; Kjeld 1991; Nishikawa 1995].

Localised softening of the heat affected zone of cold rolled sheet steel welds occurs mainly because the strain hardened base metal is annealed by austenisation and/or recrystallisation. The softening and loss in strength in the heat affected zone of the cold rolled sheet steel can be significant and cannot be recovered by subsequent heat treatment [AWS Welding Handbook Vol.1 1989]. For design purposes, therefore, a downgrading of the strength rating is required. However, suppliers have been reluctant to advise on strength because of lack of previous research to quantify the properties of the welded joint. Currently, the only Australian guidelines are given in the Lysaght Referee [Lysaght Referee 1988] which indicates that the mechanical properties revert to those of zinc coated annealed steel sheet (G250 and G300 grades – 250 and 300 MPa yield strengths). The implied loss of over 250 MPa in yield strength appears to be highly conservative. Therefore the research reported here was undertaken to investigate the effect of the arc welding on Zn alloy coated structural steel sheet.

The main aim of research project was to establish the structural and property changes in the weld zone of G550 grade zinc alloy coated structural steel sheet, joined by gas metal arc welding (GMAW) and self shielded flux cored arc welding (FCAW) techniques in order to quantify the loss of strength associated with the welding processes and to optimize the welding procedure in terms of minimizing the softening. The project elucidated the effect of the zinc alloy coating on the soundness of the weld bead and explored fundamental aspects of the impact of the fusion welding process on the cold deformed ferrite structure of the base steel. The results on the weldability of high tensile cold rolled steels could be of considerable value to the steel designer, and have the potential for incorporation into Australian standards.

The loss of strength of GMA and FCA welded ZINCALUME^{TM} and ZINC-HI-TEN^{TM} G550 0.55 to 1.0mm thick sheet steels have been studied and correlated with the effect of heat input, the welding conditions, (such as welding process, shielding gas, electrode orientation, welding control mode, travel speed) and the type of Zn alloy coating. The microstructures of the HAZ associated with the strength loss have been characterised

and the welding thermal cycles have been recorded in order to understand and interpret the softening of the HAZ of arc welded cold rolled sheet steels.

The thesis has ten chapters consisting of five chapters concerned with literature review: (the GMA and FCA welding processes in Chapter 2; recovery annealed cold rolled steels in Chapter 3; the HAZ in Chapter 4; the weld metal in Chapter 5; and the effect of fusion welding on galvanised steel in Chapter 6). The materials and experimental procedures are outlined in Chapter 7, the results are summarised in Chapter 8, the discussion is presented in Chapter 9 and is followed by the Conclusions in Chapter 10.

CHAPTER 2

GAS METAL ARC WELDING AND SELF-SHIELDED FLUX CORED ARC WELDING

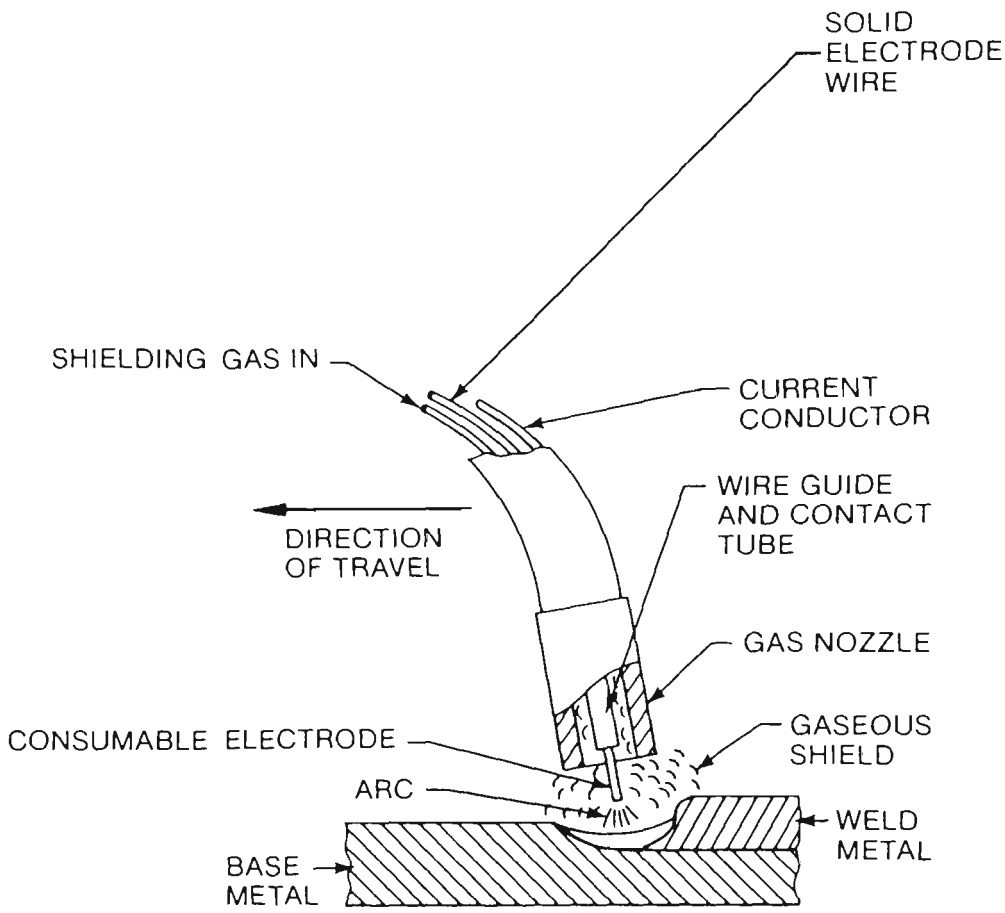

Figure 2.1 Principle of the Gas Metal Arc Welding (GMAW) process [After Welding Handbook Vol.2 1991].

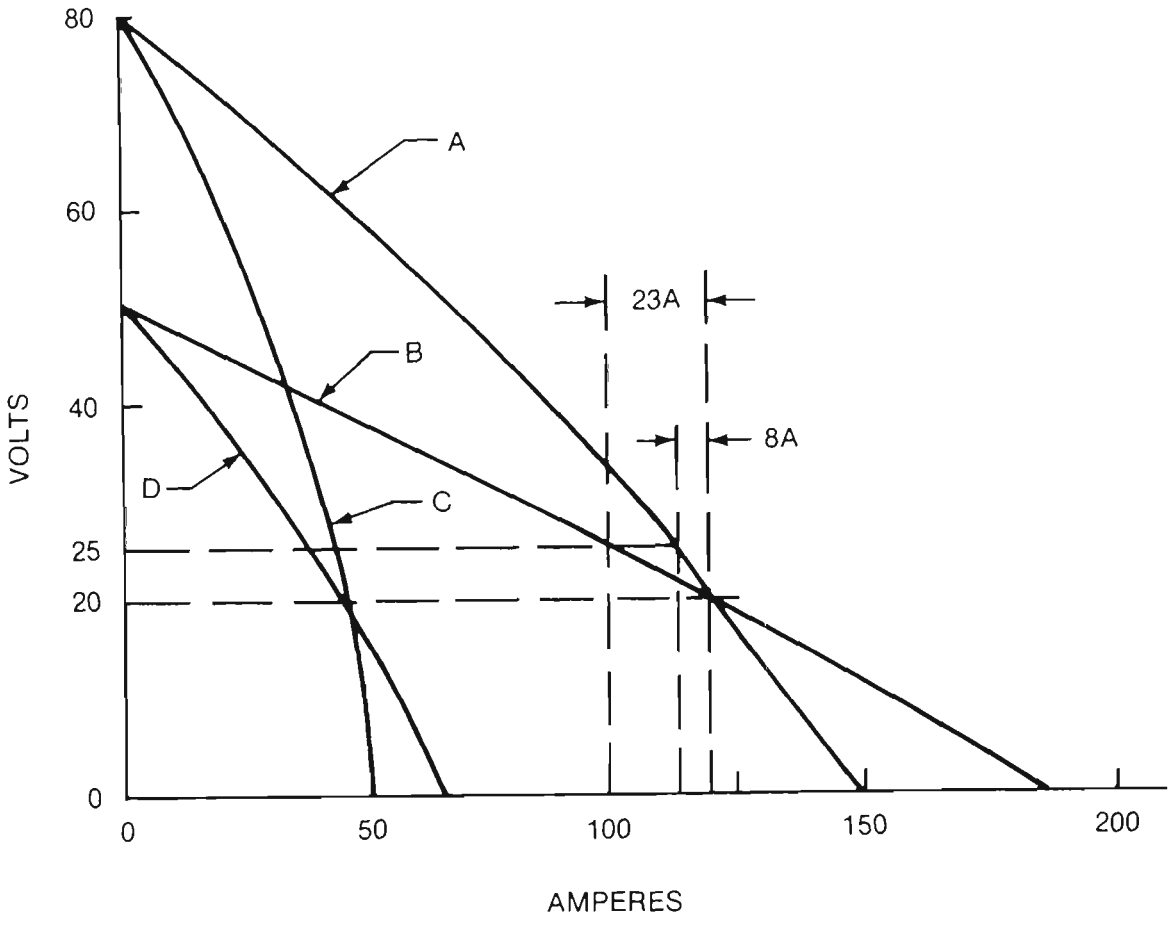

Figure 2.2 Typical Volt-Ampere (V-A) output curves for a constant-current power source [After Welding Handbook Vol.2 1991].

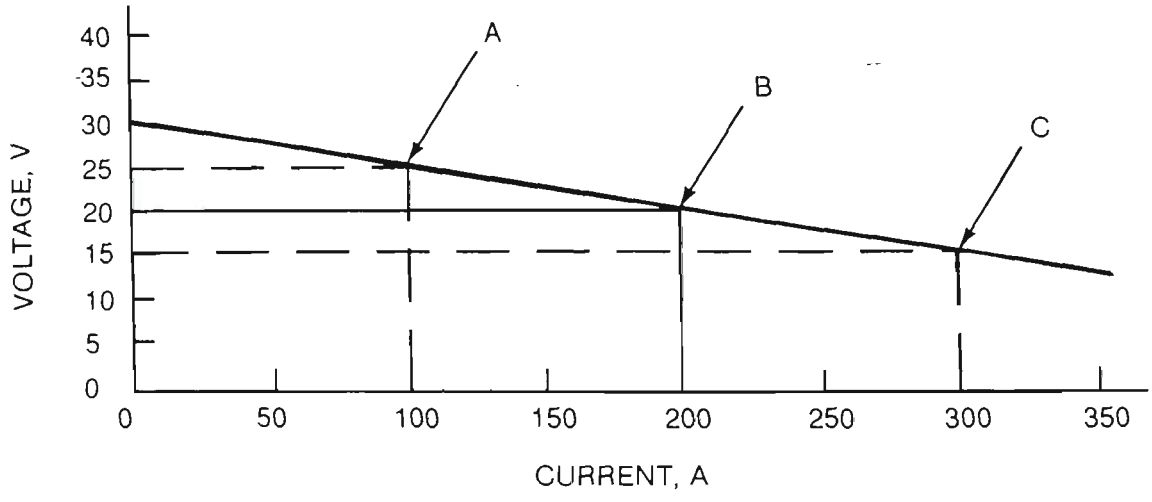

Figure 2.3 Typical Volt-Ampere curve for a constant-voltage power sauce [After Welding Handbook Vol.2 1991].

2.1 GAS METAL ARC WELDING (GMAW)

Gas metal arc welding (GMAW) is a type of arc welding processes, which uses an arc as a heat source between a continuous filler metal electrode and the weld pool to join pieces of metal. The arc and weld pool are shielded by an external shielding gas to prevent the weld pool from atmospheric oxidation. The GMAW process is illustrated in **Figure 2.1**.

All position welding is possible if the shielding gas, electrode and welding variables are chosen appropriately. The GMAW process has been widely used in automotive and construction industries for the past four decades due to its advantages of continuous wire feed, high deposition rate, fast welding speed and deep penetration using spray transfer.

2.1.1 Power Sources for Arc Welding

Welding power sources are classified as constant current and constant voltage based on the static volt-ampere characteristics of the power supply. **Figure 2.2** shows typical VOLT-AMPERE (V-A) output curves for a constant-current power source. With curve A and C, which have an open circuit voltage of 80 V, a steady increase in arc voltage results in a decrease (8 A) in current. The change in current is relatively small, especially with the lower output curve C. With curves B and D, which have an open circuit of 50 V, a significant decrease in current (23 A) occurs with an increase in arc voltage. A typical VOLT=AMPERE curve for a constant-voltage power source is illustrated in **Figure 2.3**. At starting point B, an increase or decrease in voltage A or C (5 V) produces a large change in current (100 A). This V-A characteristic is normally used for a constant electrode feed process in order to maintain a constant arc length.

2.2 METAL TRANSFER IN GMAW PROCESS

Short circuit, globular and spray transfers modes are the three common metal transfer mechanisms which are found in the GMAW process as shown in **Figure 2.4**. The type of metal transfer that can be achieved during GMAW depends on the combination of the

shielding gas, power source (magnitude and type of welding current) and electrode (composition, diameter and extension). The arc stability is largely dependent on the mode of metal transfer, which in turn is influenced by the effect of the gas on the surface tension and work function of the material and the resultant arc root behavior.

2.2.1 Short Circuiting Transfer

The "short circuit" transfer mode has an arcing and short circuit phase: when welding commences, an arc is struck between the electrode and work piece and weld pool is formed; the tip of the continuous welding wire dips into the weld pool and causes a short circuit (A), (B), (C) and (D) resulting in a rapid temperature rise in the wire and melting of the electrode wire tip. An arc is subsequently formed between the wire tip and the weld pool (E) and (F). The arc maintains the electrical circuit and produces sufficient heat to keep the weld pool fluid. This sequence is repeated at a frequency range from 20 to 200 times per second. Short circuit transfer produces a small, fast-freezing weld pool and is suited for joining thin sections. The benefits of the low heat input are to reduce distortion and minimize burn through which is suitable for joining the Zn alloy coated sheet steels.

Although metal transfer takes place only during short circuiting, the molten weld metal surface tension is affected significantly by the shielding gas composition due to its effects on the drop size and the duration of the short circuiting.

2.2.2 Globular Transfer

Globular transfer is characterised by a drop size with a diameter greater than that of the electrode. With a positive electrode (DCEP), globular transfer occurs at a rate of a few drops per second and the relatively low current only slightly higher than that used in short circuiting transfer. The average voltage used in globular transfer is higher than that used in short circuiting transfer and allows a longer arc length. The high voltage greatly limits the globular transfer mode in production applications and may result in lack of fusion, insufficient penetration and excessive reinforcement.

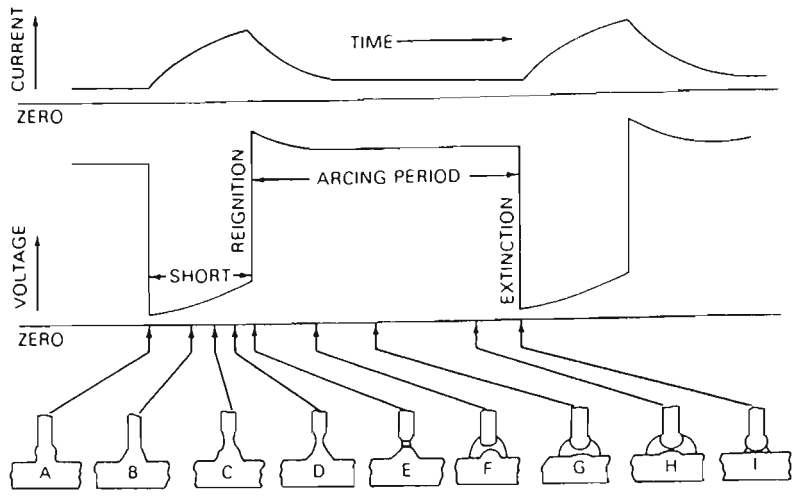

(a)

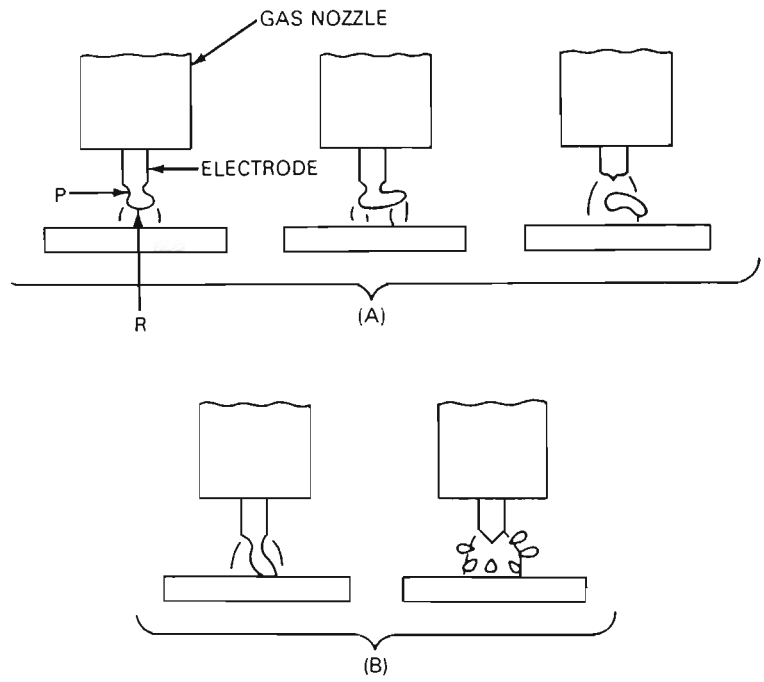

(b)

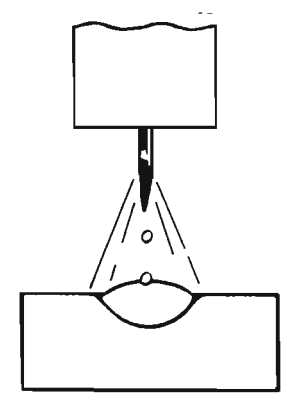

(c)

Figure 2.4 Schematic three metal transfer modes from **(a)** short circuit metal transfer; **(b)** globular transfer; and **(c)** spray transfer [After Welding Handbook Vol.2 1991].

2.2.3 Spray Transfer

Spray transfer is used for joining thick plate due to the high current and voltage employed in the process. Droplets of metal are detached from the electrode and cross the arc in "free flight" (**Figure 2.4 (c)**). The spray transfer is normally operated with direct current and a positive electrode (DCEP). The current level at which above a spray transfer occurs is critical value which is called the transition current. This transition current depends on the liquid metal surface tension and is inversely proportional to the electrode diameter and the electrode extension. It varies with filler metal melting temperature and the shielding gas composition. For 0.9 mm mild steel electrode wire with 98% argon and 2% oxygen shielded, the transition current is about 165 ampere [AWS, Welding Handbook, Vol. 2, 1991]. And below this value, transfer occurs in the globular mode.

The spray transfer mode results in a highly directed stream of discrete drops that are accelerated by arc forces to velocities that overcome the effects of gravity and therefore this process can be used in any thickness and any position. However, applying the process to thin sheets may be difficult because of the high currents needed to produce the spray arc.

2.3 GMAW PROCESS PARAMETERS

Weld penetration, weld bead geometry and overall weld quality are affected by the welding current, polarity, arc voltage, travel speed, electrode extension, electrode orientation (tilt from the vertical), weld joint position, electrode diameter and shielding gas composition, electrode composition as well as gas flow rate [AWS, Welding Handbook, Vol.2 1991]. These variables are not completely independent and changing one requires changing one or more of the others to produce the desired results.

2.3.1 Welding Current

If all other variables are held constant, the welding current increases as wire feed rate is increased. **Figure 2.5** gives the typical welding currents versus wire feed speeds for

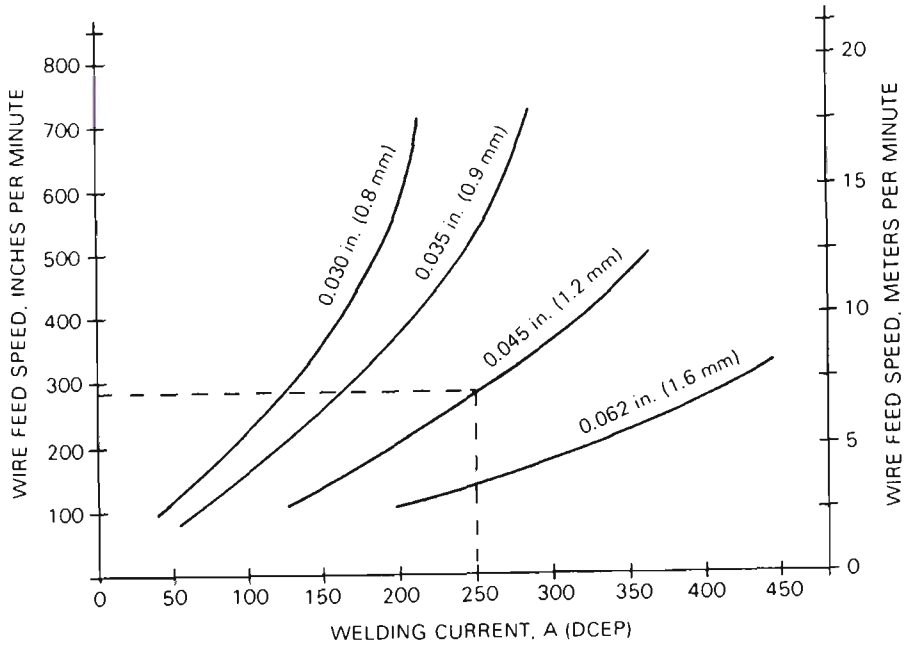

Figure 2.5 Typical welding currents versus wire feed speeds curve for carbon steel electrodes [After Welding Handbook Vol.2 1991].

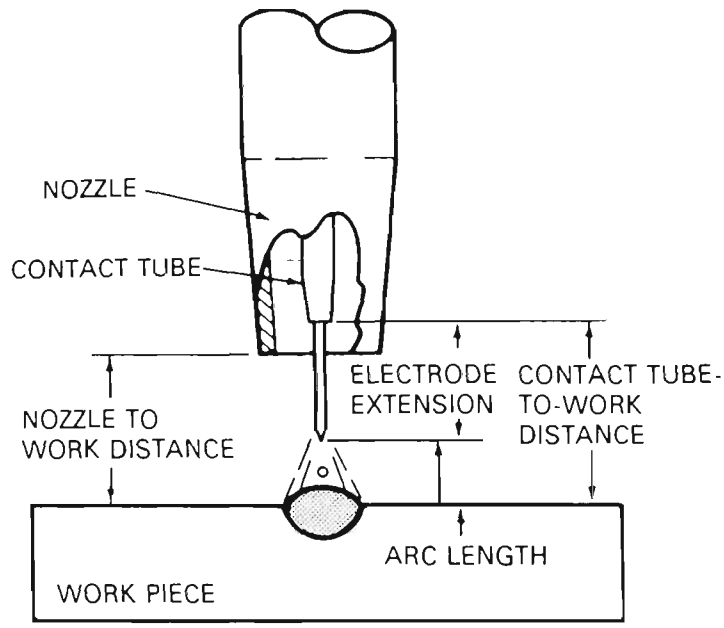

Figure 2.6 A schematic of physical arc length in electrical terms [After Welding Handbook Vol.2 1991].

carbon steel electrodes. At low-current levels for each electrode size, the curve is nearly linear. An increase in the welding current results in an increase in depth and width of weld penetration, the deposition rate and the size of the weld bead.

2.3.2 Polarity

When the welding gun power lead is connected to the positive terminal, the polarity is defined as DCEP (direct current, electrode positive). While the gun connected to the negative terminal is referred to as DCEN (direct current, electrode negative). The vast majority of GMAW applications use DCEP. This condition yields a stable arc, smooth metal transfer, relatively low spatter, and good weld bead characteristics and highest depth of penetration for a wide range of welding currents.

2.3.3 Arc Voltage

Arc voltage is directly related to arc length when all other variables are held constant. Unlike the arc length, arc voltage depends on many other variables such as, the type of electrode and shielding gas, the welding technique and even the length of the welding cable. Although arc length has a great influence on arc stability and weld quality, arc voltage is a parameter used more commonly in welding because it can be more easily monitored and adjusted. **Figure 2.6** is a schematic drawing of physical arc length in electrical terms. The most appropriate arc voltage for a given application is also dependent on sheet metal thickness, type of joint (butt, fillet, T-joint etc.), welding position (flat, overhead, vertical, etc.), electrode diameter and shielding gas composition.

With other variables held constant an increase in voltage tends to widen and flatten the bead profile. High voltage may induce weld porosity, excessive spattering and weld undercut. Reducing voltage results in narrowing of the weld bead and produces a higher weld profile and deeper penetration. If the voltage is too low, stubbing of the electrode on the work piece will occur.

2.3.4 Travel Speed

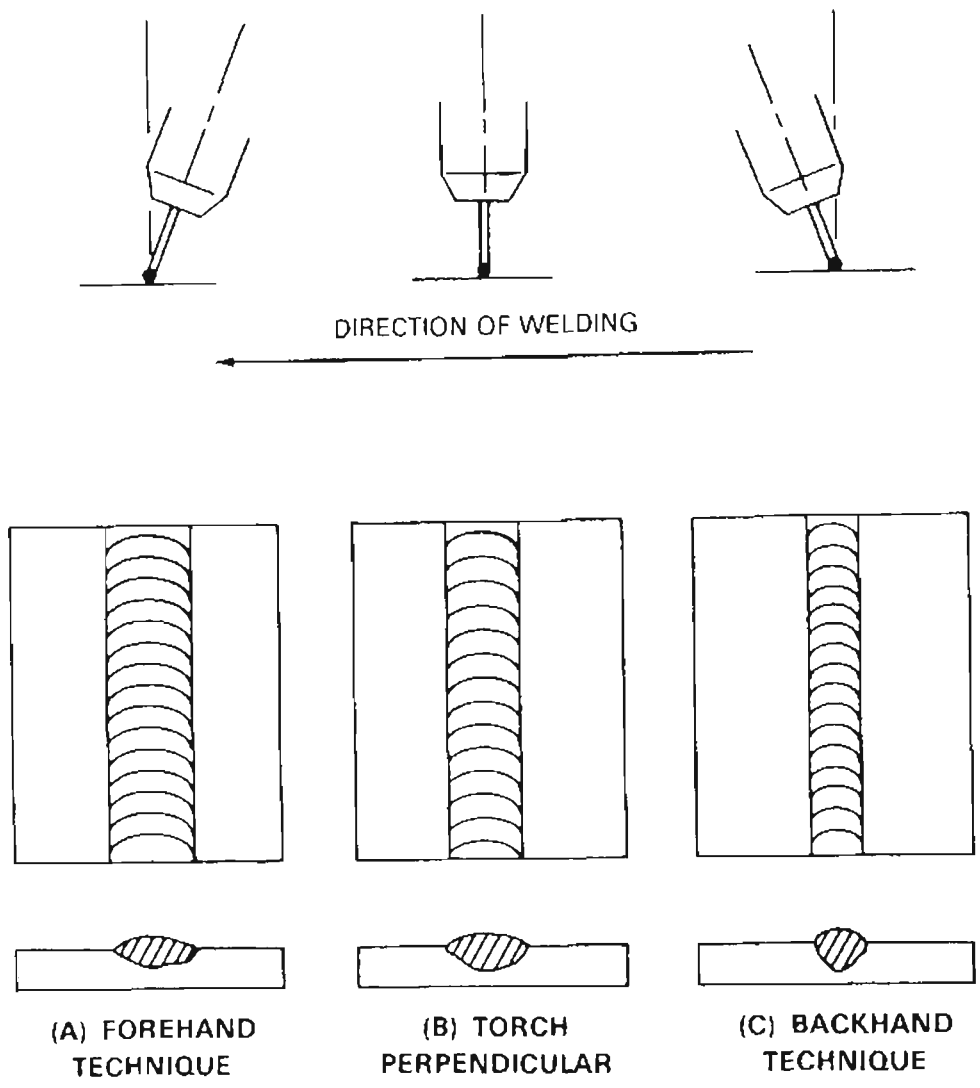

Figure 2.7 Electrode orientation and its effect on the weld bead profiles and penetration [After Welding Handbook Vol.2 1991].

With all other conditions held constant, weld penetration is a maximum at an intermediate travel speed. If the travel speed is too slow, it results in the reduction of effective penetration and a wide weld bead due to the fact that the welding arc impinges on the molten weld pool, rather than on the base metal. If the travel speed is too high, there is a tendency towards under cutting along the edges of the weld bead because there is insufficient deposition of filler metal to fill the path melted by the arc.

The welding speed used for galvanized steels is normally 15 to 20% slower than that used on uncoated steels to allow sufficient time for zinc vaporisation, otherwise the zinc coating ahead of the weld pool will be trapped and vaporised causing porosity [BHP Steel, Handbook, Vol. 4]. This is even more evident in lapped welds. The thicker the zinc coating the slower the welding speed will be, although this is also governed by joint configuration and welding position.

2.3.5 Electrode Extension

Electrode extension is the distance between the end of the welding gun contact tube and the end of the electrode (**Fig.2.6**). An increase in electrode extension increases electrical resistance heating of the wire and results in a subsequent increase in electrode melting rate. The desirable electrode extension is generally from 6 to 10mm for short circuiting transfer and 13 to 25mm for other types of metal transfer.

2.3.6 Electrode Orientation

Orientation of an electrode with respect to the weld joint affects weld bead shape and penetration as shown in **Figure 2.7**. When the electrode is changed from the perpendicular to a lead angle (forehand welding) with all other conditions unchanged, the penetration decreases and the weld bead becomes wider and flatter. Maximum penetration is obtained in the flat position with the drag technique (backhand welding), at a drag angle of about 25 degrees from perpendicular. Backhand welding also produces a more convex, narrower bead, a more stable arc, and less spatter on the work piece. However, the forehand technique allows clear vision of the joint ahead of the

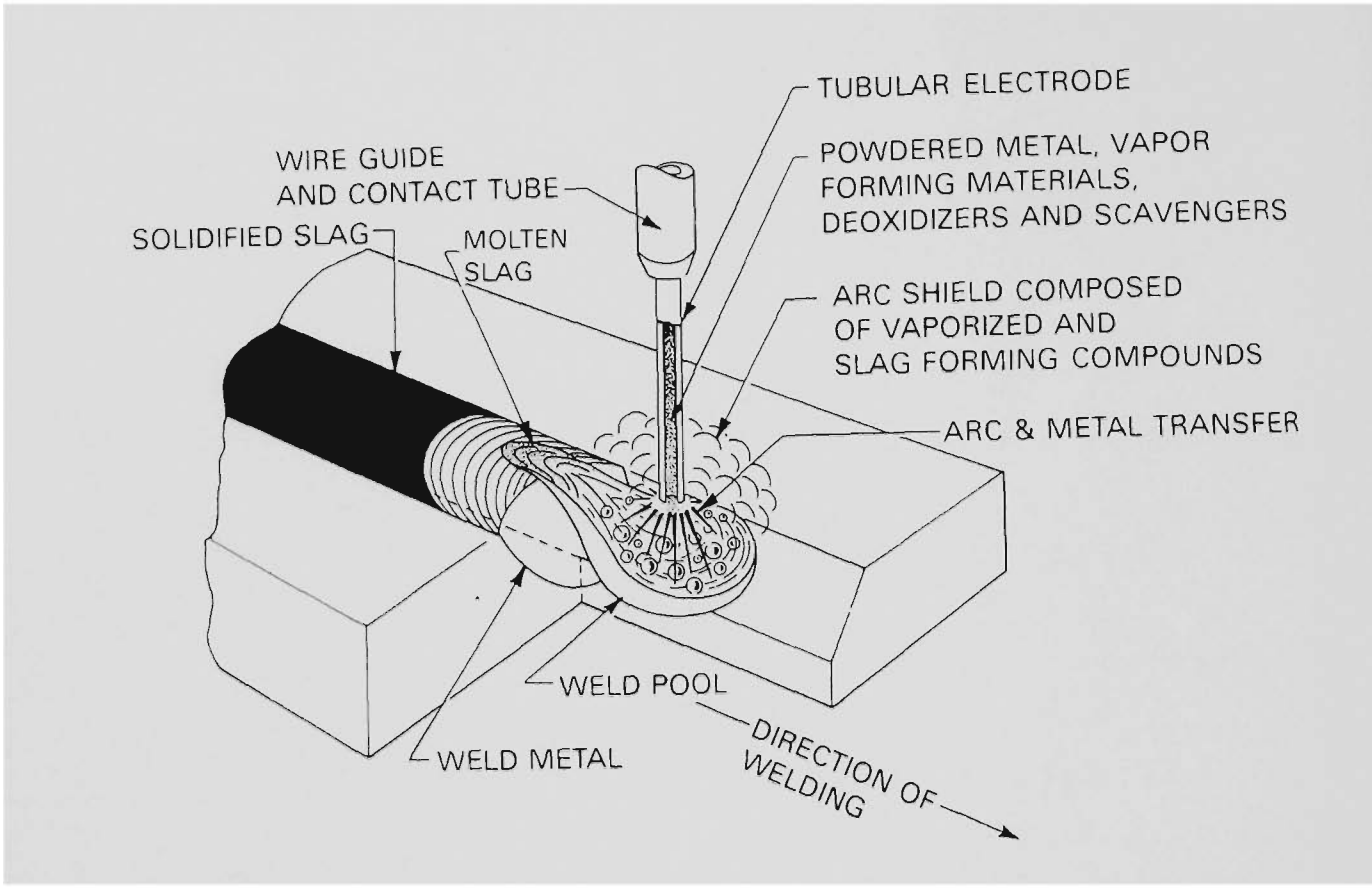

Figure 2.8 Principle of the Self-Shielded Flux Cored Arc Welding (FCAW) process [After Welding Handbook Vol.2 1991].

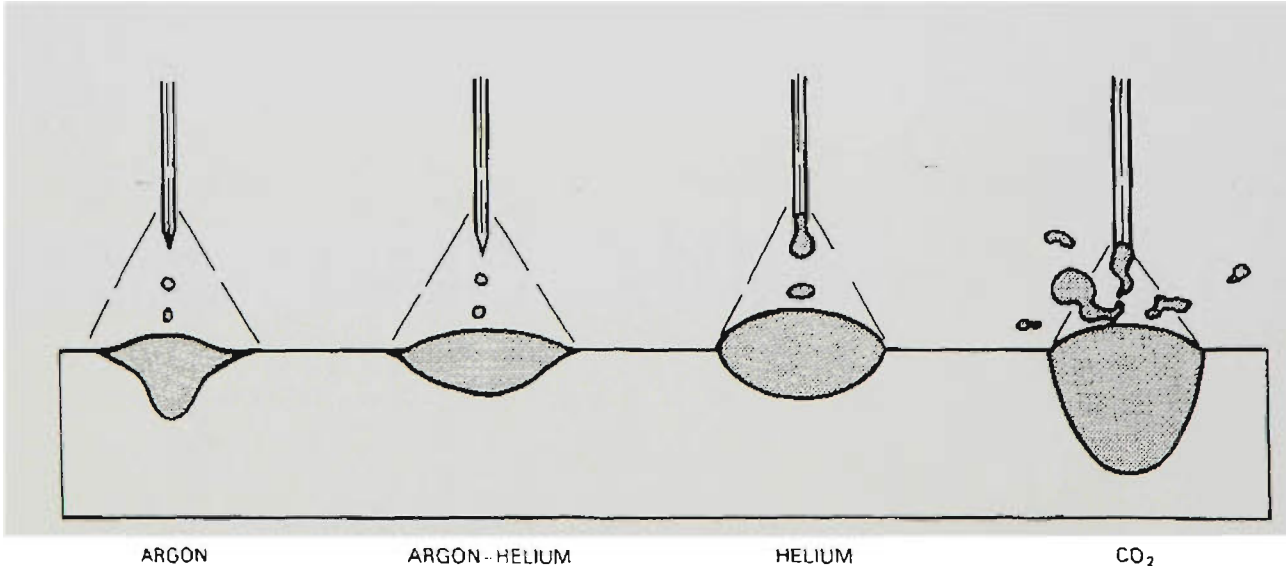

Figure 2.9 Effect of shielding gas on weld bead profile [After Welding Handbook Vol.2 1991].

weld pool and allows easier volatilization of zinc ahead of the weld pool which Zn alloy coated steels.

2.3.7 Electrode Size

Electrode diameter has a direct influence on weld bead configuration. A large electrode requires higher minimum current than a smaller electrode for the same metal transfer characteristics. In turn the higher current generates larger, more fluid weld deposits and results in higher deposition rates and greater penetration.

2.3.8 Gas Flow Rate

Gas flow rate can be an important variable in a GMAW process, too little shielding may generate weld defects by allowing external contaminants to enter the weld pool, and a high flow rate may slow cause turbulence and may disturb the weld pool again causing defects. A flow rate of around 16 litre/min is a good starting point.

2.4 FLUX CORED ARC WELDING (FCAW)

Flux cored arc welding (FCAW) is an arc welding process which also employs an arc between a continuous filler metal electrode and the weld pool. Although the FCAW process operates in a similar manner to GMAW process, the electrode used in FCAW is different to the solid wire used in GMAW. The flux cored electrode has an outer metal sheath with a core consisting of flux or a mixture of flux and metal powder, resulting in an extensive slag cover on the face of a weld pool during welding. Two types of shielding method; self-shielded and external gas shielded can be used in FCAW to protect the arc and weld pool.

In self-shielded FCAW, shielding is obtained by means of vaporization of flux ingredients, which displace the surrounding air. Apart from this, molten metal droplets are also covered by the slag to protect the molten weld pool and slag metal reactions in the weld pool may be used to control weld metal chemistry. **Figure 2.8** illustrates the self-shielded FCAW.

FCAW process is widely used in automotive and fabrication industries for the fabrication of carbon and low alloy steels, stainless steels and cast iron. It has the advantages of high deposition rate, alloying additions from the flux core, slag shielding and support, and improved arc stabilization and shielding. [Norrish 1992].

2.5 CONSUMABLES FOR GMAW AND FCAW

GMAW consumables include the shielding gas and the type of electrode. These consumables are an important consideration in welding galvanized steel.

2.5.1 Shielding Gases

Shielding gas is employed in arc welding mainly to provide a suitable medium for stable operation of a sustained low-voltage arc and to prevent the contamination of the molten weld pool by the atmosphere. Contamination of a weld pool can lead to low strength, or low ductility in the weld metal. An excess of welds defects, such as pits and blow holes, trapped slag and porosity can also be induced by poor shielding or the presence of carbon monoxide, nitrogen and hydrogen in the arc atmosphere.

Shielding gas can significantly influence the overall performance of a welding system. It promotes a stable arc (no wandering/uniform shape), and uniform metal transfer while at the same time controlling the mode of metal transfer in conjunction with other welding parameters [Lyttle and Stapon 1990]. Shielding gas can affect the properties of the weld metal, the shape of weld bead and weld penetration. It can interact with the filler wire as it becomes molten to influence the weld metal strength, toughness and corrosion resistance. It can also affect the residual content of interstitial elements such as hydrogen, nitrogen and oxygen dissolved in the weld metal. **Table 2.1** shows some physical properties of pure gases that are used as or in shielding gases. Typical weld bead profiles under Ar, He, CO_2 and their mixtures are shown in a **Figure 2.9**.

Table 2.1 Physical properties of Ar, He, O_2 and CO_2

Gas chemical symbol	Ar	He	O_2	CO_2
Density kg/m^3	1.784	0.178	1.326	1.977
Specific heat ratio kcal/kg at 20°C	0.125	1.25	0.128	0.197
Ionization potential eV	15.759	24.587	13.618	(14.0)

2.5.1.1 Inert shielding gases

Inert gases argon and helium are used for GMAW of non-ferrous and ferrous metals. The main physical differences between Ar and He are density, thermal conductivity and arc characteristics. Helium is ten times lighter (0.178 kg /m^2) than Ar (1.78 kg/m^2) and therefore less effective than Ar shielding as it has a tendency to rise from the pool surface. Normally, He requires approximately two to three times higher flow rates than Ar to provide an equal protection.

Helium has a higher thermal conductivity (1.25 kcal/kg) than Ar (0.125 kcal/kg) and produces an uniform arc plasma in terms of transmitting energy. Therefore, a wide low weld bead with good fusion and penetration can be obtained with He shielding gas. Ar arc plasma, on the other hand, is characterised by a high-energy inner core and a low energy outer zone resulting in a 'finger' type penetration.

Helium has a higher ionisation potential (24.587 eV) than Ar (15.795 eV) and consequently requires higher arc voltage than Ar. As a result, arc ionisation is more difficult in He than Ar and true axial spray transfer cannot be achieved at any current level in pure He shielding gas. Thus, GMAW shielded with He arc produces more spatter and rougher bead surface than Ar shielded arcs.

2.5.1.2 Mixture of Ar and He

Although pure Ar shielding is used in many applications for welding non-ferrous materials, it does not provide suitable metal transfer characteristics for steels due to the poor arc stability and the poor weld pool fluidity characteristics of an Ar shielded weld

resulting in undercutting at the edge of the weld bead. This poor weld bead shape is due to low arc energy, low heat input and rapid cooling rate and the high surface tension of liquid iron in Ar atmospheres.

Pure He is generally restricted to more specialised areas because of limited arc stability. However, a mixture of Ar-He can overcome some of these problems by means of increasing heat input and can improve the weld bead shape.

2.5.1.3 Oxygen addition to Ar and He

Although oxygen is not used solely as a shielding gas, it is a vital component in shielding gas mixtures for welding steel. Experience has shown that in GMAW of carbon steels, the addition of a certain percentage of oxygen to Ar can significantly improve arc characteristics and reduce the surface tension of weld metal. This effect is a result of its active gas characteristics in that the oxygen can dissociate in the arc intensifying the arc plasma, hence increasing heat input and improving weld penetration and edge wetting. Oxygen also promotes spray transfer in GMA welded steels to give a virtually spatter-free, high productivity process.

2.5.1.4 Carbon dioxide shielding gas

Carbon dioxide is a reactive gas widely used as a shielding gas in GMAW of carbon and low alloy steels. CO_2 shielding gas enables a high welding speed, high joint penetration and low cost. Very sound weld deposits can be achieved by using CO_2 shielding gas, but mechanical properties of weld metal may be adversely affected. With CO_2 shielding, the metal transfer mode is either short circuiting or globular and with the latter transfer mode the arc is quite harsh and produces a high level of spatter.

CO_2 is chemically active, its molecules dissociating at the top of arc at arc temperatures above 6000°C in an endothermic reaction to form excited species of oxygen and carbon monoxide:

$$\mathbf{2CO_2 \Leftrightarrow 2CO + O_2 - 136\ calories}$$

The CO will recombine at the bottom of the arc and has exothermic reaction in contact with the workpiece resulting in a superheat on the transferring molten filler metal and creating deep penetration, a fluid weld pool and promoting the deposition of convex weld beads. On the other hand this reaction produces a disruptive force upward into the arc causing unstable arcs and welding spatter.

CO_2 is not only widely used alone as a shielding gas in GMAW but it is widely used as addition to Ar and He inert gases. The optimum amount of O_2 and CO_2 additions to the inert gases depends on the parent metal, the joint geometry, the welding position and the welding technique. Experimentally, additions from 1 to 5% O_2 or from 3 to 25% CO_2 to Ar produce a noticeable improvement in arc stability and freedom from undercut by eliminating the arc wander caused by cathode sputtering.

2.5.1.5 Shielding gases used for GMAW and FCAW on Zn alloy coated steels

A large amount of valuable research work on welding galvanized steel was carried out in the late 60s in Europe and the United States due to the increasing demand for galvanized steels in automotive industry. The application of galvanized steels has been increasing not only for spot welded parts but also for arc welded parts. The details of welding conditions are well documented [Puech 1959; Boekholt 1964; Van Eijnsbergen 1967].

Shielding gas plays a very important role in arc welding processes because of its effect on the metal transfer and microstructure and properties of welds. Practically, shielding gas and gases mixtures used for arc welding mild steels can also be used for the galvanised steels. The least expensive and most common shielding gas in GMAW of steels is CO_2. Suitable conditions have been determined for CO_2 welding and argon and CO_2 mixes (typically 80% argon/20% CO_2) of 1.58 mm and 3.18 mm galvanized steel using a short circuiting arc [Gregory 1968].

Unlike the GMAW of uncoated steel, the reduction of spatter by using the argon and CO_2 shielding gas mixture does not apply to galvanised steel in respect of superior

surface appearance, weld bead shape and less spatter compared with welding in CO_2 shield. However, the GMAW of galvanised steel using CO_2 induces high spatter levels and the spatter problem can be eliminated by the use of silicon based or petroleum based anti-spatter sprays, sprayed onto the sheet surface prior to welding [Gregory 1968].

Generally, arc welding in the short circuit transfer mode using CO_2 or high levels of CO_2 (>15%) appears to reduce porosity compared to low levels of CO_2 (=1 ~5%). This result was interpreted on the bases that the high level of CO_2 induces a higher voltage for a given wire speed and consequently increases heat input [Black 1993; Black and Lange 1993]. Thus, it is implied that the higher porosity resulting from the low levels of CO_2 is due to a lower operating voltage for a given wire feed rate, and generating lower arc energy and heat input compared to that of the high levels CO_2 gas. Although the CO_2 level in shielding gases has been shown to be a less critical for the spray transfer mode, gas containing 10-16% CO_2 tends to produce sounder welds in spray mode than gases with lower levels of CO_2. The addition of helium effectively increases arc voltage and heat input [Black 1993; Porter 1983].

"Argoshield" gases produced by CIGWELD contain various percentages of carbon dioxide, oxygen, helium, hydrogen and argon: Argoshield 50 (91.9% Ar + 5% CO_2 + 3.1% O_2), Argoshield 51 (81.25% Ar +16% CO_2 + 2.75% O_2) and Argoshield 60 (98.5% argon + 1.5% O_2). Used in conjunction with Autocraft LW1 (CIGWELD) welding wire (copper coated steel wire) have been successfully used for GMAW on light gauge galvanized steels in terms of weld bead shape and penetration requirements. A silicon bronze wire with Argoshield 70 (99.3% Ar + 0.7% O_2) has also been recommended [Howes 1992]. However, Argoshield 54 (91.5% Ar + 7%CO_2 + 1.5% O_2) is recommended by the BHP steel.

2.5.2 Electrodes for GMAW and FCAW of Zn Alloy Coated Steels

Generally, electrode wires, such as AWS A5.18 ES4 and ES6 used in GMAW of mild and low alloy steels can be used for joining the galvanised steel. The ES4 wire is designed primarily for GMA welding on mild and low alloy steels using Ar based

shielding gases. ES6 contains higher Si and Mn was recommended for use with CO_2 or with single pass welds under Ar based gases. It was reported that a liquid Zn penetration cracks were present in galvanised steel welds using ES6 wire and CO_2 shielding gas [Gregory et al. 1969]. However, investigation carried out at BOC indicated that there was no cracking problem for any welds of Zn coated steels and the ES6 can reduce the spatter level due to the increased Si and Mn content [Black 1993; Black and Lange 1993].

Small diameter electrode wires should be selected for welding thin sections to achieve a high current density with a high degree of self-adjustment of the arc so that the arc length remains constant [Gregory 1968].

Commercial wires of self-shielded flux cored arc welding such as Shield-Cor 15 (produced by CIGWELD) and Fabshield 21B (provided by WIA-Welding Industry of Australia) are specially designed for single pass welding of mild and Zn alloy coated thin gauged steels. They both require DC electrode negative polarity in order to minimize the risk of burn through on thin plate.

CHAPTER 3

RECOVERY ANNEALED, COLD ROLLED, ZINC ALLOY COATED LOW CARBON SHEET STEELS

Figure 3.1 Typical microstructure of cold rolled steel in longitudinal rolling direction [After Metal Handbook Vol.7 1972].

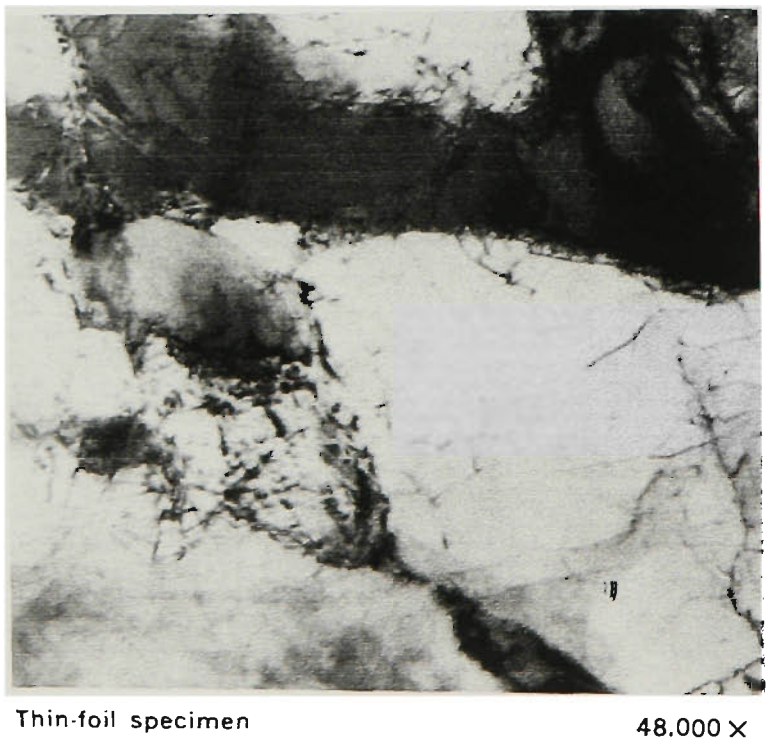

Figure 3.2 TEM micrograph of microstructure showing the tangled dislocation networks in subgrains of the cold worked steel [After Metal Handbook Vol.7 1972].

3.1 RECOVERY ANNEALED C-Mn COLD ROLLED STRUCTURAL SHEET STEELS

High strength, recovery annealed C-Mn structure sheet steels are produced by a combination of cold rolling and annealing. The high strength of the recovery sheet steels is controlled by both the degree of cold rolling reduction and the extent of restoration of the deformed structure by the use of a subsequent controlled annealing treatment. Hot dip zinc or zinc alloy coating are also deposited on the sheet steels for corrosion protection.

Recovery annealed sheet steels are widely used for fabricated structural members in the building and construction industries as well as in the automotive body parts due to mainly a lower cost than high strength low alloy steels. The use of coated steels in automotive construction has increased dramatically over the past decade. Statistics also show that between 60% and 100% of the components in present day auto-bodies are coated steels, either pure zinc or zinc alloy coatings [Chatterjee and Waddell 1996].

3.2 MICROSTRUCTURE AND PROPERTIES OF COLD ROLLED STRUCTURAL SHEET STEELS

Microstructure of a metal changes during cold working in three major ways: a change in grain shape and increasing total grain boundary area are observed first; followed by the accumulation of the dislocations within the grains; and then with a change of crystal orientation relative to the direction of the applied stress (rolling direction). These changes are not random and involve rotations, which are directly related to the crystallography of the deformation. As a result, the grains achieve a preferred orientation, or texture, which becomes stronger as deformation proceeds. The properties of a rolled sheet or plate depend on the direction in which the properties are measured [Asland 1996].

The recovery annealed cold rolled steels are a class of low carbon sheet steels with a typical chemical composition as given in **Table 3.1**. **Figure 3.1** shows the typical microstructure in longitudinal sections (rolling direction). It is clearly shown that the

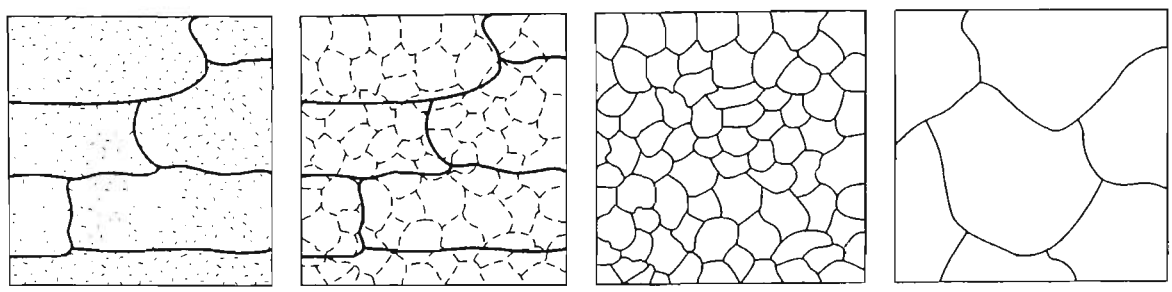

Figure 3.3 The effect of annealing temperature on the microstructure of cold-worked metals: (a) cold worked, (b) after recovery, (c) after recrystallisation, and (d) after grain growth [After Askeland 1996].

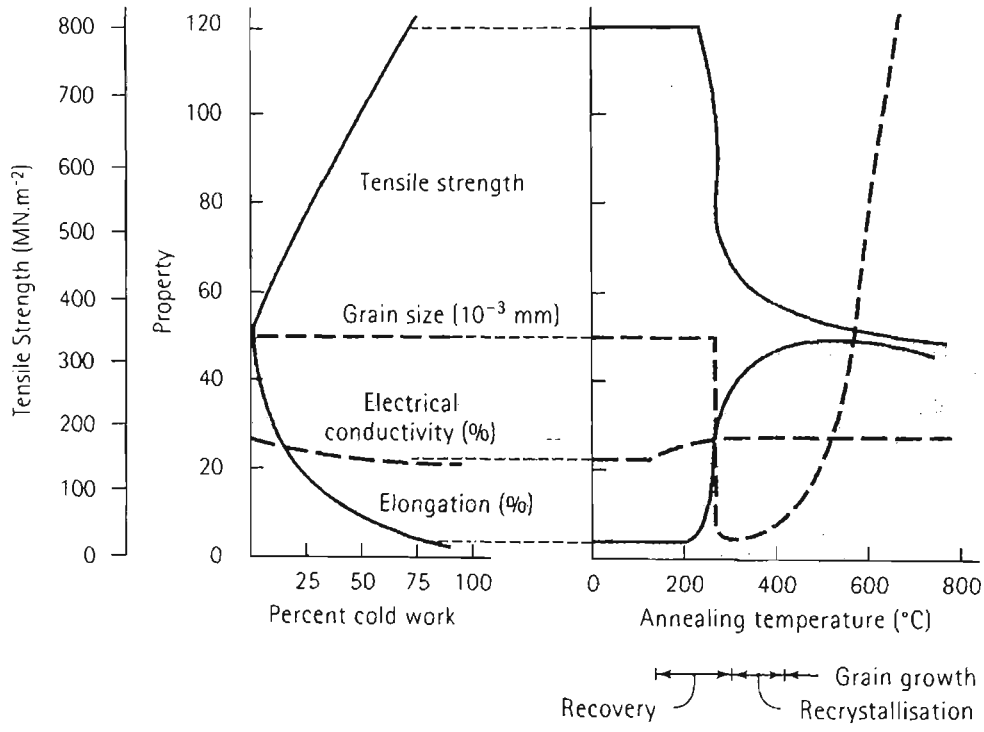

Figure 3.4 The effect of cold work on the properties of a brass (a), and the effect of annealing temperature on the properties of a brass of 75% cold-worked [After Askeland 1996].

ferrite gains are elongated by deformation along the rolling direction. The tangled dislocation networks present after cold rolling are converted by heat treatment into an imperfect subgrain structure resulting in a decrease in the yield and tensile strengths and an increase in the ductility (**Figure 3.2**). The time and temperature of the heat treatment are a function of steel grade, cold reduction and sheet thickness and are controlled to permit partial recovery without recrystallisation. The recrystallisation temperature depends strongly on the thickness reduction of cold rolling.

Table 3.1 Typical chemical composition of the recovery annealed, Zn alloy coated sheet steels (wt.%)

C	P	Mn	S	Al	N
0.04-0.07	0.01-0.02	0.2-0.3	0.01-0.02	0.03-0.05	0.001-0.005

The recovery annealed steel has high tensile strength (up to 780 MPa) and relatively low ductility (down to 1%). Softening can occur if the strain hardened base metal is annealed by reaustenisation and/or recrystallisation. The consequent softening cannot be recovered by subsequent heat treatment [AWS Welding Handbook, Vol. 1, 1987] which limits the usage of the cold rolled low carbon steels.

3.3 ANNEALING HEAT TREATMENT

Annealing is a heat treatment aimed to eliminate deformation-induced damage. Annealing process can be broadly divided into three distinct processes: recovery, recrystallization and grain growth, as shown in **Figure 3.3**. **Figure 3.4** illustrates the effect of cold rolling on the properties of brass.

3.3.1 Recovery

Recovery occurs prior to recrystallization resulting in restoration of physical properties of the cold worked metal and without any significant change in microstructure. The cold worked metal consists of deformed grains with a large number of tangled dislocations resulting in the increase in strength, hardness and electrical resistance and a reduction in ductility. When the metal is heated up to about 205 ~ 230°C, the additional thermal

energy permits the dislocations to move and form the boundaries of a polygonised subgrain structure without a substantial change in dislocation density. Although the residual stress has decreased to a relatively low level, the strength of the metal is still relatively high and the ductility improves, but is still rather low because the microstructural changes are minor.

3.3.2 Recrystallization

Recrystallization occurs by the nucleation and growth of new grains containing few dislocations in which a group of new grains form and grow in the deformed grains of the cold worked metal. These grains consume the old grains and eventually all signs of the deformed grains disappear. The new microstructure resembles the microstructure prior to cold working and the metal is softer and more ductile than it was in the cold worked condition because the number of dislocations is greatly reduced.

The recrystallization temperature of a deformed metal depends on the composition of the metal, the reduction by cold work and the heating rate.

3.3.3 Grain Growth

Grain growth occurs in cold rolled metal with prolonged heating after recrystallization. Grain growth results in the hardness and strength of the metal decreasing significantly.

3.4 ZINC ALLOY COATINGS OF SHEET STEEL

Corrosion resistant materials such as zinc and zinc alloys are often coated on the surface of steel sheet to extend its service life. Sheet steels with Zn coating are called galvanized steels (BHP trade name ZINC-HI-TEN in Australia), which are produced by either electrogalvanizing or hot-dip galvanizing. The most common coating method used is hot-dip galvanizing which can be applied by either a batch method or in a continuous process. Continuous hot-dip galvanizing is only applied to sheet, wire and tube and normally has a coating weight of 40 to 366 g/m^2 corresponding to a coating thickness of 6 to 52 μm.

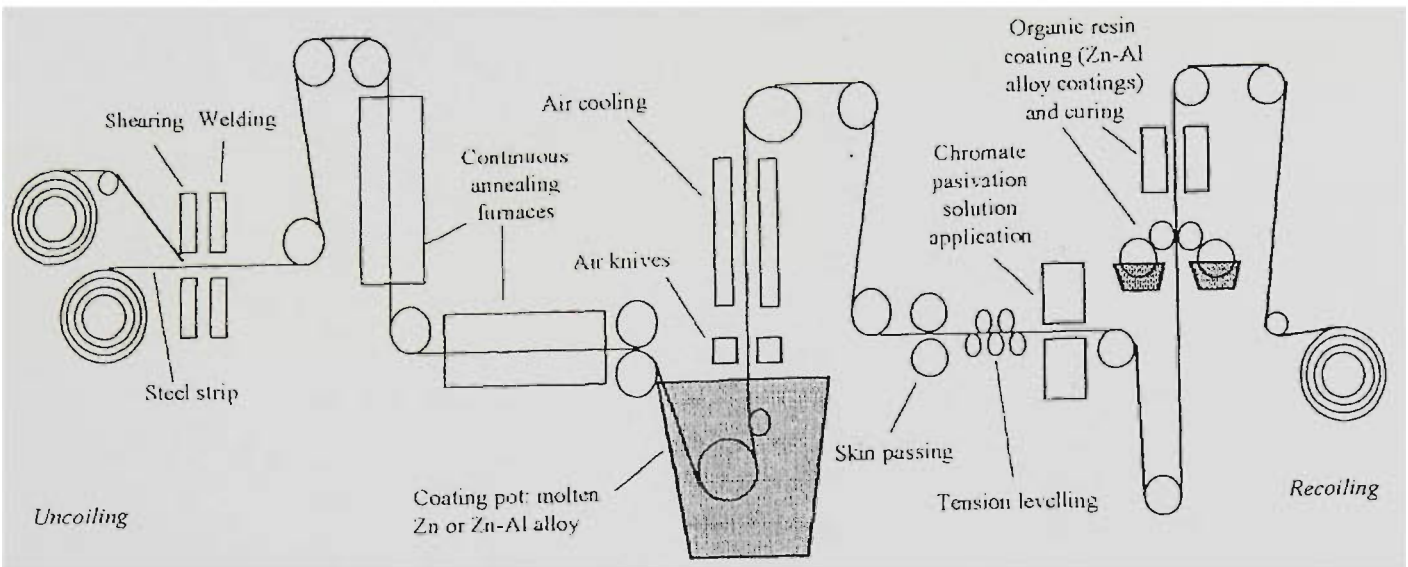

Figure 3.5 Schematic representation of a molten metal coating line [After Mcintosh 1999].

The zinc can be alloyed with aluminum to improve performance. The two most widely used zinc-aluminum hot-dip galvanizing coating are Galfan (trade name in US), a Zn-5%Al-0.1% m isch-metal coating, and Ga lvalume (trade na me in U S), a Zn-55%Al-1.5%Si coating. The former is known as ZINC-HI-TEN and latter is called ZINCALUME in Australia under license by BHP.

Hot-dip-coated, low carbon steel sheet is available with a broad range of mechanical properties from 241 to 620 MPa [ASM, Specialty Handbook, 1996]. Compared to uncoated steel, the hot-dip-coated, low carbon steel sheet has slightly less ductility because of the thermal effects of the coating process on the precipitation of carbon in the steel and associated age hardening.

3.4.1 Zinc and Zinc Alloy Coating Processes

The process of hot-dip galvanizing is shown schematically in **Figure 3.5**. Steel strip in coil form is loaded into the entry uncoiler and then passes into a direct fired furnace to burn away any oil/lubricant residuals on the strip surface and to heat the strip up to an annealing temperature required for the specified mechanical properties. The strip then travels through a radiant tube furnace to reduce iron oxide on the strip surface. The clean strip is then dipped into the metal coating bath, which contains Zn or Zn alloy molten metal at a temperature around 600°C. By passing through the bath, a Zn or Zn alloy coating layer is formed by alloying with the iron on the strip surface. The thickness of the coating is controlled by applying pressurized air streams to the strip surface using a set of air knives (stripping nozzles) to blow away any excessive amount of coating metal. After the solidification of the coating, the strip undergoes certain post hot-dip treatments, such as skin passing, tension leveling (involving cold work to improve the strip surface, shape and tensile properties) and chromate-based chemical passivation t o p revent t he c oating from any unexpected wet corrosion a ttack during storage or transportation. An organic coating is applied to some aluminum-zinc coated steels to provide lubrication.

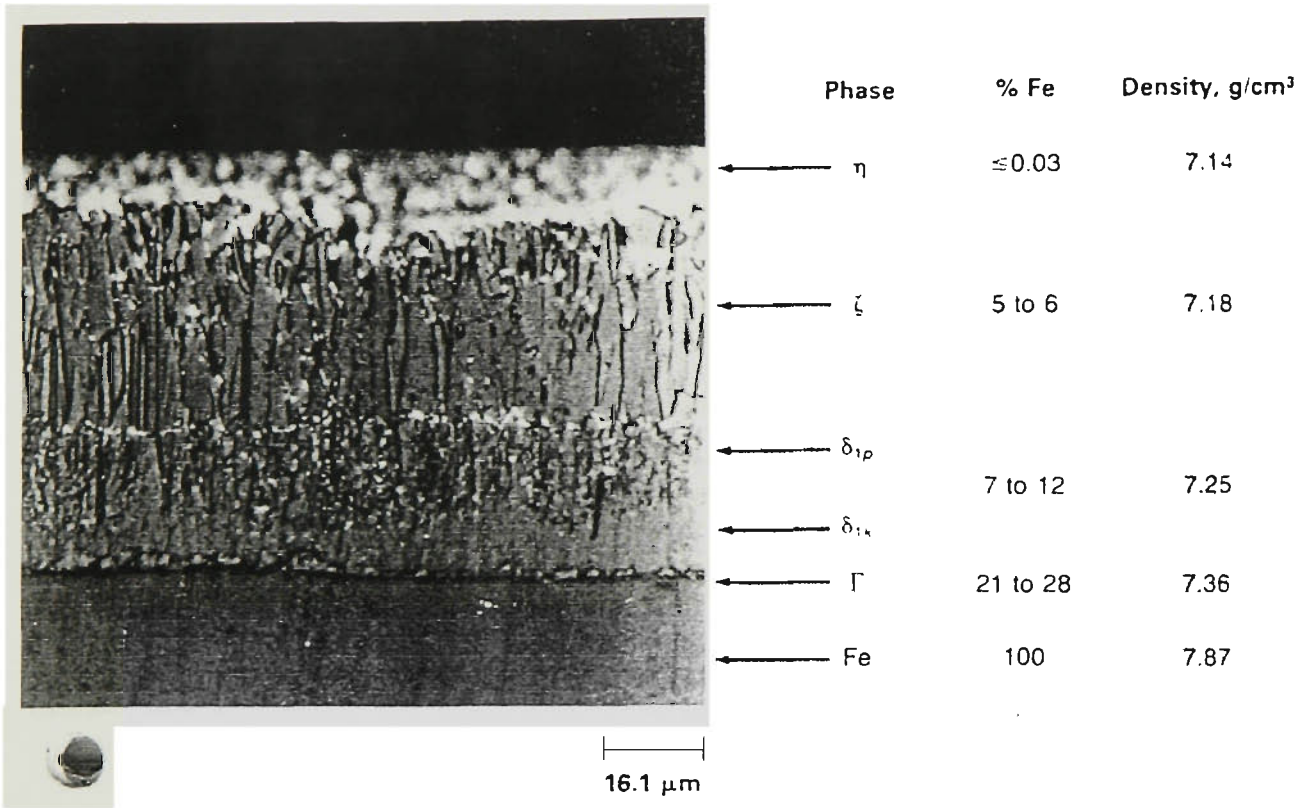

Figure 3.6 Typical hot-dip galvanized coating with various layers [After ASM Specialty Handbook 1996].

3.4.2 Microstructure of Zinc Coating

A typical coating thickness for general purpose galvanized steel is about 19 μm per side with a coating weight of 275 g/m^2 to both sides. In general, aluminum additions in the range of 0.1 to 0.2% are added to the zinc bath in order to prevent formation of a thick, continuous layer of zinc-iron intermetallic that could lead to poor coating adhesion during forming. The aluminum reacts preferentially with the steel to form a thin layer of an iron-aluminum intermetallic compound that acts as a barrier and delays the growth of the zinc-iron intermetallic layer.

Figure 3.6 shows that the microstructure of a typical hot dip galvanized coating consists of a series of layers. The relative properties and identification of these layers are given in **Table 3.2**. Each successive layer contains a higher proportion of zinc laminating with an outer layer which is relatively pure zinc. However, there is no real line of demarcation between the iron and the zinc, only a gradual transition through the series of zinc-iron intermetallic, providing a powerful bond between the base metal and coating.

Table 3.2 Properties of alloy layers of hot-dip galvanized steels

Layer	Alloy	Iron, %	Melting point °C	Crystal structure	Diamond pyramid micro-hardness	Alloy characteristics
Eta (η)	Zinc	0.03	419	Hexagonal	70-72	Soft, ductile
Zeta (ξ)	$FeZn_{13}$	5.7-6.3	530	Monoclinic	175-185	Hard, brittle
Delta (δ)	$FeZn_7$	7.0-11.0	530-670	Hexagonal	240-300	Ductile
Gamma(Γ)	Fe_3Zn_{10}	20.0-27.0	670-780	Cubic	...	Thin, hard, brittle
Base metal	Iron	...	1510	Cubic	150-175	...

It should be noted that the layers vary in hardness with the free zinc layer (η) being relatively soft, while the alloy layers are even harder than annealed base metal. The structure of the galvanized coating, particularly the relative thickness of δ and ξ layers is primarily influenced by the steel chemistry and, to a lesser extent, by the galvanizing temperature and the duration of immersion [Jagannathan 1992]. The comparison of

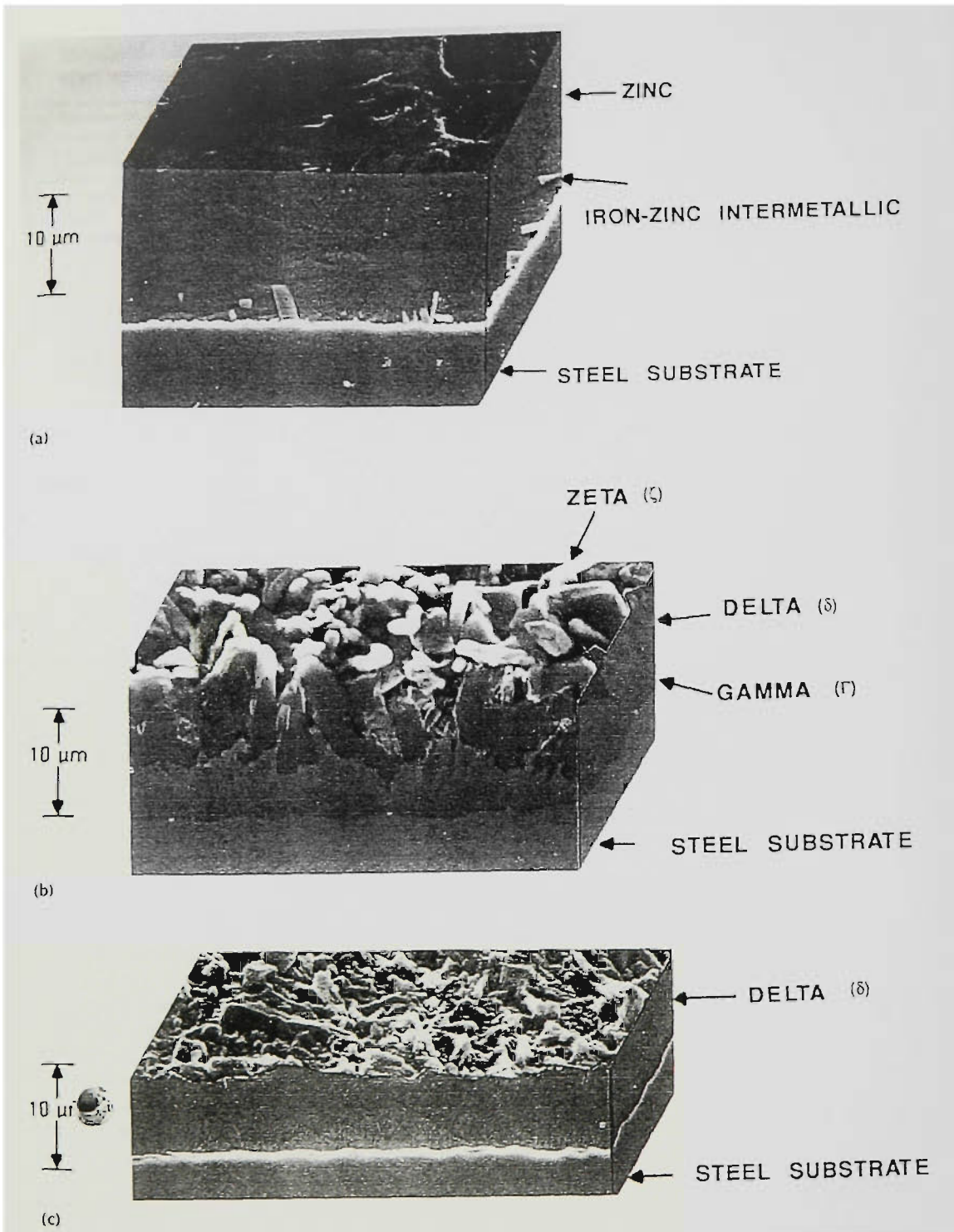

Figure 3.7 Comparison of continuous hot-dip coating surface morphologies and microstructures. (a) Galvanized coating microstructure; (b) Galvanneal coating microstructure composed of ξ, δ and Γ microstructure; (c) Galvanneal coating microstructure composed of mostly δ phase [After ASM Speciality Handbook 1996].

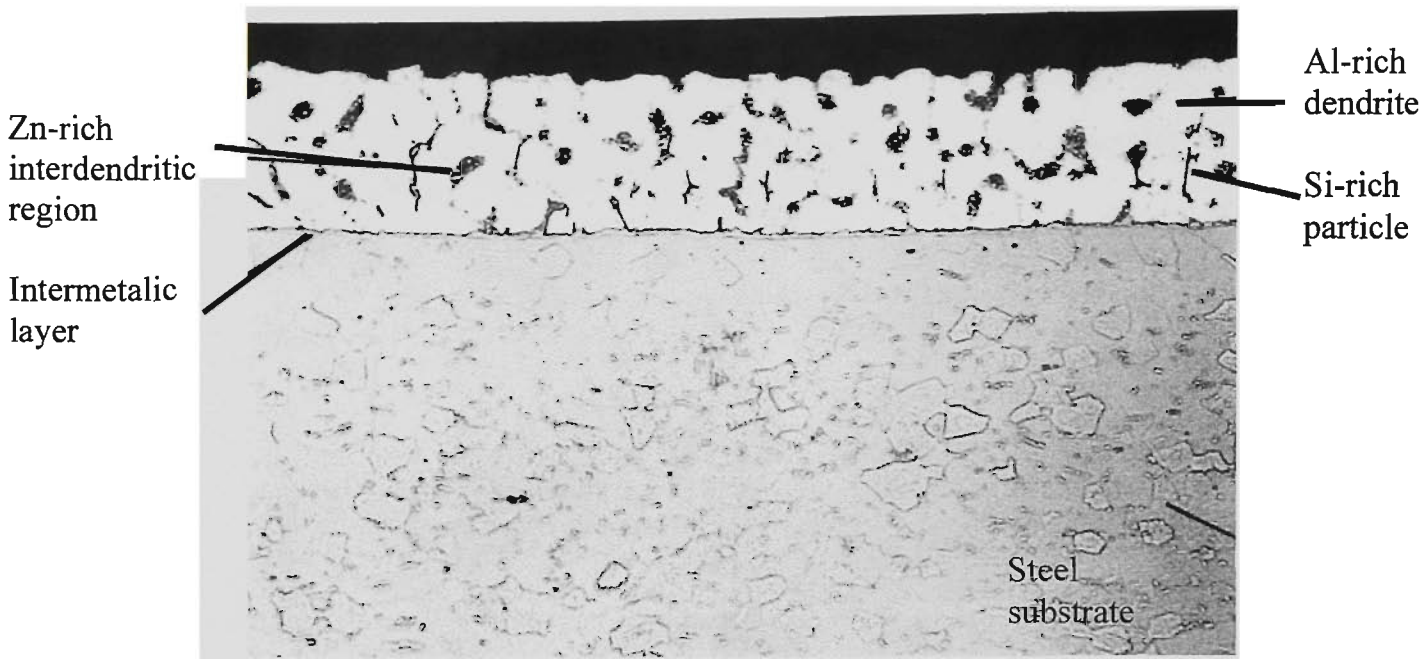

Figure 3.8 Microstructure of an aluminium-zinc coating of ZA sheet steel [After ASM Handbook Vol.1 1990].

continuous hot-dip coating surface morphologies and microstructures are shown in **Figure 3.7**. The galvanized coating is very adherent because it is metallurgically bonded to and integral with the steel.

3.4.3 Microstructure of Zinc Aluminum Coating

With a normal composition of 55%Al, 43.5%Zn, and 1.5%Si (wt.%), the Zn-Al coating provides the durability and high temperature resistance of aluminum coatings with the sacrificial protection characteristics of Zn coatings. The silicon is added to the coating bath to control the growth of intermetallic layer. Coating thickness for aluminum-zinc coatings is usually in the range of 20 to 25 μm. Two main coating weights are produced 150 and 200 gms/m^2 to both sides of the steel sheet.

The 55Al-Zn coating has a two-phase structure of cored aluminum-rich dendrites and a zinc rich interdendritic constituent. This overlay is bonded to the steel substrate by a thin intermetallic layer whose structure are various depending on the compositions. If the intermetallic layer consists of 48%Al, 24%Fe, 14%Zn, and 11%Si (wt.%), a X-ray diffraction suggests the structure similar to $Al_{13}Fe_4$ [ASM Specialty Handbook 1996]. If the intermetallic layer has a composition of 71.4%Al, 18.5%Fe and 7.4%Si (at.%), the phase was assigned as Fe_2Al_5 [BHP Internal Report]. However, a structure of $Fe_5Si_2Al_2$ is determined when the intermetallic layer containing of 74.1%Al, 18.5%Fe and 7.4%Si (at.%) [BHP Internal Report]. A quarternary phases are also assigned if the intermetallic layer consist of 69.7%Al, 15.0%Fe, 9.6%Si and 5.7%Zn or 69.9%Al, 20.1%Fe, 6.2%Si and 3.7%Zn (at.%) [BHP Internal Report]. In addition, silicon particles are often found in the interdendritic region, as shown in **Figure 3.8**. By volume, the coating is approximately 80% (Al+Si) and 20%Zn. The effect of cooling rate during solidification is manifested in the spacing between the dendrite arms. Faster cooling results in finer spacing, which improves corrosion resistance.

3.5 F USION JOINING OF GALVANIZED STEEL SHEET

Fusion welding is a welding process in which two pieces of a metal are joined together by heating up to its melting point and forming a molten pool between the parts which

solidifies to form a weld. The three most important characteristics of a fusion welding process in terms of the effect on the properties of the joint are the intensity of the heat source, the heat input rate per unit length of weld and the effectiveness of the method used to shield the weld from the atmosphere [Lancaster 1999].

Galvanized steel sheet can be joined by the same fusion welding processes as uncoated steel and the coating is normally not removed. However, with thick steels and thick coatings removal of the coating can be beneficial to improve the weldability of the galvanized steels by reducing spatter and porosity in the welds. The most common fusion welding processes used in joining the galvanized steel sheet are manual metal arc welding (MMA), GMAW, FCAW, oxyacetylene welding, tungsten gas welding, spot welding and laser welding.

3.5.1 Manual Metal Arc Welding (MMA)

In MMA, coalescence of pieces of metal is produced by heat from an electric arc that is maintained between the tip of a covered electrode and the surface of the base metal in the joint being welded.

The MMA welding conditions for 1mm to 3mm thick galvanized sheet steel were published in the 1960s [Lundin 1969; Gregory 1969]. Rutile and basic coated electrodes were recommended because the rutile slag and deposited silicon levels of around 0.2% were demonstrated to produce crack free fillet welds [Puech 1959].

Compared to the uncoated steel, a higher heat input is needed to remove the zinc from weld pool and lower welding speed is used (10 to 20% lower) to burn off as much zinc as possible in front of the weld pool [BHP Handbook, Vol. 4]. A larger gap is also necessary between the sheets in butt joints due to the decreased penetration with galvanized sheet welds.

3.5.2 GMAW and FCAW

Galvanized steel sheet can be joined by GMAW using a solid electrode wire and FCAW using a cored material electrode wire. The welding procedures are similar to those for uncoated low carbon steel. Travel speed is also slower on galvanized steel to allow the zinc coating to volatilize ahead of the weld pool. The required reduction in speed depends upon the thickness of the zinc coating, the joint design, and the welding position. Root openings must be greater than for uncoated steel to obtain good joint penetration and provide a path for vaporized zinc to escape.

Pulsed GMAW is specially designed for joining thin sheet steel and it provides a lower heat input than normal GMAW. Pulsing current enables higher weld metal deposition rates, better control of weld penetration and improve weld metal mechanical properties. It also produces less fuming of the zinc surface [WDF Article 1984].

GMAW was for some time used only with CO_2 as the shielding gas but there were many problems. These included weld porosity, unstable arc characteristics, lack of consistent wetting properties (leading to poor fusion) and weld spatter. Although the pulsing technique, new gas shielding formulations and spray on spatter release compounds can now take care of most of these drawbacks, in the mid 1970s FCAW and MIG braze arc welding (MBAW) were seen to provide the solution. FCAW was used for galvanized materials greater than 1.5mm thick and MBAW was used for materials from 0.71mm to 1.47mm thick [Jud 1984].

Only minor equipment changes are required to convert from the GMAW process to the FCAW process. Due to the larger diameter of the wire, drive rolls, wire liners and welding gun contact tip replacement is required. In addition, a straight polarity electrical hook-up is required, i.e. electrode negative ground positive and no external gas shielding is required for self-shielded FACW. The FCAW process minimizes weld spatter and produces a higher quality weld than GMAW with a CO_2 shielding gas [AWS, Welding Handbook, Vol.2 1991].

3.5.3 Oxyacetylene Welding

Oxyacetylene fusion welding uses acetylene combustion with oxygen as a heating medium, joining workpiece together by melting both the base metal and filler wire.

The heat input, weld bead size and shape, and weld puddle viscosity can be controlled by controlling the gas flow and the filler metal. Oxyacetylene fusion welding can be employed for Zn alloy coated steel welding, especially in the repair industry. It has been reported that the Zn alloy coating was completely and partially removed for up to 12mm from the weld due to the effect of welding heat [Palmer 1953]. The corrosion resistance therefore was reduced in this region. Beyond this region up to a further 20mm from the weld, a change in the appearance was observed without any deterioration in corrosion resistance.

3.5.4 Gas Tungsten (TIG) Arc Welding

Gas tungsten arc welding uses an arc between the tungsten electrode (non-consumable) and the weld pool with or without additional filler metal. Joining coated steels is a challenge for gas tungsten-arc welding. An erratic arc behavior can be caused by zinc or spatter due to its contamination to the tungsten electrode. Porosity may be developed in the weld metal because the lack of deoxidizers when no filler metal is used. The TIG welding process can be used to produce brazed welded joints and the suitable conditions for braze welding butt and lap joints in 1.2mm galvanized sheet with silicon-bronze or tin-bronze filler rod have been published [Etude 1960].

3.5.5 Spot Welding

Spot welding is a resistance welding process in which coalescence of metal is produced at the faying surfaces by the heat generated by the resistance of the work to the passage of electric current [AWS, Welding Handbook, Vol. 2, 1991].

Spot welding is commonly used to join coated steel sections thinner than 5mm thick if the coating is lighter than $300g/m^2$. Spot welding is also a major process used for

joining automotive components. It has been reported that a typical family car is held together by 3000-4000 spot welds and a typical car plant will make over one million spots per day [Chatterjee 1996]. The electrode life is much shorter when welding coatings up to 450g/m^2 [AWS Welding Handbook, Vol. 4, 1998], because Zn melts at 419°C, well below the temperature produced momentarily at the electrode-to-work interface. The molten Zn easily alloys with the surface of the copper based electrode, hence resulting in build-up of Zn on the electrode tip. The electrode life in resistance spot welding depends greatly on the type of the coating, i.e. galvanized, Zn-Al or Al. The higher the Al content in the coating, the shorter the electrode life due to the harder intermetallic compounds formed at the electrode surface in Zn-Al coated steel than Zn coated steel [Eriguchi et al. 1995]. However, the electrode life in spot welding can be improved by adopting PVD (physical vapor deposition) coating to the spot welding electrodes [Finlay et al. 1997], or by changing the electrode tip shape or angles, as well as the electrode materials [AWS, Welding Handbook, Vol.4 1998].

The ratio of zinc coating weight to sheet thickness can affect the welding quality [Gregory 1968]. Sound CO_2 spot welds can be made in 3mm sheet having a zinc coating weight of 381g/m^2, while spot welds in 1.6 mm galvanized sheet with same zinc coating weight have adequate strength but the welds contain porosity. Cracking is also most often observed when Zn is present at the weld root, particularly with fillet welds and T-joint welds. The cracking in weld metal may be caused by the intergranular penetration of zinc into the weld metal. The cracking problem in the weld metal can be minimized by the proper design of the welding process, choice of correct consumable, selection of the galvanizing base metal, joint type, root opening and the ratio of thickness to coating weight.

3.5.6 Laser Welding

Laser welding uses a high-energy coherent beam of light of a fixed wavelength as a heat source. The high-intensity beam is produced by stimulating emission of electromagnetic radiation in suitable gaseous or solid materials. In welding applications the two most common types of laser are the CO_2 gas laser and neodymium: yttrium aluminum garnet

(Nd:YAG) solid state laser [Bransch et al. 1991; Bransch 1991; Svelto 1982; Hoult 1990].

In CO_2 lasers, the active medium is a mixture of carbon dioxide, helium and nitrogen, which is electrically excited to produce laser radiation of wavelength 10 .6μm. Such lasers are commercially available with output powers up to 25 kW. Most of the laser used for high-productivity welding are in the 2 to 5 kW range [Martyr 1987; Norris 1990; Powley 1992; Wirth 1985]. The laser power can be delivered in the form of a continuous wave or in a series of pulses.

Laser welding of thin galvanized steel sheet (0.8 ~ 1.5mm) is becoming increasingly popular in the fabrication of agricultural equipment, vehicle body shells, automotive products and domestic appliances. Welding steels which have been electro-plated or hot-dip galvanized with a Zn-based coating presents some problems [Heyden 1988]. Due to the rapid heating and cooling cycles, Zn vapor can become trapped in the weldment, causing porosity. The key issues for the successful laser welding are the coating thickness, the coating uniformity and the joint configuration.

Butt laser joints normally do not show any serious problems because there is no coating at the joint interface. The Audi car company Thyssen Stahl has been producing 2m long laser butt welds on the 0.75mm galvanized sheet steels successfully for several years. These welded sheets are subsequently pressed into car floor panels. After laser welding, the Zn coating does not appear to enter and adversely affect the weld metal because the Zn coating is vaporized 1~1.5mm away from the welds.

However, lap laser joints can show serious problems as the Zn vapor cannot escape easily and can result in high degrees of porosity. High power lasers can produce enough heat ahead of the weld pool to boil off some volatile coating materials.

The size and distribution of the Zn vapor trapped in the weld bead is very much dependant on the Zn coating thickness. The Zn vapor trapped in the weld metal can be distinguished in two ways. Very small and well dispersed pores along the length of the weld normally occurs when the Zn coating thickness is less than 15μm. A large volume

of Zn vapor and blowholes are caused by a Zn coating thickness of more than 15μm. Improvement can be achieved by using a pulsed laser beam and a high power (>1 KW) Nd: YAG laser. The most successful way to reduce the volume of Zn porosity and blowholes is to maintain a small gap (~0.1mm) in between the lap joint faces, thus allowing the Zn vapor to exit between the sheets as well as through the weld keyhole.

CHAPTER 4

HEAT AFFECTED ZONE

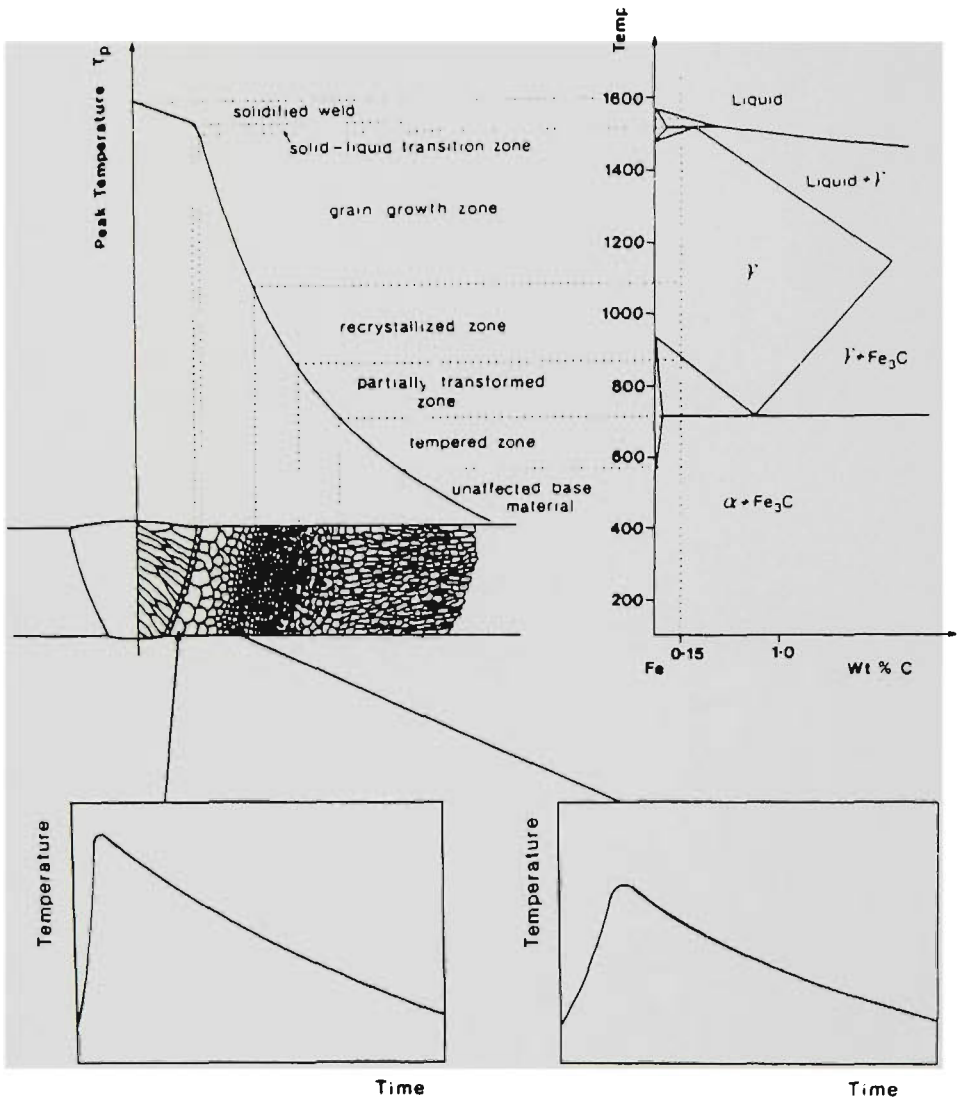

Figure 4.1 A schematic diagram of the different regions of HAZ corresponding to various peak temperatures and the Fe-C phase diagram [After Easterling 1986].

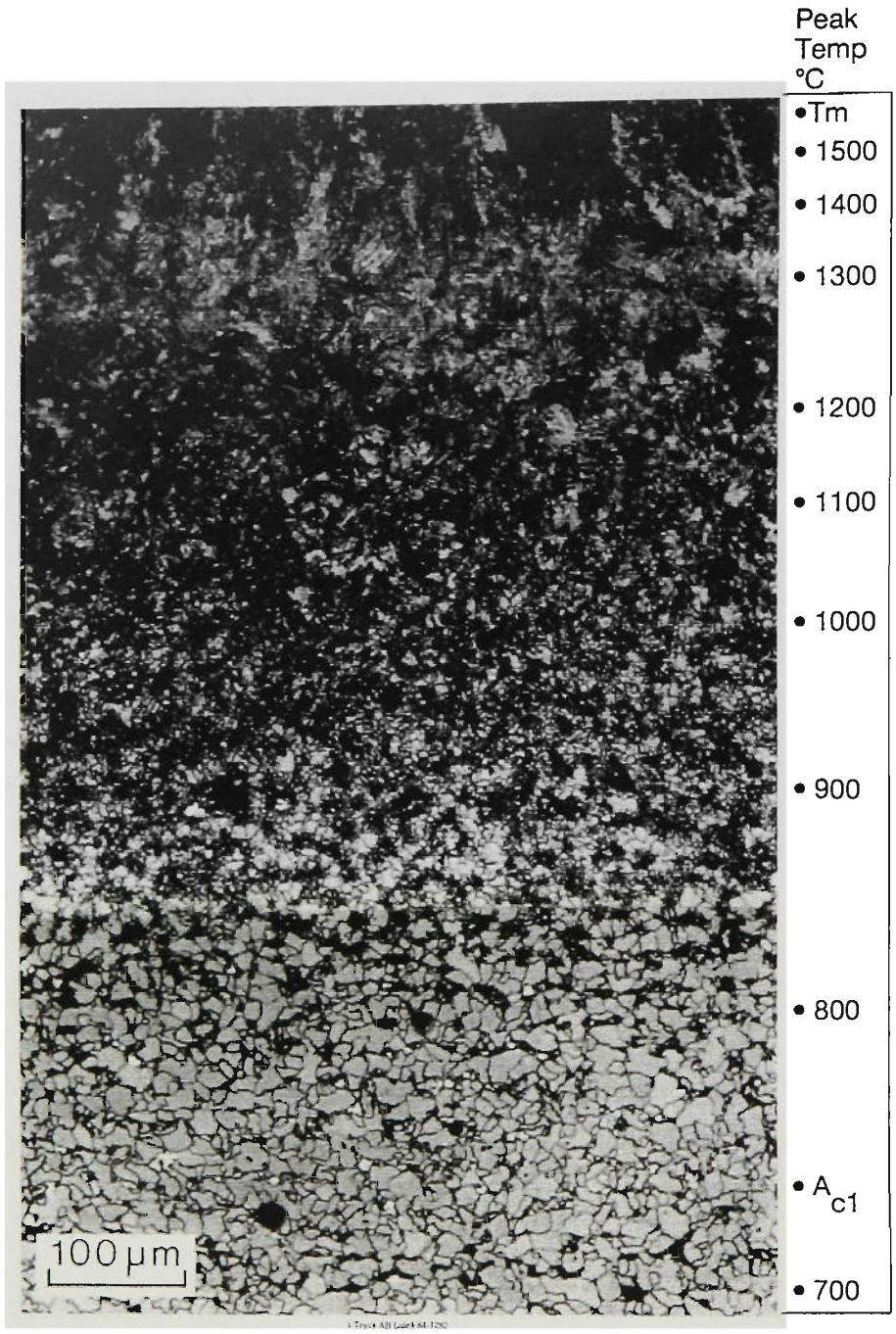

Figure 4.2 The HAZ microstructure of GMA welded Nb-microalloy steel [After Easterling 1986].

4.1 INTRODUCTION

The heat affected zone (HAZ) of a weldment is a portion of the base metal in which the structure and properties have been altered due to heating to various peak temperatures and cooling rapidly during fusion welding. **Figure 4.1** shows a schematic diagram of the HAZ structure as a function of the peak temperature. **Fig 4.2** illustrates the different regions in the HAZ defined by the different peak temperatures. Although each sub-region has its own distinct microstructure and mechanical properties, no sharp transition boundary exists between adjacent regions. The structure of the HAZ is therefore determined by the welding conditions, prior thermal and mechanical history and more importantly, the chemical composition of the base metal.

4.2 THE WELD THERMAL CYCLE

The weld thermal cycle of the base metal is caused by a rapid heating and cooling process applied to the welding work piece during the welding process. It results in very steep temperature gradients in the base metal and affects the solidification process in the weld metal and phase transformations in both the weld metal and the heat affected zone (HAZ) of the base metal.

Although it is difficult to measure the temperature distribution within the weld pool, the weld thermal cycle experienced by a point in the HAZ can be measured [CSIRO 1989; Wang et al. 1989] and theoretically predicted [Alberry et al. 1977]. The prediction of the thermal cycle in the HAZ is based on the relationship between the cooling rate of the HAZ and the welding heat input.

4.2.1 Heat-Flow Equations

The arc welding heat source is considered to result in two distinct heat transfer processes. Heat is first transferred from the source to the surface of the base metal and then, by conduction, from the contact area to colder regions of the base metal. Because that two processes are somewhat competitive, the effectiveness of a welding heat source

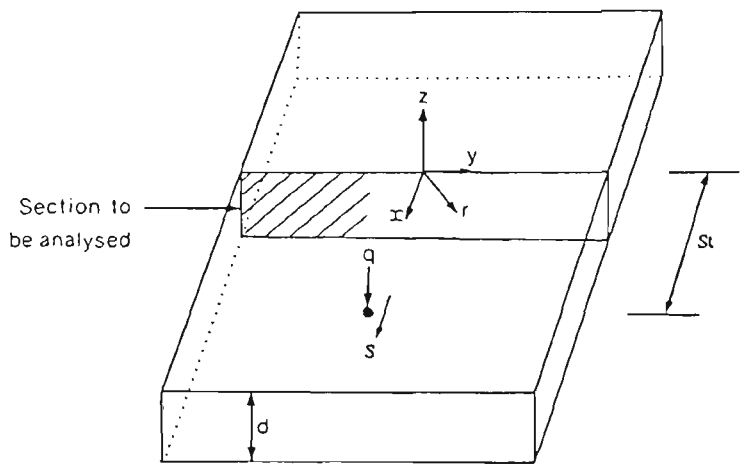

Figure 4.3 Welding configuration in terms of a point heat source (**q**) and a constant velocity (S) [After Easterling 1992].

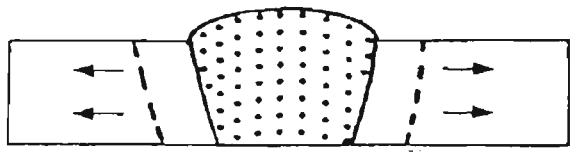

Figure 4.4 Two-dimensional heat flow in welding [After Easterling 1992].

depends fundamentally and critically on its intensity. The heat source must transfer sufficient energy at high intensity to produce local melting. The higher intensity of the heat source, the more powerful the heat flow. Hence the concept of energy input has been adopted to describe the intensity of the heat source in the welding process. It is called the arc energy input in the arc welding process. The arc energy input is the quantity of the energy introduced per unit length of weld from a traveling heat source, such as an arc, expressed in joules per meter or millimeter (or joules per inch).

The heat-flow equation or heat input equation is based on assuming that the moving heat source energy input (**HI**) (measured in J/mm, kJ/mm or MJ/m) moving at a constant speed **S** along the **x** axis of a fixed rectangular co-ordinate system, as shown in **Fig.4.3**.

$$\mathbf{HI} = \eta \frac{VI}{S} \text{----------} (4.1)$$

Where V is welding voltage, I is welding current and η is the arc efficiency (η=0.7 - 0.85 for manual metal arc welding, and η=0.66-0.75 for metal-inert gas (argon) welding) [Easterling 1992].

Assuming that the thermal conductivity (λ - J m $^{-1}$ s $^{-1}$ K^{-1}) and the specific heat (ρ) × density product (c) (ρc-the volume thermal capacity, J m $^{-3}$ K $^{-1}$) are constant, the differential equation for heat flow for the co-ordinates in **Fig.4.3** is given by equation (4.2).

$$\frac{\partial^2 T}{\partial x^2} + \frac{\partial^2 T}{\partial y^2} + \frac{\partial^2 T}{\partial z^2} = 2\lambda \frac{\partial T}{\partial t} \text{----------} (4.2)$$

Where T is temperature (K), t is the time (s) and λ is the thermal conductivity. Equation (4.2) is only for a fixed co-ordinate system. Equation (4.2) then can be modified to equation (4.3),

$$\frac{\partial^2 T}{\partial x^2}+\frac{\partial^2 T}{\partial y^2}+\frac{\partial^2 T}{\partial z^2}=-2\lambda\frac{S\partial T}{\partial \xi}+2\lambda\frac{\partial T}{\partial t}\text{----------(4.3)}$$

Where $\xi = x - St$ ----------(4.4)

ξ is the distance between a fixed reference point and the point heat source traveling at speed S after time t.

In most welding situations, the temperature distribution around a heat source of uniform velocity will be a constant. For instance, if **H I** is a constant, $\frac{\partial T}{\partial t}=0$, and therefore equation (4.3) can be simplified to

$$\frac{\partial^2 T}{\partial x^2}+\frac{\partial^2 T}{\partial y^2}+\frac{\partial^2 T}{\partial z^2}=-2\lambda\frac{S\partial T}{\partial \xi}\text{----------(4.5)}$$

When the heat loss through the surface is negligible and taking the dimensions of the weld plate into account, then for a fixed position in the HAZ at a radial distance r [$r = (x^2 + y^2 + z^2)^{1/2}$] from the heat source, the heat flow is three-dimensional for thick plate. Thus equation (4.5) can be simplified to produce equation (4.6).

$$T - T_0 = \frac{HI}{2\pi\lambda t}\exp(-\frac{r^2}{4at})\text{----------(4.6)}$$

For thin plates (two dimensional heat flow), **Fig. 4.4** simplification of the equation 4.5 gives,

$$T - T_0 = \frac{HI}{d(4\pi\lambda\rho ct)^{1/2}}\exp(-\frac{r^2}{4at})\text{----------(4.7)}$$

where a ($= \lambda / \rho\, c\, m^2\, s^{-1}$) is the thermal diffusivity and d is the plate thickness. $T_0 (K)$ refers to the initial temperature prior to welding. The above equations are obtained

based on the assumption that the application of heat to a particular point (**r**) in the HAZ is instantaneous.

4.2.2 Thermal Cycles of the Base Metal

It is well known that very steep temperature gradients exist in the base metal due to the rapid heating and cooling during the welding process. The thermal cycle for a given point in the base metal can be represented by a simple temperature - time diagram. This is so because the heat flow during the welding of a thick plate is proportional to the thermal conductivity - λ (see equation 4.6), while for a thin plate, it is proportional to both λ and the specific heat per unit volume of the base metal ρc (see equation 4.7).

The important transformation temperature range of A_3-A_1 is between 800°C-500°C. Easterling claimed that the cooling time through this temperature range ($\Delta t_{8/5}$) is constant for a given welding process, weld geometry and base metal, at least within the HAZ of the base metal (at a peak temperature, T_p>900°C). Thus it is assumed that $\eta HI / S \propto \Delta t_{8/5}$ = constant. Hence, $\Delta t_{8/5}$ has been widely used to characterize the effect of a weld cycle on the HAZ.

In order to calculate the cooling time $\Delta t_{8/5}$ of a thick plate, equation (4.6) can be simplified to equation (4.8).

$$T_p - T_0 = \left(\frac{2}{\pi e}\right)\frac{HI}{\rho c r^2} \qquad \text{----------(4.8)}$$

where T_p refers to the peak temperature of the thermal cycle and **e** is the base of natural logarithms (= 2.718). The cooling time $\Delta t_{8/5}$, therefore, is given by equation (4.9),

$$\Delta t_{8/5} = \frac{HI}{2\pi\lambda\theta_1} \qquad \text{----------(4.9)}$$

where θ_1 is defined by equation (4.10),

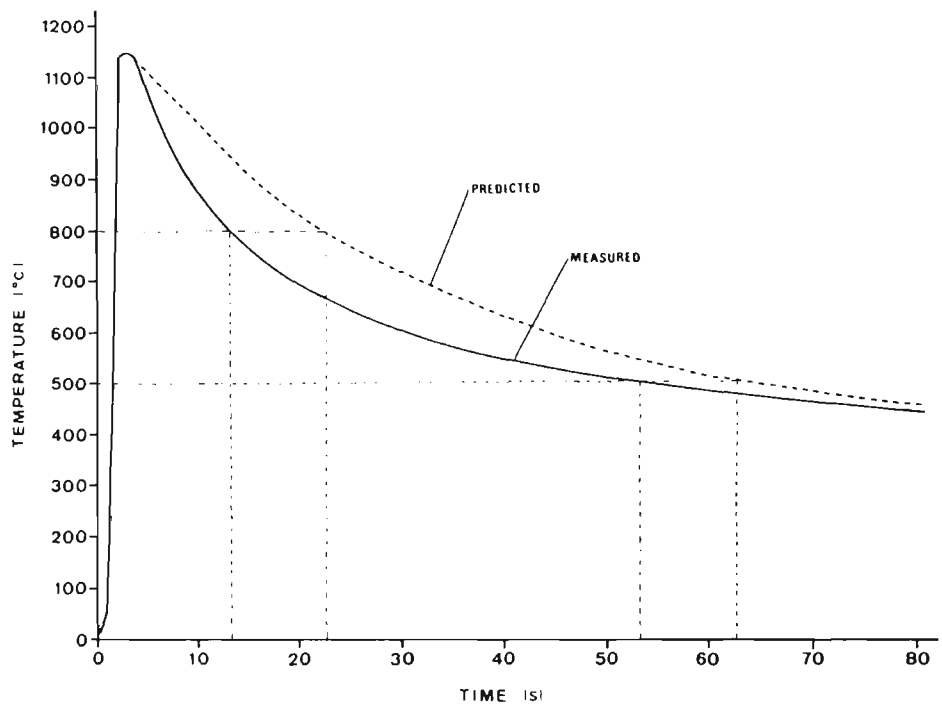

Figure 4.5 Comparison of measured and predicted thermal cycles in a thin plat of Nb-microalloyed steel welds [After Easterling].

$$\frac{1}{\theta_1} = \left(\frac{1}{773 - T_0} - \frac{1}{1073 - T_0}\right) \text{----------(4.10)}$$

Equation (4.11) can be derived from these equations and it shows that the equations T_p, T_0 and Δt completely characterize the weld cycle.

$$T_p - T_0 = \frac{\theta_1 \Delta t}{t} \exp - \left(\frac{\Delta t}{et}\left(\frac{\theta_1}{T_p - T_0}\right)\right) \text{----------(4.11)}$$

For the thin plate case equations (4.12) and (4.13) hold, where θ_2 is given by equation (4.14). Hence equation (4.15) is obtained.

$$T_p - T_0 = \left(\frac{2}{\pi e}\right)\frac{HI}{d\rho c 2r} \text{----------(4.12)}$$

$$\Delta t_{8/5} = \frac{(HI)^2}{4\pi\lambda\rho c\theta_2^{\,2} d^2} \text{----------(4.13)}$$

$$\frac{1}{\vartheta_2^{\,2}} = \frac{1}{(773 - T_0)^2} - \frac{1}{(1073 - T_0)^2} \text{----------(4.14)}$$

$$T - T_0 = \vartheta_2 \left(\frac{\Delta t}{t}\right)^{1/2} \exp - \left(\frac{\theta_2^{\,2} \Delta t}{2et(T_p - T_0)^2}\right) \text{----------(4.15)}$$

The important correlations between cooling time $\Delta t_{8/5}$ of the HAZ and the welding heat input *(HI)* are established by equations (4.9) and (4.13). They indicate that $\Delta t_{8/5}$ is proportional to heat input for thick plate and to the square of heat input for thin plate. The higher the heat input applied during welding, the longer the cooling time, or the slower the cooling rate in the HAZ.

Comparing the calculated and measured temperature-time profiles, the results agree fairly well (see **Fig.4.5**). However, the choice of equation used in a particular case is governed not only by plate thickness, but also by the welding process and even the type

of material. Thus, the critical thickness d' - equation (4.16) can be obtained by equating the both equations (4.9) for a thick plate and (4.13) for a thin plate. The critical thickness defines the thickness of cross-over or the boundary condition between this two equations.

$$d' = \left\{ \frac{HI}{2\rho c} \left(\frac{1}{773 - T_0} + \frac{1}{1073 - T_0} \right) \right\}^{1/2} \text{----------(4.16)}$$

From equation (4.16), it is seen that the critical thickness d' is dependent on the heat input *(HI)* of the welding process, the type of material (ρc) used and preheat temperature T_0 used.

Equations (4.9) and (4.13) (also known as the Rosenthal equations) indicate that, regardless of the values of voltage *(V)*, current *(I)* and welding speed *(S)*, welds deposited with the same value of heat input *(HI)* will have identical cooling times $\Delta t_{8/5}$, and hence identical HAZ microstructure and properties. In 1978, however, Kohno and Jones first time reported that the retention time above 1000 °C and $\Delta t_{8/5}$, as well as $\Delta t_{5/3}$ were changed with a change in both the welding current *(I)* and welding voltage *(V)*. Wingrove (1987) later demonstrated that the HAZ microstructure and hardness are not solely dependent on *(HI)*. Since the HAZ is determined by the cooling rate, this implies that the cooling rate of the HAZ can differ at constant heat input, depending on the values of *V, I* and *S* which produce the heat input *(HI)*. Wingrove claimed that the Rosenthal analysis, which is based on a moving point heat source, is an oversimplification of a complex phenomenon, since the 'pinching off' and travel of molten metal droplets from the tip of electrode are affected by arc temperature, droplet size distribution and rate of transfer of droplets. This hypothesis was confirmed by Ahmed and Jarvis of the CSIRO (1998). They claimed that the cooling rate was higher for a higher welding speed *(S)* at constant heat input *(HI)*.

However, the Rosenthal approach appears to be adequate as a first approximation and if only one of the parameters: voltage *(V)*, current *(I)* and welding speed *(S)* is varied to increase the heat input *(HI)*, it is commonly observed that the higher input does result in a slower cooling rate in the HAZ [Lin et al. 1988].

4.3 HAZ MICROSTRUCTURE

The HAZ is a zone in which the welding heat cycle has produced one or more transformation from the initial state to the state produced by heating. The HAZ microstructure and properties therefore change because of the very steep temperature gradient on both heating and cooling. The thermal gradient across the HAZ results in the formation of several distinct regions for a single bead weldment [Easterling 1986]. These regions consist of the five zones which are listed in **Table 4.1**.

Table 4.1 Regions of the HAZ and their temperature range

Name of the zone	Temperature range
1) Grain coarsened region - GC	1530 ^{0}C - 1100 ^{0}C
2) Grain refined region - GR	1100 ^{0}C - 900 ^{0}C
3) Intercritical or Transformed region - IC	900 ^{0}C - 750 ^{0}C
4) Subcritical or Tempered Region- SC	750 ^{0}C - 650 ^{0}C
5) Unchanged base metal	650 ^{0}C - below

These sub-zones can be distinguished by particular microstructural features, but there are no sharp transitions between them.

4.3.1 Grain Coarsened Region (GC)

The grain coarsened region (GC) of the HAZ is the area immediately adjacent to the fusion line (**Fig.4.1**). In this region, the base material experiences a thermal cycle with peak temperature beyond the austenite grain coarsening temperature, in the range of 1100°C-1500°C for most steels. In low carbon steels, delta phase may also occur at the higher temperature in this region. Generally for non micro-alloyed steels, the rate of grain growth of the austenite increases rapidly once the temperature exceeds about 1050°C [Savage 1972; Kilpatrick 1972], which is a typical grain coarsening temperature. Although the final transformation product of this region is determined by many factors, a ferritic structure is expected for lower carbon equivalent (CE) steels and

lower temperature transformation products, such as Widmanstatten ferrite side-plates, bainite and martensite for higher CE steels.

The GC region is regarded as the most dangerous region of the HAZ in terms of mechanical properties because cold cracks occur most commonly in this area. The cold cracking results from the embrittlement by structures, such as Widmanstatten ferrite side plates, upper bainite, martensite-austenite (MA) islands and twinned martensite. Increase in the austenite grain size effectively enhances the formation of these unfavorable microstructural constituents.

Grain size is one of the key factors in determining the strength and toughness of a material, and an alloy's susceptibility to cold cracking and reheat cracking in welds. Concerning austenite grain growth through a weld thermal cycle, Ikawa et al. (1977) reported that the maximum increase in grain size occurs in the initial stages of grain growth. In fact, it was found that 80% of the grain growth occurred during the heating part of the thermal cycle for tungsten inert gas (TIG) and submerged arc (SA) welded microalloyed high strength steels. This phenomenon may be caused by the higher driving force available at the initial stage of grain growth [Easterling 1992].

This type of rapid grain growth could be related to $\alpha \rightarrow \gamma$ transformation by a diffusionless mechanizm, i.e. a martensitic mechanism during heating [Sekino et al. 1970; Albutt et al. 1966]. According to the martensitic mechanism, the $\alpha \rightarrow \gamma$ transformation by a diffusionless mechanism could happen during heating at rates of 200-300°C/s in the temperature range of 800-1100°C. This transformation produces some homogeneous plastic deformation in the austenite formed [Cahn 1965], and accelerates the primary recrystallization of austenite at high temperature (Easterling 1992). Austenite recrystallisation occurs with an enhanced driving force under this condition and hence, precipitates may not be effective in inhibiting austenite grain growth and reducing the grain size. Therefore, it has been suggested that coarse grains could be eliminated by reducing the heating rate in the temperature rage 800-1100°C so that the phase change of $\alpha \rightarrow \gamma$ occurs by the normal diffusional mechanism.

4.3.1.1 Grain growth

It is well known that higher energy grains with a fine size and fewer sides are unstable and tend to shrink at the expense of coarsening grains. Therefore, during the completion of the $\alpha \rightarrow \gamma$ phase transformation in steels, as the growing γ phases have consumed all the strained material, the metal can only lower its energy further by reducing its total area of grain surface. Consequently, grains with more sides begin to swallow grains with fewer sides, with the result that the small grains shrink and the larger ones grow.

For fusion welding, the grain growth in the HAZ depends on,

1) the duration of the heating (residence time) at temperatures above the grain coarsening temperature;
2) the composition of base metal;
3) the peak temperature reached in the HAZ;

Among these factors, the peak t emperature has the most significant e ffect on grain coarsening due to its key effect in determining the time of heating and cooling (residence time) [Easterling 1986]. For steel, it is found that for isothermal heating the final mean grain size d_t is given by

$$d_t^n = kt + d_0^n \quad \text{---------- (4.17)}$$

where k is a constant, t is time and d_0 is the initial grain size. Although the final grain size will increase with increasing peak temperature and residence time, the residence time is the only significant variable in determining the final grain coarse in the HAZ and the grain size in weld metal. Because the maximum peak temperature is the melting point and the grain size at the fusion boundary which is more interested to us is not affected by welding process. However, welding processes having characteristically high values of heat input (q/v) are expected to generate coarse grain in the HAZ and weld metal, as the residence time is roughly proportional to the parameter q/v (the heat input rate).

The residence time can be reduced by either using a heat source that generates a deep weld pool or reducing the heat input [Lancaster 1999].

4.3.1.2 Prediction of prior austenite grain size

A number of papers have been published on developing models for predicting the austenite grain size, since the prior austenite grain size is an important factor in determining HAZ properties [Alberry et al. 1977; Ashby and Easterling 1982; Alberry and Jones 1982]. These models were based on elementary kinetic models for grain growth, particle dissolution and integrated over the weld cycle. Theoretical predictions of grain growth in a weld thermal cycle show reasonable correspondence with experimental weld simulated specimens. Although good agreement was expected between predicted grain size and that of weld simulated samples, in applying the model to the real weld HAZs, the grain size predicted using the equation is larger than what is observed in weld simulated samples [Alberry et al. 1977]. This may be caused by steep thermal gradients in the actual HAZ, which inhibits austenite grain growth known as 'thermal pinning'. The thermal pinning factor was, therefore introduced by Alberry et al. to the equation to predict the grain size in the actual weld HAZ.

4.3.2 Grain Refined Region (GR)

The temperature range of the grain refined region is about 900-1100°C. Because of the low peak temperatures and rapid weld thermal cycles, the austenite grain size formed during $\alpha \rightarrow \gamma$ transformation on heating is very small which results the production of the fine grained ferrite-pearlite on transformation during cooling. Although some carbide may not have fully dissolved during heating, the carbon content in the austenite is enriched by partitioning as ferrite forms on cooling, producing austenite islands that transform to perlite. Other possible second constituents are bainite or martensite-austenite depending on the cooling rate and the composition of the steel.

4.3.3 Intercritical Region (IC)

The temperature range in the IC region is about 750-900°C. The pearlite in the base metal is quickly austenized due to its lower $\alpha \rightarrow \gamma$ transformation temperature. The

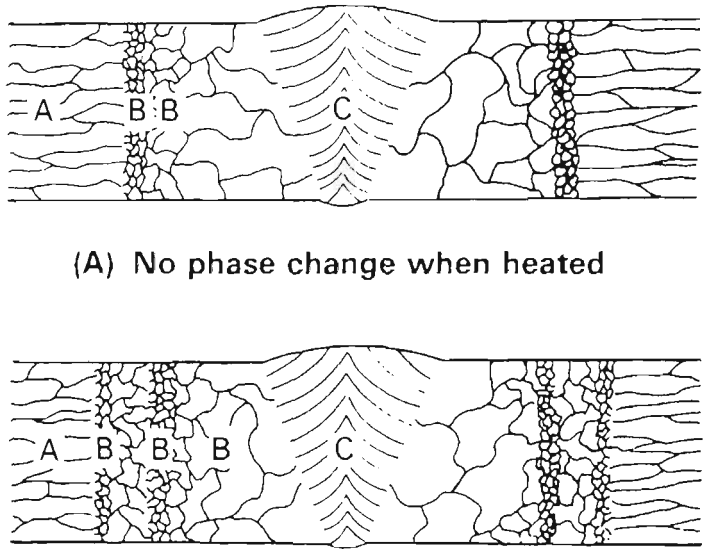

Figure 4.6 Recrystallisation of cold worked grains in HAZ [After Welding Handbook Vol.1 1989].

austenite is enriched in carbon to a much higher value than the average in the base metal. As a result, the transformation product of these austenite regions on cooling can be pearlite (dark phase), upper bainite, auto-tempered martensite or high carbon (twinned) martensite depends on the cooling rate. The hardness of this constituent mainly depends on its carbon content.

4.3.4 Subcritical Region (SC)

The SC region is also described as the spheroidized carbide region and this region corresponds approximately to the temperature range of 650-750°C. No $\alpha \rightarrow \gamma$ transformation occurs during the heating cycle and the most significant structural change in annealed a hot rolled steel is partial spherodisation of the lamellar of Fe_3C. In cold rolled steel, static recovery and recrystallization of the deformed structure can occur.

4.3.5 Region of Unchanged Base Metal

If the temperature of the base metal does not exceed 650°C and little structural change occurs during welding. However, dynamic strain ageing can be caused by the combination of welding residual stress and carbon and nitrogen atoms in solution. Substructures present in deformed base metal, such as subgrain boundaries, grain boundaries and dislocations may be affected by dynamic strain ageing. For instance, moving dislocations can sweep up interstitial impurities, such as C and N, during heating. On subsequent cooling, the solute atoms enriching the dislocations are trapped and embrittlement can result.

4.3.6 HAZ Microstructure of Cold Rolled Structural Steel

Figure 4.6 shows the cross section of HAZ fusion welded annealed cold rolled structural steel. The unaffected base metal **A** shows the typical elongated grains as a result of the mechanical deformation. Fine equiaxed grains were formed where the HAZ temperature exceeded the recrystallization temperature **B**, and grain growth took place at higher temperatures near the fusion zone.

Since steels exhibit allotropic transformations, the HAZ of cold rolled structural steels will have two recrystallized zones during fusion welding, as illustrated in **Figure 4.6 (b).** The first fine-grained zone results from recrystallization of the cold worked alpha phase. The second fine-grained zone results from the allotropic transformation to the high temperature phase, and re-transformation to ferrite on cooling.

The recrystallized HAZ is softer and weaker than the cold worked base metal, and the strength cannot be recovered by heat treatment [AWS Welding Handbook Vol.2 1989].

4.4 S IMULATION OF HAZ MICROSTRUCTURE

It is well known that grain size is a key factor in determining its strength and toughness of structural materials. Generally, the smaller the grain size, the better properties. In the HAZ, the mechanical properties are mainly determined by the microstructure of the grain growth region due to its coarse grain size. Because the real weld HAZs has non-uniform microstructure, it is difficult to conduct mechanical property tests on the HAZ. A weld simulation technique was, therefore developed by Nippes and Savage in order to obtain i nformation about the microstructure and p roperty g radient across H AZ. T he simulation technique was based on producing a synthetic HAZ microstructure in a small scale specimen by means of heat treatment.

4.4.1 Uses of Weld Thermal Simulators

Weld thermal simulators were developed to overcome the difficulty in conducting mechanical tests, such as Charpy V-notch impact and crack opening displacement (COD) tests on real HAZ. The structural gradient in the HAZ and the specimen form are two major problems causing difficulty in carrying out mechanical testing on the real HAZ. Practically, a large scatter occurs for values of Charpy impact energy and COD of weld HAZs, because of the difficulty of notch tip location in say the GC HAZ.

An equation for a simulated sample was developed by Widgery (1972) that predicted, for a grip gap of 25mm, that the temperature will be within 1% of the peak temperature

over a band 2.5 mm wide at the mid-length of the sample. This result is useful for samples to be toughness tested because it is easy to locate a notch in a 2.5mm wide band. Hence, extensive toughness assessment of the HAZ has been carried out on weld simulated HAZ microstructures [Tomita et al. 1985; Inagki et al. 1964; Vitek and David 1990].

The weld simulator has also been used to study mechanical properties of the HAZ, such as hardness [Lewis and Wu 1963; Nippes et al. 1960], tensile strength [Szuki and Tamura 1959; Nippes et al. 1955; Suzuki and Tamura 1961], notch tensile s trength [Grotke 1964], and stress rupture strength [Nippes et al. 1955].

Studies of fracture in hot tension testing [Dolby 1972] and hot cracking problems associated with welding have also been investigated [Widgery, Conf. Proc. 1972] using a simulator specially equipped with a hot testing facility. In addition, the weld simulation technique provides a very useful method for the continuous cooling transformation study of the HAZ. The effect of preheat and postweld heat treatments (PWHT), multi-run welds, etc., can also be easily incorporated into the programmed thermal cycle.

The first simulators were built by Nippes and Savage in 1949. A very rapid heating rate similar to that experienced in the HAZ during welding were achieved by electrical resistance heating, or by a high frequency (HF) induction furnace. In resistance heating, specimens are clamped to a pair of water-cooled metal grips. The control thermocouple is either spot welded to the surface or embedded inside the sample. A varying input current and voltage control the parameters of heating cycle, such as heating rate and peak temperature. The c ooling r ate can be controlled by a djusting b oth voltage and current inputs and the cooling water flow rate through the grips, as well as the type and design of metal grips [Apps and Andrade 1985]. A fast cooling rate can also be obtained by using helium cooling [Lundin et al. 1989] and water spray cooling.

4.4.2 Comparison of Weld and Thermally Simulated HAZ Microstructures

Weld thermal cycle simulation under the laboratory conditions is useful to the understanding of the microstructural and property changes in the HAZ. Thermal cycles can be programmed by using the Rosenthal or similar equations or data from thermocouples embedded in actual welds to produce the required temperature-time profile. A dilatometer can also be employed to impose the thermal cycle and record phase transformation.

Comparing simulated and real welds, in general, there appears to be satisfactory correlation with respect to both microstructure and mechanical properties. The comparisons have been mainly based on qualitative examination of the microstructural constituents, such as, martensite or bainite. Little attention has been given to comparing quantitative information on the proportions of constituents in the microstructures present.

For similar thermal cycles in the HAZ of real welds and in simulated samples, a discrepancy in austenite grain size was first reported by Dolby and Widgery (1972). Similar results have been reported by other workers [Berkhout 1972; Harrison and Farrar 1989; Akselsen 1987]. The possible reasons for the discrepancy in microstructure could be:

1. Differences in heating rate;
2. Differences in cooling rate;
3. Incorrect measurement of the highest peak temperatures;
4. The large temperature gradient in real welds which can effectively inhibit grain growth;
5. The solution of precipitates, e.g. aluminum nitride, caused by their high local resistance to the heating currents in the simulated specimen, thus, allowing easier grain growth.

The heating rate can affect the rate of dissolution and coarsening of precipitates and thus the grain growth. Grain growth during heating is also affected by the temperature at which recrystallization and/or phase transformation occur. Recrystallization is also dependant upon the degree of prior deformation of the base metal. The cooling rate, in

conjunction with the grain size and prior thermal history, determines the final microstructure.

Incorrect measurement of peak temperature can occur by using the wrong sort of thermocouple, or by not taking account of the thermal gradient at free surfaces of the test sample, or the gradient along the axis of the sample.

The effect of temperature gradient in real welds, is in some ways the most difficult to account for in simulated samples. The problem is that if rapid changes occur in grain size across the HAZ a grain growth inhibiting effect is present due to pinning from the small grains. It is difficult to simulate this effect in the test samples used for simulation. The effect is clearly more dominant in low heat input welds, or in high speed welding since the heat input, welding speed and plate thickness are important factors in controlling the width of the HAZ and the temperature gradient in terms of the austenite grain size developed in the HAZ [Lin and Druce 1988; Pang et al. 1990]. However, low heat input and high welding speed are beneficial in keeping the austenite size to a minimum level and producing a narrow HAZ.

Charpy impact tests on simulated specimens have been reported [Commission of the European Communities 1974] to give consistently higher transition temperatures than tests on actual weld HAZs. This difference can be attributed to the inaccuracy in simulating the microstructure, such as coarser grains in the simulated sample due to absence of the thermal gradients that exists in weld HAZ, as mentioned previously. Another possible reason is that unlike the actual weld HAZ, the simulated Charpy specimen has a uniform microstructure across the ligament below the notch and is therefore likely to give lower toughness values.

4.5 PROPERTIES OF THE HAZ

The properties of the HAZ include the weldability and mechanical properties of the HAZ.

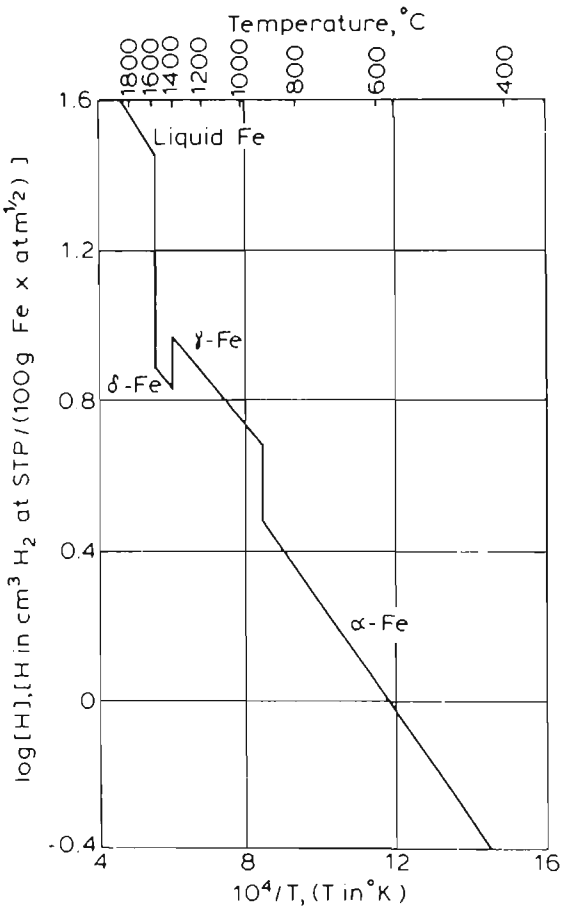

Figure 4.7 The solubility of hydrogen in iron [After Easterling 1992].

The weldability is the susceptibility of a steel to cracking problems associated with the welding process. Cracking in fusion welding can occur in both weld metal, (such as solidification cracking) and in the HAZ (such as liquation cracking and cold cracking). Of these types of cracking, cold cracking (or hydrogen induced cracking) is the most serious, least understood, and most widely encountered cracking problem associated with the HAZ.

HAZ hardness, tensile strength and toughness are important mechanical properties of weld joints. HAZ hardness reflects the type of the microstructure and gives a direct indication of the strength, toughness and hardenability of the HAZ. The HAZ toughness testing has been widely used to assure the quality of the HAZ because it represents the crack resistance of the weldment.

4.5.1 Cold Cracking

Cold cracking is induced by the combination of a sufficient hydrogen concentration, an applied tensile strength and a susceptible microstructure [Easterling 1992].

4.5.1.1 Effect of hydrogen on cold cracking

It is suggested that hydrogen behaves in b.c.c iron more like a proton than an atom due to its much higher diffusivity than carbon and nitrogen [Fast 1976]. It is also evident that stress has a significant effect on the diffusion of hydrogen atoms in iron than temperature [Beck et al. 1966]. The decrease in hydrogen diffusion and increased scatter below 200 °C can be caused by the fact that hydrogen becomes trapped in the various defects and being transforms to molecular hydrogen.

The solubility of hydrogen in ferrite is much lower than in austenite, as shown in **Figure 4.7**. However, the diffusivity is higher in ferrite than in austenite. During transformation remnant austenite is enriched in hydrogen and lower temperature products, such as martensite transformed from the austenite are susceptible to cold cracking, because of high hydrogen enrichment at defects, such as lath-packet boundaries or twinned plate boundaries. It has been found that the presence of twinned (high carbon) martensite is

more da ngerous t han lath (low c arbon) martensite since t he f ormer h as a l ower M_s transformation temperature than the latter. Any factors that decrease the transformation temperature, like increasing austenite grain size and increasing carbon equivalent, will increase the susceptibility of the material to cold cracking. The grain coarsened region of the HAZ therefore, is the region in which the greatest risk of hydrogen cracking exists for both C-Mn and low alloy steels due to its coarse grain structure [Coe 1973].

In general, the harder the microstructure, the greater is the risk of cracking [Coe 1973; Karppi 1978]. This is consistent with the trend that lower transformation temperature products have higher susceptibility to cold cracking because of there higher hardness.

4.5.1.2 Effect of stress on cold cracking

Residual stress in the weldment is induced by both the temperature gradient and the γ-α phase transformation. The temperature gradient can cause compressive stress during the heating up and tensile stress during cooling. In addition, mechanical properties, such as elastic modulus E, yield strength and Poisson's ratio change during the weld thermal cycle.

However, an important contribution to residual stress is considered to be the dilatation associated w ith p hase t ransformation in s teel. T he phase transformation temperature range depends on the grain size, the peak temperature reached and the cooling rate. The higher the peak temperature the lower the γ-α transformation temperature and the larger dilatation. A base metal with larger grain size tends to have a lower transformation temperature due to the reduction in the grain boundary surface area for nucleation of ferrite.

4.5.1.3 Effect of microstructure on cold cracking

Cold cracking (or hydrogen induced cracking) in the HAZ is mainly because its susceptible microstructure [Lundin 1986]. The susceptible microstructures in terms of cold cracking include:

1. harder grains consisting of martensite or bainite;
2. coarse prior-austenite grain size;
3. slag inclusions or coarse carbide particles lying in grain boundaries;
4. a high dislocation density.

The cold cracking occurs mostly in the grain coarsened region of the HAZ because of the low transformation temperature which results in lower temperature transformation products, such as martensite, bainite and Widmanstatten ferrite side plates. The high dislocation densities associated with these products, together with fine carbide particle hardening, are likely to result in a hard, low ductility matrix.

4.5.2 Prediction of Cold Cracking by Carbon Equivalent (CE)

The carbon equivalent (CE) is adopted to assess the weldability of the materials in terms of the effect of the alloying elements on the transformation characteristics, indicated by the CCT diagram of the steel. Much useful information can be obtained by the CE value. For example, it can reflect the likely microstructure of the HAZ, the transformation temperature, the likelihood of martensite formation in the steel, the hardness and the hardenability of the steel. The established CE formulae are based on hardness and cracking test data [Hart and Harrison 1987].

The weldability and serviceability of steel is dependent on the optimum combination of the CE level and strength requirement. The CE level in steel should be kept as low as possible to reduce the risk of cold cracking as well as minimizing the cost. If the strength of the steel must be maintained at a high level, this can be achieved by increasing the alloy element level resulting in an increase in the CE. Lower CE level steels with high strength can be achieved by improving the rolling technology to produce strain hardening [Killmore et al. 1989] and by using microalloying additions to obtain fine grained steel with an optimum combination of strength and toughness.

For many years CE formulae have been widely and successfully used for assessing the risk of cold cracking in the HAZ of steels. Among a group of different CE formulae the following three have been most widely used

CE (IIW) = C+Mn/6+(Ni+Cu)/15+(Cr+Mo+V)/5 ----------(4.18)

Pcm = C+Si/30+Mn/20+Cu/20+Ni/60+Cr/20+Mo/15+V/10+5B ----------(4.19)

CEN = C+A[C] [Si/24+Mn/6+Cu/15+Ni/20+(Cr+Mo+V+Nb)/5+5B]-----(4.20)

Where **A[C] = 0.75+0.25 tanh [20 (C – 0.12)]** ----------(4.21)

The CE formula was developed by the International Institute of Welding (IIW) and was incorporated into the British Standard in 1974 [IIW Doc. 1967; British Standard 5135]. The Pcm formula was proposed by Ito and Bessyo in 1968 and later was adopted by the Japanese Welding Engineering Society [Ito and Bessyo 1968]. Based on the above two CE formulas, the CEN formula was produced by Yurioka et al. [Yurioka et al. 1981].

The differences between the CE (IIW) and Pcm formulae may be attributed to differences in the type of steels produced in each period. The correlation between CE (IIW), Pcm and CEN was given by Yurioka in 1990 [Yurioka 1990]. It has been claimed that CE (IIW) is suitable for steels with greater than 0.18% C and Pcm for less than 0.16% C, whereas CEN is suitable for steels with a carbon content in both ranges [Suzuki 1983 and 1984].

The CE equation is used for controlling the chemistry of the steel in order to obtain good weldability. Good weldability is ensured by placing a maximum allowable value on HAZ hardness, since the hardened microstructure of a weld HAZ is susceptible to cold cracking. A value of 350HV is considered to be the critical HAZ hardness. A CE (IIW) value of 0.4 has been, claimed to be value corresponding to a HAZ hardness of 350HV [AWRA 1982].

However, a CE (IIW) value of 0.4 need not to limit the hardness to 350HV because the HAZ hardness is also determined by the cooling rate $\Delta t_{8/5}$ [Brisson et al. 1984].

4.5.3 HAZ hardness

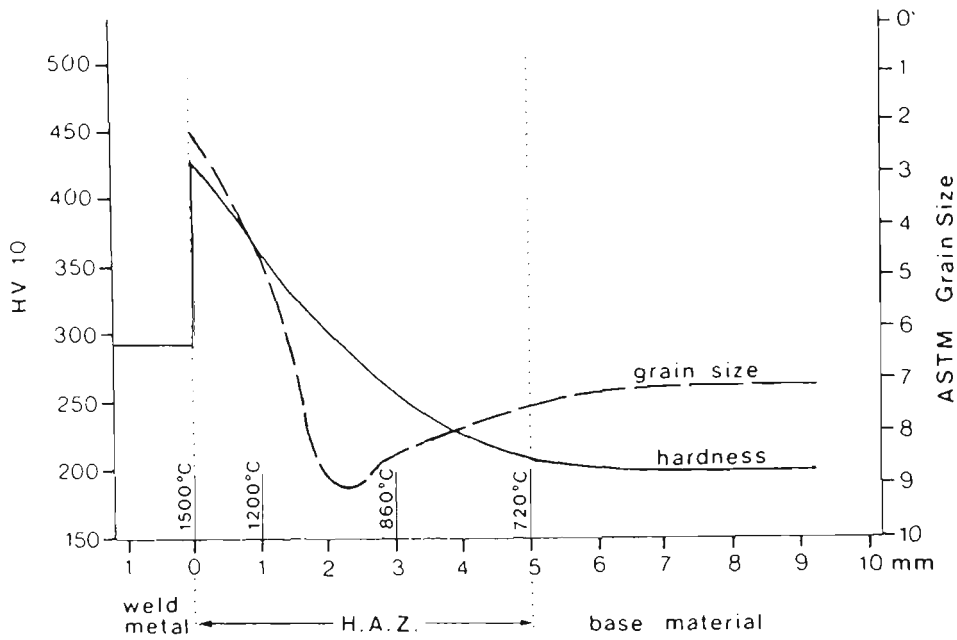

Figure 4.8 Microhardness in HAZ of a structural steel [After Schweisstechnik 1980].

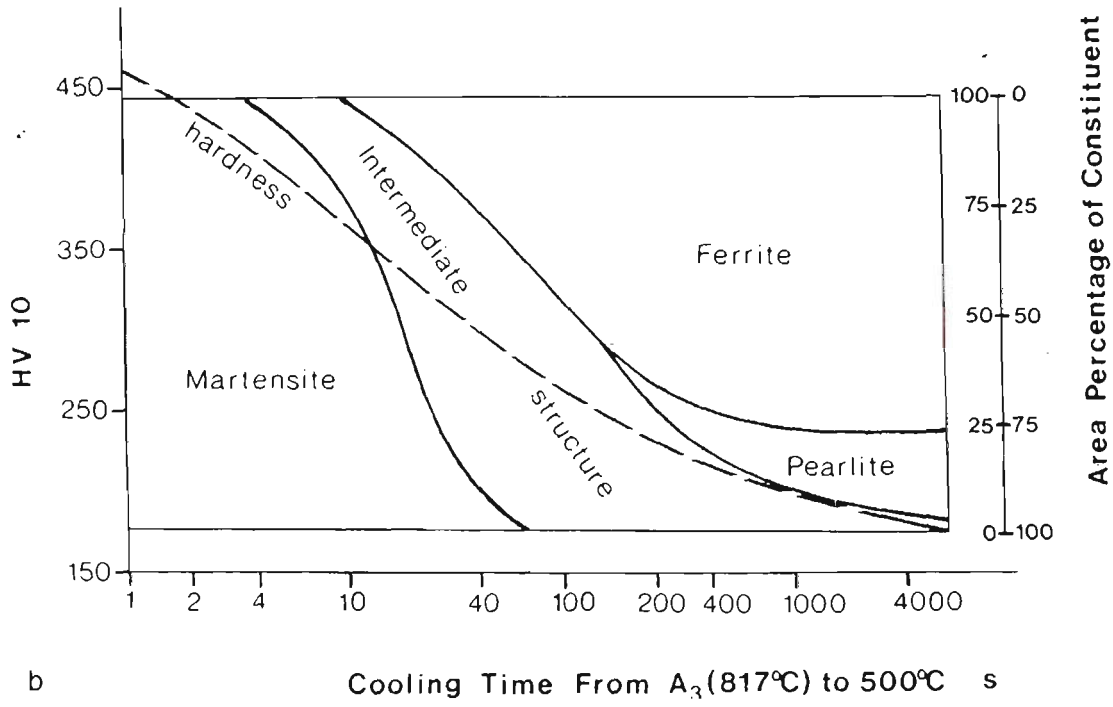

Figure 4.9 Microstructure-hardness diagram [After Inagaka and Sekiguchi 1960].

4.5.3.1 HAZ hardness and its measurement

HAZ hardness depends on the hardenability of the steel, the cooling rate and the prior austenite grain size. The value of HAZ hardness gives a useful indication of the composition of a steel, microstructural constituents and presence of martensite. The HAZ hardness also serves as a bases for characterizing the HAZ strength, toughness and hardenability of a steel [Welland 1989]. HAZ hardness is regarded as a rough index describing the susceptibility to cold cracking [Yurioka 1990].

It has been shown that the HAZ hardness is superior to CE in predicting cold cracking tendency, especially at low carbon levels because that the HAZ hardness reflects the effects of both composition and cooling rate [Rogerson and Jones 1983; Nagumo 1983]. It has been shown that the HAZ hardness correlates reasonably well with implant cracking test results [Karri 1978; Bryhan 1981; Tanaka and Kitada 1976].

A typical HAZ hardness of a structural steel traverse across the HAZ is shown in **Figure 4.8** From the base metal towards the fusion line, hardness increases to a maximum at the fusion line, indicating a harder microstructure and the presence of martensite as a result of a large austenite grain size in the grain coarsened region near the fusion line. Lower heat input, or faster cooling rate of the HAZ, results in a harder HAZ. A relationship between peak HAZ hardness and cooling time Δt_{8-5} is shown in **Figure 4.9**. This figure indicates that an increase in heat input will increase $\Delta t_{8/5}$ and in turn, will decrease the hardness.

Hardness testing methods were reviewed by the International Institute of Welding [IIW 1986]. The Vickers test is considered to be the preferred method to test HAZ hardness as it covers the whole engineering range of hardness values. Loads of 5 and 10 kg are found to be most appropriate for assessing the HAZ hardness in the light of the HAZ dimensions, ranging from fractions of a millimetre to a few millimetres. The lower the load, the higher the error in HAZ hardness tests because of the reduced size of the indentation.

Two hardness measurement methods are recommended in various standard specifications [German Standard; British Standard and French Standard]; they are tangential method (along a line parallel to the surface of the plate) and a contour method (along the contour of the fusion line). The Australian Standard AS 2205.6.1 adopts the tangential method with the hardness traverses near the surface parallel to and 2 mm below the plate surface.

4.5.3.2 Prediction of maximum HAZ hardness

A model for prediction of maximum HAZ hardness based on the CE value and the cooling rate $\Delta t_{8/5}$ was developed to indicate the susceptibility of HAZ to cold cracking. The maximum hardness in the HAZ occurs in the GCR adjacent to the fusion boundary. High austenitization temperatures in this zone give rise to high hardenability, which in turn encourages the formation of martensite and/or lower bainite. It is a thin zone (generally less than 0.25 mm in width) that can be considered as a shell of sensitive material around a weld where cold cracking is driven by high residual stress levels and hydrogen injected from the weld pool.

Among those regression expressions for predicting maximum HAZ hardness of C-Mn and low alloy steels the Nippon Steel system for C < 0.3 wt% developed by Yurioka in 1987 is widely used [Arata et al. 1979; Yurioka et al. 1987 and 1981; Suzuki 1985;Cottrell et al. 1984 Boothby 1985; Duren 1985; Teresaki 1981; Beckert 1973 and Seyffarth 1979]:

$$\mathbf{HV_{max} = 442C+92CEIII+206+(402C-90CEIII+80)\,.\,arctan(X)} \quad \text{----------(4.22)}$$

where

$$X = \frac{\log \Delta t_{8-5} - 2.30CEI - 1.35CEIII + 0.882}{1.15CEI - 0.673CEIII - 0.601} \quad \text{----------(4.23)}$$

$$CEI = C + \frac{Si}{24} + \frac{Mn}{6} + \frac{Cu}{15} + \frac{Ni}{12} + \frac{Cr}{8} + \frac{Mo}{4} + \Delta H \quad \text{----------(4.24)}$$

$$CEII = \frac{Si}{24} + \frac{Mn}{5} + \frac{Cu}{10} + \frac{Ni}{18} + \frac{Cr}{5} + \frac{Mo}{2.5} + \frac{V}{5} + \frac{Nb}{3} \quad \text{----------(4.25)}$$

where ΔH is a term accounting for B level.

ΔH = 0	when B ≤ 1 ppm
ΔH = 0.03	when B = 2 ppm
ΔH = 0.06	when B = 3 ppm
ΔH = 0.09	when B ≥ 4 ppm

HV_{max} is the Vickers Pyramid Number (10 kg load) which is the parameter widely used by welding research community for HAZ measurements. The input to this system is the chemical composition of the base metal and cooling time Δt_{8-5}. Based on the equation of 4.11 and 4.15 the cooling time Δt_{8-5} for both thick and thin plate can be obtained as follows [Adams 1958; Van Adrichem 1971]:

3-D model (for thick plate):

$$\Delta t_{8-5} = \left(\frac{\eta VI}{S}\right) \frac{1}{2\pi\lambda}\left[\frac{1}{500-T_0} - \frac{1}{800-T_0}\right] \quad \text{----------(4.26)}$$

2-D model (for thin plate):

$$\Delta t_{8/5} = \left(\frac{\eta VI}{Sd}\right) \frac{1}{4\pi\lambda\rho c}\left[\frac{1}{(500-T_0)} - \frac{1}{(800-T_0)}\right] \quad \text{----------(4.26)}$$

The critical thickness of the plate is therefore determined by the following equation:

$$\mathbf{d'} = \left[HI\frac{1}{2\rho c}\left(\frac{1}{500-T_0} + \frac{1}{800-T_0}\right)\right]^{\frac{1}{2}} \quad \text{----------(4.27)}$$

When the thickness **d** is smaller than **d'** the plate is called thin plate otherwise is called thick plate. The following thermal constants are recommended: thermal conductivity, λ = 0.025 J(mm°C s) and volumetric heat capacity ρc = 0.0045J/(mm^3°C). The heat input per unit length of weld is $HI = \eta \frac{VI}{S}$ (J/mm), where V is voltage (volts), I is current (amps) and S is welding speed (mm/s). η represents the fraction of the power that actually reaches the workpiece which is process dependent: SMA – 0.75; GMA – 0.75; SAW – 0.90.

The prediction of the maximum HAZ hardness gives a reliable indication of the risk of cold cracking. The maximum HAZ hardness is also a well known useful indicator of the tensile strength of steels [Bibby et al. 1998]. In this regard the following relationship may provide significant indirect information when dealing with cold cracking in the HAZ.

$$\mathbf{S_t = 3HV_{max}} \text{ ----------(4.28)}$$

$\mathbf{S_t}$ is the tensile strength in MPa and $\mathbf{3HV_{max}}$ is the maximum HAZ hardness as Vickers Pyramid Number (VPN).

4.5.4 Toughness of HAZ

Toughness is the capacity of a material to absorb energy by deforming plastically before fracture. Toughness is determined by the combined strength and ductility of a material and is measured by the amount of work absorbed during the propagation of a crack through a structural member or a standard specimen. The fracture toughness is one of the most important mechanical properties of the HAZ since it represents the crack resistance of HAZ in industrial applications for a given welding procedure.

The Charpy V-notch impact test [Australian Standard 1544.2, 1989] and the crack opening displacement (COD) test [Verburg 1974/3.4] are normally used for the HAZ toughness measurements. However, a toughness testing of the HAZ is usually carried

out on a simulated HAZ microstructure due to the difficulty in the correct placement of a notch tip in a suspected low toughness region.

The Charpy impact test is widely used to evaluate the toughness of the HAZ because the test bar (10mm×10mm×55mm standard size) is cheap to produce and the test procedure and testing machine are relatively simple. However, the results of impact test cannot reflect the real toughness of the material because of the size effect, the strain rate and the site of the notch. The strain rate of the impact test (ca. 10^5–10^6 s^{-1}) is much higher than the strain rate usually generated by construction work loading conditions. Finally, the notch of a standard impact bar (2mm depth in an angle of 45° and 0.25mm radius at the bottom of the notch) may not be sited in the right position relative to actual defects, such as crack, slag inclusions undercutting etc., resulting in inaccuracy of the toughness value. Higher transition temperatures than actual weld HAZs in Charpy impact tests of the simulated specimens were reported in 1974 [Commission of European Communities 1974]. This could be caused by the absence of thermal gradients and microstructural gradients in the simulated samples resulting in the lower toughness than the actual weld HAZ.

The results of COD test have been reported to be more reliable than impact tests because the thickness of the test sample is equal to the original plate thickness and the notch tip can be placed at the region of sensitive microstructure [Kudoh and Pisarski 1986]. However, the time and expense of COD tests are two disadvantages. This is required to produce a pre-crack at the notch tip and the test involves complicated and expensive instruments. As consequences, the Charpy impact test is still widely used in the welding industry, as it provides a useful quality control test for ranking the toughness of materials.

4.5.4.1 Effect of microstructure on HAZ toughness

The toughness of the HAZs is degraded by the following microstructural constituents: coarse grains, upper bainite structure, martensite-austenite (MA) constituent and twinned martensite, as well as age hardening.

A grain coarsened region consisting of grain boundary ferrite and ferrite side plates normally embrittle of the HAZ, due to a low cleavage resistance despite a low HAZ hardness [Dolby 1979; Watanabe et al. 1986]. The coarsened microstructure linked with a coarse prior austenite grain size is induced by a relatively high peak temperature. Precipitates of TiN can be used as a means of pinning the grain boundaries in order to reduce the prior austenite grain growth and refine the microstructure [Wang et al. 1989; Chipperfield et al. 1985; Nakano et al 1986].

Embrittlement in the HAZ can also occur in the partially transformed region and the intercritically reheated grain coarsened region in multipass welds due to the formation of high carbon martensite-austenite (MA) islands [Tomita et al. 1985; Uchino et al. 1986]. These islands are formed from austenite enriched in carbon and alloying elements in regions corresponding to original pearlite colonies [Akselsen et al. 1988; Uchino et al. 1986; Eichhorn 1986]. As a result, twinned martensite with high carbon can be formed from the austenite. The MA islands have a detrimental effect on the HAZ toughness and an increase in the volume fraction of MA islands can cause a significant deterioration of toughness [Nakanishi 1986; Aksalsen 1988].

However, so far the mechanism of the deterioration of the toughness by the presence of the M-A constituent has not been clarified. The M-A constituent fractures preferentially at low stress and/or strain levels because the interfacial energy between M-A islands/matrix ferrite decreases with the segregation of carbon, resulting in crack propagation along the M-A constituent/matrix ferrite interfaces [Nakanishi et al. 1986; Stevenson 1979]. Cracking initiating from voids at the interface of the martensite and ferrite has also been suggested and demonstrated by some researchers [Gerbase et al. 1979; He et al. 1984].

A different suggestion was made by some researchers that the initiation of cleavage fracture occurs in the ferrite as a result of extensive build-up of dislocations at the ferrite/martensite interface [Akselsen et al. 1988; Ramberg et al. 1986]. The stress concentration developed at the interface is caused by the significant difference in yield

strength and is enhanced by the difference in flow strength between the martensite and ferrite [Chen et al. 1984; Kim and Thomas 1981].

4.5.4.2 Effect of microalloying element on HAZ toughness

The strong carbide-nitride forming elements such as titanium (Ti), niobium (Nb) and Vanadium (V) can affect HAZs toughness through changing the HAZs microstructure. These elements play an important role by particle pinning, resulting in the refinement of the austenite grain size. The fine austenite grain size is the one of key factor to ensure the desired properties in the HAZ.

A small Ti addition (0.005 to 0.010%) can significantly restrict austenite grain growth in a HAZ structure and therefore resulted in a improved HAZ toughness [McCutcheon et al. 1983]. Nb and/or V can be added to the Ti in order to provide the required degree of grain refinement. However, the addition of Ti to Nb-containing HSLA steels results in the large particles which are stable even up to the melting point of the steel and can have detrimental effect on the mechanical properties [Chen et al. 1987]. This is because that the much higher content of side plate ferrite in (Ti,Nb) steel than in (Ti) steel as a result of Nb forming caps on the surface of TiN particles and reducing their potency for nucleating acicular ferrite.

Among various carbonitrides, such as TiN, TiC, VN, AlN and NbN, only TiN is likely to survive at the peak temperature of the grain coarsened region without complete solution, but the coarsening of these precipitates is inevitable [Easterling 1992]. It can therefore be concluded that the partial substitution of carbon by nitrogen in carbides is beneficial because the nitrides coarsen more slowly than carbides [Honeycombe 1985].

Ti-containing oxides (Ti_2O_3) are believed to enhance considerably the nucleation of acicular ferrite, resulting in improvement of the HAZ toughness [Homma et al. 1986]. Ti_2O_3 is more stable than TiN at a high temperature and provides active nucleation sites for fine intergranular ferrite formation. On cooling Ti_2O_3 containing steel exhibit less deterioration in notch toughness in the grain coarsened region of the HAZ.

Reports on the effect of Nb on HAZ toughness are contradictory. It has been reported that Nb contents up to 0.18% have some influence on $\gamma \rightarrow \alpha$ transformation, shifting it to a shorter time and restricting martensite transformation even at very high cooling rate. This effect could result in an increase in the toughness of the HAZ [Hulka and Heisterkamp 1983]. However, the opposite conclusion was reached by Cane and Dolby, that Nb steel has a lower HAZ toughness after submerged arc welding at heat inputs of 5 and 7 kJ/mm. The detrimental effect of Nb is caused by its effect on the $\gamma \rightarrow \alpha$ transformation temperature at slow cooling rates. By depressing the transformation temperature, the more brittle upper bainite was developed, lowering the resistance to cleavage.

Like Nb, V was also found to cause the as-welded HAZ notch toughness to increase initially and then decrease as the V content increased [Bonomo and Rothwell 1971; Hannerz and Holmquist 1974].

Apart from the Ti, Nb and V, Ca combined with TiN increase the HAZ toughness through the formation of calcium oxysulfide particles to complement the effect of TiN on pinning due to their higher stability in the high temperature range of the weld thermal cycle. A small content of boron (less than 0.0015%) can improve the HAZ toughness due to its reaction with free nitrogen to form BN at the early stage of the cooling cycle of welding [Nakano et al. 1985].

4.5.4.3 Effect of welding parameters on HAZ toughness

The HAZ microstructure and properties are affected mainly by the heat input, which in turn is determined by the welding voltage, current, travel speed and arc efficiency. Changing any of these factors changes the HAZ microstructure and in turn would affect the HAZ properties.

Large heat inputs result in a coarser HAZ structure because of the slow cooling rate. Coarse austenite grains enhance the formation of undesirable microstructure, such as coarse grain size, coarse grain boundary ferrite, upper bainite and martensite austenite

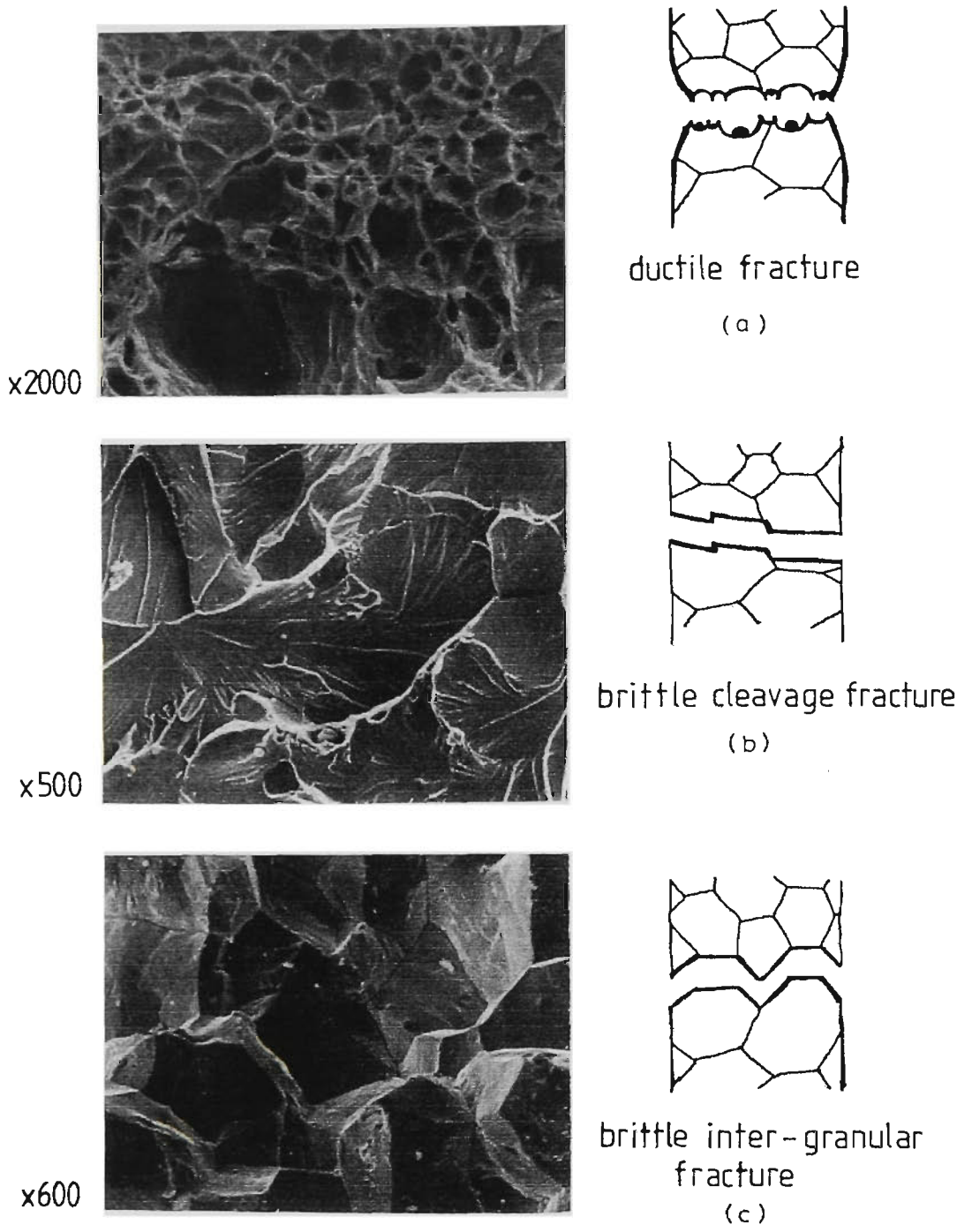

Figure 4.10 SEM micrographs of fracture surface showing (a) ductile fracture; (b) and (c) brittle fracture [After Askeland 1996].

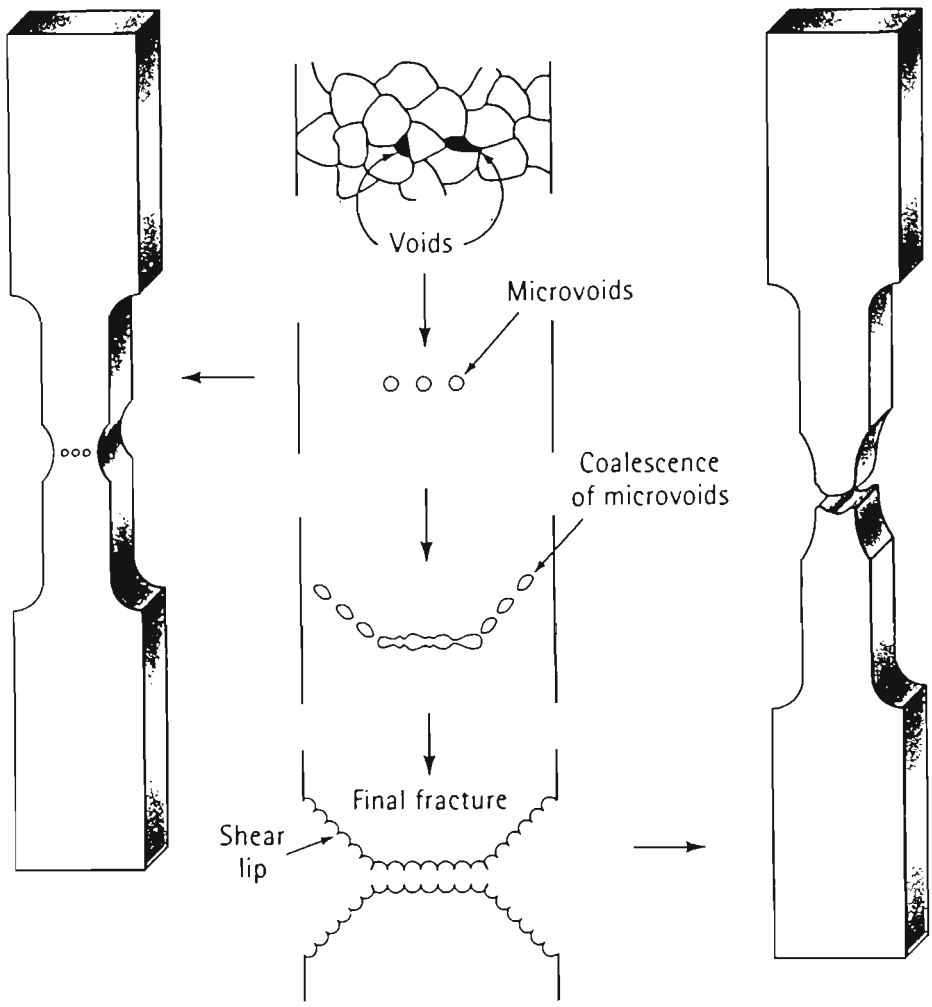

Figure 4.11 A schematic ductile fracture mechanisms [After Askeland 1996].

constitute (MA) and reduce the HAZ toughness [Illin and Razikov 1966; Amono et al. 1986]. By reducing the heat input, a fast cooling rate results in the refinement of microstructure and improves the toughness. However, a fast cooling rate can also promote formation of martensite/bainite. The optimum heat input, is dependant on the welding processes and the materials used. The heat input must be kept above a critical value to avoid formation of martensite and twinned martensite, due to their detrimental effect on the HAZ toughness [Lebedev et al. 1986].

Concerning the submerged arc welded C-Mn steel, changing the welding speed at the constant heat input results in a change in the retention time and cooling rate [Ahmed and Jarvis 1998]. This can have implications for the HAZ properties, since the HAZ microstructure is determined by the cooling rate.

4.5.5 Fracture in Metals

A fracture is formed when a metal is broken into separate parts. Basically, there are two kinds of fracture in metals - ductile fracture and brittle fracture. **Figure 4.10** shows examples of the fracture surfaces of ductile and brittle failures in steels. A ductile failure is characterized by the surface 'dimpling' due to localized plastic flow occurring around small inclusions. Ductile fracture occurs in a trans-granular (through the grains) manner in metals that have good ductility and toughness resulting a considerable amount of deformation, such as necking in the failed component. In a simple tensile test, ductile fracture begins with the nucleation, growth and coalescence of micro-voids at the center of the test bar (see **Figure 4.11**). Slip also makes a contribution to the ductile fracture of a metal when the resolved shear stress reaches the critical resolved shear stress (at 45° to the applied tensile stress according to Schmid's law).

Brittle fracture occurs in high strength metals or metals with poor ductility, low toughness and little or no plastic deformation occurred. Initiation of the crack occurs at small flaws, which cause a concentration of stress. The crack propagates most easily along specific crystallographic planes, such as {100}surface facets by cleavage. The brittle cleavage fracture surface appears comparatively flat, featureless and has a brightly reflecting characteristics due to the freshly broken trans-crystalline facets.

Brittle inter-granular fracture occurs along grain boundaries has a less bright appearance and a surface consisting of grain shapes. Normally, the brittle fracture surface is flat and perpendicular to the applied tensile stress.

CHAPTER 5

THE WELD METAL

Weld metal is defined as a liquid region obtained by fusion of the base metal and filler metal during execution of the welding. The microstructure of the weld metal is determined by the mixture of the constituent of both base and filler metal. The solidified weld bead can generally be detected without magnification. The metal added to the liquid state is called deposited metal [Granjon 1991].

5.1 SOLIDIFICATION OF THE WELD METAL

Weld solidification is a fundamentally different process to that of ingot casting, however it has certain features in common with continuous casting. The solidification of weld metal has particular characteristics, such as:

1. impurities in the weld pool;
2. non-metallic inclusions in base metal and weld metal;
3. dilution of the weld filler alloy;
4. considerable turbulence and good mixing in the molten metal;
5. smaller molten metal volume than the base metal;
6. similar compositions of the molten metal and base metal;
7. a very large temperature gradient across the melt;
8. a dynamic welding solidification process, strongly affected by welding speed;
9. preheating effect on base metal for high energy welds or multi-run welding.

For most carbon and low alloy steels, the rapid solidification and cooling rates involved in fusion welding result in higher strength and lower toughness than the base metal even though they may have similar chemistries.

5.1.1 Dilution of the Weld Metal

Dilution occurs during fusion welding as a result of the base metal being locally heated above its melting point. The final composition of the weld metal is dependant upon both the chemistry of the base and filler metal. Depending on the amount of base metal added, the final composition of weld metal can be approximated using the dilution equation as follows:

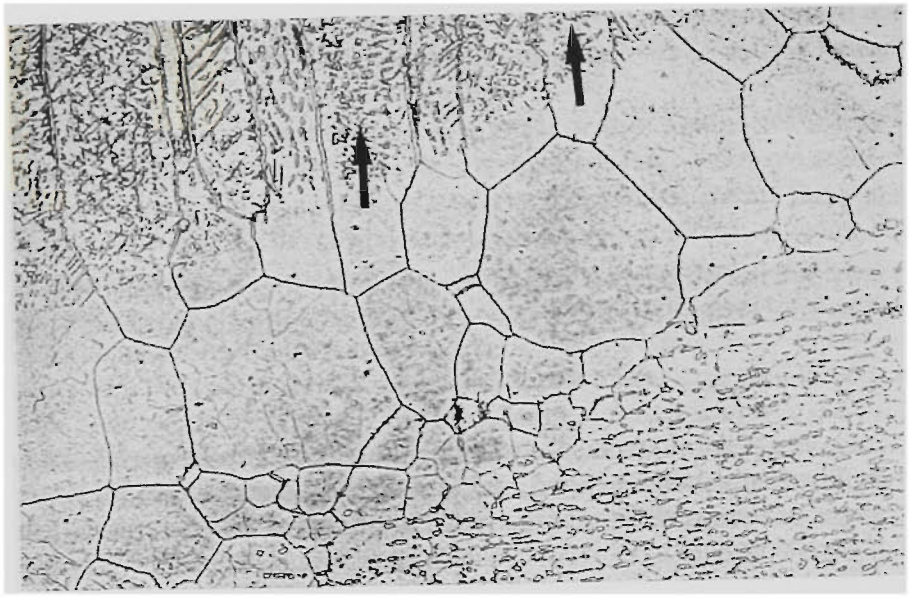

Figure 5.1 Optical micrograph showing the columnar grains of the weld metal formed by epitaxial solidification from the fusion line of the base metal [After Honeycombe and Gooch 1976].

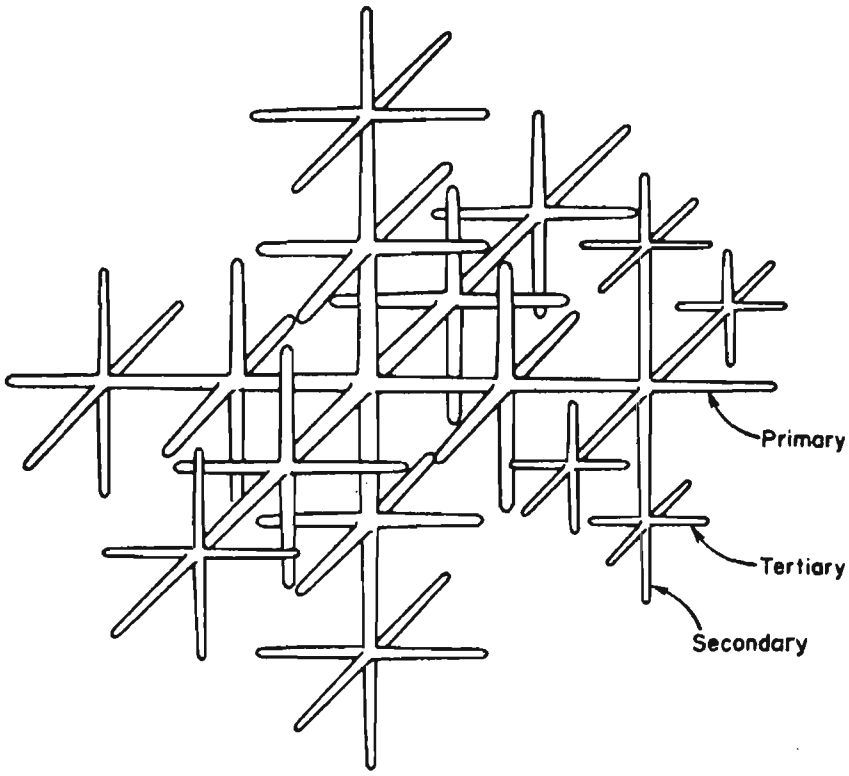

Figure 5.2 A fully developed dendrite. The primary, secondary and tertiary arms all correspond to <100> growth directions in cubic metals [After Easterling 1992].

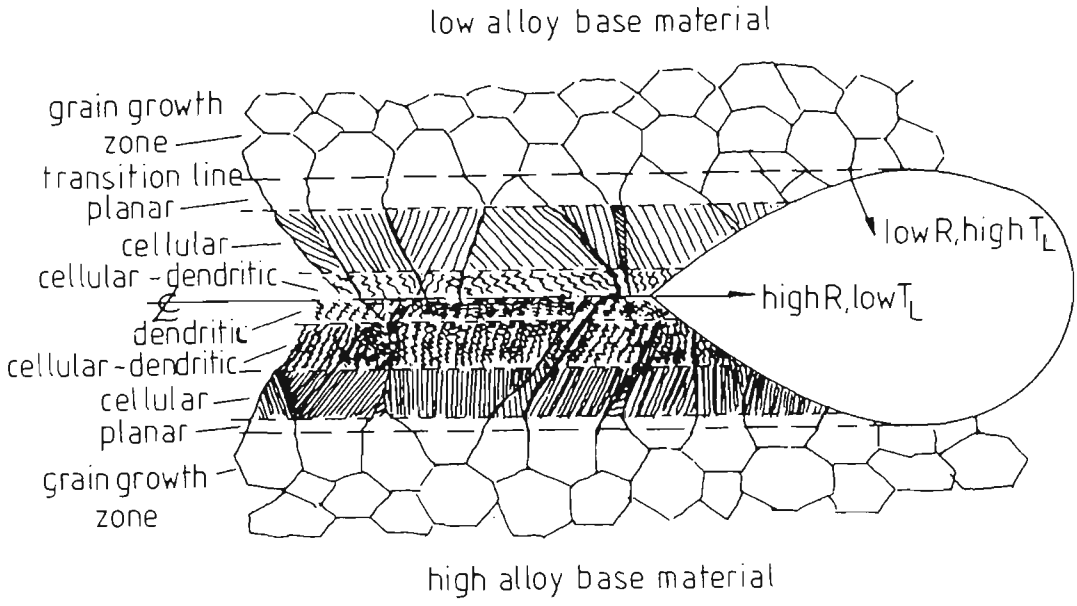

Figure 5.3 Schematic illustration of the various types of growth products developed during the solidification of weld metal as a function of alloy composition, crystal growth rate and temperature gradient in the melt [After Easterling 1992].

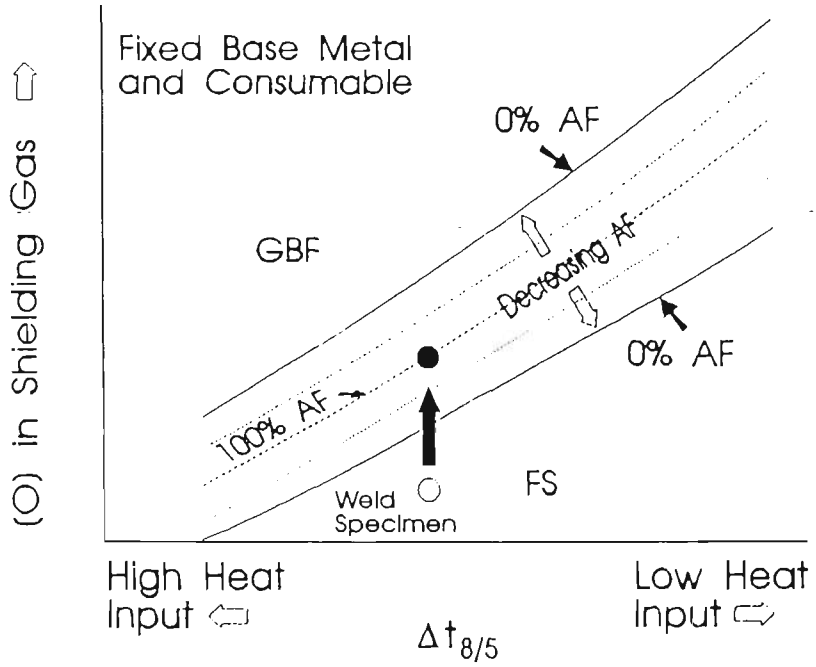

Figure 5.4 Effect of the oxygen potential in shielding gas on the microstructure of the weld metal [After Liu, Olson, Ibarra and Runnerstam 1993].

Dilution, %=[(weight of base metal melted)/(total weight of fused metal)]×100 -------5.1

In a single-pass weld, the element content in the weld metal can be approximated using the following formula:

Specific element in weld metal=(that element in the base metal×dilution)+[that element in the filler metal×(1−dilution)] -------5.2

The initial solidification of the weld metal occurs epitaxially, as shown in **Figure 5.1**. X-ray diffraction has confirmed that the crystals of the weld metal are derived from grains of the base metal. [Savage and Aaronson 1966]. The epitaxial solidification is a heterogeneous process in which the initial grain size of the weld metal is inherited directly from the grain growth zone of the base metal.

The epitaxial grain growth occurs by the development of a planar growth front, but with a decrease in the temperature gradient and an increase in constitutional supercooling by segregation, the crystal growth process changes to cellular growth. The cellular microstructures are only stable for a limited range of temperature gradients. When the temperature gradient falls below a certain level, the primary cells become unstable and develop secondary arms, and then tertiary arms of a dendritic structure (Easterling 1992). **Figure 5.2** shows schematically a growing dendrite. In this case, the dendrite spacing will largely reflect the degree of segregation at the dendritic boundaries, with a finer spacing being associated with less segregation. **Figure 5.3** illustrates schematically the solidification process of the weld metal during a weld run.

5.1.2 Microstructure and Properties of the Weld Metal

The weld zone structure is very important in terms of mechanical properties. Since a finer weld structure gives improved mechanical properties, various methods for obtaining or refining the weld structure have been developed: such as magnetic stirring, ultrasonic cavitation and chemical inclusion [Surian, et al. 1991; Pal and Majumdar 1995; Davis and Garland 1975].

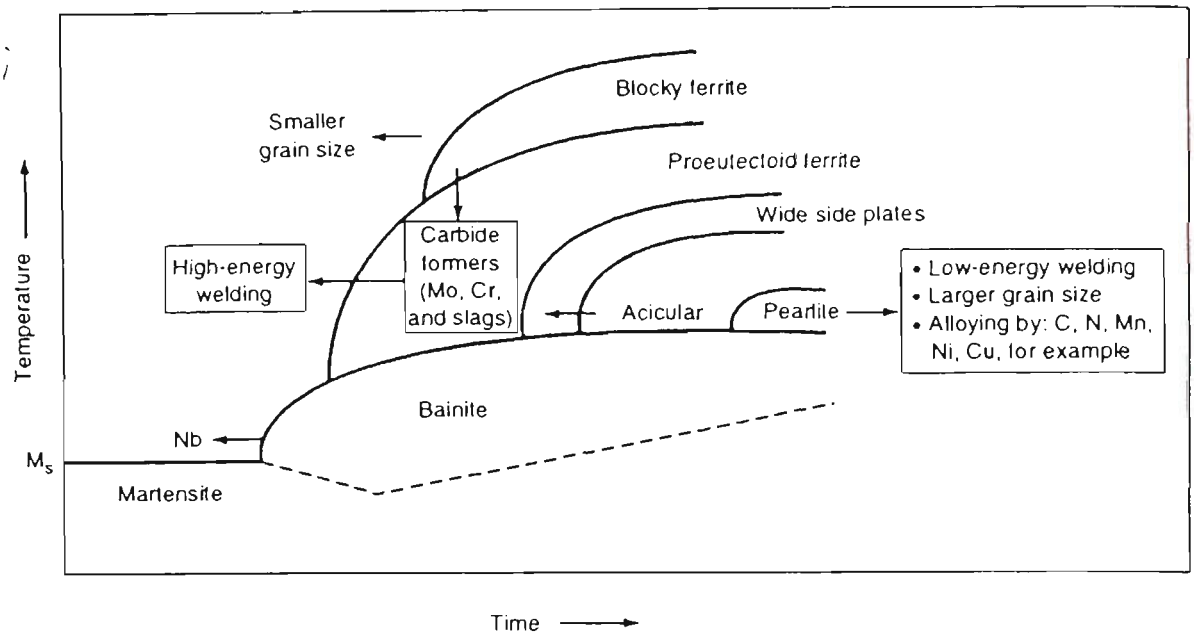

Figure 5.5 Schematic CCT diagram for steel weld metal showing the effect of microstructure and alloying on transformation product [After Easterling 1986].

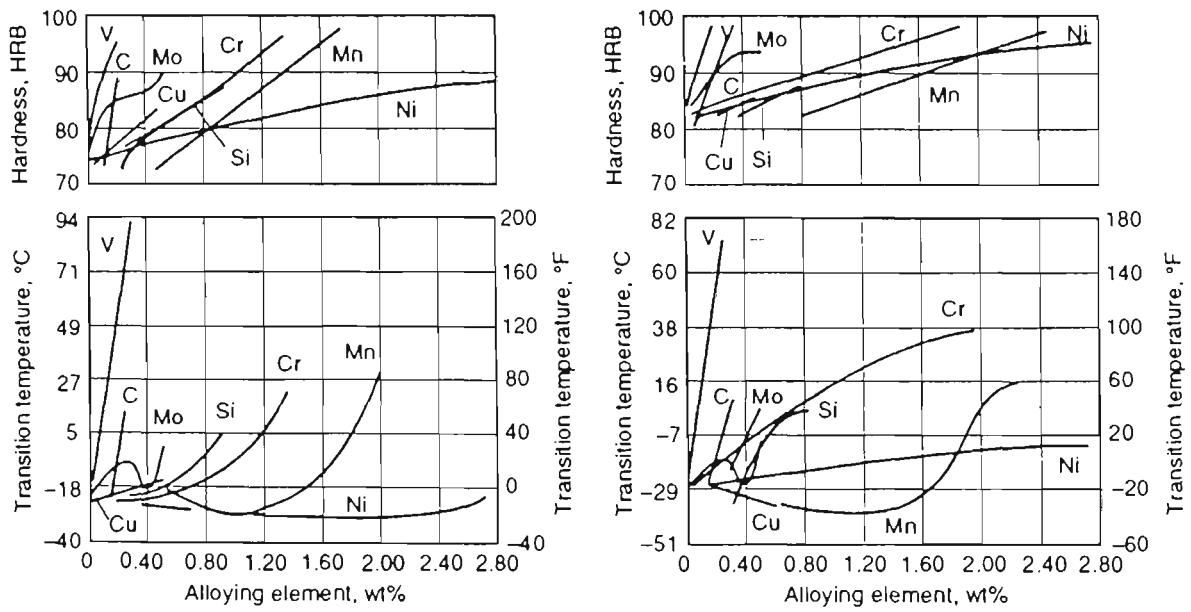

Figure 5.6 Effect of alloy additions on hardness and notch toughness of weld metal (a) Submerged arc weld metal; (b) Gas-metal arc weld metal [After Ito and Bessyo 1968].

It is well known that an increase in the carbon content of low and medium strength weld metal will increase in the yield and tensile strength and decrease in the ductility. It is claimed that an increase in the carbon content increases the amount of acicular ferrite at the expense of grain boundary ferrite [Surian et al. 1991]. However, the role played by different alloying elements is fairly complex, and the carbon may behave differently in the presence of other elements, i. e. manganese, silicon and oxygen [Den Ouden 1975]. For the C–Mn system, the best combination of tensile and fracture properties is obtained with a carbon content in the weld metal in the range of 0.07 to 0.09 % [Evans 1981]. Increasing the carbon content in the range of 0.05 to 0.12 % is also claimed by Surian (1991) to increase the yield strength, tensile strength and weld metal hardness.

In addition to the alloying contents and cooling rate, the effect of weld metal oxygen has a considerable effect on the weld metal microstructure, as shown in **Figure 5.4**.

The weld metal microstructure in carbon and low-alloy steels contains a variety of constituents, ranging from primary ferrite to acicular ferrite to bainite to martensite. The effects of alloying elements and cooling on the weld metal microstructure are expressed in the CCT diagram shown in **Figure 5.5**. **Figure 5.6** illustrates the effect of alloying elements on the hardness and notch toughness of weld metal.

Following a comprehensive review on the effect of welding procedures on weldment properties, the following conclusions were drawn [Chen and Pollack]:

1. Welding procedures and mechanical properties do not have a direct cause-effect relationship;
2. The mechanical properties of any weld metal are attributable only its soundness, microstructure and chemical composition;
3. There is no direct relationship between the current setting of a welding machine and the final properties of the weldment.

The true cause-and-effect relationship is believed to lie in the change in the heat input, which influences the microstructure of the weldment and, in turn will affect the mechanical properties of the weldment However, it has been shown that the

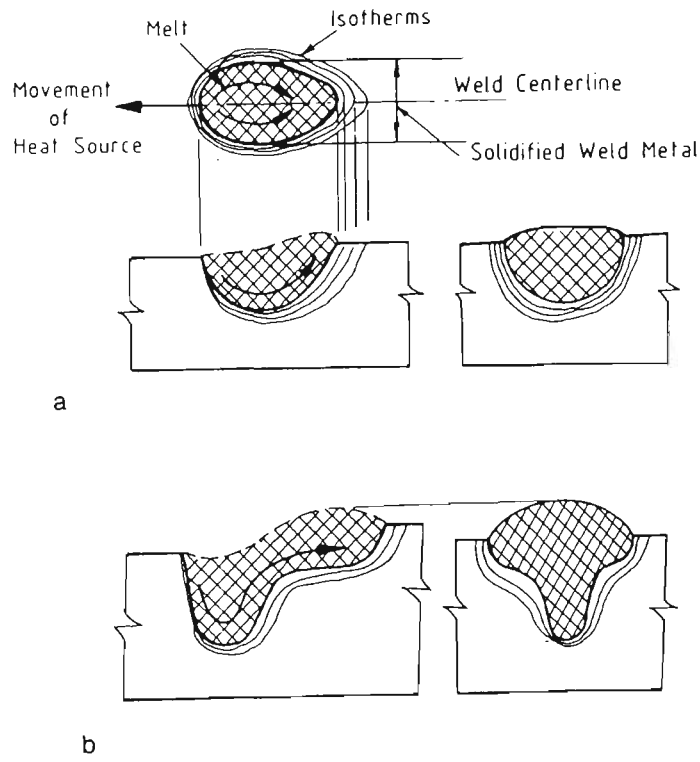

Figure 5.7 Schematic illustration of the transition from a symmetrical to unsymmetrical weld pool shape due to turbulence effects [After Easterling 1992].

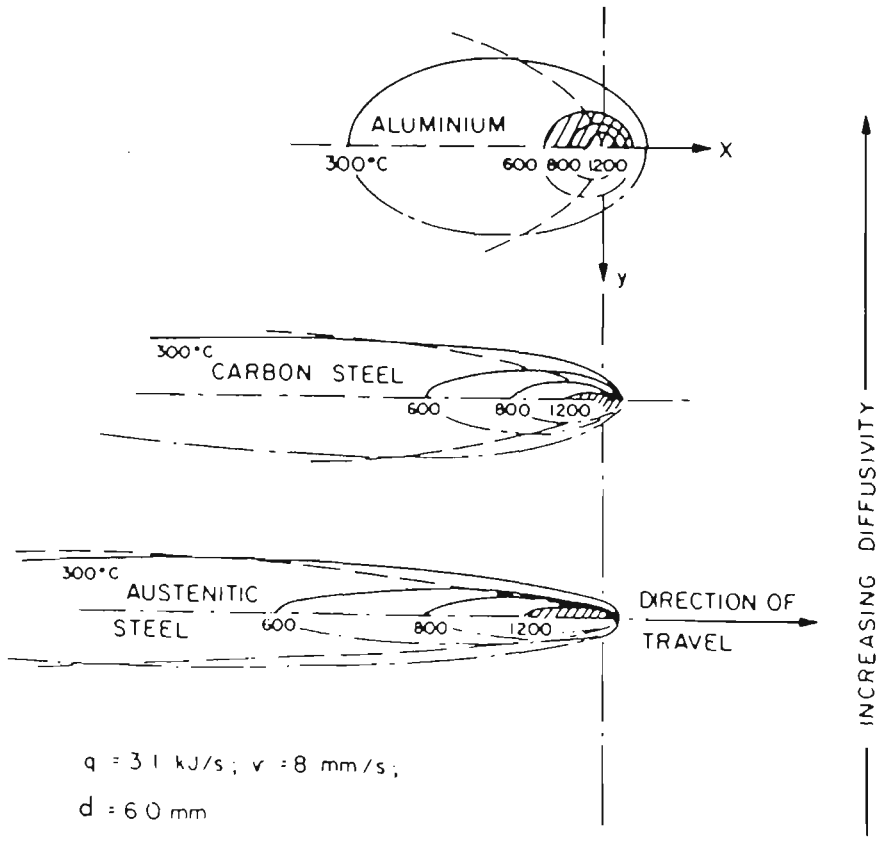

Figure 5.8 Effect of thermal conductivity on isotherm shapes calculated using the Rosenthal equations [After Gray et al. 1975].

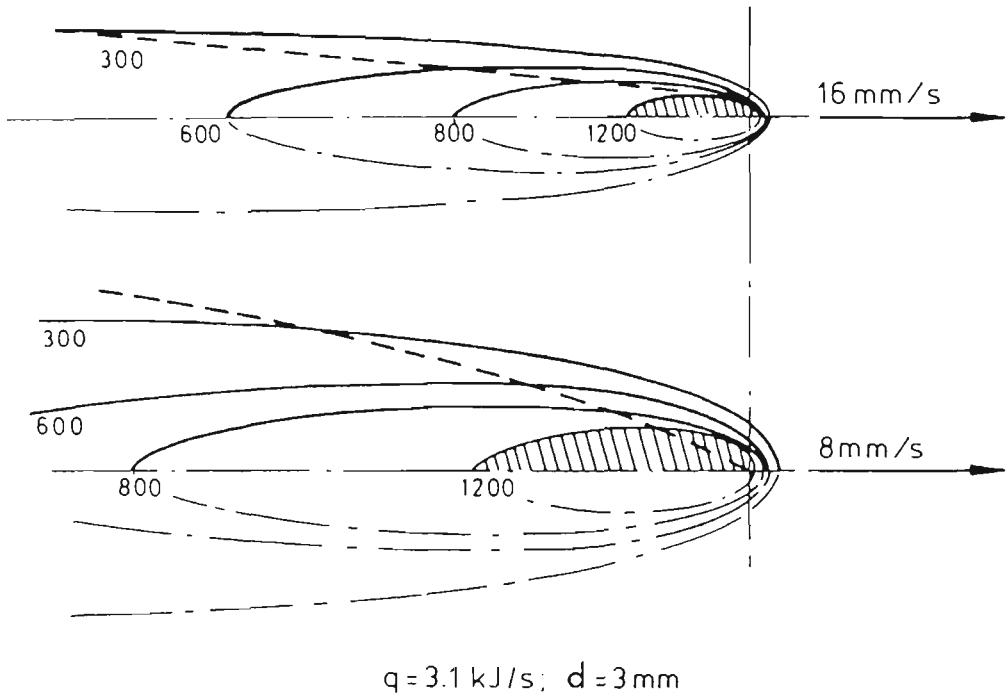

Figure 5.9 Influence of welding speed on isotherm shape in as mild steel [After Gray et al. 1975].

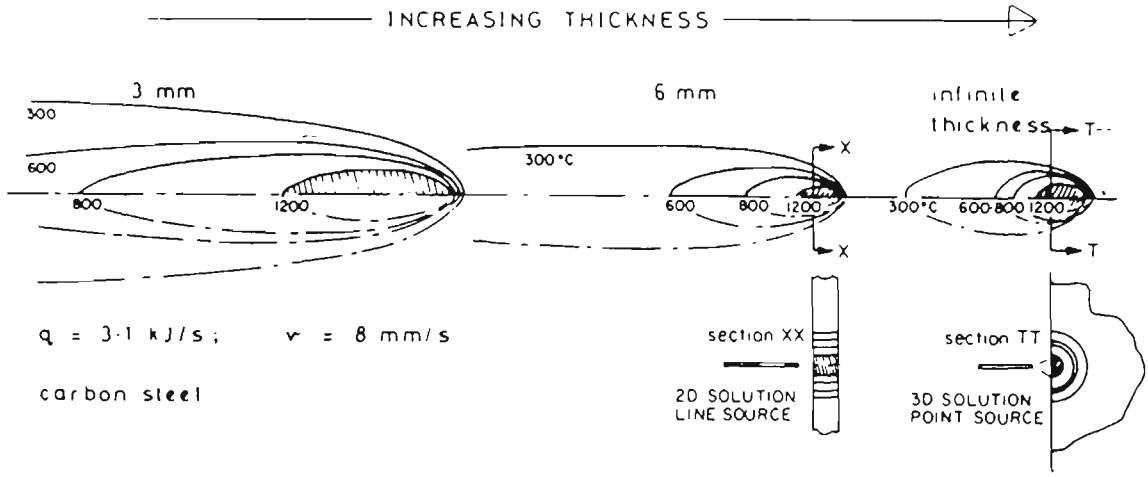

Figure 5.10 Effect of the plate thickness on isotherm shape [After Gray et al. 1975].

combination of variables determining the heat input are also influential in determining the structure and properties of the weldment [Chen and Pollack].

5.2 GEOMETRY OF WELD METAL

The geometry of the weld bead is significantly affected by the heat flow and fluid flow because of its effects on the temperature gradient in the weld pool and solidification behavior of the weld. Both of symmetrical and unsymmetrical weld pool shape can occur as a result of liquid turbulence during fusion welding, as shown in the **Figure 5.7**.

The surface tension of the melt and its interaction with the welding arc is a key sector affecting the turbulence and the shape of the pool [David et al. 1989; Zacharia et al. 1991]. This type of surface tension-influenced convection is known as **Maragoni convection**.

Oxygen and sulphur content in the melt are considered to have a strong effect on the surface tension. Electromagnetic forces and buoyancy within the melt can also influence the turbulence of melt [Zacharia et al. 1991]. It is, therefore suggested that the corresponding weld pool isotherms, i.e. the temperature field in the melt is even more complex than the predicted model.

The way of that the heat flux, thermal conductivity and plate thickness affects the geometry of the weld metal is discussed by equation (5.3). The distance between the isotherms, $i_{x,y,z}$, depends on the direction from the heat source, $r_{x,y,z}$.

$$\mathbf{i} \propto \mathbf{q}/(\lambda \nu \mathbf{d}) \text{----------} (5.3)$$

Here, **q** is the heat flux, λ is the thermal conductivity, **d** is the thickness of the plate, and ν is the velocity of the heat source. A comparison between the isotherm distributions for different materials, heat flux, thickness of plate being welded and travel speed can be plotted, see **Figure 5.8, Figure 5.9** and **Figure 5.10**.

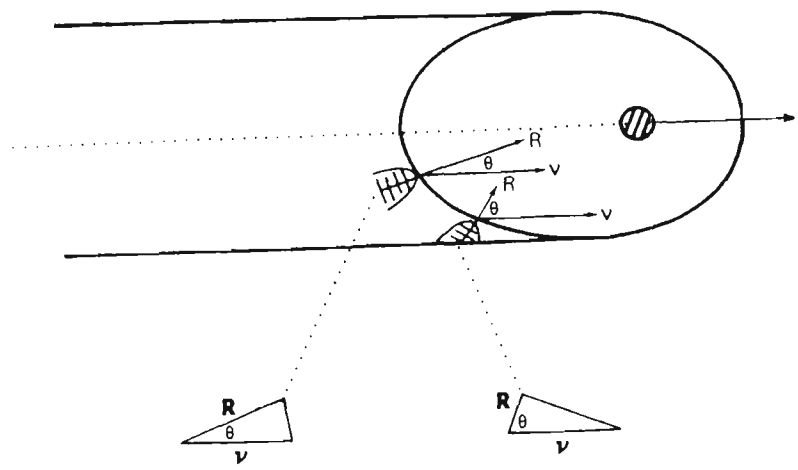

Figure 5.11 The relationship between crystal growth speed and welding speed in terms of rate vectors [After Easterling 1992].

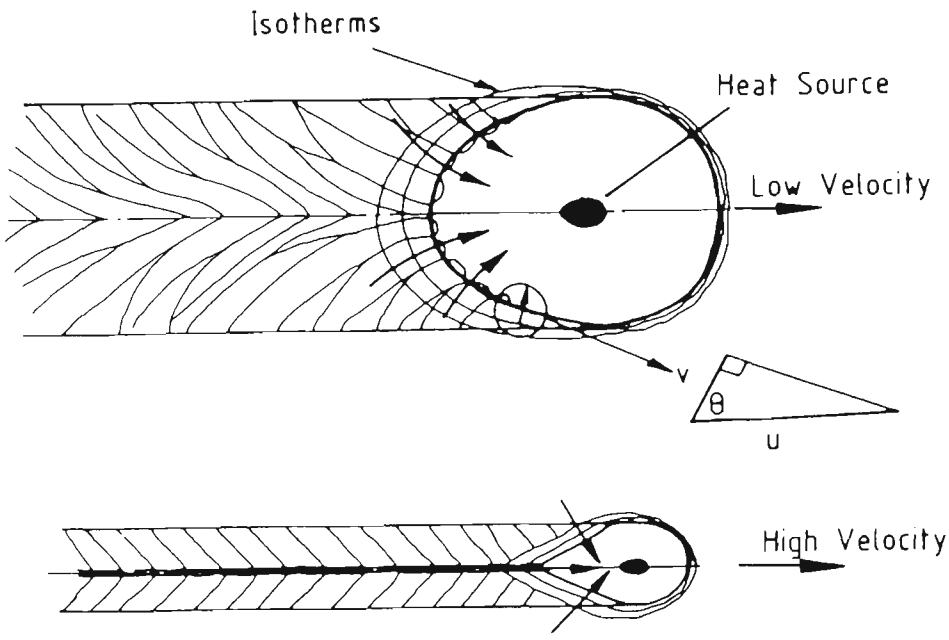

Figure 5.12 The effect of welding speed on the shape of the melt and on the mode of crystal growth [After Easterling 1992].

Any factors changing the geometry of melt will influence the mechanism of solidification. The crystal growth always occurs in a direction perpendicular to the isotherms, as illustrated in **Figure 5. 11**. Thus, the relationship between the crystal growth speed **R** and welding speed **v** can be expressed by following equation:

$$\mathbf{R} = \mathbf{v} \cos \theta \text{----------} (5.4)$$

where the θ is the angle between **R** and **v**. Since welding speed **v** is constant, **R** is dependent on the position of the liquids. The fast growing crystal should be at the weld central line behind the moving heat source ($\theta \cong 0$) and the slowest growing should be at the edge of the weld. The crystal growth characteristics have a strong effect on the microstructure and toughness of welds, as shown in **Figure 5.12**. At low welding speed, the crystal growth is able to keep up with the moving heat source in an orderly and symmetrical way, but continues curvature of the crystals is necessary. Changes in the direction of crystal growth occurs in the case of high welding speed due to the fact that at high welding speed crystal growth is directed mainly towards the weld centerline leading to a sharp contact plane of crystals growing from opposite boundaries, as shown in the **Figure 5.12**.

It is well known that the crystal growth tends to occur most rapidly along certain preferred crystallographic directions, such as <100> in the case of b.c.c. and f.c.c. metals. The crystals can grow more rapidly in the <100> direction than in more closely packed directions <111> in b.c.c. and <110> in f.c.c.. However, change in the orientation of the solidifying crystals has to occur by means of re-nucleation of grains with more favorable orientation in order to maximize growth rate along the steepest temperature gradient. The re-nucleation at an atomic level is likely to occur on the surface of the existing crystals.

All welding variables that influence on the heat flow and fluid flow will affect the weld bead geometry, such as voltage, current, speed, welding orientation and shielding gases, etc.

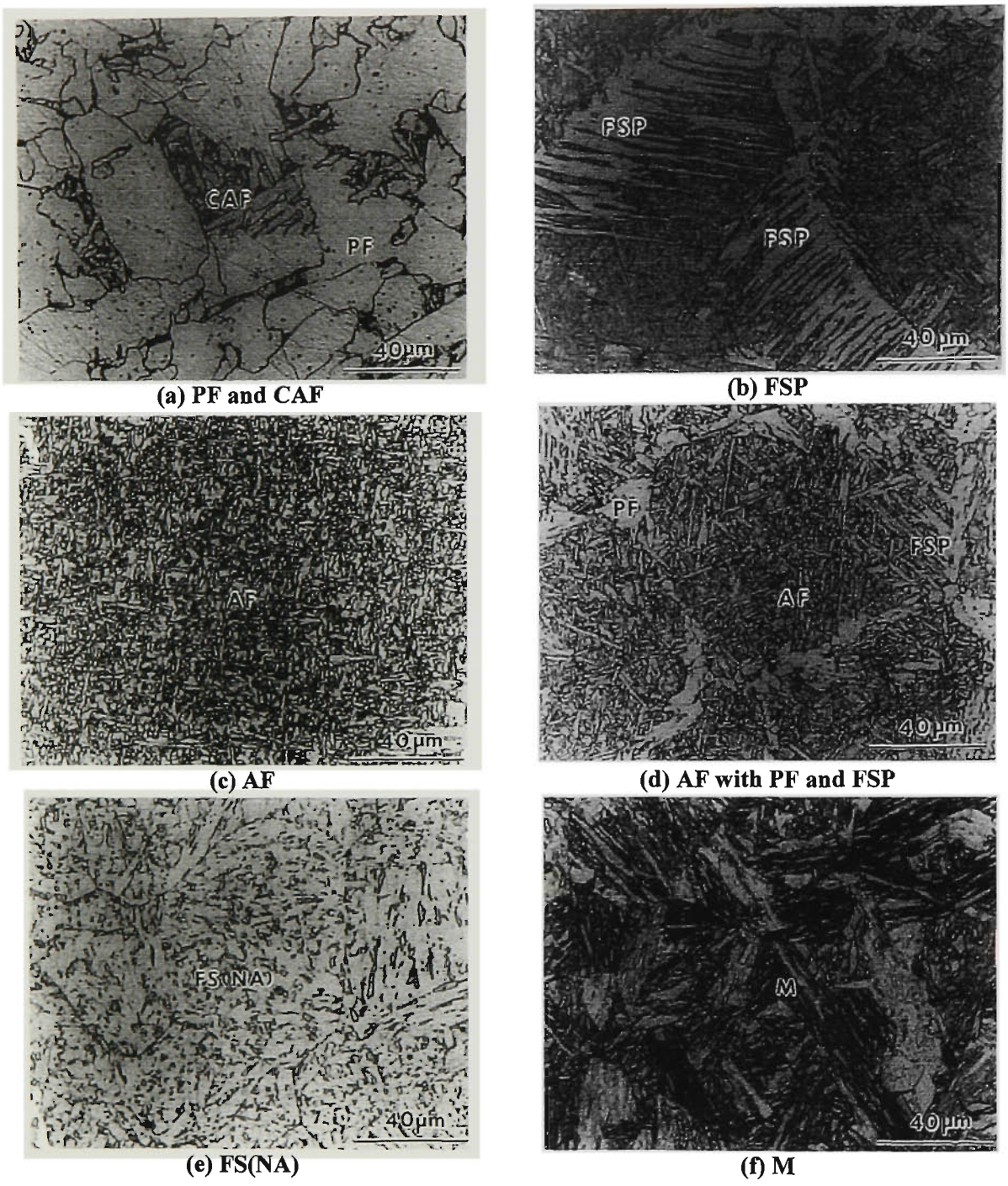

Figure 5.13 Typical weld metal microstructural constituents for C-Mn and low alloy weld metals [After Zhang and Ferrar 1995].

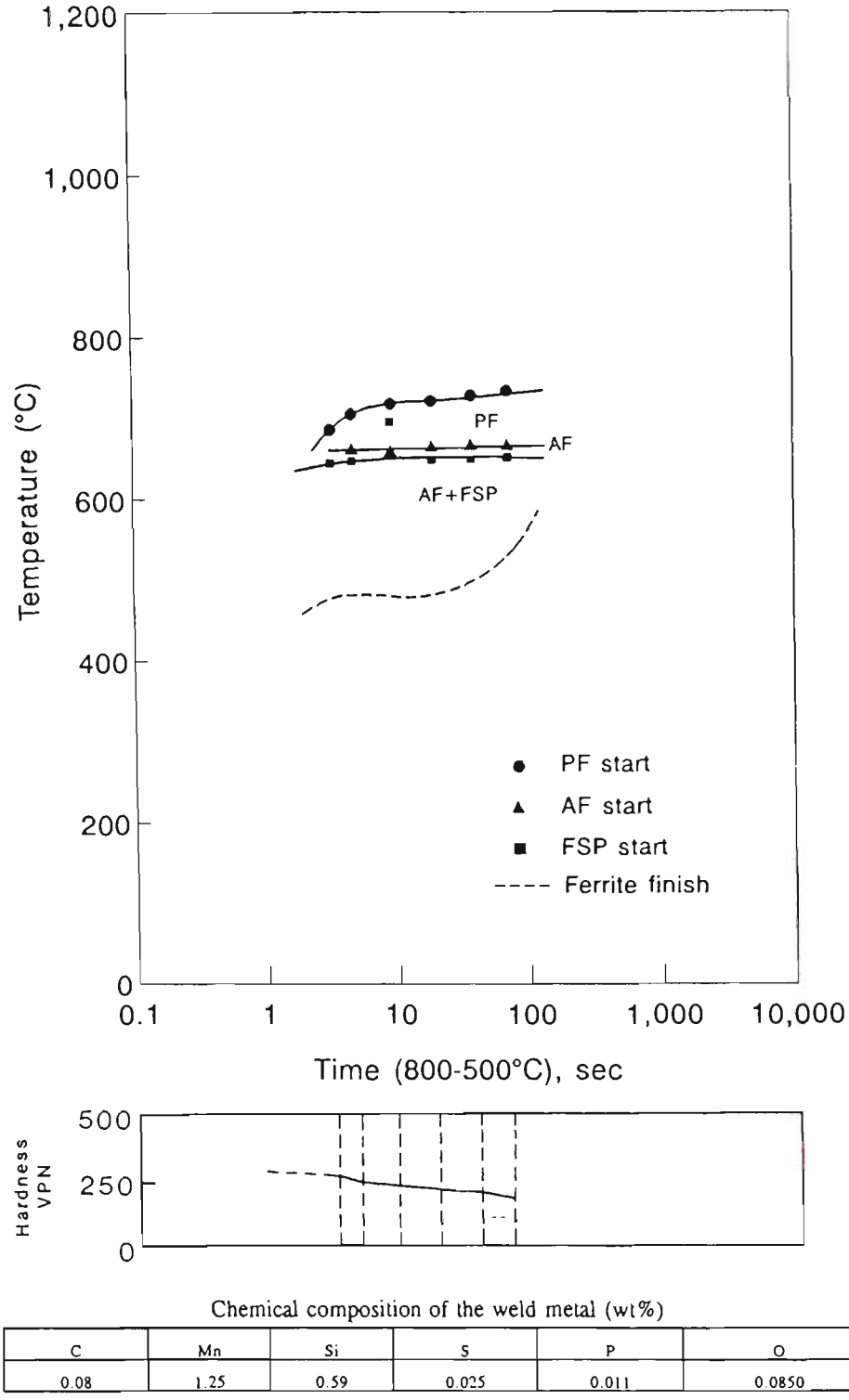

Chemical composition of the weld metal (wt%)

C	Mn	Si	S	P	O
0.08	1.25	0.59	0.025	0.011	0.0850

Figure 5.14 Typical CCT diagram for low C-Mn flux cored arc (FCAW) weld metal [After Zhang and Ferrar 1995].

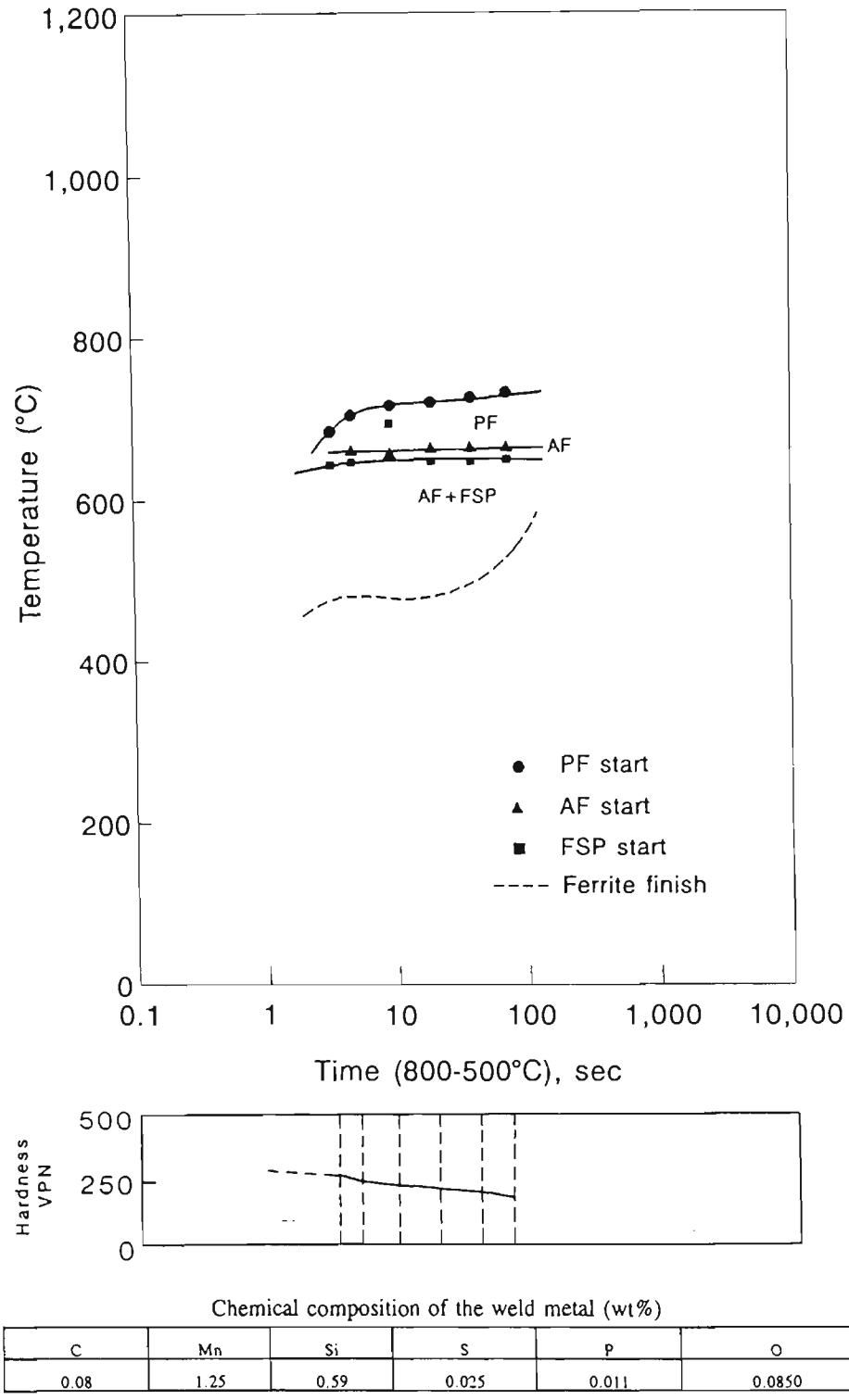

Chemical composition of the weld metal (wt%)

C	Mn	Si	S	P	O
0.08	1.25	0.59	0.025	0.011	0.0850

Figure 5.15 Typical CCT diagram for low C-Mn gas metal arc (MIG) weld metal [After Zhang and Ferrar 1995].

5.3 CONTINUOUS COOLING TRANSFORMATION DIAGRAMS AND PHASE TRANSFORMATION IN LOW C-Mn ALLOY STEEL WELDS

Although the character of the weld metal microstructure depends on alloy content, cooling rate, presence of non-metallic inclusion nuclei and plastic strain, the final microstructure will depend mainly on the cooling rate. The Continuous Cooling Transformation (CCT) diagram clearly represents the effect of cooling rate on transformation start and finish temperature, and complementary metallography can be used to establish the microstructure and the hardness. **Figure 5.13** shows the typical weld metal microstructural constituents for C-Mn and low alloy weld metals. The transformed microstructure from the γ to α usually consists of different forms of the ferrite phase, such as polygonal ferrite (PF), ferrite side-plate (FSP), acicular ferrite (AF), coarse acicular ferrite (CAF), ferrite with non-aligned second phase (FS(NA)), lath ferrite (LF) and martensite (M). In CCT diagrams each transformation product is represented by a separate curve, thus it is possible to form a mixed microstructure. **Figure 5.14** shows the CCT diagram for a low C-Mn flux cored wire (FCAW) weld. A typical CCT diagram for low C-Mn and low alloy gas metal arc weld (MIG) is illustrated in **Figure 5.15**.

5.4 NON-METALLIC INCLUSIONS IN THE WELD METAL

Non-metallic inclusions in weld metals are either exogenous or indigenous, dependent on their origin. The former arises from entrapment of welding slag and surface scale and the latter are formed within the system as a result of deoxidation and desulphurisation reactions or solid state precipitation reactions (nitrides, carbides) during solidification. Apart from the heterogeneous of the indigenous inclusions, both inclusions are very similar in terms of the chemistry (multiphase particles), shape (angular or spherical particles) and crystallographic properties resulting from the complex alloying systems [Roberts et al. 1982; Farrar 1974; Kluken et al. 1988; Dieter 1986]. However, the oxide inclusions in C-Mn steel welds are predominantly glassy, spherical, manganese silicates [McRobie et al. 1985].

Very low free oxygen content in the uncombined state is expected due to the low oxygen solubility in iron. However, a major amount of the oxygen is present as oxide inclusions resulting from reactions of oxygen with deoxidizing elements, such as silicon, manganese, titanium and aluminium in the molten weld pool. Some inclusions tend to be trapped in the molten pool because the cooling rate is too fast to let them to grow in the melt or separate from the liquid steel to the layer of molten slag covering the weld [Liu and Olson 1986]. And the inclusions may remain in the form of a fine dispersion of particles throughout the weld metal. The presence of these second phase particles will affect both the mechanical properties and the phase transformation of the weld metal.

The inclusion characteristics depend on the choice of atmosphere, welding technique, flux, consumables and subsequent cooling rate [Kiessling 1989]. Microanalysis of weld metal inclusions generally reveal the presence of titanium, manganese, aluminium and silicon [Barritte at al. 1981; Pargeter 1981]. The inclusions may contain many phases, which depend mainly on the flux and metallic additions. The phases may include: Al_2O_3, MnO, TiO, Ti(O,N), Ti(O,C), SiO_2 [Dowling et al. 1986]. In general, weld metal inclusions are smaller in size than the inclusions in the base metal, but the inclusion concentration can be high. The size range for weld metal inclusions is about $0.1\mu m < \mathbf{d} < 3\mu m$, where **d** is the diameter of inclusion.

Non-metallic inclusions in weld metal play two important but opposing roles.

1. They affect the decomposition of austenite by aiding nucleation of acicular ferrite within the austenite grains, and also suppress the formation of brittle bainitic structures, thus increases toughness of the weld metal;

2. They have a detrimental effect on toughness of the weld metal by debonding from the base metal or cracking under the plastic strain of dislocation pileups.

Good weld metal toughness and maximum resistance to the propagation of a fast running cleavage crack can be obtained when a large portion of fine acicular ferrite grains is present in the weld microstructure [Taylor and Farrar 1975]. Nucleation of

acicular ferrite is accelerated when there is a combination of large austenite grains and a high density of intragranular inclusions. The inclusions probably nucleate acicular ferrite by acting as inert substrates and reducing the energy barrier for nucleation [Ricks et al. 1982]. Each inclusion can nucleate several grains [Kiessling 1989]. It is claimed that acicular ferrite is usually the main structural component for an oxygen content of 300ppm in the weld metal [Abson et al. 1978]. It was also suggested that the optimum oxygen content of the weld metal should be about 300ppm, this being the amount that encourages acicular ferrite formation at oxide inclusions without loss of toughness due to an excess of inclusion volume fraction [Liu and Olson 1986].

The inclusions may also act as both ductile and cleavage fracture initiation sites. Cracking can be related to the different inclusion size distributions and the way in which these inc lusions influence the degree of pinning of prior austenite grain boundaries [Cochrane and Keville, 1978]. In ductile fracture, inclusions act as microvoid nucleation sites; after nucleation, the voids grow, link up with microvoids growing in an adjacent region, and form a fracture surface [Hill and Passoja 1974]. As a result of this, the toughness of the weld metal will be reduced with an increase in the number and size of inclusions [Kiessling 1989]. Hence, ductile crack growth will be promoted by an increased size and decreased separation of inclusions [Chin 1969; Van Stone at al. 1985; Abson and Pargeter 1986]. For cleavage fracture, non-metallic inclusions lying within the plastic zone ahead of the crack tip were found to be active as cleavage initiation sites. Once nucleated the crack spreads into the surrounding matrix as a brittle crack [McRobie and Knott 1985; Tweed and Knott 1987]. Under conditions, where oxide inclusions are located along the ferrite grain boundaries, susceptibility to weld metal brittle fracture is increased for a total oxygen content in the weld of more than 350 ppm [Potapov 1993]. These inclusions block dislocations and serve as crack initiation sites as the weld metal is deformed.

The effect of inclusion type and distribution on the acicular ferrite nucleation is more significant than the total volume fraction. Titanium containing oxides (TiO) are considered to be particularly effective in promoting intragranular nucleation of acicular ferrite [Evans 1986]. Apart from TiO, TiN, Al inclusions, MnO, V(CN), VN and

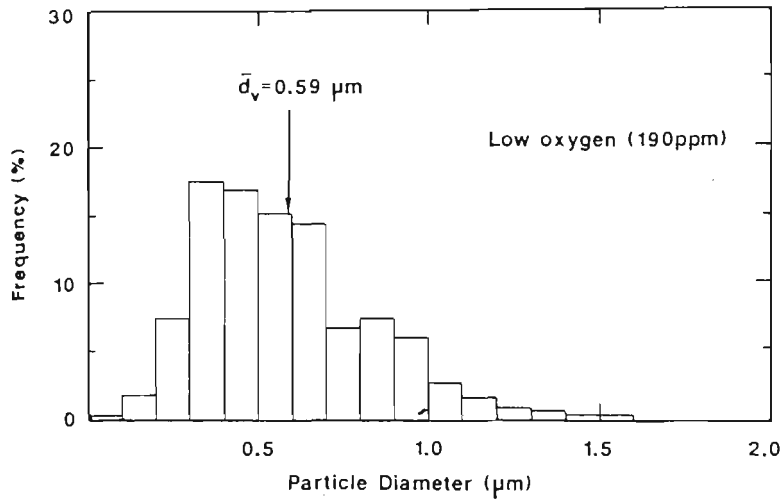

(*a*)

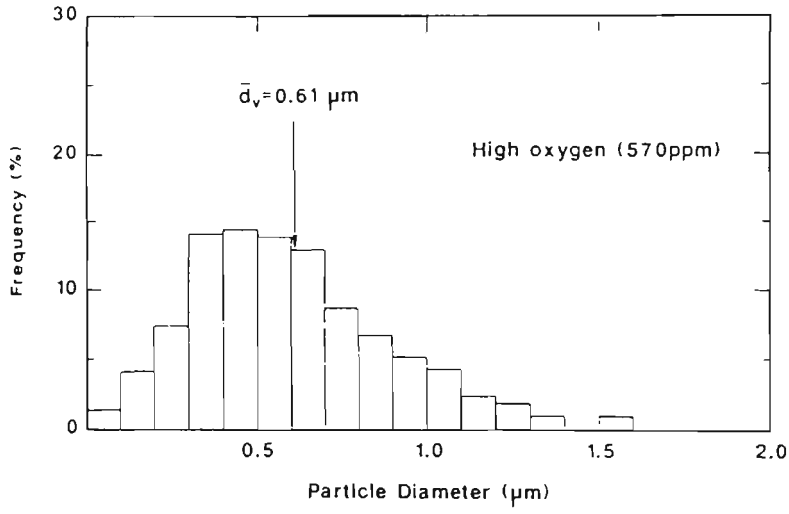

(*b*)

Figure 5.16 Effect of oxygen on 3-D inclusion size distribution [After Kluken and Grong 1989].

MnSi/TiO have also been reported to nucleate acicular ferrite [Mori et al. 1981; Ohkita at al. 1984; Ito and Nakanishin1975; North et al.1979 ; Bhatti at al. 1984 Koukaki 1979; Grong et al. 1986].

Ahlblom et al. (1983) concluded that the high fractions of acicular ferrite are normally associated with small diameter inclusions. In contrast, Lui and Olson (1986) claimed that coarse austenite grains with a large number of inclusions with diameters larger than 0.2 μm resulted in a high acicular ferrite content. They also indicated that the weld metal with high oxygen content and high grain boundary ferrite content could be associated with fine prior austenite grains with a large number of inclusions of diameter less than 0.1 μm. Work reported by Dallam et al. (1985) also showed that the mean particle size of inclusions decreased with increasing oxygen content. However, Ferrante and Farrar (1982) and Cochrane at al. (1983) reported that the mean inclusion diameter increased with increasing weld metal oxygen content. They also found that prior austenite grain sizes larger than 45 μm tended to result in acicular ferrite. Kluken and Grong (1989) and Babu et al. (1995) later also reported that increasing the weld metal oxygen content results in displacement of the weld metal inclusion size distribution to larger diameters. **Figure 5.16** illustrates the effect of oxygen on the 3–D inclusion size distribution.

CHAPTER 6

EFFECT OF FUSION WELDING ON GALVANIZED SHEET STEELS

Fusion welding on galvanized steel has more problems than fusion welding of uncoated steels. The effect of the zinc alloy coating and the substantial localized softening in the HAZ of the cold rolled sheet, induced by the welding thermal cycle, are two significant problems attending the joining of galvanized sheet steel by fusion welding. Zinc and zinc alloy coatings can lead to rapid degradation of spot welding electrode in the fabrication of steel sheet by resistance spot welding [Sawhill et al. 1974; Boniszewski et al. 1965 and 1974]; produce weld metal porosity (blowhole and pits) in arc and laser welding [Takenouchi and Shimizu 1992; Wyatt 1993]; induce arc instability and spatters, and cause intergranular cracking in the weld metal [Gregory 1968]. High strength cold rolled steel suffers a loss in strength in the HAZ as a consequence of fusion welding [Moro and Dunne 1990]. Therefore, a downgrade in strength in the weld fabrication of cold rolled steel has to be taken into account. The strength lost in the HAZ cannot be restored through later heat treatment.

6.1 WELDABILITY OF GALVANIZED SHEET STEELS

In general, the weldability of steel is evaluated on the bases of ability to resist cracking. Toughness of the weldment is also a critical factor for service requirement. "Good weldability" is determined by several factors [Easterling 1992], such as

1) type of welding process;
2) environment;
3) alloy composition; and
4) joint design and size.

The factors are decisive to the steel's weldability and unsuitability of any of these factors may cause cracking problems.

6.1.1 Weld Cracking of Arc Welded Joints in Galvanized Steel

Although most fusion welding techniques can be used for joining galvanized steels, welds in galvanized steel using carbon steel electrodes are subject to cracking. The

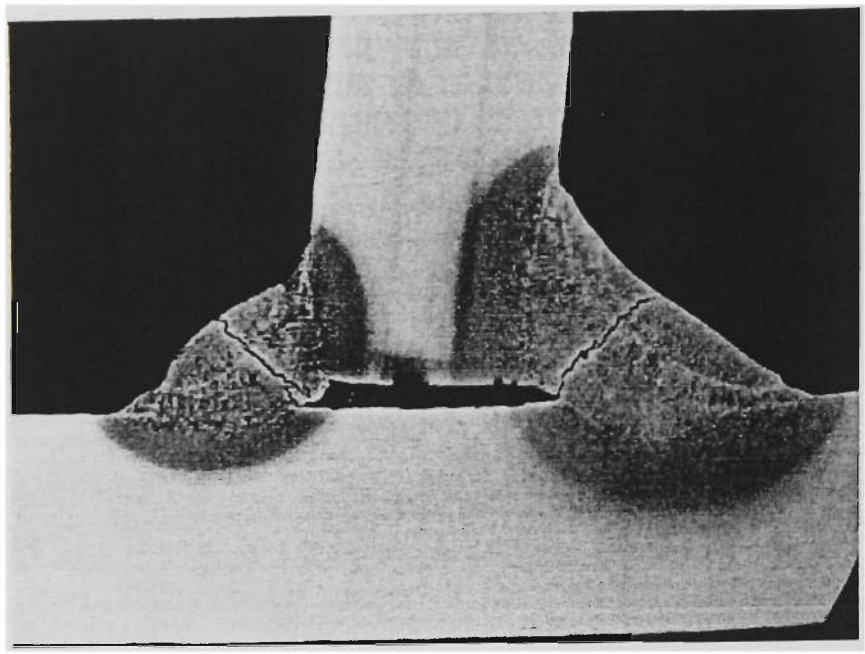

Figure 6.1 Cross section of 6.4 mm GMA cracked fillet welds of galvanized steel with CO_2 shielding gas [After Welding Handbook Vol.4 1998].

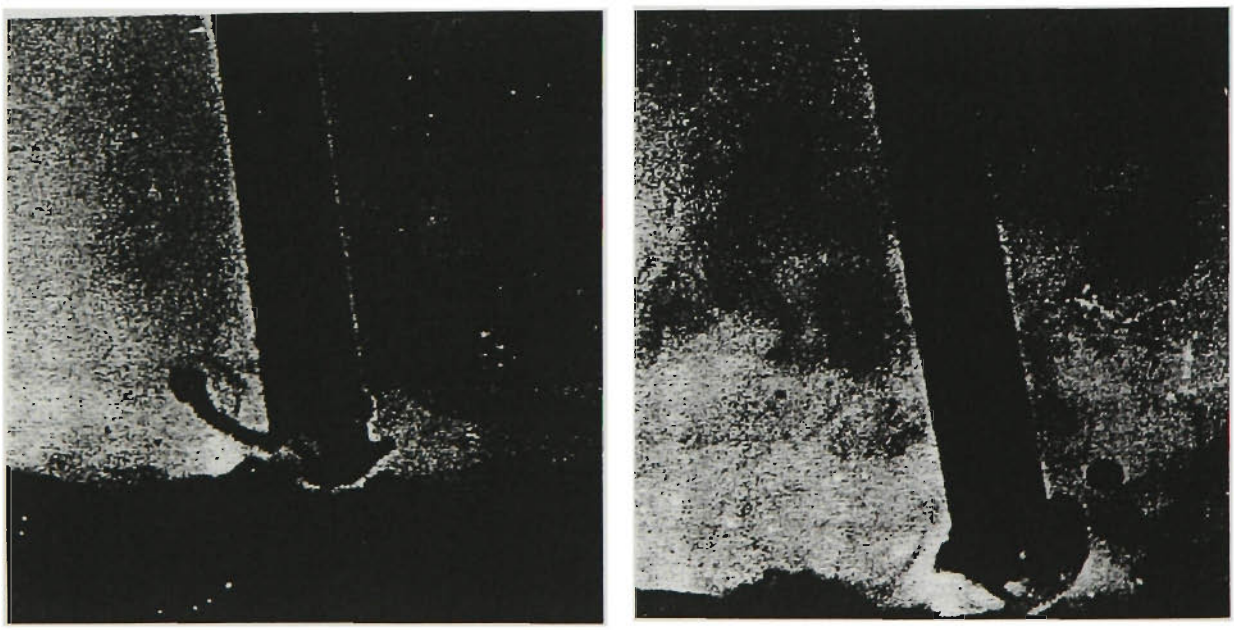

(a) (b)

Figure 6.2 High speed motion pictures of CO_2 short-circuiting arc on galvanized sheet steels showing (a) repulsion of molten electrode tip forming spatter immediately before short circuiting and (b) arc re-ignition and spatter formation (different short circuiting from (a) [After Gragry1969].

cracking is caused by intergranular penetration of zinc into the weld metal and is sometimes called zinc penetration cracking. It occurs most often along the throat of a fillet weld as shown in **Figure 6.1**. Sometimes cracking is also observed in the base metal in HAZ [AWS Welding Handbook Vol.4 1998].

It is believed that steel is embrittled by molten zinc because that Zn has a considerable solid solubility in iron. As a result, Zn and iron form an intermetallic compound at Zn melting temperature. Steel weld metal is easily attacked by molten zinc along its grain boundaries and forms a brittle compound that fractures when a sufficient residual tensile stress is present. This mechanism, however can only explain the cracks caused by fused zinc in steel welds over extended periods of time. Since the chances are remote for forming a brittle, zinc- rich phase during short intervals of arc welding, more studies are needed before the zinc-related cracks in steel welds can be explained satisfactorily.

The zinc-related cracking is affected by following factors:

1) galvanized coating thickness;
2) galvanized steel thickness;
3) joint type and root opening;
4) welding process; and
5) electrode classification.

More severe cracking occurs for thicker Zn coatings. Cracking tends to be less prevalent with shielded metal arc welding (SMAW) than with gas metal arc welding (GMAW) because of the lower travel speed and a higher heat input of SMAW which results in volatilization of a great amount of zinc ahead of the molten weld pool. With GMAW, intergranular penetration of Zn has been reported in fillet welds in 6.35mm galvanized steel while with SMAW cracking did not occur even with 12.7mm galvanized steel [Welding Handbook Vol.4 1998]. Welding consumables low in silicon are preferred. Based on experiments, weld metal containing about 0.2% silicon or less is usually free from zinc penetration cracking. Excessive amounts of silicon or magnesium introduced to the weld metal may concentrate within dendrites during solidification allowing intrusion of molten zinc from the coating.

Cracking and/or porosity is less severe when zinc fume can escape rapidly ahead of the weld pool. Therefore, a joint with a large root opening is preferred and butt welds are less susceptible to pores/cracking than lap welds.

6.2 WELDING QUALITY

6.2.1 Surface Appearance

Although a large amount of spatter is evolved in GMAW of galvanized steel, the surface appearance of welds made with a short-circuiting arc using CO_2 shielding has been shown to be satisfactory [Gregory 1968].

6.2.2 Spatter

A greater amount of spatter can be produced by GMAW on galvanized steel with a short-circuiting transfer mode. Generally, spatter can be controlled in welding the uncoated steel by changing the inductance of the choke in the circuit of the power source. Unfortunately, this procedure does not help in GMAW of galvanized steel [AWS 1983].

High speed motion picture observations of a CO_2 shielded arc on uncoated steel were made by Salter in 1964 [Salter 1964]. This work showed that the metal droplets formed on the end of the melting electrode were not transferred smoothly across the arc but appeared to be repelled by a force within the arc when welding current was below 400 ampere. This might be caused by a short circuiting transfer mode. The short-circuiting occurs about 100 times/s., and each short circuit causes a momentary rapid rise in current which fuses the molten metal contact and re-establishes the arc. The re-ignition is accompanied by the ejection of small particles of molten metal in the form of spatter.

In 1969, E. N. Gregory and his research group took high speed motion picture films of CO_2 shielded short-circuiting arc welding on galvanized steel. It was discovered that the repulsive force on the end of the electrode appeared to be much greater than for welding

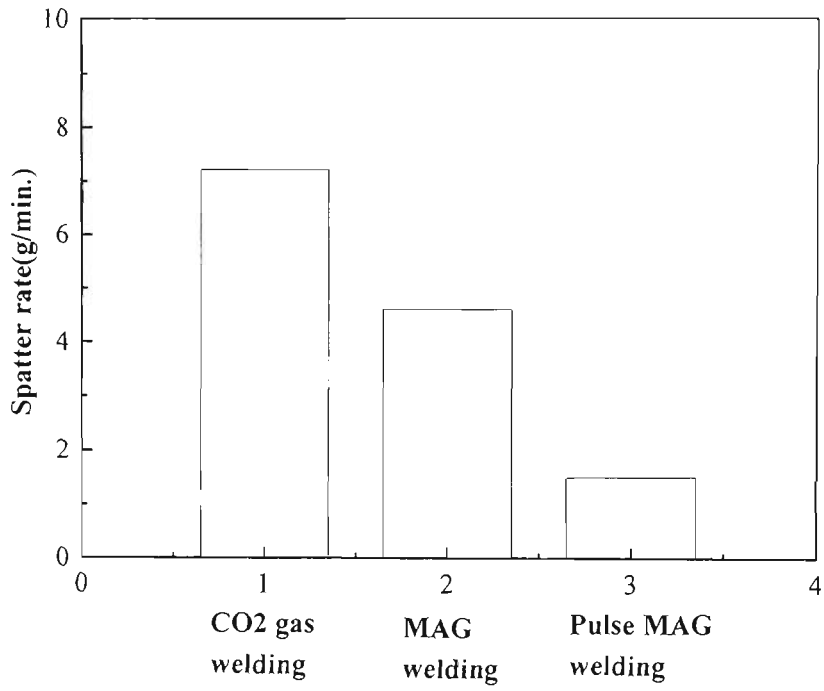

Figure 6.3 Effect of welding process on spatter rate for galvanized steel sheet [After Takenouchi and Shimizu 1992].

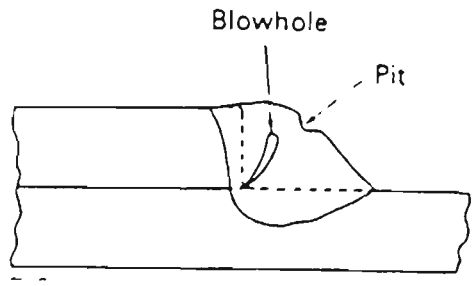

Figure 6.4 Schematic graph showing blowholes and pits developed in th3e arc welds [After Takenouchi and Shimizu 1992].

of uncoated steel. This effect might be the result of Zn vapor streaming to exert a direct repulsive force on the end of the molten electrode as shown in **Figure 6.2**. It was concluded that spatter formation in CO_2 short-circuiting arc welding of galvanized steel is due both to short-circuiting and to an upward repulsive force which acts on the molten tip of the filler metal or electrode [Gregory 1969]. The extent of spatter depends on the particular welding power source, welding processing and welding wire [Gregory 1968].

The change from thyristor to inverter control system, brought about a reduction of the amount of spatter to 1/3 to 1/2 of that with thyristor control [Mita 1990]. The effect of welding process on the amount of spatter is illustrated in **Figure 6.3** which clearly shows that the spatter rate was reduced drastically for lap fillet MAG welding of galvanized steel using an inverter controlled pulse power source [Yamamoto 1989].

The effect of welding wire on the spatter rate for CO_2 welding of steel was reported by Arai in 1983 [Takenouchi and Shimizu 1992]. It was found that the spatter rate decreases with increasing Si, Ti, and Mn in the welding wire and decreasing C and Al. These trends could be caused by the effect of the welding wire constituents on the number of short circuits. An increase in the number of short circuits reduces the spatter rate [Arai 1983].

6.2.3 Arc Stability

Welding current and voltage waveform are used to determine the arc stability. It had been claimed that the arc for GMAW of galvanized steel using both CO_2 and 80%-Ar with 20%-CO_2 shielding gas remained the same as for the uncoated steel [Gregory 1969]. However, a reduction in welding current and transfer frequency for GMAW of galvanized steel were observed and this might be caused by the Zn coating at the cathode reducing the voltage, current and electrode burn-off rate.

6.2.4 Porosity in Weld Metal

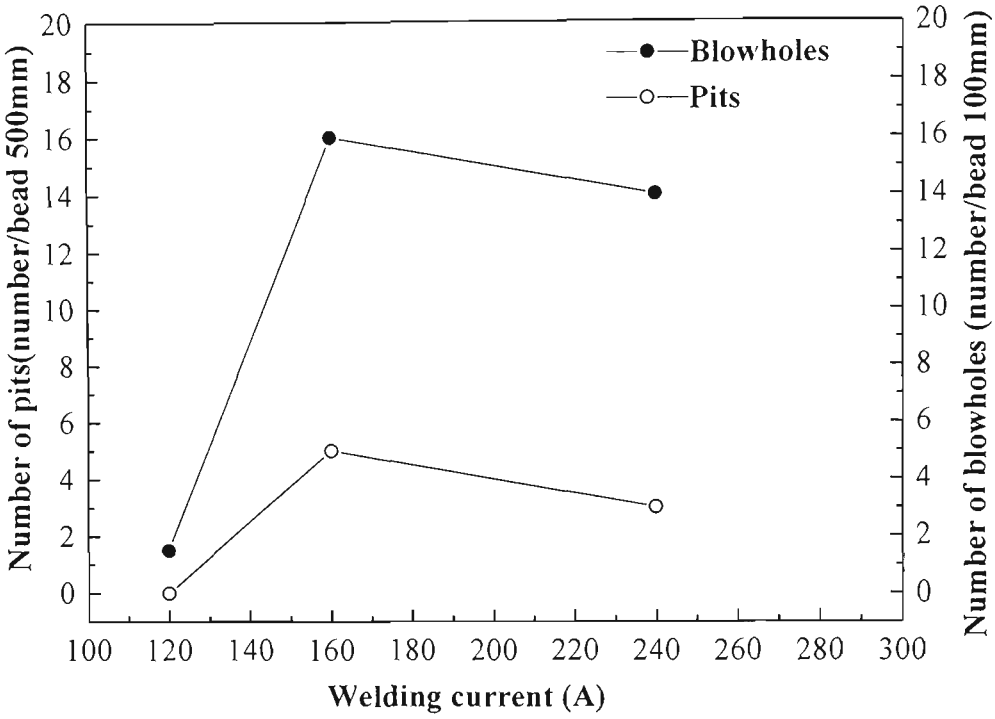

Figure 6.5 Effect of welding current on blowholes and pits in galvanized steel sheet welds [After Takenouchi and Shimizu].

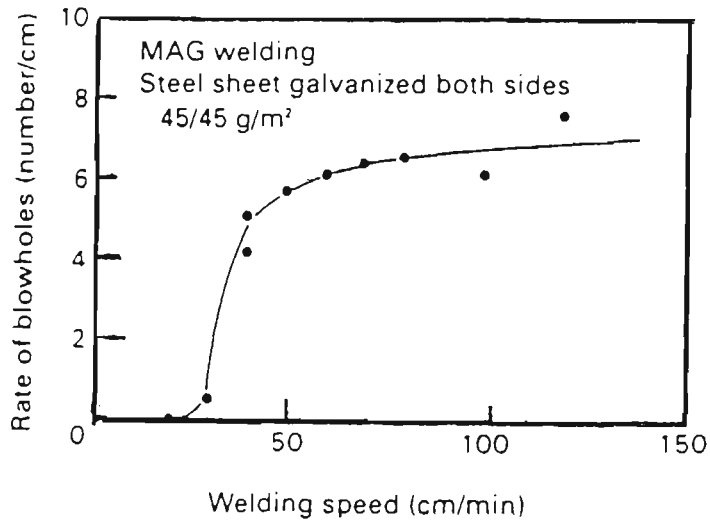

Figure 6.6 effect welding speed on blowholes in galvanized steel sheet welds [After Takenouchi and Shimizu 1992].

Porosity is developed in weld metal by nucleation and growth of gas or vapor bubbles before the molten pool is solidified. Therefore, there are two critical conditions for forming porosity: presence of gas or vapor sources in the system; and the solidification rate of the weld metal [AWS Welding Handbook Vol. 4 1998]. The lower the solidification rate of the weld metal, the lower the probability of developing porosity because the vapor bubbles have more opportunity to escape. On the other hand, for a very high solidification rate, either gas bubbles do not have the opportunity to nucleate or they nucleate and are trapped before their growth is significant. Porosity in weld metals includes blowhole and pit formation, as shown in **Figure 6.4**.

Three major factors that influence the formation of porosity are:

1) the welding process;
2) the welding wire;
3) the welding conditions.

In 1989 Yamomoto compared CO_2 GMAW with MAG welding and he found that MAG pulse welding of galvanized steel using solid wire reduces blowholes and pitting [Yamamoto 1989]. An increase in C, Ti and P reduces the porosity. It was suggested that the effect of C is connected to the increased number of short circuits related to emerging zinc vapor. In the case of Ti and P, the formation of compounds with Zn is thought to control the occurrence of porosity [Aida et al. 1989].

However, for GMAW of galvanized steel the opposite conclusion was made that fewer pores developed using welding wire which has a lower surface tension and has a positive surface tension temperature gradient [Shinoda et al. 1990]. Porosity in weld metal can be influenced by welding conditions such as welding current, speed, torch angle and gap. **Figure 6.5** and **Figure 6.6** show the effect of welding current and speed on the porosity in weld metal. It is clearly shown that the incidence of pitting and blowholes increase with increasing welding current and speed [Aida et al. 1989; Yasuda et al. 1989].

Using certain welding techniques, such as downward lap fillet MAG welding of galvanized steel with the torch angle at 15-20° and the work angle 15° it is possible to prevent the arc column from being disturbed by Zn vapour and thus to reduce the porosity [Asakawa et al. 1991].

The larger the gap for lap fillet welding, the lower the incidence of porosity [Yamamoto et al. 1989]. To prevent porosity in lap fillet arc welding of galvanized steel, it was suggested that a special compound could be applied to the surface of the overlap area before welding. This special compound is designed to react with Zn before Zn vapor forms and thus inhibits the formation of the porosity [Yasuda et al. 1989].

The mechanism of porosity formed in weld metal during arc welding of galvanized steels is proposed to be as follows:

1) the explosive combustion of Zn and the disturbance of the arc by the Zn vapor [Kozai Kurabu 1977];

2) the hydrogen within the zinc and ferroalloy layer of the galvanized steel is dissolved within the molten metal resulting in the thermal instability in the molten pool and unstable solidification leading to entrapment of the hydrogen in the weld metal. [Mukai 1989].

However, two different sets of results have been reported for the effect of H_2 and N_2 on blowhole formation. One set indicates that H_2 is the principal component and N_2 plays a minor role [Mukai 1989]. And the other set result that H_2 and N_2 are both influential [Aida et al. 1989]. Zn particles trapped on the inner surface of the porosity have also been reported [Yasuda et al. 1989; Aida et al. 1989].

6.3 W ELDING FUMES

Compared to uncoated steels, copious white fumes of Zn oxide are produced during arc welding of galvanized steel. If the fumes are inhaled in sufficient quantities they can

cause a metal fume fever. The more Zn fume produced the higher the probability of forming porosity in the weld metal. Based on the ideas of the elimination of carbon monoxide fumes in CO_2 welding, a vacuum extraction nozzle was fitted around welding torch for MMAW of galvanized steel by BWRA. The welding fume was almost removed completely, as well as reducing the porosity in weld metal [Gregory 1968].

To reducing the welding fume the following methods have been suggested by various researchers:

1) Fume extraction should be always used;
2) Removing coating from fusion area prior to welding;
3) Using fume extractor nozzles round the welding gun;
4) Using shielding gases with relatively low oxidation potential;
5) lower heat input would help to minimize the burn off the Zn coating; and
6) higher welding speed to reduce the weld size and zinc fume.

6.3 M ECHANICAL PROPERTIES

Most steels suffer an overall strength loss in the HAZ during arc welding as a result of the thermal cycle applied on the base metal. This was proved by research work carried out at Cornell University in 1970s on welded sheet steels less than 2.5mm thick. It was also demonstrated that failure during tensile testing usually occurs at the HAZ rather than in weld metal [Pekoz and McGuire 1979; Teh and Hancock 2000].

Extensive research on welding of galvanized steels was also carried out by Gregory and his group at BWRA [Gregory 1968 and Gregory 1969], Cambridge, UK for the International Lead Zinc Research Organization. The results of tensile, bend, radiographic, Charpy impact and fatigue testing showed that the properties of sound GMA and MMA welded in galvanized steel were equivalent to those of sound welds in uncoated steels [GAA 1981]. It was therefore concluded that the presence of the zinc coating had no detrimental effect on the properties of welds in galvanized steel sheet.

The research work carried out at the Sydney University has shown a drop in strength in the HAZ to 488 and 495 MPa from 596 and 529 MPa for GMA lap welded G450 1.5mm and 3.0mm GALVASPAN^{TM} cold rolled sheet steels respectively. These lower value tensile strength are higher than the nominal tensile strength of 480 MPa. The HAZ tensile strengths of GMA lap welded G450 sheet steel was not substantially affected by the heat input [Teh and Hancock 2000]. On the contrary, for GMA butt welded G550 ZA and ZHT 0.85 and 1.0mm sheet steels it has been demonstrated that the extent of strength loss is dependent on the heat input and the HAZ tensile strength range is below the nominal tensile strength of 550 MPa.

Increasing the heat input has a detrimental effect on the tensile strength in the HAZ. A large strength loss in the HAZ occurs for high heat input arc welding because of the slow cooling rate [Chen et al. 2000]. At the same nominal heat input, the lowest tensile strength was found for backhand GMA welded sheet steel compared with the forehand and perpendicular electrode orientations [Chen et al. 2001]. Laser beam welding has little effect on the tensile strength of the HAZ for the low C-Mn and coated steel sheet due to its much higher heating and cooling cycle than arc welding [Frewin 1997].

The tensile strength of the weld metal is improved by using argon and carbon dioxide shielding gas compared with shielding by an argon and oxygen mixture [Shackleton and Luca 1979]. This implies that the thermal cycle in the HAZ of the base metal can be affected by the arc characteristics and the metal transfer mechanism by employing different mixtures of shielding gases.

Although the presence of extensive porosity did not affect the static strength of cruciform tensile test specimens, it caused a reduction in fatigue strength in cases where the fillet welds were small enough for failure to occur through the weld throat as a result of the porosity affecting the propagation of fatigue cracks but not the initiation [Drarton 1969].

The effect of the intergranular cracking due to the zinc penetration in fillet welds depends on extent of the cracks and on the service requirements of the joint. In some cases the extent of the intergranular cracking will not significantly affect the strength of

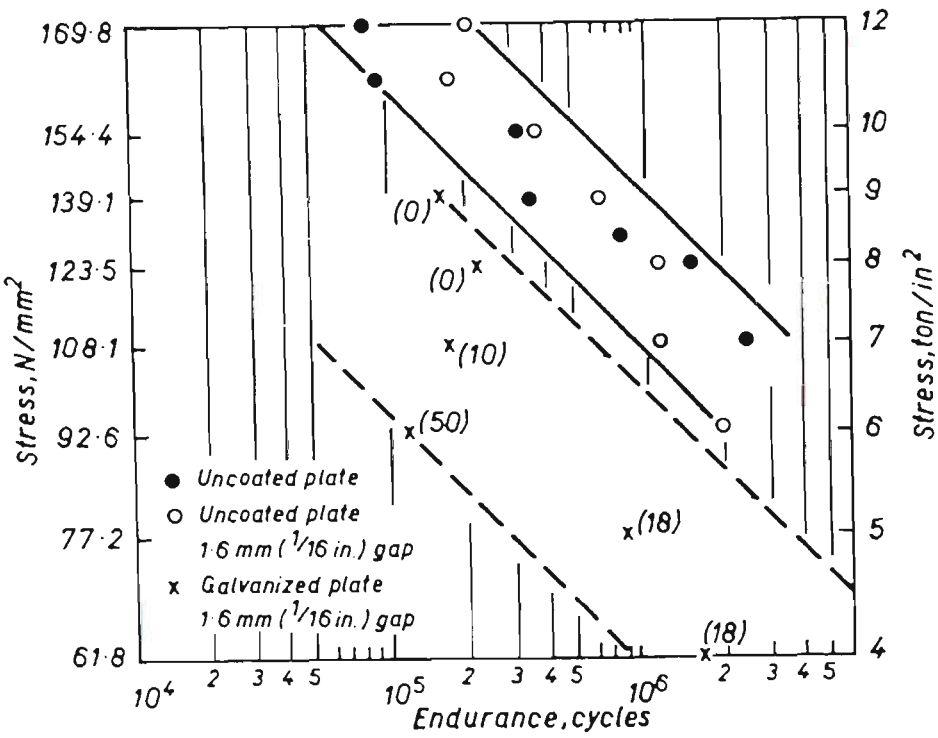

Figure 6.7 Effect of zinc coating on fatigue of cruciform joints. Numbers in brackets represent length of weld showing zinc penetrated cracking [After Gregory 1971].

the joint [Rudy 1960; Gregory 1969]. In other cases, however, intragranular cracking due to zinc can seriously affect the fatigue strength of a joint as shown in **Figure 6.7**. Different procedural tests on various materials are recommended.

6.5 CONCLUDING REMARKS

Little research has been reported on arc welding of thin gauge high strength steel sheet produced by zinc alloy coating. In particular the loss in strength of butt welded sheet has not been systematically quantified. The present research was undertaken to address this lack of data and to shed light on the structural changes in the weld zone that control the mechanical properties.

CHAPTER 7

MATERIALS AND EXPERIMENTAL METHODS

7.1 MATERIALS

ZINCALUME™ (ZA) G550 and ZINC-HI-TEN™ (ZHT) G550 grade sheet steels produced by BHP, Port Kembla, Australia, were used in this investigation. The chemical compositions of the two sheet steels are given in **Table7.1** The mechanical properties of ZA and ZHT G550 sheet steels specified by BHP are given in **Table 7.2** respectively. **Table 7.3** illustrates the actual tensile test results for the two sheet steels.

Table7.1 Chemical composition of the ZA and ZHT G550 grade structural sheet steels (wt%)

ZA										
C	**P**	**Mn**	**Si**	**S**	Ni	**Cr**	**Cu**	**Al**	**N**	**O**
0.06	0.014	0.24	0.005	0.01	0.02	0.01	0.009	0.037	0.0023	0.0016
ZHT										
C	**P**	**Mn**	Si	S	Ni	Cr	**Cu**	**Al**	**N**	**O**
0.06	0.015	0.24	<0.005	0.012	0.013	0.01	0.011	0.045	0.0025	0.002

Table 7.2 Mechanical properties of the ZA and ZHT G550G550 grade sheet steels specified by BHP

ZA SHEET STEEL

Steel Base Thickness	**Minimum specified properties** 0.42mm	≥0.60mm	**Typical properties** 0.42mm thick
Longitudinal tensile			
Yield strength, MPa			680-740
Tensile strength, MPa	550(min.)	550 (min.)	680-780
Elong. on 80mm, %	-	2 (min.)	1-6
Hardness, HR30T			75-85

ZHT SHEET STEEL

Steel Base Thickness	**Minimum specified properties** 0.42mm	≥0.60mm	**Typical properties** 0.42mm thick
Longitudinal tensile			
Yield strength, MPa	550 (min.)	550 (min.)	680 - 760
Tensile strength, MPa	550 (min.)	550 (min.)	680 - 780
Elong. on 80mm, %	-	2 (min.)	4 -10
Hardness, HR30T			75 - 85

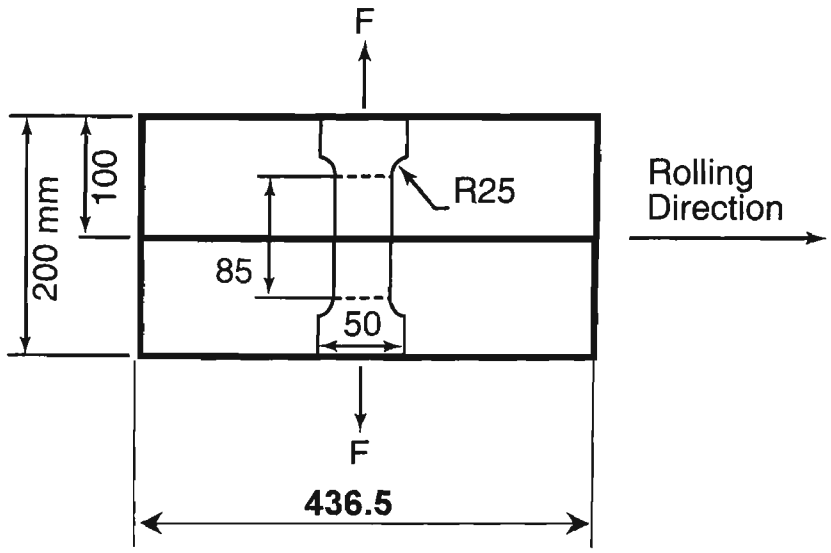

(a)

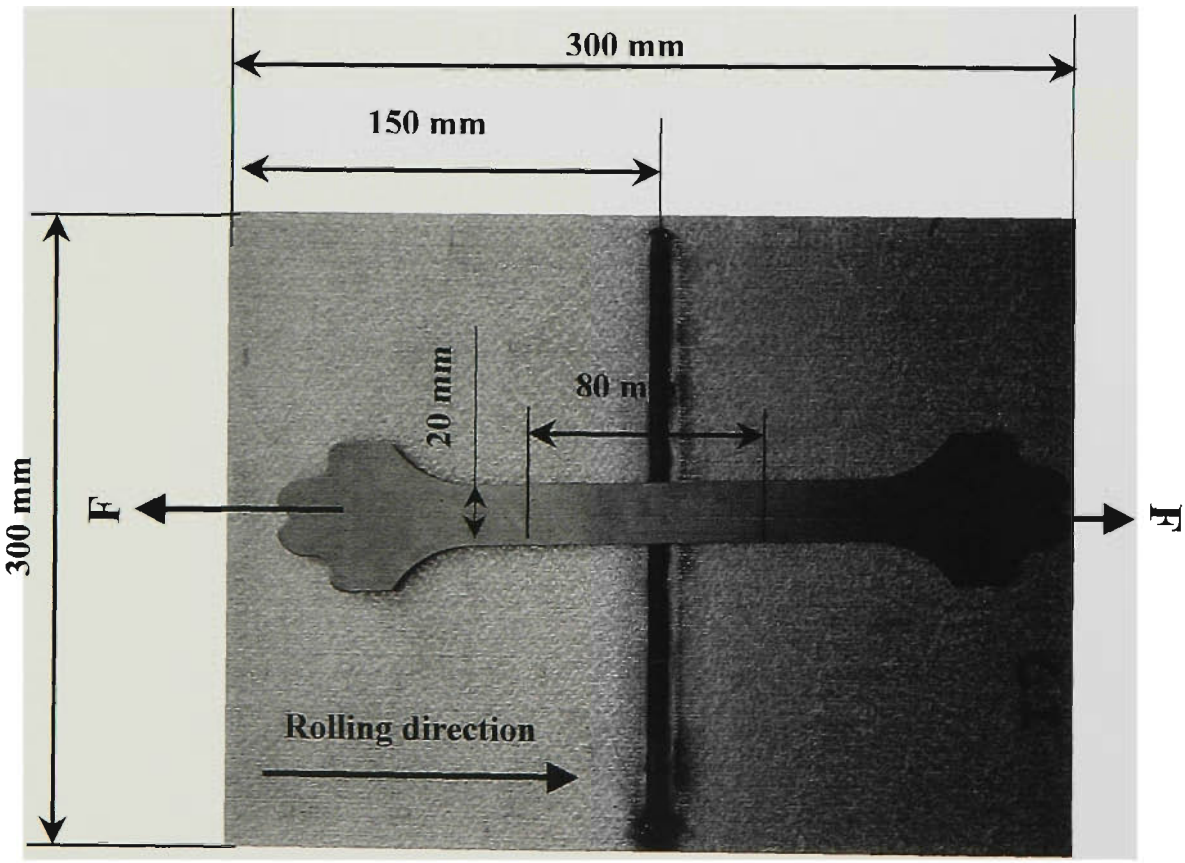

(b)

Figure 7.1 The dimensions of the steel sheet samples and the orientation of tensile test specimens for **(a)** 0.8 mm sheet steel of GMA welds and **(b)** 1.0 mm sheet steel of GMA and FCA welds.

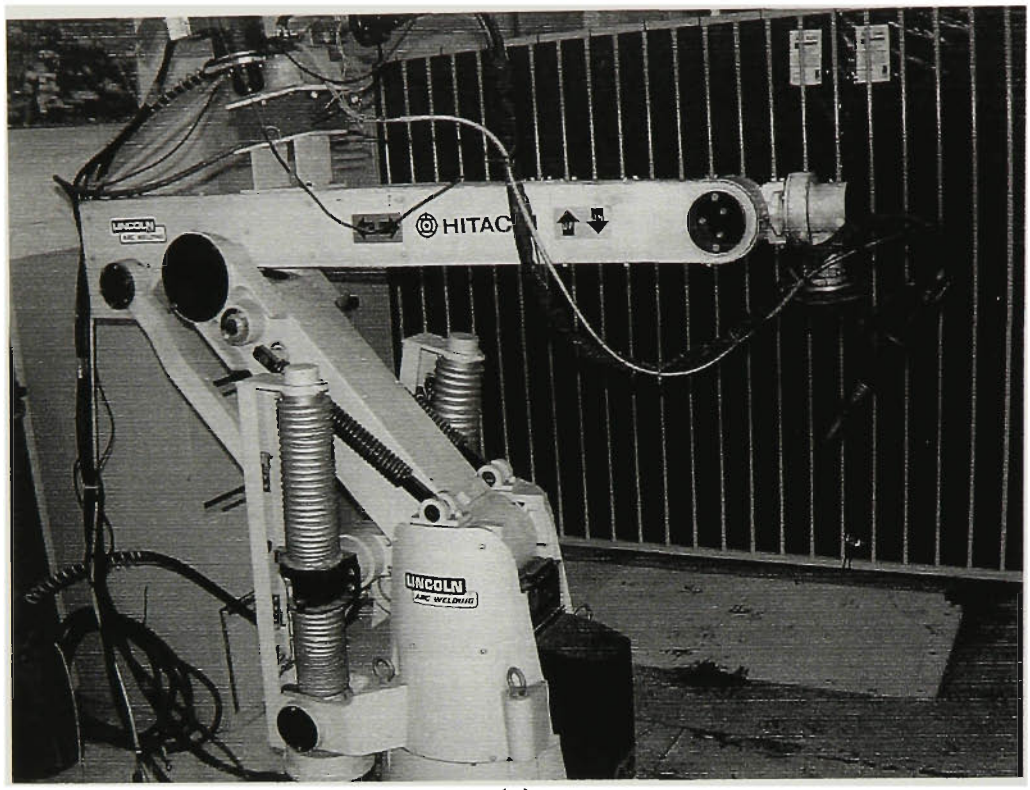

(a)

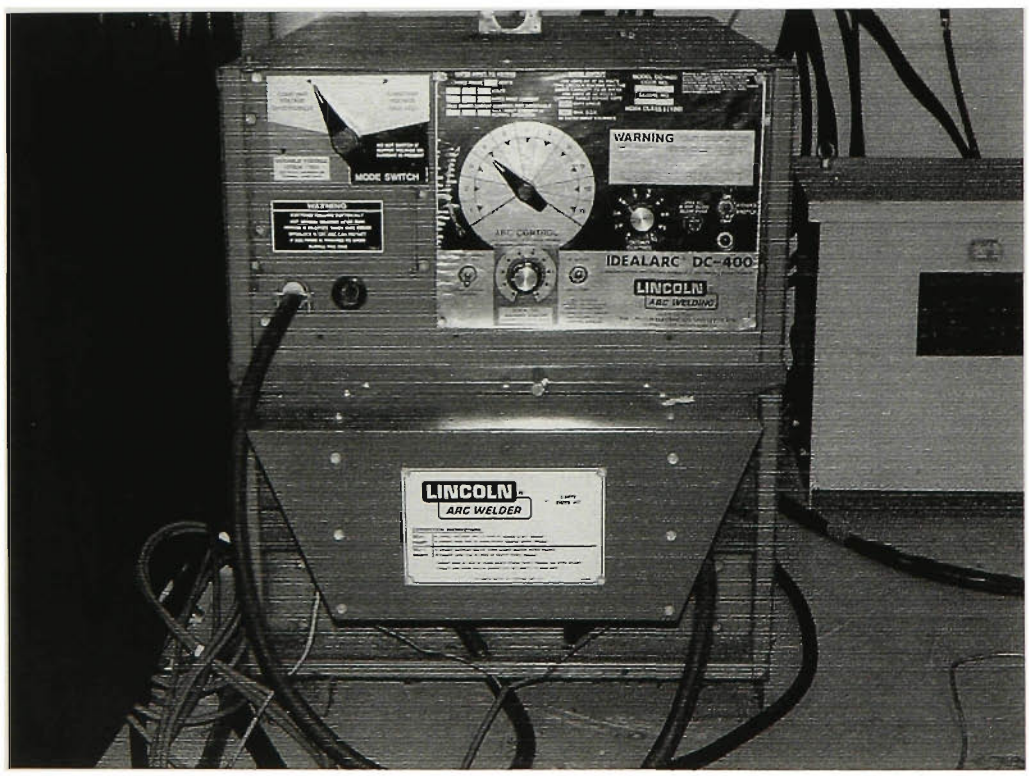

(b)

Figure 7.2 Photographs showing **(a)** the Hitach Lincoln M6060 II process welding robot and **(b)** IDEALARC DC-400 Lincoln welding power source.

Table 7.3 Actual tensile test results for the ZA and ZHT G550 1.0mm sheet steels

Sheet Steels	Tensile Strength, MPa	E longation, (%)
ZINCALUME™ G550		
Longitudinal	645	13
Transverse	725	4
ZINC-HI-TEN™ G550		
Longitudinal	655	12
Transverse	720	4

ZA G550 g rade 0.85mm and 1.0mm sheet steels and ZHT G550 grade1.0mm thick sheet steels were used for the gas metal arc welding. Self shielded flux cored arc welding was carried out using only 1.0mm thick ZA and ZHT G550 sheet steels.

The dimensions of the 0.85mm thick ZA steel sheet for GMAW were 436.5mm (parallel to the rolling direction)×100mm (in the transverse direction)×0.85mm (thick). The dimensions of the steel sheet samples used for GMAW and FCAW experiments were 300mm (transverse to the rolling direction)×150mm (parallel to the rolling direction)×1.0mm (thick) and 0.55mm (thick) (**Figure 7.1(a)** and **(b)**). The coating weights for the ZA and ZHT G550 sheet steels were 150 g/m^2 and 275 g/m^2, with a coating thickness of 25μm. The coating thickness was measured by SEM. GMAW of uncoated sheet steel was investigated by removing the coating with hydrochloric acid.

7.2 WELDING PROCEDURES

Gas Metal Arc Welding (GMAW) and Self Shielded Flux Cored Arc welding (FCAW) were used for this study. The GMA close-butted welding of G550 ZINCALUME™ and ZINC-HI-TEN™ structural steel sheet were carried out in the CRC Welding Laboratory at the University of Wollongong using an Hitachi Lincoln M6060 II process welding robot and an IDEALARC DC-400 Lincoln welding power source (**Figure 7.2 (a)** and **(b)**). The constant voltage operating mode and Direct Current Electrode Positive (DCEP) were chosen for the experiments on GMAW and FCAW unless otherwise stated.

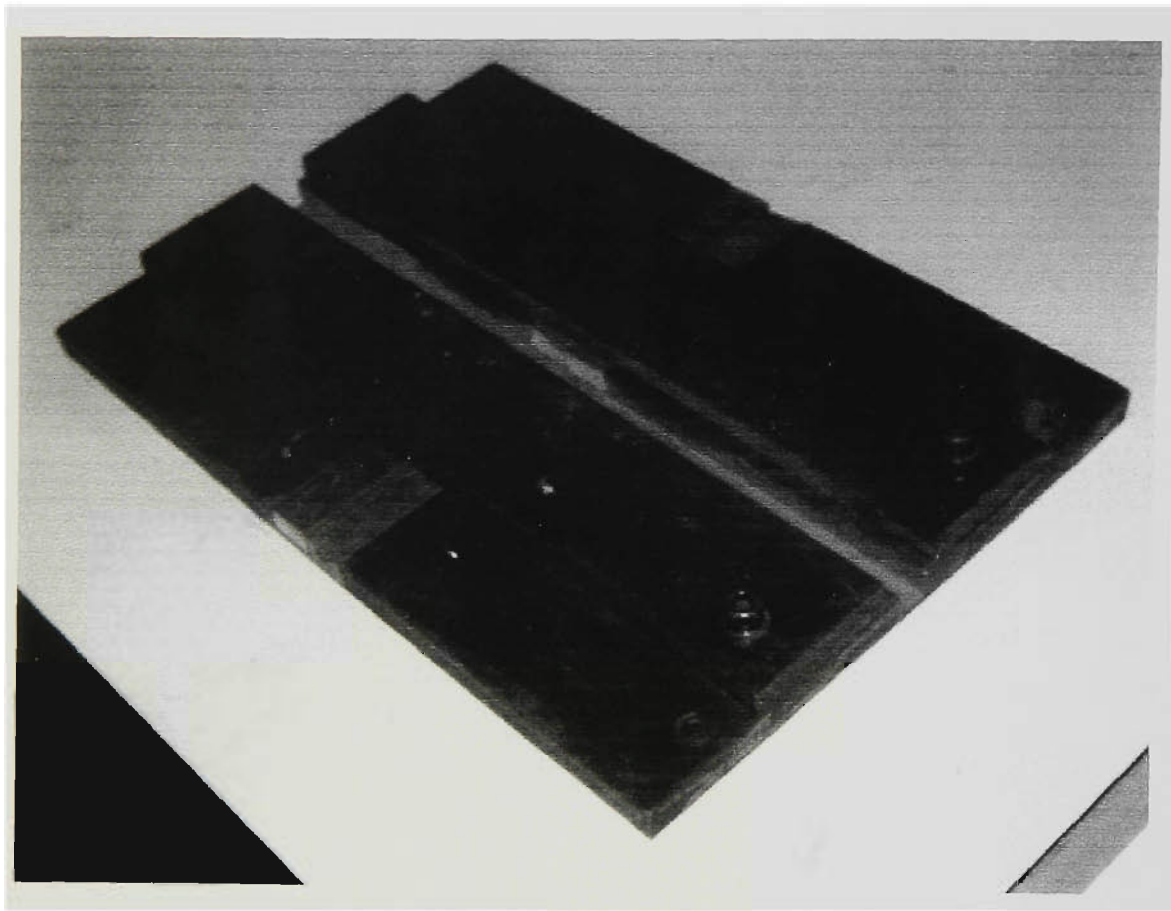

Figure 7.3 Photograph showing the jig used for GMAW and FCAW.

AWER 70S-4 electrode wire of 0.90mm in diameter produced by CIGWELD was used for the GMAW. This wire has a composition of 0.08%C, 1.16% Mn and 0.70%Si, 0.010%S and 0.015% P (wt.%). All welds were produced by a single butt welding pass on the surface of the sheet parallel to the rolling direction for the 0.8mm thick sheet steel and transverse to the rolling direction for the 1.0mm thick sheet steels. The gas flow rate was 14 litres per minute for the GMAW.

A specially designed jig was utilized for the GMAW and FCAW experiments in order to hold the sheet steel firmly to avoid distortion of the welded base metal (**Figure 7.3**)

7.2.1 GMAW Experiments

GMA butt welding was used to study the effects of the welding process variables on the microstructure and properties of ZINCALUME^{TM} and ZINC-HI-TEN^{TM} G550 grade sheet steels.

7.2.1.1 GMAW with different shielding gases

Table 7.4 gives the shielding gases used in the GMAW of ZINCALUME^{TM} and ZINC-HI-TEN^{TM} sheet steels. These gases were supplied by CIGWELD and all are commercially available.

Tables 7.4 Gas compositions (Volume%) of all shielding gases used for the GMAW

BOC Gases Australia Trade Name	**Gas Compositions (Volume %)**
Argoshield 50	91.9 Ar + 5 CO_2 + 3.1 O_2
Argoshield 51 (Universal)	81.25 Ar + 16 CO_2 + 2.75 O_2
Argoshield 52	77 Ar + 23 CO_2
Argoshield 54	91.5 Ar + 7 CO_2 + 1.5 O_2
Argoshield 60 (Stainshield)	98.5 Ar + 1.5 O_2
Argoshield 100	65 Ar + 10 CO_2 + 25 He
Welding Grade CO_2	100 CO_2

These commercially available shielding gases for the GMAW were chosen in order to investigate the effect of shielding gas on the microstructure and properties of ZINCALUME^{TM} and ZINC-HI-TEN^{TM} sheet steels, particularly, the strength loss in the

HAZ. The experiments were also designed to elucidate the influence of shielding gas on the porosity and weld bead profiles in the weld metal and thereby provide valuable information on the weldability of the ZINCALUME™ and ZINC-HI-TEN™ GMAW sheet steels with commercially available shielding gases. Among these shielding gases the Argoshield 54 is recommended by BHP for GMAW on ZINCALUME™ and ZINC-HI-TEN™ sheet steels.

In order to obtain satisfactory welds with continuous weld beads and good penetration, all welding conditions selected for the GMAW and FCAW experiments were obtained from the welding trials. The welding conditions used for the backhand GMAW and FCAW of ZINCALUME™ and ZINC-HI-TEN™ sheet steels with various shielding gases are given in **Table 7.5**.

Table 7.5 Welding conditions for backhand GMAW and FCAW with various shielding gases

Shielding gases	Heat input (J/mm)	Voltage (Volts)	Current (Ampere)	Travel speed (mm/min)
ZA STEEL				
GMAW				
(Argoshield 50)	54 – 129	16 – 18	48 – 78	420 – 850
(Argoshield 51)	57 – 136	16 – 18	53 – 83	420 – 800
(Argoshield 52)	58 – 138	16 – 18	60 – 85	420 – 800
(Argoshield 54)	59 – 133	16 – 17	62 – 83	420 – 800
(Argoshield 60)	61 – 110	16 – 18	65 – 87	420 – 800
(Argoshield 100)	59 – 107	16 – 18	51 – 77	420 – 800
(100%CO_2)	66 – 121	16	69 – 79	420 – 800
FCAW	53 – 70	14 – 15	46 – 55	480 - 590
ZHT STEEL				
GMAW				
(Argoshield 50)	70 – 110	16 – 18	53 – 84	520 - 620
(Argoshield 51)	72 – 115	16 – 17	61 – 86	520 - 620
(Argoshield 52)	72 – 114	16	64 – 88	520 - 620
(Argoshield 54)	74 – 108	16	65 – 83	520 - 620
(Argoshield 60)	84 – 110	16 – 17	64 – 85	520
(Argoshield 100)	73 – 111	16 – 18	61 – 83	520 - 620
(100%CO_2)	71 – 90	15	57 – 73	520
FCAW	66 – 80	14 – 15	59 – 69	510 - 560

7.2.1.2 GMAW with different electrode orientation

All previous studies were focused on the effect of electrode orientation on weld bead profile. Little information could be found about its influence on the mechanical properties, especially the strength loss in the HAZ of cold rolled sheet steels. In order to investigate the effect of electrode orientation on microstructure and mechanical properties of GMAW of Zn alloy coated sheet steels, three electrode orientations namely forehand, perpendicular and backhand, were selected for the GMAW of ZA and ZHT sheet steels. The welding conditions used for forehand (F), perpendicular (P) and backhand (B) GMAW of 1.0mm thick sheet steels shielded with Argoshield 50 shielding gas are given in **Table 7.6(a)**. **Table 7.6(b)** records the actual GMAW conditions for ZA G550 0.85mm thick sheet steels for the perpendicular electrode orientation and Argoshield 50 gas was used in the GMAW.

Table 7.6(a) Welding conditions used for forehand (F), perpendicular (P) and backhand (B) GMAW of ZINCALUME™ and ZINC-HI-TEN™ 1.0 mm thick sheet steels.

Electrode Orientation	Heat input (J/mm)	Voltage (Volt)	Current (Ampere)	Travel speed (mm/min)
ZINCALUME™				
Forehand (F)	61 – 134	16 – 18	60 – 84	420 – 800
Perpendicular (P)	60 – 124	16 – 18	52 – 76	420 – 800
Backhand (B)	59 – 129	16 –18	48 – 78	420 – 850
ZINC-HI-TEN™				
Forehand (F)	80 – 109	16 – 18	62 – 83	520
Perpendicular (P)	76 – 108	16 – 18	57 – 80	520
Backhand (B)	70 – 110	16 – 18	53 – 84	520 – 620

Table 7.6(b) GMAW conditions for ZINCALUME™ 0.85mm thick sheet steels

Heat input J/mm	Voltage (Volt)	Current (Ampere)	Travel speed (mm/min)
60	15	38	420
80	16	53	420
90	16	57	420
110	16	71	420

Uncoated steel			
90	16	56	420

7.2.1.3 GMAW at constant heat input

Although experiments have shown that the cooling time $\Delta t_{8/5}$ is constant in the HAZ when the peak temperature is over 900 °C [Easterling 1992], it has been reported in the past that the $\Delta t_{8/5}$ changes with a change in both the welding current and speed at a constant heat input. It has been claimed that the increase of both welding current and speed at a constant heat input results in about 30% decrease in $\Delta t_{8/5}$ [Kohno and Jones 1978; Ahmed and Jarvis 1998]. This result implies that the microstructure and mechanical properties of the HAZ is not solely dependent on the heat input.

Therefore, the current study was intended to investigate the effects of welding current and welding speed at a constant heat input on microstructure and mechanical properties of cold rolled, Zn alloy coated sheet steels, since all previous investigations have only concentrated on the thermal cycles and weld bead profiles.

The constant heat inputs chosen for the backhand GMAW of ZINCALUME™ and ZINC-HI-TEN™ sheet steels shielded by Argoshield 50 were about 80 J/mm and 100 J/mm, respectively.

7.2.1.4 GMAW with different welding control mode

GMAW can be operated using constant voltage control or current control modes. The current study addresses the effect of GMAW with constant voltage and current control modes on microstructure and mechanical properties of the Zn coated sheet steels. The heat inputs selected were about 60 J/mm and 70 J/mm for GMAW of ZA and ZHT sheet steels, respectively. Both the backhand and perpendicular torch orientation were used.

7.2.2 Self Shielded FCAW Experiments

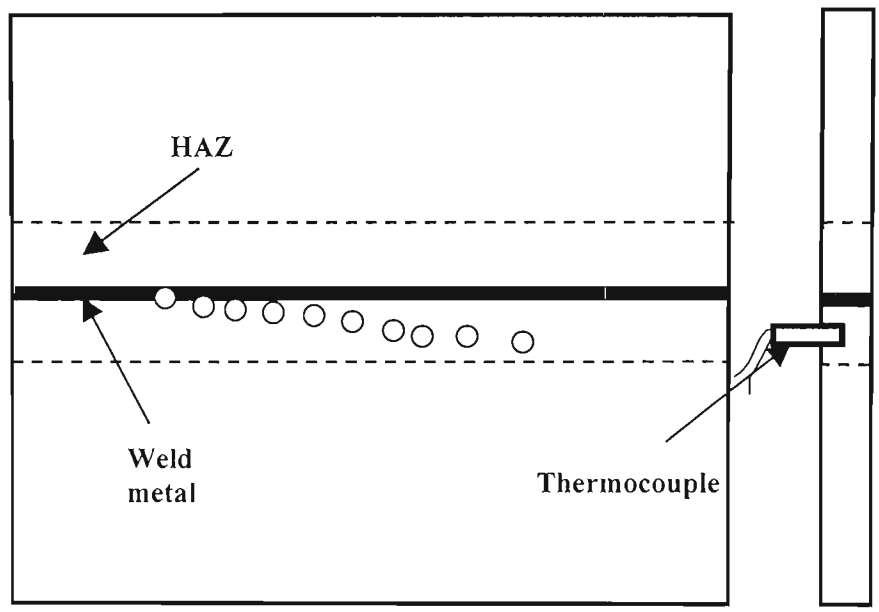

Figure 7.4 Schematic diagram showing the thermocouple placements.

Self-shielded FCA butt welding of ZA and ZHT sheet steels was carried out in the CRC welding laboratory using a 600 GMS DC Inverter Arc Welder. The constant voltage operating mode was used for the FCAW process.

The electrode wire used for the FCAW was FABSHIELD 21B (0.9 mm diameter) provided by WIA (Welding Industries of Australia). The FABSHIELD 21B is a self-shielded flux cored wire, which consists of 0.25%C, 0.32%Mn, 0.35%Si, 0.006%S, 0.015%P and 1.0%Al (wt.%) and is specially designed for galvanized and mild steel. The backhand electrode orientation was used for the FCAW. The welding conditions for the FCAW of ZA and ZHT sheet steels are given in **Table 7.5**.

7.3 THERMAL CYCLE MEASUREMENTS

Thermal cycles measurements for both the GMAW and FCAW on ZA and ZHT sheet steels were conducted using a 10 channel Datataker DT500 instrument to which a group of thermocouples was connected. The thermocouples were linked to a personal computer to record and interpret the data by means of a program called Decipher. K-type thermocouples of 0.3mm in diameter wire were used to measure the temperature profile at selected position in the HAZ. **Figure 7.4** shows a schematic diagram of the thermocouple placements. The output of all the probes and the temperature reference cell were recorded at intervals of one second. Each thermocouple was spot welded into a hole drilled half way through the thickness of the sheet and at about 5mm intervals along the weld bead. At least ten thermocouples were used on each weld, as the technique is susceptible to errors, such as poor thermal contact, coating effect and complex arc influences. Arc welding on such thin plate presents some difficulties because the range of welding process variables is small, especially the heat input. Successful thermal cycle measurement is also dependent on the stable welding conditions.

The measured thermal cycles in the HAZ were used to analyze the effect of welding conditions (such as welding current, welding speed, electrode orientations and welding processes) on the microstructure and mechanical properties. Changing the welding speed, for example, can change the cooling time $\Delta t_{8/5}$ [Kohno and Jones 1992; Ahmed

and Jarvis 1998]. **Table 7.7** gives the welding conditions for GMAW and FCAW thermal cycle measurements during welding of ZA and ZHT sheet steels.

Table 7.7 Welding conditions for GMAW and FCAW thermal cycle measurement

Code No.	Heat input (J/mm)	Voltage (Volt)	Current (Ampere)	Travel speed (mm/min)
ZINCALUME™ (GMAW)				
178598B	50	17	63	850
1642118B	120	17	70	420
175098B	80	16	62	500
1674140B	80	16	88	740
165092P	80	17	60	500
165092F	80	17	60	500
(GMAW)	60	16	43	480
(FCAW)	60	14	52	480
ZINC-HI-TEN™(GMAW)				
165297B	80	17	62	520
1652122B	100	16	76	520
16104295B	100	16	159	1040

7.4 HAZ WELD SIMULATION

The HAZ simulations of structural sheet steels were carried out at BHP Research Center using an electric resistance rapid annealing furnace specially designed for sheet steels by the Research Center. The HAZ simulation was aimed firstly at determining the recrystallization temperature of G500 sheet steels; secondly, to establish the correlation between microstructure and its thermal cycle and thirdly, to measure the tensile strength of the grain refined region in a simulated HAZ.

7.4.1 Simulation Design

ZINCALUME™ G550, 1.0mm thick sheet steel was used for the simulation. The Zn-Al coating was removed using hydrochloride acid. The simulation sample has the dimensions of 420×38×1.0 (mm). Two thermocouples were spot welded on the surface close to the centre of each sample in order to measure the thermal cycle accurately.

Tensile test specimen and cross-sections samples for microstructural characterization were selected from the position close to the center of the sample.

The peak temperatures for the HAZ simulation were in the range of 600°C to 1200°C with the aim of monitoring the microstructural change in different sub-zones of the HAZ of real welds. The heating rate was about 200°C/S, which was the maximum heating rate that the furnace could provide. Air-cooling was used after reaching the peak temperature. Tensile tests of the simulated grain refined HAZ were carried out at BHP Research Centre.

7.5 MECHANICAL PROPERTIES TESTING

7.5.1 Microhardness Testing

Vickers Microhardnesses across the HAZ width and into the weld metal were measured using a LECO Vickers Microhardness Tester with a 200 gram load.

7.5.2 Tensile Testing

Tensile properties of the 0.85mm thick ZA sheet steel welds were obtained using an Instron 1341 Testing Machine controlled by a PC. In this case, the load axis was transverse to the rolling direction of the sheet steel. Tensile test samples were made in accordance with the Australian Standard AS 2205.2.1 for transverse butt tensile tests. The gauge length was set at 85mm. Abrasive paper was attached to the both grip ends of the tensile specimen to avoid slipping during the tensile test.

Tensile properties of the 1.0 mm thick of ZA and ZHT sheet steels GMAW and FCAW welds were obtained using an Instron of SERVO-TEST 5209 (100KN) controlled by a PC. In this case, the standard samples for the tensile testing were punched into shape and milled 1mm on each side of the gauge length region to remove the cold work hardening produced by punching. The tensile loading axis was longitudinal, along the rolling direction of the sheet. To obtain representative tensile test results, at least two specimens were tested for each welding condition.

7.6 METALLOGRAPHY AND FRACTOGRAPHY

The GMAW and FCAW welds and tensile specimens were sectioned transverse to the weld run and hot mounted at 150°C using hot mounting resin with carbon filler on the top surface for edge retention and for the SEM examination. The transverse cross-section of all welds were mechanically polished using DP DUR Hard pad with 1μm diamond and subjected to both macro- and micro-examination after etching in 2.5% nital.

Weld samples for coating examination were mechanical polished using water free lubricant and then etched in 0.2 to 0.4% nital in order to preserve the coating edge.

7.6.1 Optical Metallography

Both macro- and micro-scopic metallographic techniques were used to examine the HAZ, weld metal and tensile fractures surfaces. Macro-images of weld metal profiles were examined using stereomicroscopy. Microstructural characterization of the HAZ, weld metal and tensile fractures were carried out using a Leica DMA optical microscope.

Quantitative image analysis of the non-metallic inclusions in the weld metals and the grain size determination of the simulated HAZ were carried out by using an image analyser equipped with a video camera (Video Pro 32) attached to a Leica DMA optical microscope. Measurement of the HAZ width was carried out on contiguous fields extending from the fusion boundary towards the base metal, using a Leica DMA optical microscope.

7.6.2 Electron Micrography and XRD

A Leica S440 scanning electron microscope with an accelerating voltage of 20kV was used to examine: non-metallic inclusions and porosity in the weld metal; coating damage in Zn alloy coated sheet steels after fusion welding; tensile fracture surfaces and

the microstructures of the simulated HAZs. Energy Dispersive Spectroscopy (EDS) was used to determine the alloying elements present in non-metallic inclusions and at the surface of pores, as well as in the coating after fusion welding. XRD was used to identify the fractured white etching phase at the surface of the steel in the HAZ region.

7.7 WELD METAL CHEMICAL ANALYSIS

Weld metal chemical analysis was carried out at BHP Central Laboratory, Port Kembla using Inert Gas Fusion for the identification of the light elements such as nitrogen, oxygen, and Atomic Emission Spectroscopy for other elements in the weld metal.

7.8 COATING DAMAGE ANALYSIS

Macro-and microstructures of coating damage on GMAW and FCAW welded ZA and ZHT sheets were examined using optical microscopy, SEM and EDS.

CHAPTER 8

RESULTS

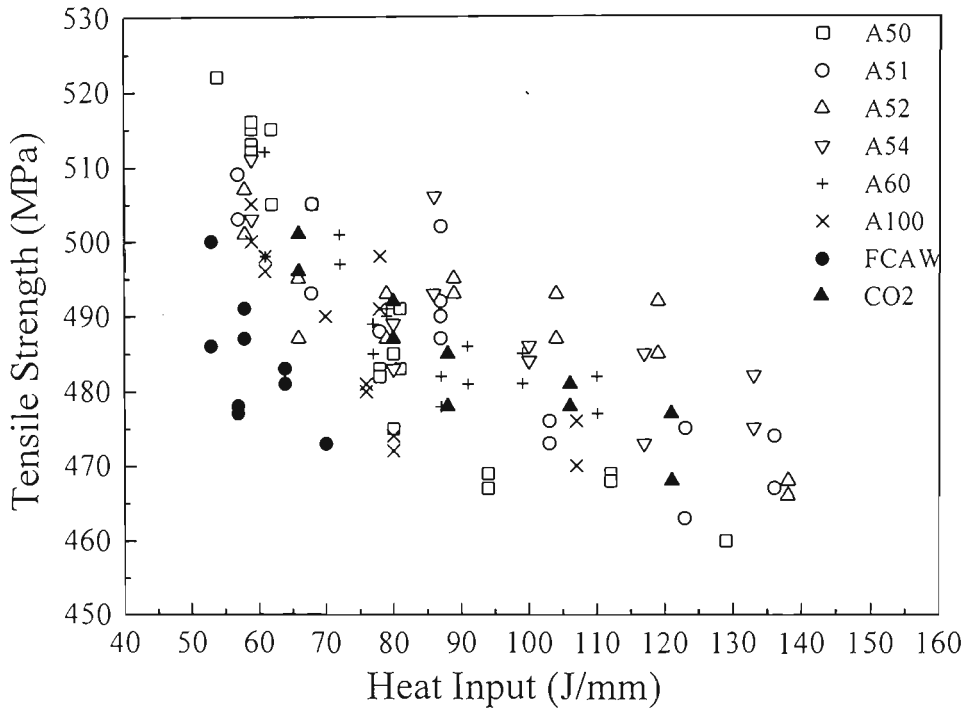

(a)

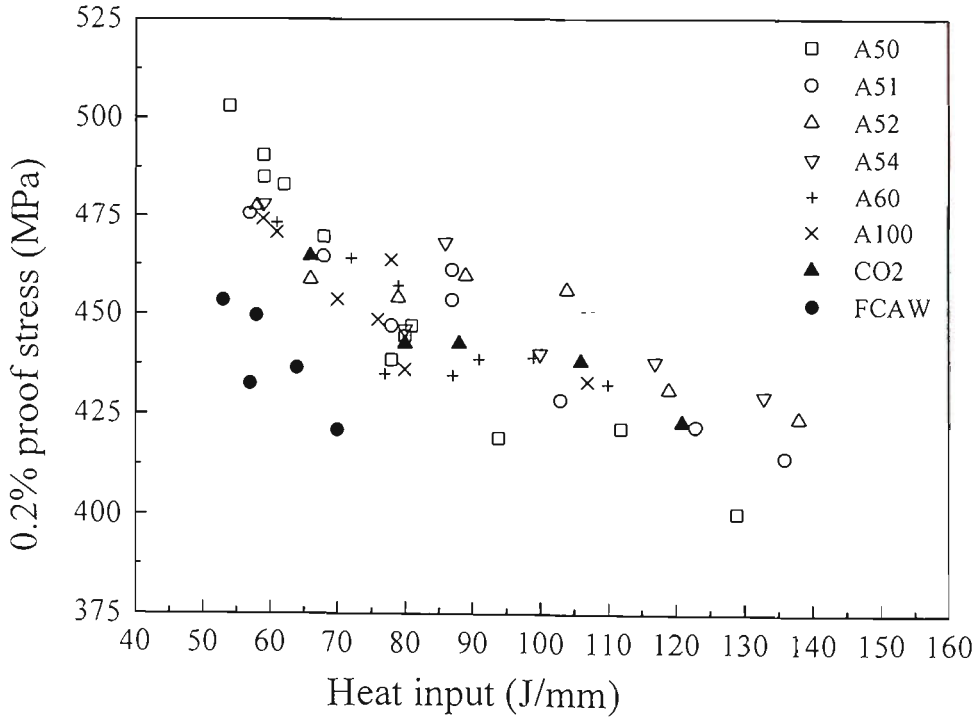

(b)

Figure 8.1 Tensile strength **(a)** and 0.2% proof stress **(b)** of GMA welded, 1.0 mm ZINCALUME™ G550 sheet steels versus heat input for various shielding gases.

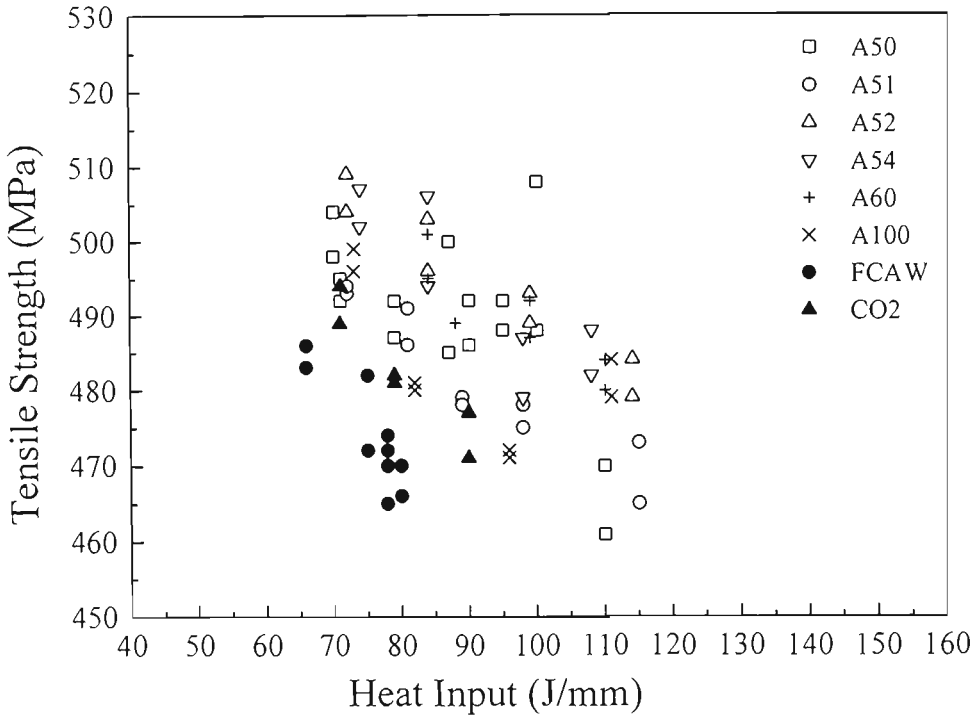

(a)

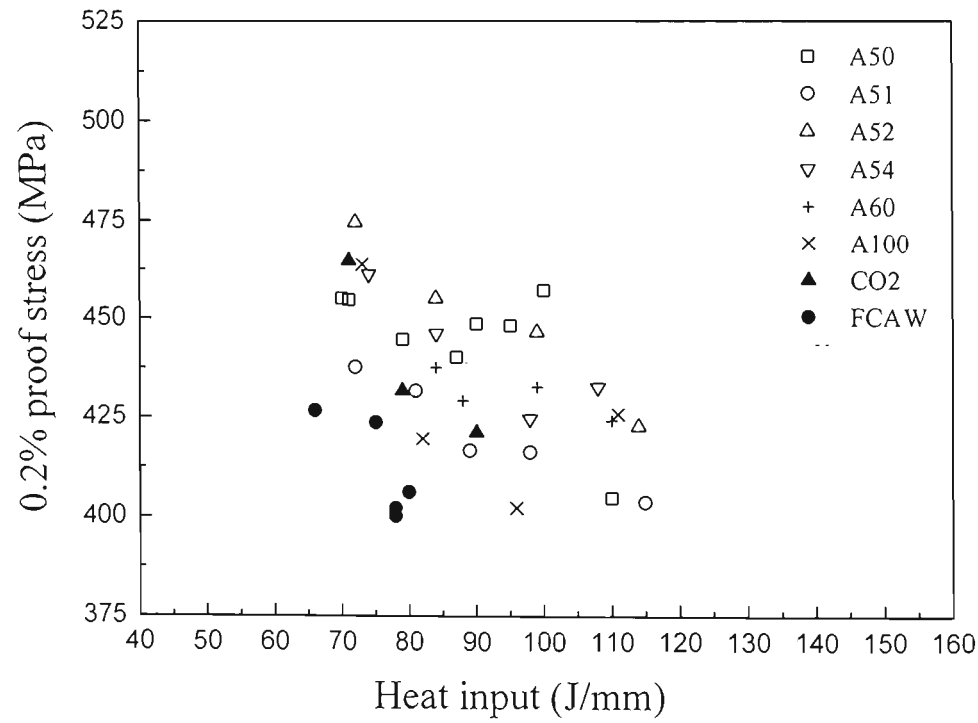

(b)

Figure 8.2 Tensile strength **(a)** and 0.2% proof stress **(b)** of GMA welded, 1.0 mm ZINC-HI-TEN^{TM} G550 sheet steels for various shielding gases.

In this chapter the mechanical properties of the GMA welded and FCA welded ZINCALUME^{TM} (ZA) and ZINC-HI-TEN^{TM} (ZHT) G550 grade sheet steels will be presented first. This is followed by the microstructural characterization of the HAZ, the tensile fracture surface, and the weld metal. The results of thermal cycle measurements for the HAZ and the microstructures and mechanical properties of HAZ simulated samples are also presented. Finally, results are reported for the characterization of the change to the Zn-Al and Zn coatings by the welding processes.

8.1 MECHANICAL PROPERTIES AND FRACTURE CHARACTERISTICS

8.1.1 Tensile Strength and Proof Stress

The tensile strength and the 0.2% proof stress of the HAZ in the GMA and FCA welded 1.0 mm thick ZA and ZHT G550 grade sheet steels, as a function of heat input for the 'backhand' electrode orientation and the indicated shielding gases are given in **Figures 8.1** and **Figure 8.2**. At least two samples for each welding condition were used for the tensile test. It should be noted that for the same welding process the ZA has a wider processing window than the ZHT for obtaining acceptable quality of welds. As can be seen, the tensile data show a general decrease with increasing heat input and fall into bands. The tensile strengths and proof stress of the FCAW samples were distinctly lower than those measured for GMA welded samples. In other words, for the same nominal heat input the tensile strength and the proof stress of the FCAW samples are generally lower than those of the GMAW samples. Both the tensile strength and proof stress decrease with the increase of the heat input. At the same nominal heat input the tensile strength of GMA welded ZA and ZHT sheet steels varied by about 25 MPa as a result of using different shielding gases. A difference in average tensile strength of about 30 MPa between GMA and FCA welded sheet steels was observed at the same nominal heat input.

Both the ZA and the ZHT samples have rather poor elongations at failure, with the former giving a range between 2% and 3.5% and the latter a range between 2.5% and

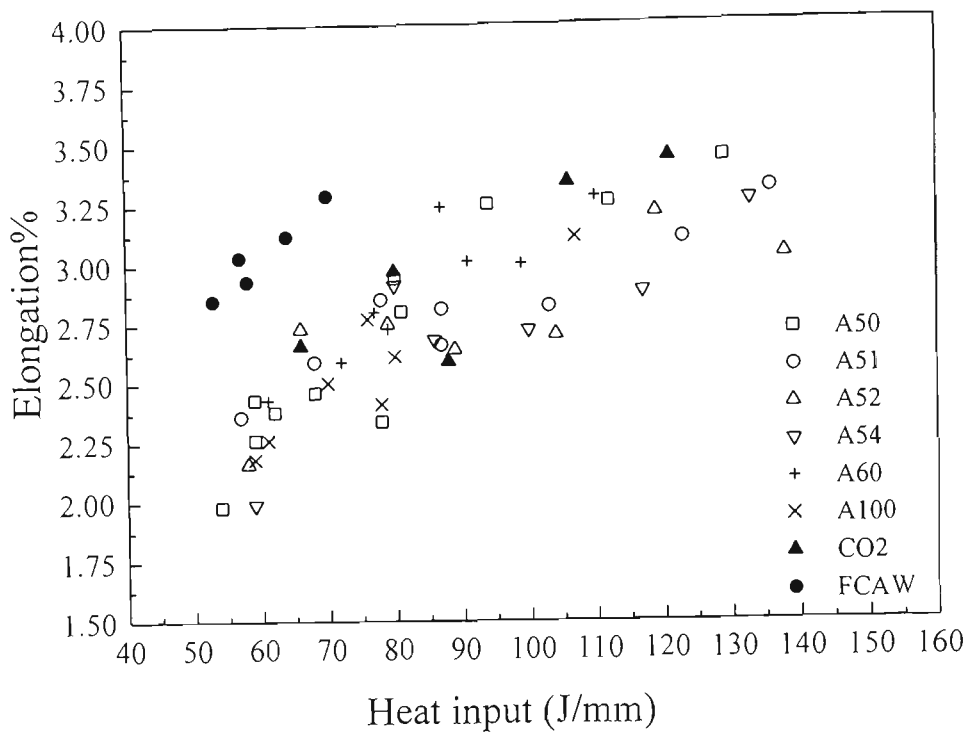

(a)

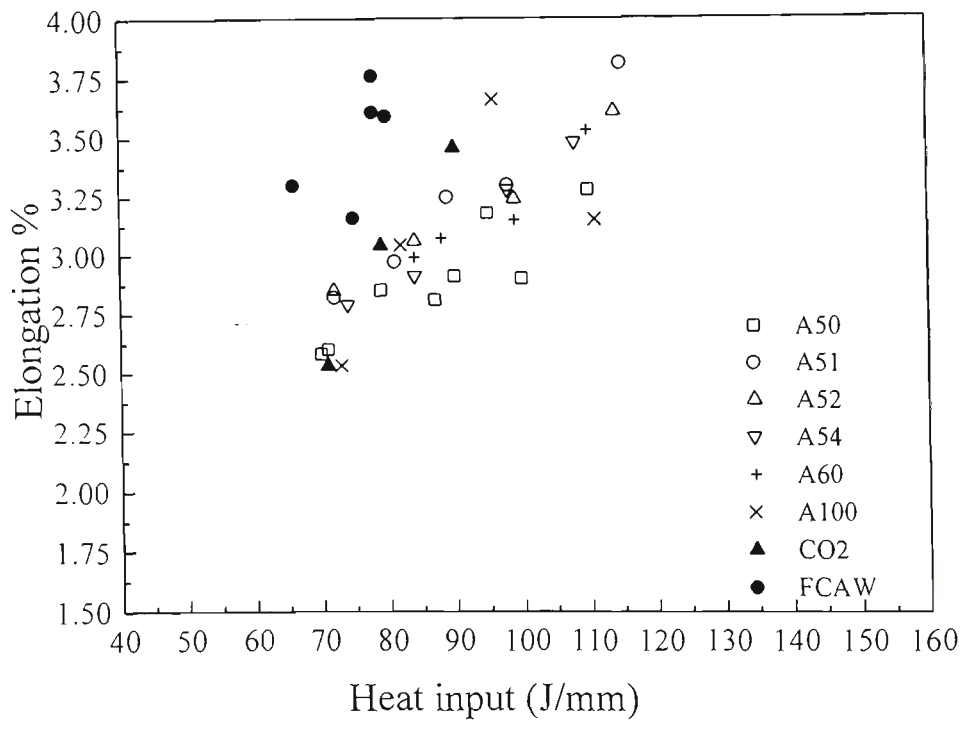

(b)

Figure 8.3 Elongations % as a function of heat input for GMA and FCA welded, 1.0 mm G550 sheet steels of **(a)** ZA and **(b)** ZHT sheet steels.

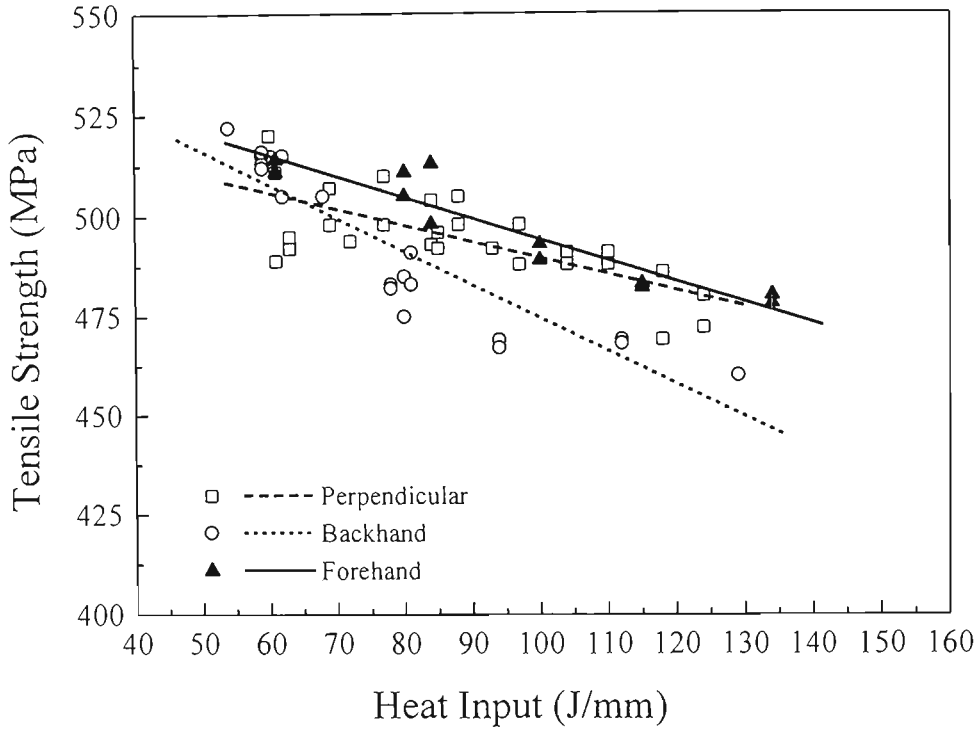

(a)

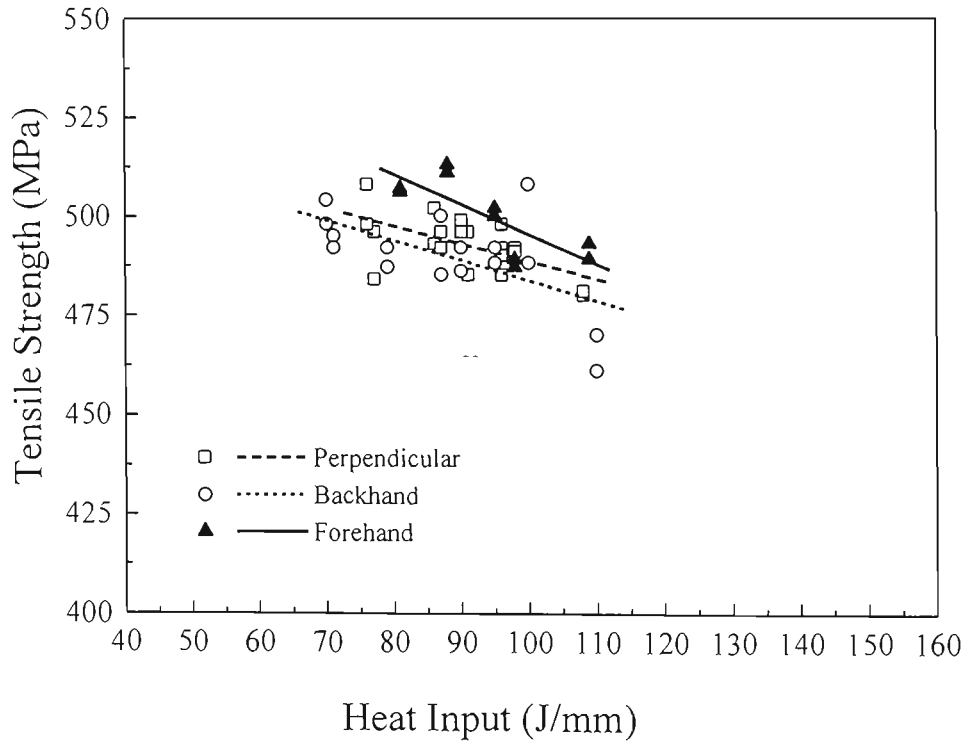

(b)

Figure 8.4 Variation of tensile strengths of the GMA welded G550 sheet steels of **(a)** ZA and **(b)** ZHT using various torch angles.

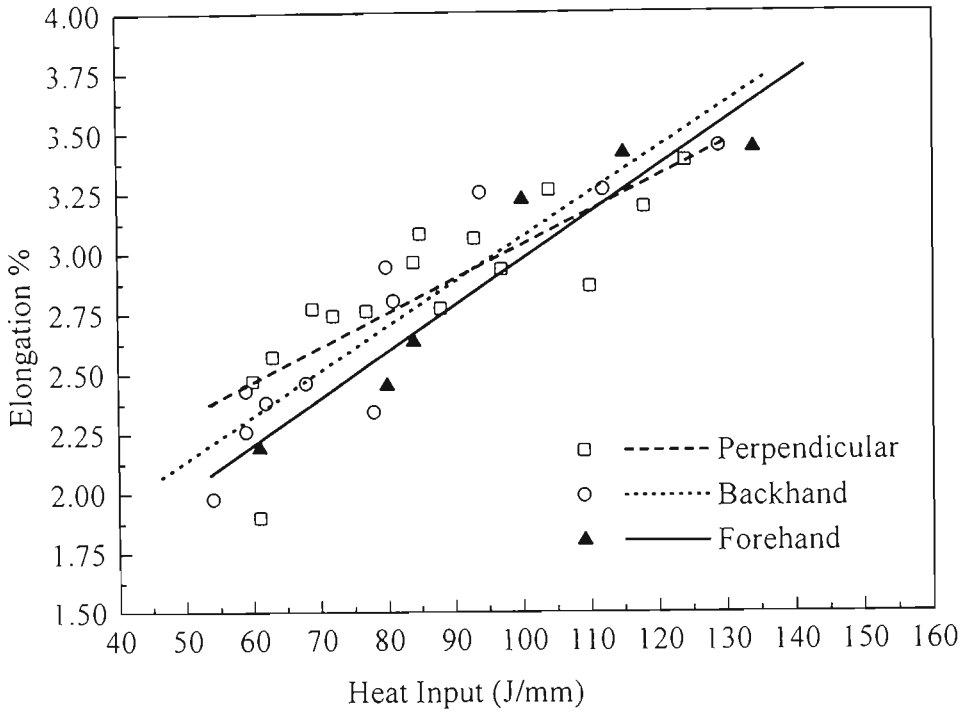

(a)

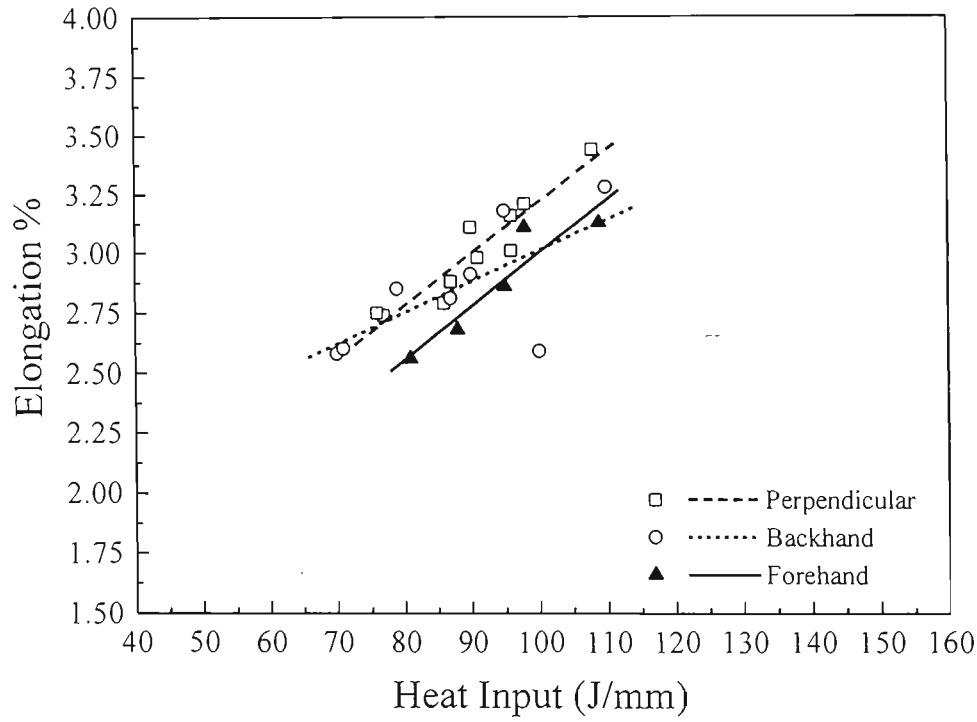

(b)

Figure 8.5 Elongation % as a function of heat input for GMA welded ZA **(a)** and ZHT **(b)** sheet steels using different torch orientation.

Table 8.1 Average tensile strength and proof stress of GMA butt welded ZINCALUME™ and ZINC-HI-TEN™ G550 at the heat input of 80 J/mm using perpendicular (P), backhand (B) and forehand (F) welding techniques.

Orientation	Heat-Input (J/mm)	Tensile Strength (MPa)	Proof Stress (MPa)	Elongation (%)
ZA (P)	80	502±4	469±8	2.77±0.08
ZA (B)	80	480±5	445±9	2.94±0.04
ZA (F)	80	505±8	470±7	2.63±0
ZHT (P)	80	498±5	458±6	2.79±0.17
ZHT (B)	80	488±3	440±14	2.81±0.14
ZHT (F)	80	507±1	475±0	2.56±0.09

Table 8.2 Average tensile strength and proof stress for GMAW of ZINCALUME™ and ZINC-HI-TEN™ at a constant heat input of 80 J/mm and 100 J/mm respectively using backhand electrode orientation and shielding by Argoshield 50.

Welding Speed (mm/min.)	Tensile Strength (MPa)	Proof Stress (MPa)	Elongation (%)
ZINCALUME™			
420	483±1	439±3	2.34±0.14
530	493±4	456±10	2.97±0.37
630	492±1	458±3	3.03±0.21
740	485±2	446±8	2.84±0.09
ZINC-HI-TEN™			
520	488±0	444±0	2.98±0
650	487±3	427±5	3.31±0.06
780	494±2	443±0	2.99±0.07
910	488±1	433±4	3.14±0.09

4%. The variation is a function of heat input, as shown in **Figures 8.3**. The higher the heat input the higher the elongation. At the same nominal heat input but different shielding gases, a difference of 0.5% and 0.75% in elongation occurred for GMA welded ZA and ZHT sheet steels. The FCAW samples of both sheet steels tend to have higher elongations than the GMAW samples at the same nominal heat input (**Figure 8.3**).

8.1.1.1 Effect of electrode orientation on tensile strength

Table 8.1 summarizes the cross weld tensile properties of the GMAW ZA and ZHT sheet steels at the same nominal heat input of 80 J/mm using three different electrode orientations, namely perpendicular (P), backhand (B) and forehand (F). It can be seen that the backhand technique resulted in a higher tensile strength reduction than the other two techniques while the forehand orientation has resulted in the lowest tensile strength loss. The same relationship between the tensile strength and the electrode orientation was observed across the whole range of the heat inputs for both the materials as shown in **Figure 8.4**. **Figure 8.5** shows the plots of elongation versus heat input for the GMAW ZA and ZHT sheet steels using the perpendicular, backhand and forehand welding techniques. It appears that the backhand technique gives higher overall elongation than other techniques whereas the forehand gives lower elongation for the heat inputs used in this experiment.

8.1.1.2 Effect of welding speed on tensile strength

The effects of welding speed on the tensile properties of the GMA welded sheet steel were studied at a constant heat input. **Table 8.2** summarizes the tensile properties of the GMA welded ZA and ZHT sheet steels with constant heat inputs of 80 J/mm and 100 J/mm respectively. It seems that the welding speed up to 910 mm/min. has little effect on the final tensile properties.

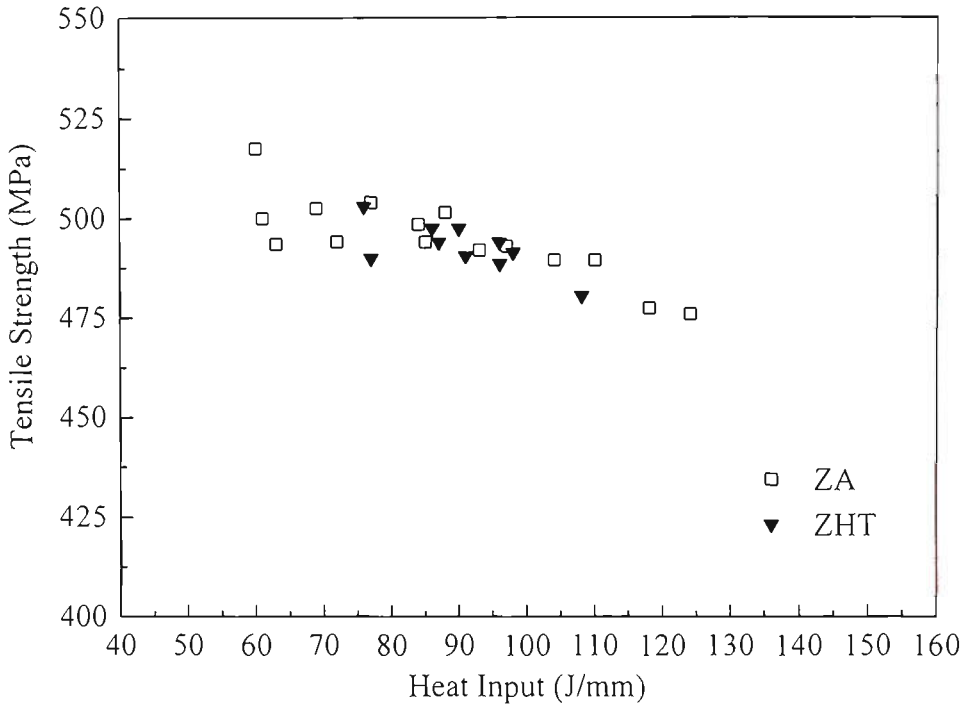

(a)

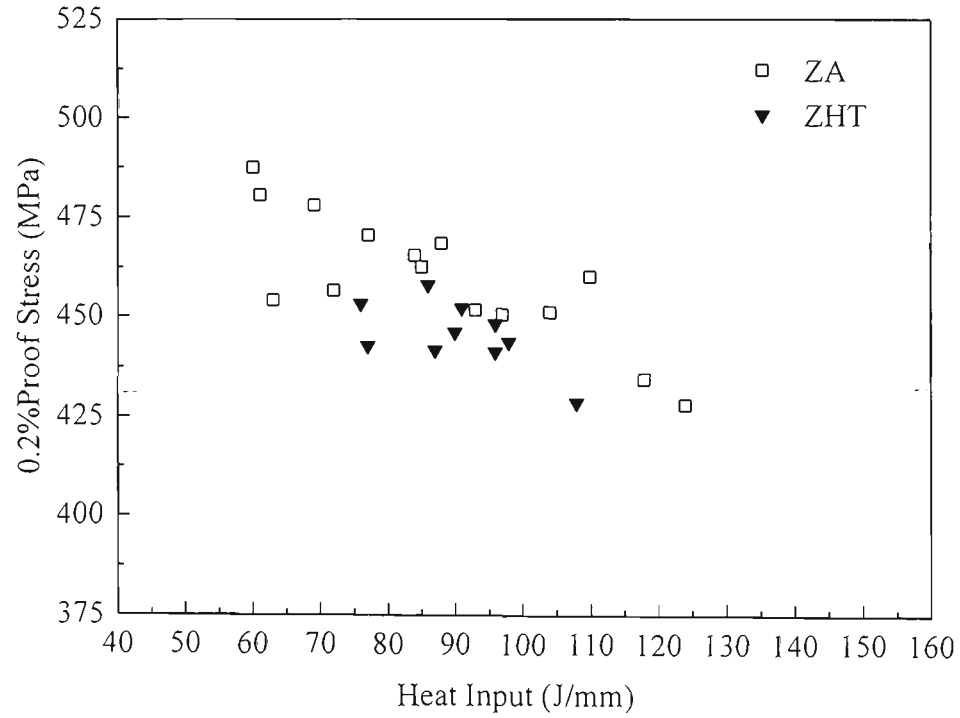

(b)

Figure 8.6 Tensile strength **(a)** and 0.2% proof stress **(b)** of the GMA welds made with the torch perpendicular shielded by Argoshield 50 for ZA and ZHT G550 sheet steels.

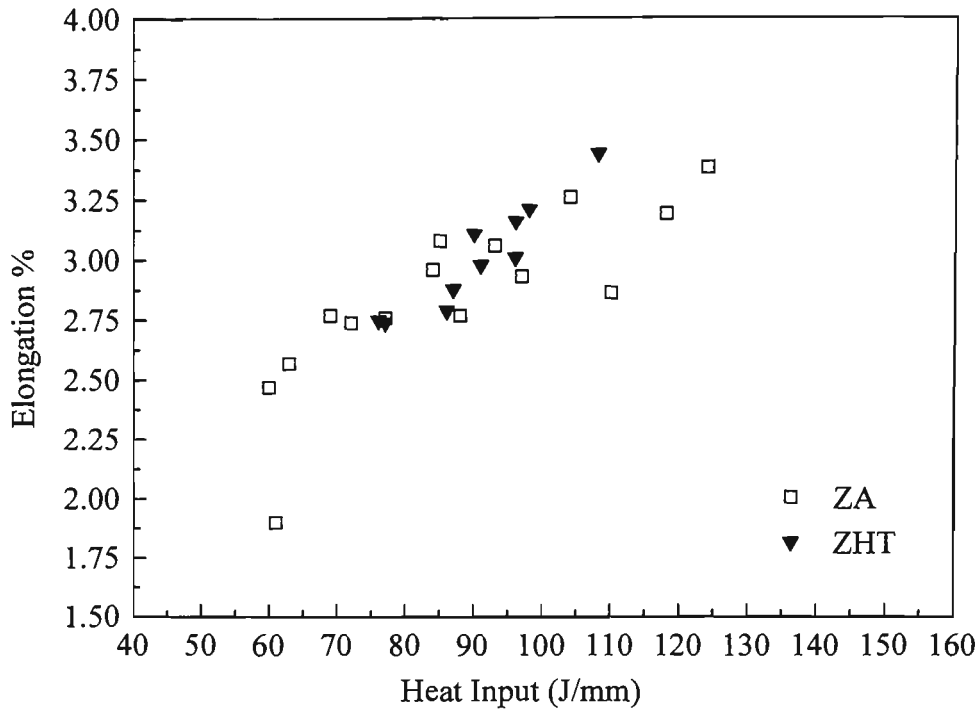

Figure 8.7 Elongation % as a function of heat input of GMA welds made with the torch perpendicular shielded by Argoshield 50 for ZA and ZHT G550 sheet steels.

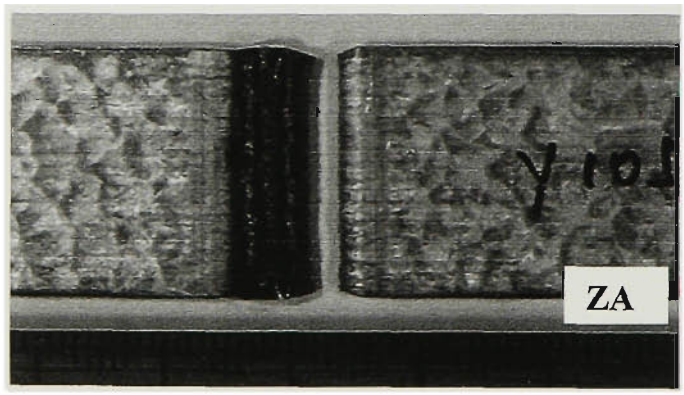

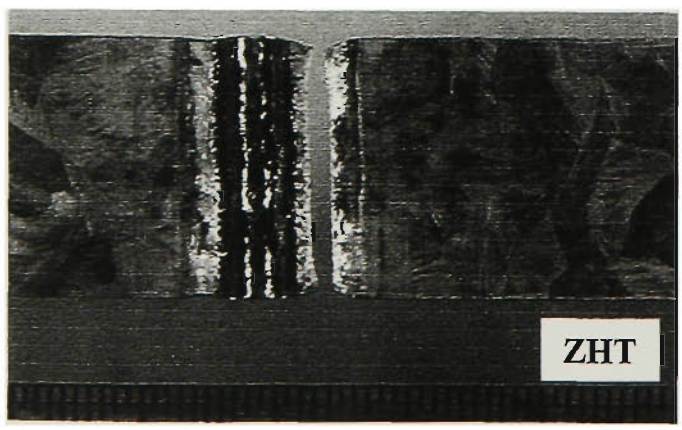

Figure 8.8 Typical macrographs showing the tensile test specimen fractured in the HAZ of GMA welded ZA and ZHT 1.0 mm sheet steels.

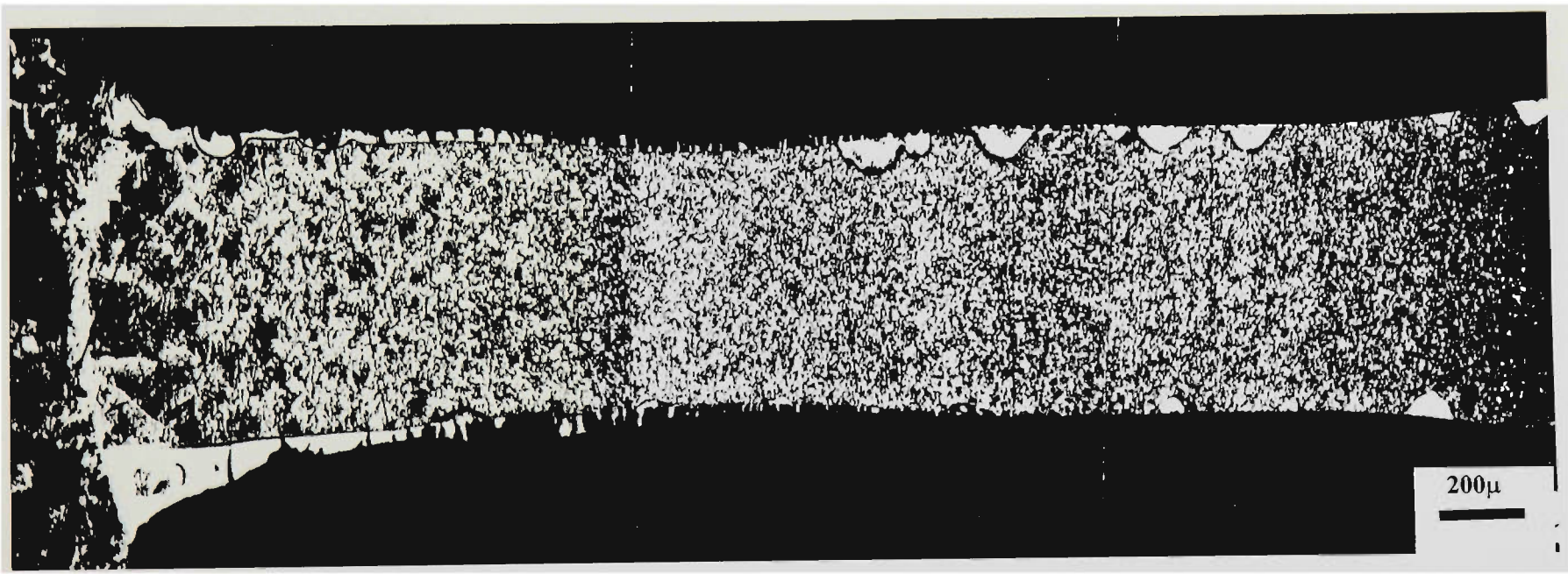

Figure 8.9 Localised deformation of HAZ during the tensile test (at 90 J/mm GMAW ZINCALUME^{TM} G550 0.85mm).

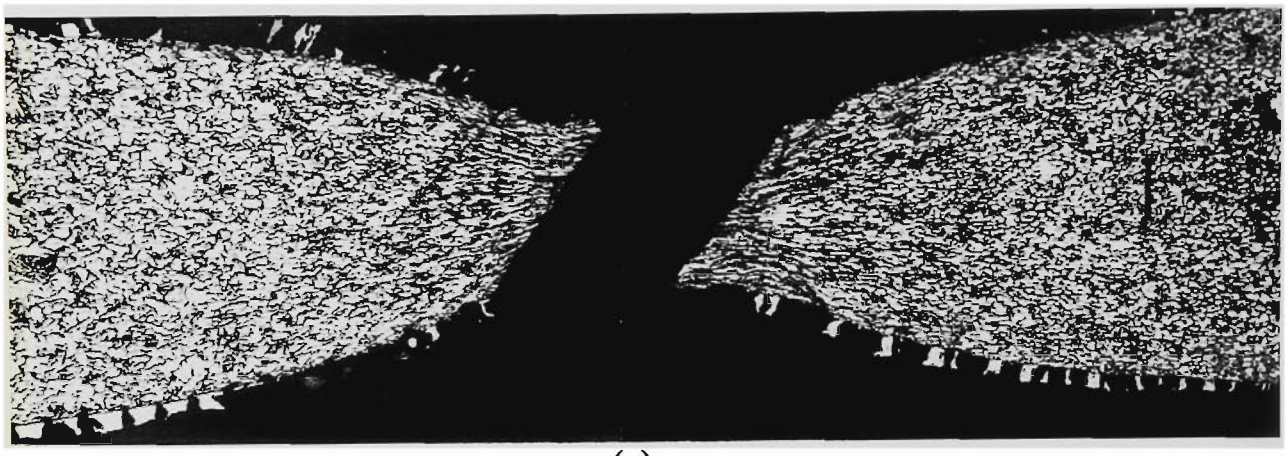

(a)

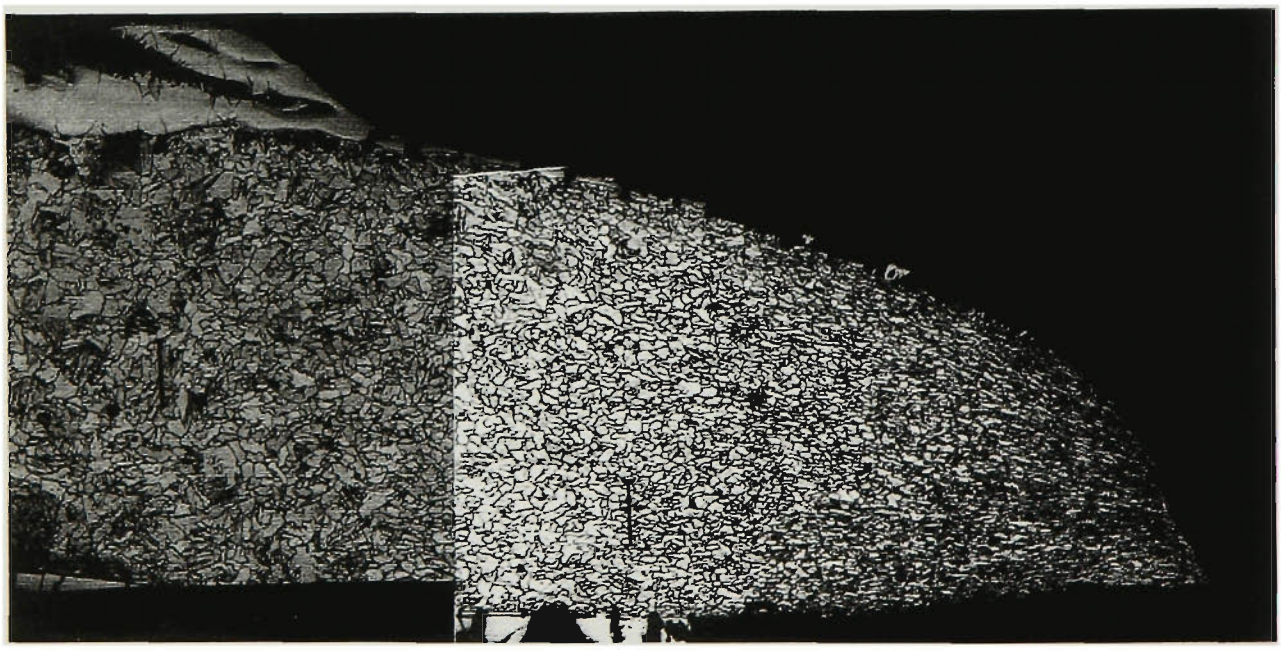

(b)

100μ

Figure 8.10 Cross-sectional microstructure of **(a)** fracture region of tensile test; **(b)** microstructural feature region adjacent to the weld metal of GMA ZINCALUME™ G550 0.85mm steel welds.

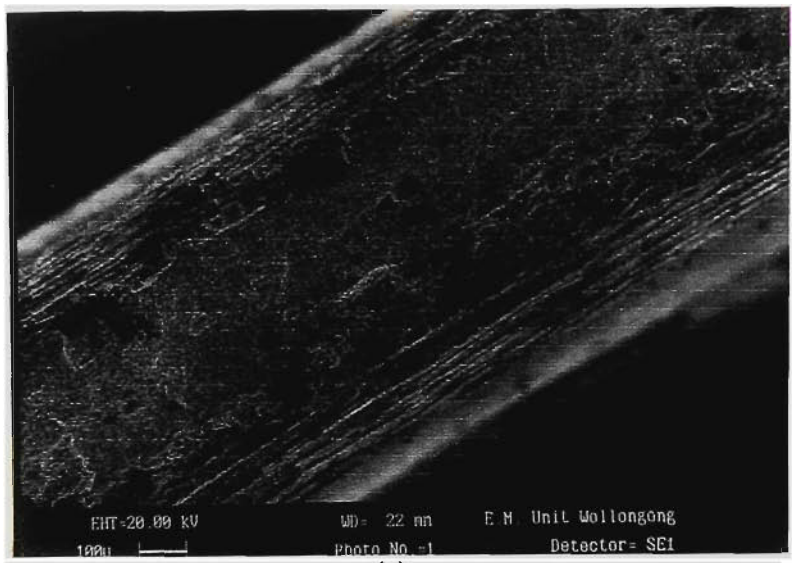

(a)

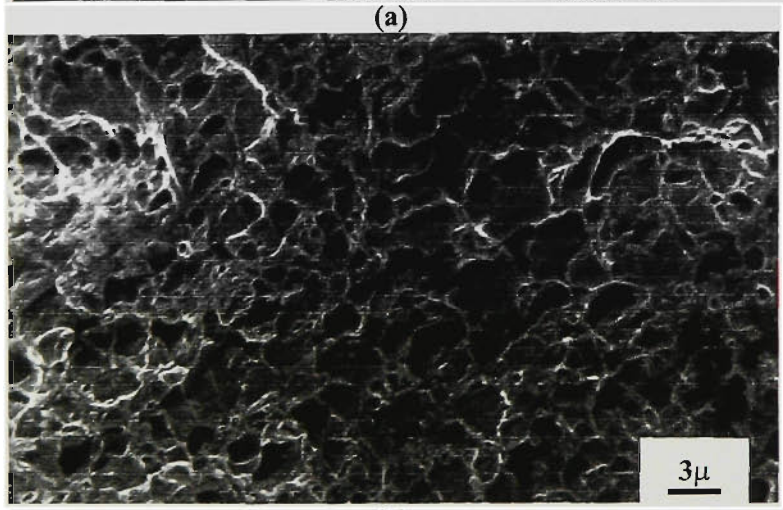

(b)

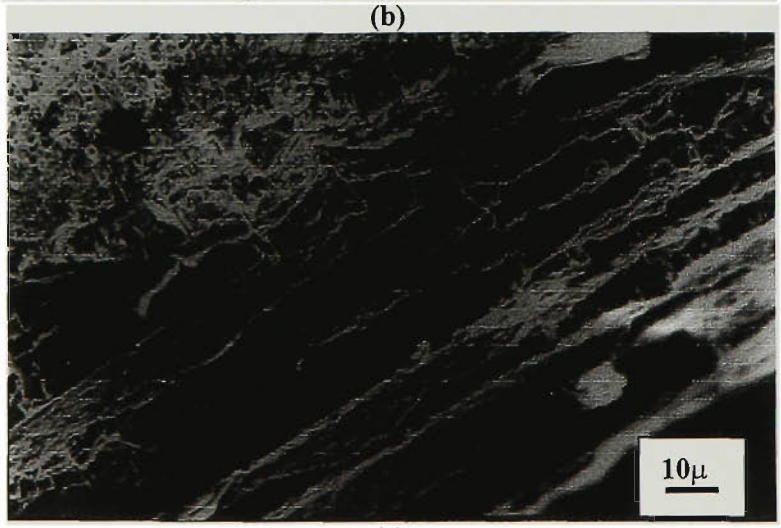

(c)

Figure 8.11 SEM micrographs showing **(a)** a typical fracture surface of tensile test specimen; **(b)** the equiaxed dimples at the centre; **(c)** the shear lip at the edge. (at 90 J/mm, GMA ZINCALUME^{TM} G550 0.85 mm steel welds).

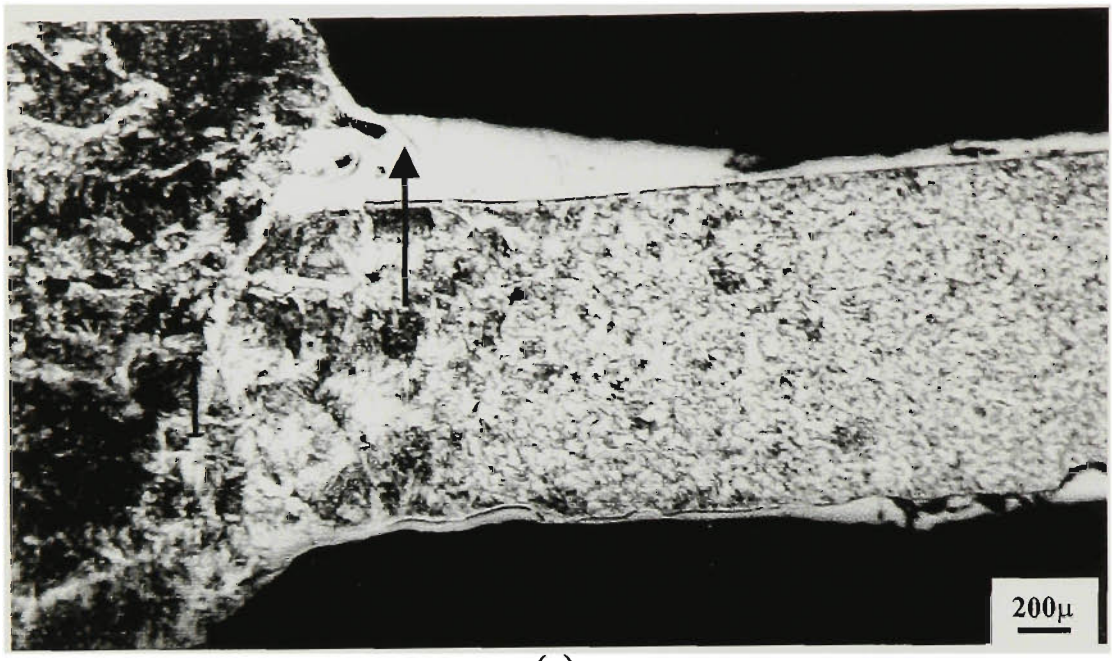

(a)

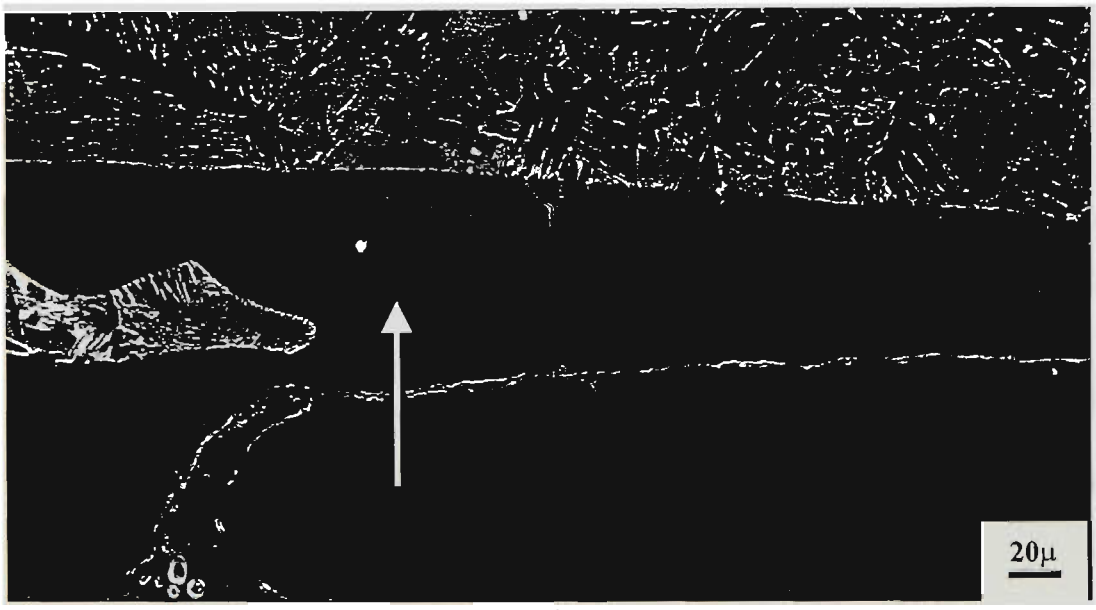

(b)

Figure 8.12 Micrographs showing the Al-rich alloy white layer formed during arc welding **(a)** optical micrograph and **(b)** SEM micrograph.

Table 8.3 Average tensile strength and proof stress of backhand GMAW ZA and ZHT sheet steels using current control and constant voltage control mode, shielded by Argoshield 50

	Heat Input (J/mm)	Tens.Strength (MPa)	Proof Stress (MPa)	Elongation (%)
Current Control				
ZA	60	488±1	454±2	2.83±0.33
ZHT	70	487±0	443±7	2.94±0.06
Constant voltage				
ZA	60	510±1	493±3	2.16±0.03
ZHT	70	496±3	450±2	2.74±0.21

Table 8.4 Average microhardness HV0.2 of the HAZ, subzones and base metal of GMA welded ZA G550 0.85 mm sheet steel

HI (J/mm)	HAZ	(GC	GR	IC	SC)	Weld Metal	Base Metal
60	153	(166	138	132	149)	248	
80	155	(165	152	145	147)	215	
90	150	(160	143	134	151)	222	227
110	147	(156	139	133	148)	217	
Uncoated							
90	154	(168	143	130	143)	234	

8.1.1.3 Effect of welding control mode on tensile strength

The effects of the control mode, current control and constant voltage control, on the tensile properties of the GMA welded ZA and ZHT sheet steels were also studied. It was found that the constant voltage mode gives higher strengths and slightly lower elongation than the current control mode for both the GMAW ZA and ZHT sheet steels at heat inputs of 60 and 70 J/mm respectively, as shown in **Table 8.3**.

8.1.1.4 Effect of Zn alloy coatings on tensile strength

The tensile properties and elongations of the GMAW ZA and ZHT G550 sheet steels shielded with Argoshield 50 are given in **Figure 8.6** and **Figure 8.7** respectively. The tensile strengths and elongations of the GMAW ZA and ZHT samples are very similar at the same heat input. However, the proof stresses of the GMAW ZA samples are higher than those of the GMAW ZHT samples at the same nominal heat input.

8.1.2 Fracture Characteristics

All of the tensile test specimens fractured in the HAZ. **Figure 8.8** shows typical macrographs of the tensile fractures. Localised necking at the fracture site is evident in these macrographs. **Figure 8.9** illustrates the localised deformation of the HAZ on the side opposite the fracture site. The microstructure near the fracture region is given in **Figure 8.10** which shows that the fracture occurs in the grain-refined region close to the grain-coarsened region. Scanning electron microscopy of the fracture surface reveals that the fracture surface of the tensile test specimen consists of fine and uniform equi-axed dimples at the centre and the shear lip at the edge of the fracture surface as shown in **Figure 8.11**. The fracture was generally at a 45° slant to the sheet surface, as is commonly observed in tensile fractures of sheet [ASM, Metals Handbook, Vol.10]. Thus, the fracture was ductile in nature and occurred in the grain-refined region adjacent to the grain-coarsened region of the HAZ.

Figure 8.12 shows a fractured white etching phase at the surface of the steel in the HAZ region, which has been identified as an intermetallic compound close to Fe_3Al using

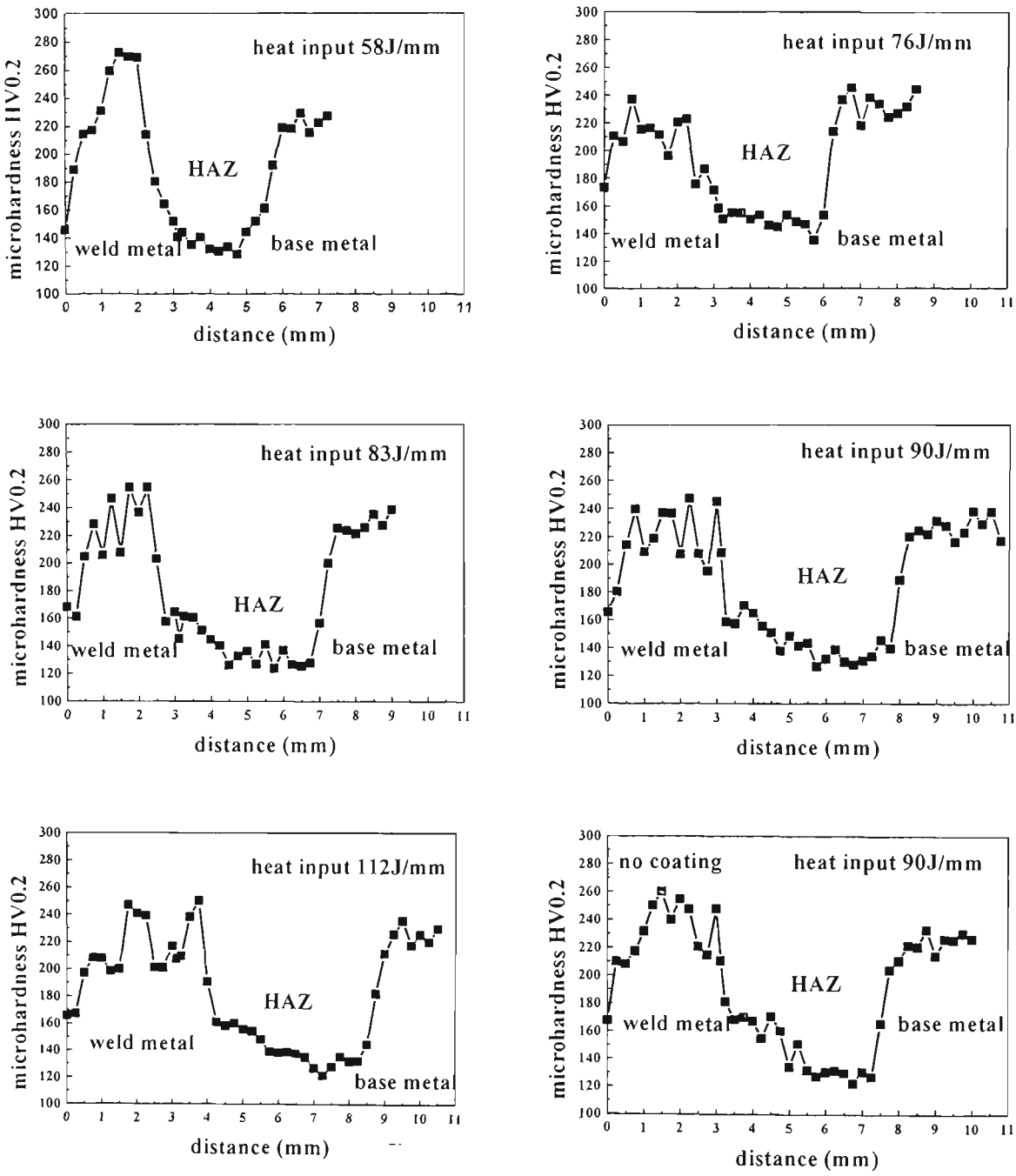

Figure 8.13 Microhardness profiles across weld metal and HAZ for samples GMA welded ZA sheet steel using the indicated heat input except for uncoated sample (profile shown at lower right).

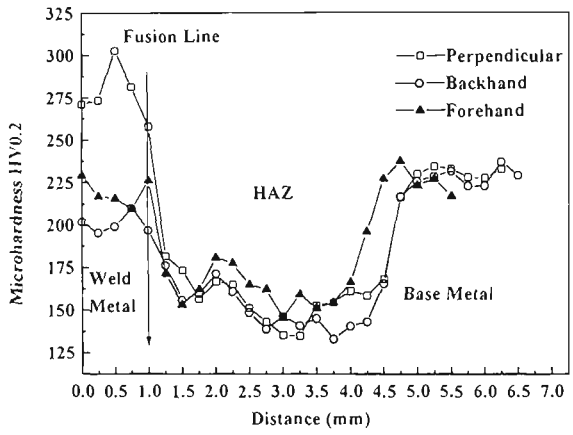

(a)

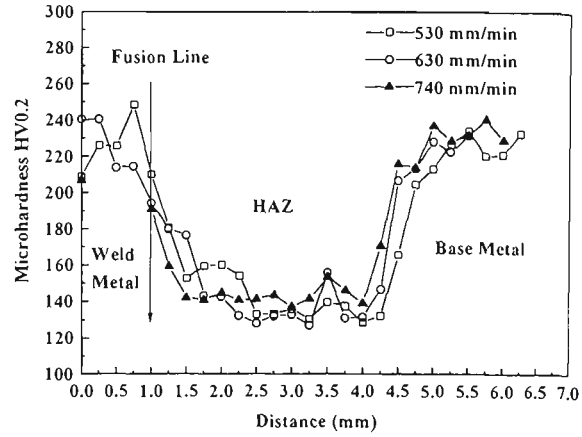

(b)

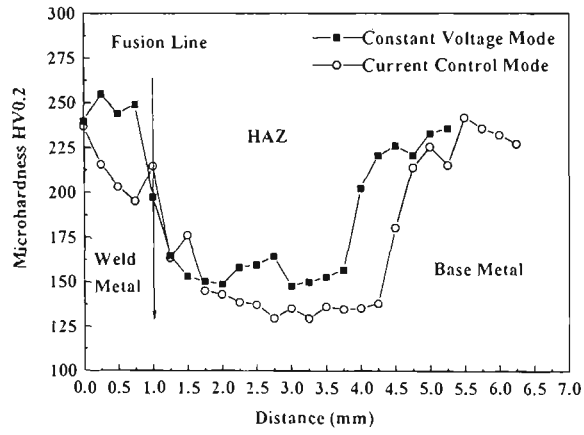

(c)

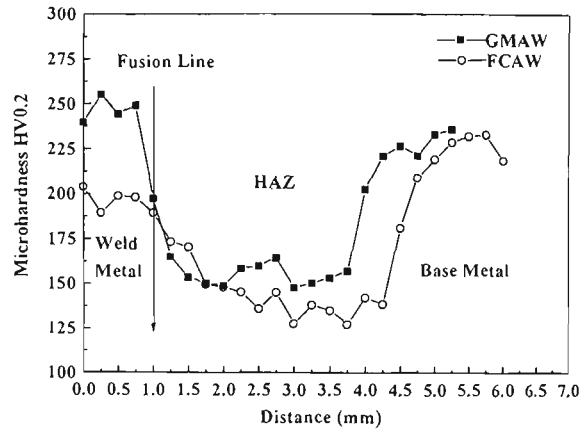

(d)

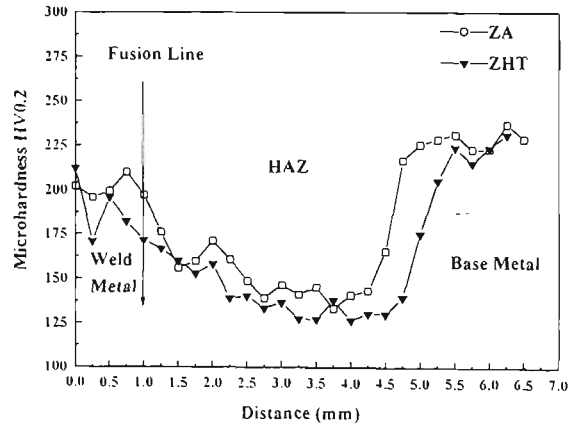

(e)

Figure 8.14 Microhardness profiles across weld metal and HAZ for ZA and ZHT G550 sheet steel backhand welds (unless stated otherwise) **(a)** at heat input of 80 J/mm using various electrode orientations; **(b)** at heat input of 80 J/mm for different travel speeds; **(c)** at heat input of 60 J/mm using different control modes; **(d)** at heat input of 60 J/mm for GMA and FCA welding processes; **(e)** at heat input of 80 J/mm for ZA and ZHT GMA welds.

XRD. This is a residue of the interaction of the base steel with the Zn-Al coating under arc welding conditions. As most of the Zn is volatilized, Al reacts with Fe in the substrate at the elevated temperature induced by the weld thermal cycle, producing the intermetallic compound. This phase is brittle, with a mean microhardness of about 356 $HV_{0.2}$ and fractures readily under tensile loading.

8.1.3 Microhardness of HAZ

Vickers microhardness tests were carried out with a 200g load across the weld metal and HAZ with the indentation at 0.25mm intervals along two parallel lines with the indents offset by 0.05mm.

8.1.3.1 Effect of heat input

The micro-hardness results value for the weld metals and the HAZ of the GMAW ZA G550 and uncoated G550 sheet steels were measured and the results are summarized in **Figure 8.13**. The mean values of the microhardness of the HAZ as well as those of each sub-zone such as GC (Grain Coarsened), GR (Grain Refined), IC (Intercritical or Partially Transformed) and SC (Subcritical or Tempered Region) are given in **Table 8.4.** As expected, the hardness value of the weld metal and the HAZ generally decreases with increase of the heat input. It is also noted that the width of the HAZ of the uncoated steel was narrower than that of the coated counterpart for a similar heat input, which implies the effective heat inputs experienced by the coated and uncoated samples may not be the same.

8.1.3.2 Effect of electrode orientation

The micro-hardness test results of the GMA welded G550 ZA sheet steels at the heat input 80 J/mm are summarized in **Figure 8.14 (a)**. As can be seen, the hardness of the weld metal for the perpendicular and forehand welds is higher than that of the backhand welds. It also seems that the HAZ of the forehand electrode orientation has the highest micro-hardness values, which is consistent with the results of the tensile tests given earlier in the section.

8.1.3.3 Effect of travel speed

The micro-hardness test results of the GMA welded G550 ZA sheet steels at the heat input 80 J/mm with different travel speeds are summarized in **Figure 8.14 (b)**. For a constant heat input, the hardness of the HAZ does not appear to be affected significantly by the travel speed.

8.1.3.4 Effect of control mode

Figure 8.14 (c) shows the micro-hardness results of the GMAW G550 ZA sheet steels at the heat input 60 J/mm using the current control and constant voltage modes. The HAZ and weld metal have higher hardness values in the constant voltage control mode than those of the current control mode, but the former has a narrower HAZ zone than that of the latter.

8.1.3.5 Effect of welding process

Figure 8.14 (d) shows the micro-hardness profiles of the GMA and FCA backhand ZA G550 welds at the heat input of 60 J/mm. The GMAW process resulted in higher micro-hardness in both the weld metal and HAZ and a narrower HAZ than those of the FCAW process.

8.1.3.6 Effect of zinc alloy coating

The micro-hardness test results of the GMAW G550 ZA and ZHT sheet steels at the heat input 80 J/mm are summarized in **Figure 8.14 (e)**. The hardness values of the weld metal and HAZ for the ZA welds are slightly higher than the ZHT welds which also have a wider HAZ.

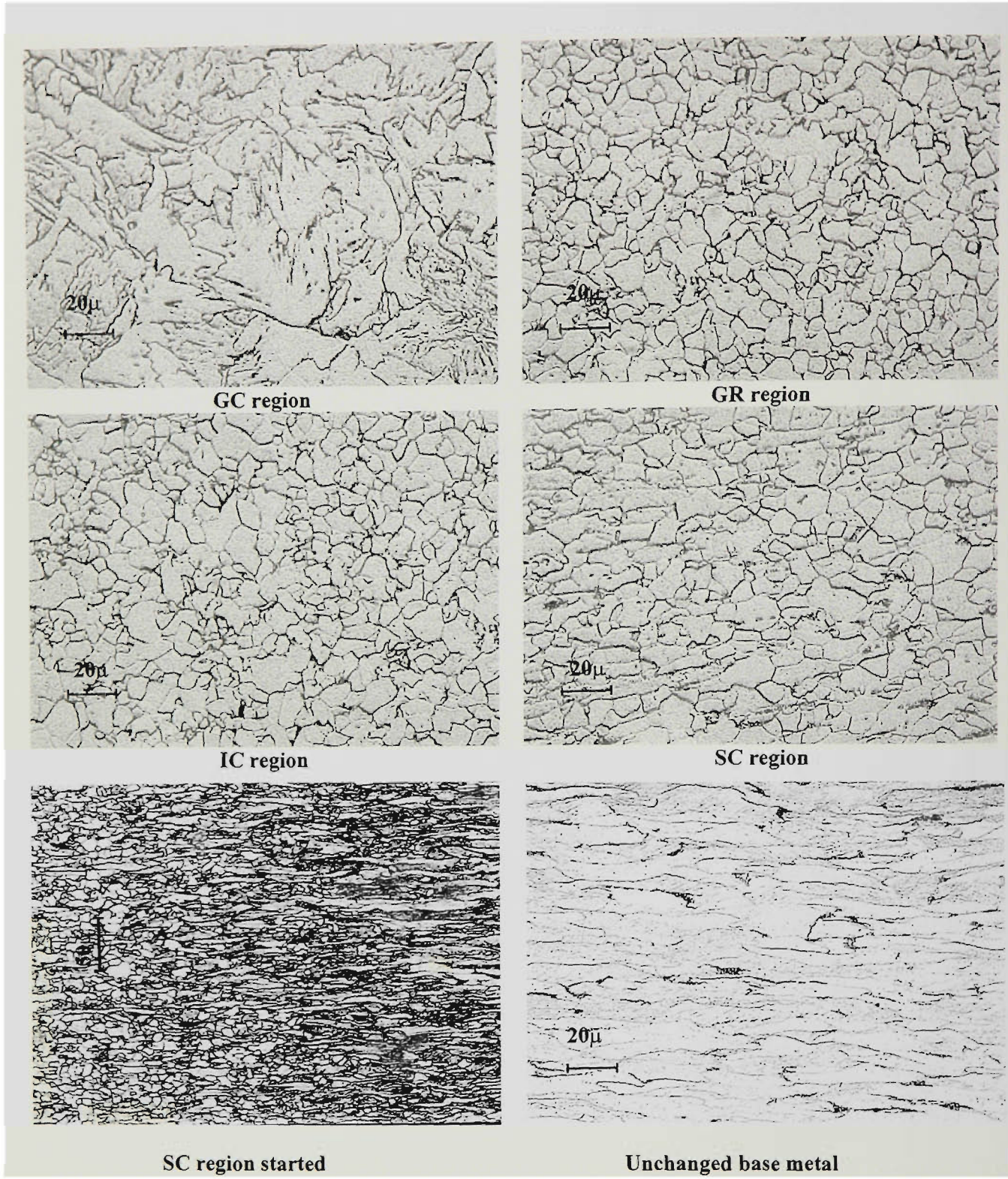

Figure 8.15 Typical microstructures of the sub-zones of the HAZ and base metal of GMA welded ZA sheet steels.

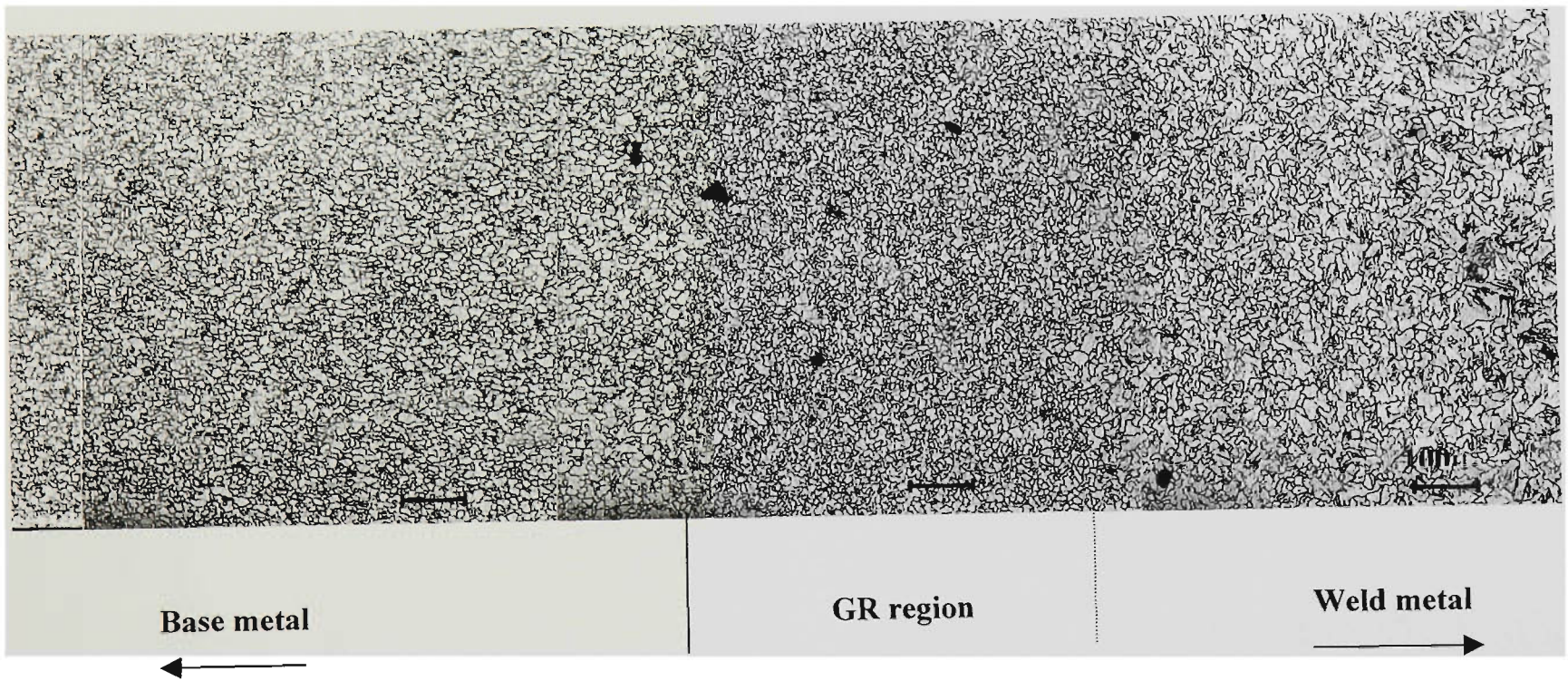

Figure 8.16 Optical micrograph showing the narrow band grain-refined region in HAZ for the FCA welded ZA welds.

8.2 HEAT AFFECTED ZONE (HAZ)

8.2.1 Microstructure of the HAZ

Fusion welding of these cold rolled steels produced a HAZ with a distinctive structure gradient. The HAZ could be characterized and further divided into subzones in terms of different types of microstructures with different mechanical properties. The sub-zones and their approximate peak temperature range are: GC-grain-coarsened region (1490-1100 °C); GR-grain-refined region (1100-900 °C); IC-Intercritical or transformed region (900-750 °C); and SC-subcritical or tempered region with a peak temperature of less than 750 °C. Sub-zone SC or the "tempered" region is characterized by recrystallisation, partial recrystallisation and enhanced recovery of the "cold rolled" structure. Although each region can be described in terms of dominant microstructural features, no sharp transition boundary exists between adjacent regions. For instance, there is no sharp transition from the grain-coarsening region to the grain-refined region and from the Intercritical or partially transformed region to the subcritical or tempered region. **Figure 8.15** shows typical microstructures of the sub-zones of the HAZ and base metal of the ZA G550 sheet steel. In the grain coarsening region there are two characteristic sub regions: Widmanstatten side-plate ferrite and polygonal ferrite. The former is observed at close to the fusion line and is very coarse as shown in **Figure 8.15** and the latter has a gradual grain size reduction from the Widmanstatten sub-zone to the grain-refined subzone. The grain-refined region is a narrow band and as the name implies, is made of very fine equi-axed ferrite grains (**Figure 8.16**). The intercritical or partially transformed region consists of mixed fine and coarser grains. The subcritical or tempered region has very similar optical microstructure to that of the partially transformed region. The various welding processes are unlikely change the basic structural characteristics of HAZ although different processes may vary the total width of HAZ, or the width of the each individual region, or the grain size of the grain-coarsened region close to the fusion line.

8.2.2 Width of the HAZ

Table 8.5 Approximate HAZ widths and weld metal (WM) areas of GMA ZINCALUME™ G550 1.0mm welds with different heat input. GC-grain - coarsened; GR – grain-refined region; IC-Intercritical or partially transformed region; SC-Subcritical or tempered region.

Heat Input (J/mm)	HAZ (mm)	GC to GR (inc.) (mm)	IC to SC (mm)	WM area (mm^2)
60	2.72	1.55	1.17	4.06
80	3.75	2.09	1.66	4.79
90	4.14	2.39	1.75	6.70
110	4.32	2.58	1.74	7.32
130	4.65	2.68	1.97	7.95

Table 8.6 Approximate HAZ width and weld metal (WM) areas of GMA welded ZINCALUME™ and ZINC-HI-TEN™ G550 sheet steels at a heat input of 80 J/mm using perpendicular, backhand and forehand electrode orientations, shielded by Argoshield 50.

Electrode Orientation	HAZ (mm)	GC to GR (inc.) (mm)	IC to SC (mm)	WM area (mm^2)
ZINCALUME™				
Perpendicular	3.42	1.88	1.54	5.02
Backhand	3.68	2.18	1.50	5.57
Forehand	3.08	1.80	1.28	3.59
ZINC-HI-TEN™				
Perpendicular	3.74	2.06	1.68	5.26
Backhand	3.73	2.13	1.60	5.61
Forehand	3.34	1.98	1.36	4.60

The width of the HAZ was obtained by measuring the perpendicular length from the fusion line to the end of the microscopically visible tempered region. It is found that the width varies with heat input, electrode orientation, surface coating, weld speed and control mode etc.

8.2.2.1 Effect of the nominal heat input on the width of HAZ

Table 8.5 shows the effect of the heat input on the average width of the HAZ for the ZA G550 1.0 mm thick GMA welded sheet steels (shielded by Argoshield 50). The average width of the HAZ clearly increased with the increase of heat input. Since the cooling time from 800°C to 500°C ($\Delta t_{8/5}$) can be considered directly proportional to the heat input [Easterling 1992], a higher heat input correlates with a larger value of $\Delta t_{8/5}$ and a lower cooling rate. As expected, the 130 J/mm heat input resulted in the largest weld metal area, the largest average HAZ width and therefore the lowest average cooling rate.

8.2.2.2 Effect of electrode orientation and zinc alloy coating

The width measurements of the HAZ of the GMA welded ZINCALUME^{TM} and ZINC-HI-TEN^{TM} sheet steels at a heat input of 80 J/mm with various electrode orientations are given in **Table 8.6**.

Comparing the perpendicular and forehand electrode orientations, the backhand technique produced the largest fusion zone and widest HAZ for both the GMAW ZA and ZHT G550 sheet steels. Furthermore, the GMAW ZA sheet has a smaller HAZ width and a smaller fusion weld bead area than the GMAW ZHT steel sheet at the same nominal heat input and with the same electrode orientation.

8.2.2.3 Effect of travel speed

The results of the HAZ width and weld metal area of the GMA ZA and ZHT welds at the heat inputs of 80 J/mm and 100 J/mm with variation of electrode travel speed are summarized in **Table 8.7**. Clearly, the faster travel speed, the narrower the HAZ

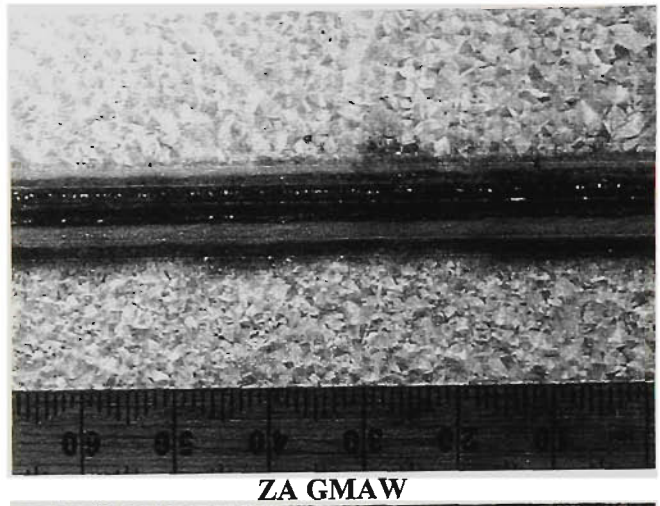

ZA GMAW

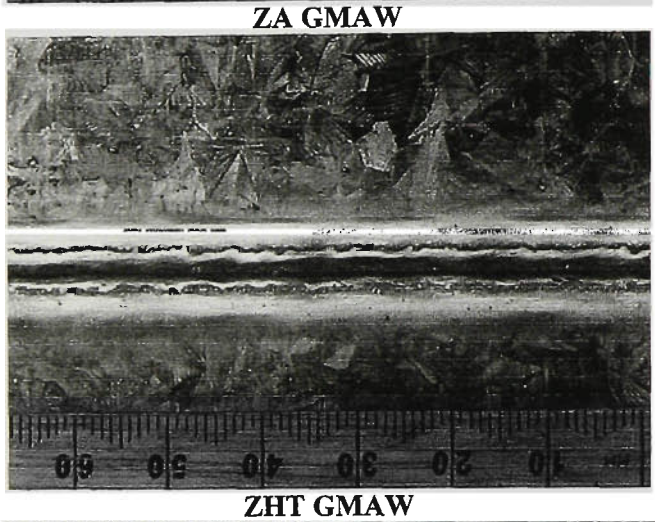

ZHT GMAW

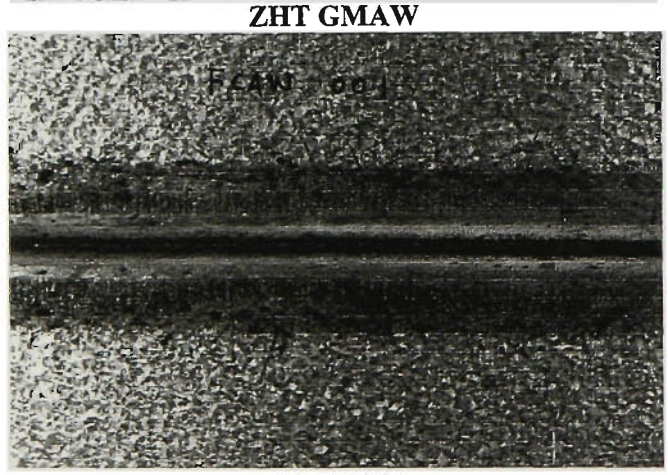

ZA FCAW

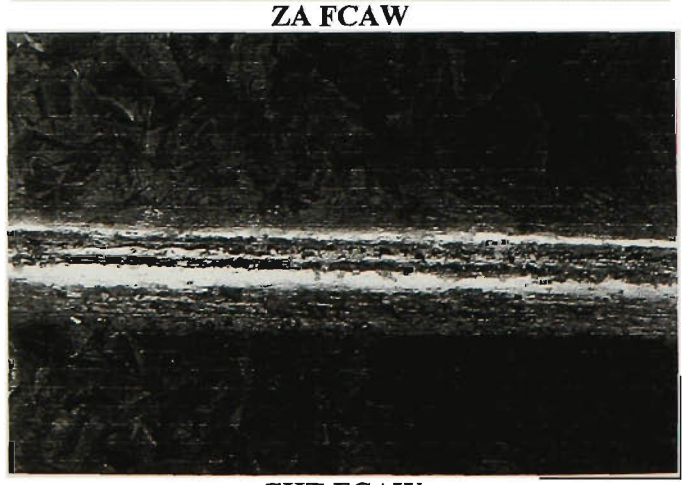

ZHT FCAW

1mm

Figure 8.17 (a) Macrographs showing the GMA and FCA welded ZA and ZHT welds.

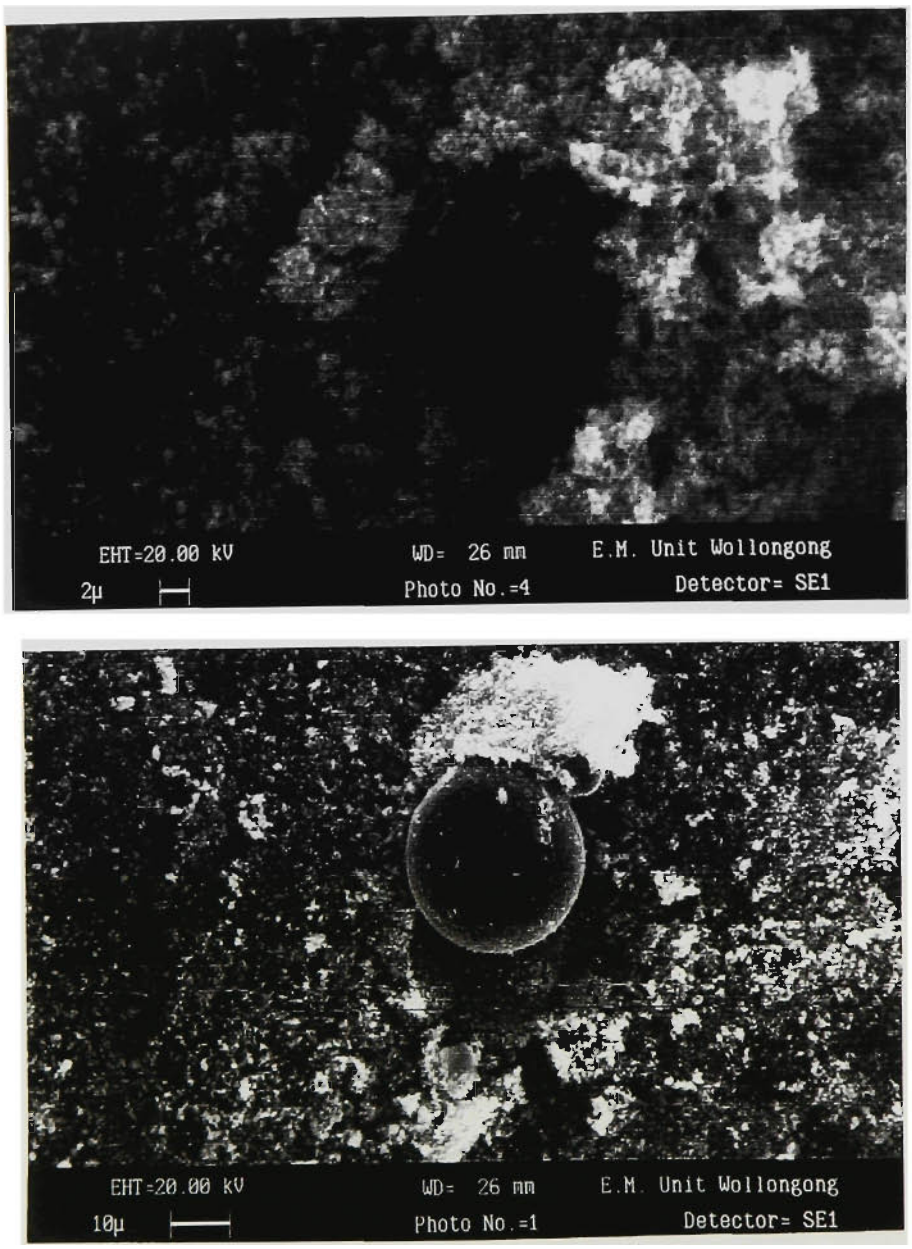

Figure 8.17 (b) SEM micrographs showing Zn oxides and spherical particles of Fe oxides from the Zn powder collected after GMAW ZINC-HI-TEN^{TM} G550 1.0 mm sheet steel.

Table 8.7 Approximate HAZ widths and weld metal areas of the GMA ZINCALUME™ and ZINC-HI-TEN™ welds.

Heat Input (J/mm)	Trav. Speed (mm/min.)	HAZ (mm)	GC to GR (inc.) (mm)	IC to SC (mm)	WM area (mm^2)
ZA					
80	420	3.57	2.08	1.44	5.44
80	530	3.61	1.96	1.65	5.35
80	630	3.46	1.89	1.57	6.23
80	740	3.16	1.68	1.48	6.33
ZHT					
100	650	3.33	2.01	1.86	7.9
100	780	3.91	2.20	1.71	7.47
100	910	3.86	2.08	1.78	6.98
100	1040	3.89	2.02	1.87	5.8

Table 8.8 Approximate HAZ width and weld metal area of GMA welded ZA and ZHT sheet steels using current control mode (CC) and constant voltage control mode (CV).

Control mode	Heat Input (J/mm)	HAZ width (mm)	GC to GR (inc.)(mm)	IC to SC (mm)	WM area (mm^2)
ZINCALUME™					
CC (B)	60	3.29	1.76	1.53	5.09
CV (B)	60	2.90	1.71	1.19	4.21
ZINC-HI-TEN™					
CC(B)	70	3.68	1.94	1.74	5.38
CV (B)	70	3.42	1.79	1.63	4.33

Table 8.9 Approximate HAZ widths and weld metal areas of GMAW and FCAW for ZINCALUME™ and ZINC-HI-TEN™ sheet steels

Welding Process	Heat Input (J/mm)	HAZ (mm)	GC to GR (inc.) (mm)	IC to SC (mm)	WM area (mm)
ZA					
GMAW	60	2.72	1.55	1.17	4.06
FCAW	60	3.32	1.86	1.46	3.76
ZHT					
GMAW	70	3.35	1.85	1.50	4.02
FCAW	70	3.88	2.32	1.56	3.89

width. However, the weld metal area seems to be less affected by the travel speed and does not show any systematic trend.

8.2.2.4 Effect of welding control mode

The results for the HAZ width and weld metal area of GMA welded ZA sheet steel at the heat input of 60 J/mm and ZHT sheet steel at the heat input of 70 J/mm using current control and constant voltage control mode are summarised in **Table 8.8**. It is clearly shown that the current control mode produces a wider HAZ and a larger weld metal area than using the constant voltage control mode.

8.2.2.5 Effect of welding process

The FCAW process produced a larger HAZ, but a smaller weld metal area than the GMAW process at the same nominal heat input for both the ZA and ZHT sheet steels, as shown on **Table 8.9**.

8.3 WELD METAL

8.3.1 Surface Appearance of the Weld Metal

Figure 8.17 (a) shows macro views of the welds of the ZA and ZHT GMAW and FCAW sheet steels. The surface appearances of the weld beads on the ZA and ZHT of GMAW and FCAW sheet steels were generally satisfactory. Although spatter was present on the surface of the welds, there were no obvious macro defects. The welds appeared to be continuous and the weld bead was sound and smooth.

Figure 8.17 (a) also shows that a white coating was present along the ZA weld bead and a thick white powder was found along the ZHT welds. XRD has revealed that the white coating of the former welds has a composition close to that of Fe_3Al intermetallic compound (same as **Figure 8.12**). The thick white powder of the latter welds, however, was determined by EDS to consist of zinc oxides and spherical particles of Fe oxides in sizes less than 30μm in diameter (**Figure 8.17 (b)**).

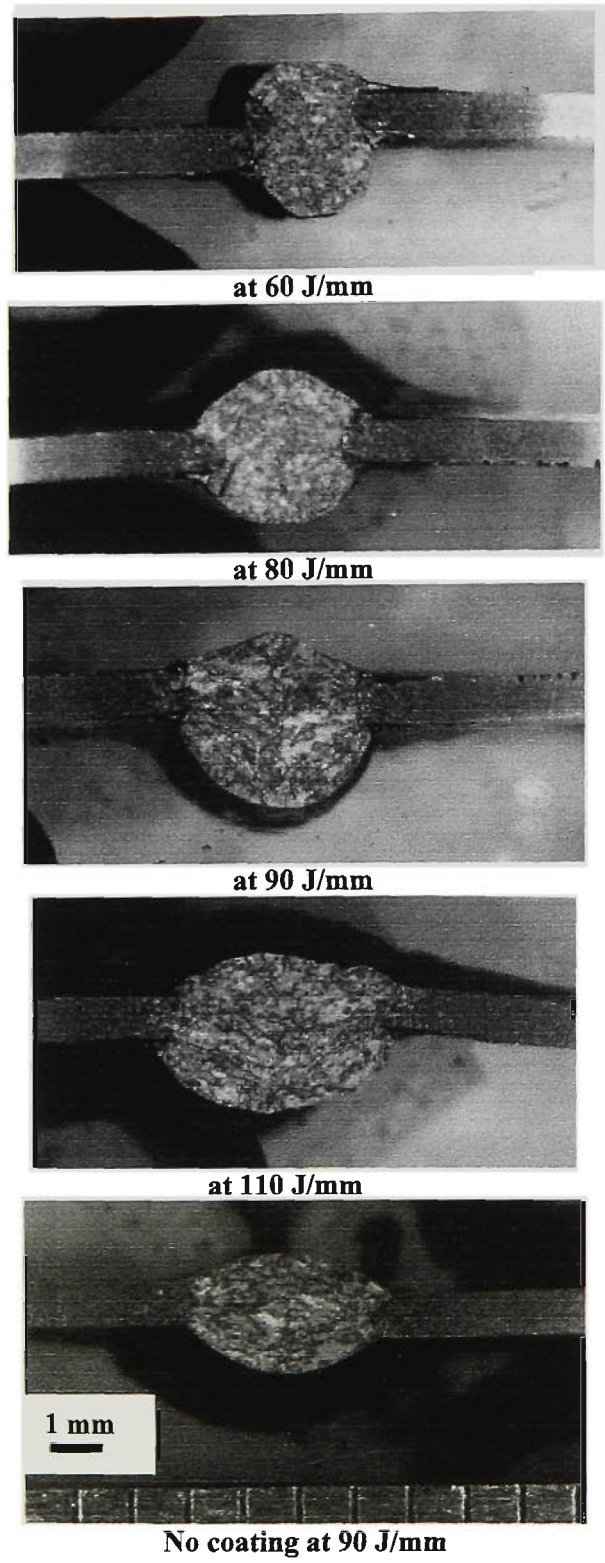

Figure 8.18 Macro-photographs of weld metal cross-sections of GMA welded ZINCALUME^{TM} G550 0.85 mm sheet steel corresponding to different heat inputs.

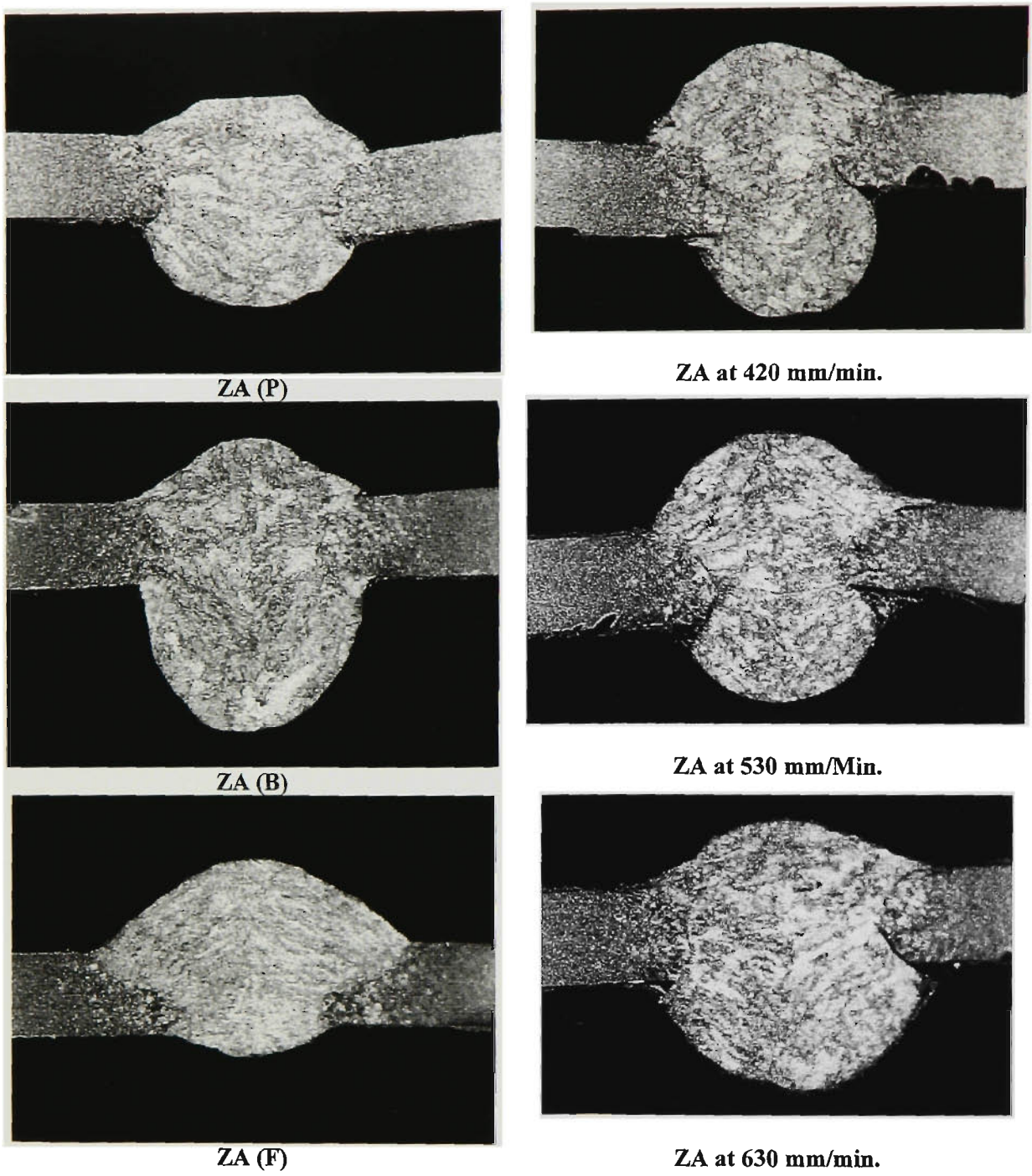

Figure 8.19 Macro-photographs of the weld metal cross-sections for the GMA welded ZA sheet steel: column **(a)** at heat input of 80 J/mm using various electrode orientations and column **(b)** at different travel speeds.

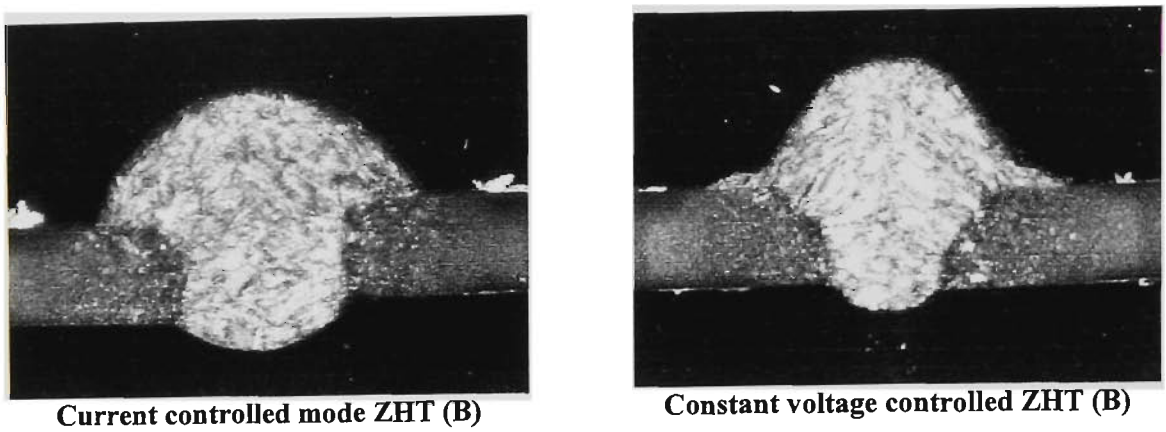

Figure 8.20 Macro-photos of weld metal cross-sections and weld bead of GMA welded ZINC-HI-TEN™ 1.0mm sheet steels at heat input of 70 J/mm using current controlled and constant voltage modes.

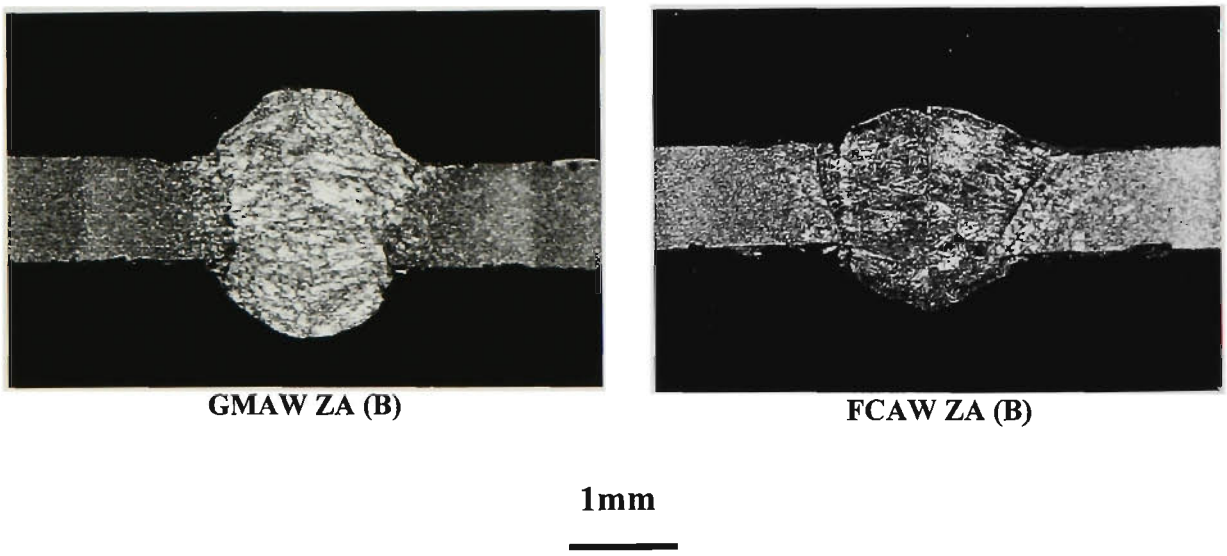

Figure 8.21 Macro-photographs showing the weld metal cross-sections of GMA and FCA welded ZINCALUME™ G550 1.0mm sheet steels at heat input of 60 J/mm.

Table8.10 Chemical compositions (wt.%) of the weld metals with various heat input for GMA welded ZA G550 1.0 mm sheet steels

HI(J/mm)	C	P	Mn	Si	S	Ni	Cr	Cu	Al	Zn	N	O
60	.08	.017	.63	.36	.014	.019	.016	.044	.7	.38	.0051	.0125
80	.08	.017	.75	.43	.015	.018	.016	.053	.5	.038	.0049	.0115
90	.075	.017	.84	.51	.016	.016	.018	.058	.34	.38	.005	.015
110	.08	.018	.86	.52	.016	.017	.018	.062	.38	.031	.0046	.013
130	.08	.017	.83	.5	.15	.017	.018	.058	.46	.038	.0044	.0135

Table8.11 Chemical compositions (wt.%) of the weld metals of GMA welded, A50 shielded ZA and ZHTG550 1.0 mm sheet steels using (P) perpendicular, (B) backhand and (F) forehands electrode orientation at a heat input of 80 J/mm

E.Orien.	C	P	Mn	Si	S	Ni	Cr	Cu	Al	Zn	N	O
ZA(P)	.085	.017	.8	.49	.015	.017	.02	.069	.66	.074	.0048	.014
ZA(B)	.08	.017	.75	.43	.015	.018	.016	.053	.5	.038	.0049	.0115
ZA(F)	.085	.018	.81	.47	.015	.018	.017	.061	.4	.013	.0045	.0135
ZHT(P)	.055	.015	.37	.12	.013	.015	.012	.024	.038	.016	.0044	.032
ZHT(B)	.05	.017	.56	.3	.016	.016	.016	.041	.024	.03	.0051	.027
ZHT(F)	.066	.014	.26	.025	.013	.015	.011	.013	.046	.014	.01	.03

Table8.12 Chemical compositions (wt.%) of the weld metals of GMA welded ZA at various welding speeds (at heat input of 80 J/mm)

Trav.Speed (mm/min)	C	P	Mn	Si	S	Ni	Cr	Cu	Al	Zn	N	O
530	.08	.018	.79	.47	.016	.018	.016	.056	.53	.036	.005	.014
630	.08	.018	.77	.45	.015	.019	.016	.055	.64	.03	.004	.0145
740	.08	.017	.74	.43	.015	.019	.016	.053	.52	.035	.005	.0135

Table8.13 Chemical compositions (wt.%) of the weld metals of GMA and FCA welded ZA and ZHT at heat input of 60 J/mm and 80 J/mm respectively

Welds	C	P	Mn	Si	S	Ni	Cr	Cu	Al	Zn	N	O
ZA												
GMA	.08	.017	.63	.36	.014	.019	.016	.0044	.7	.038	.0051	.0125
FCA	.13	.012	.31	.07	.008	.027	.014	.013	1.1	.084	.055	.0035
ZHT												
GMA	.05	.017	.56	.3	.016	.016	.016	.041	.024	.03	.0051	.029
FCA	.125	.012	.34	.055	.007	.023	.015	.015	.55	.068	.045	.006

8.3.2 Weld Bead Geometry and Compositions

8.3.2.1 Effect of heat input

Macro-photographs of the cross-sections of the weld beads of the perpendicular GMAW ZA 0.85 mm sheet steel and the uncoated steel sheets are shown in **Figure 8.18**. These macro photos clearly show that the volume of the weld metal increased with the increase of the heat input due to the greater volume of deposited filler and more extensive melting of the base sheet. It is also noted that the welds in the uncoated sheet steel were flatter and smoother than those of the Zn-Al coated steel. The chemical compositions of the weld metals produced for various heat inputs are given in **Table 8.10**.

8.3.2.2 Effect of electrode orientation

Figure 8.19 (a) shows macro-photographs of the cross-sections of the weld bead of the ZA sheet steel welds obtained using the three different electrode orientations: perpendicular, backhand and forehand. As expected, the backhand orientation produced a more convex with a deeper penetration than those of the other two orientations. Furthermore, the backhand weld has a lower oxygen content than the perpendicular and forehand welds, as shown in **Table 8.11**.

8.3.2.3 Effect of travel speed

Figure 8.19 (b) shows the weld bead cross-sections of the GMA welded ZA G550 sheet steel at a constant nominal heat inputs of 80 J/mm at travel speeds from 530 to 740 mm/min.. It is clearly shown that the higher the travel speed, the larger the weld metal area. The chemical compositions of the weld beads are given in **Table 8.12**.

8.3.2.4 Effect of the control mode

Figure 8.20 shows macro-photographs of the cross-sections of the weld bead of the GMAW ZHT sheet steels obtained using constant voltage and current control modes.

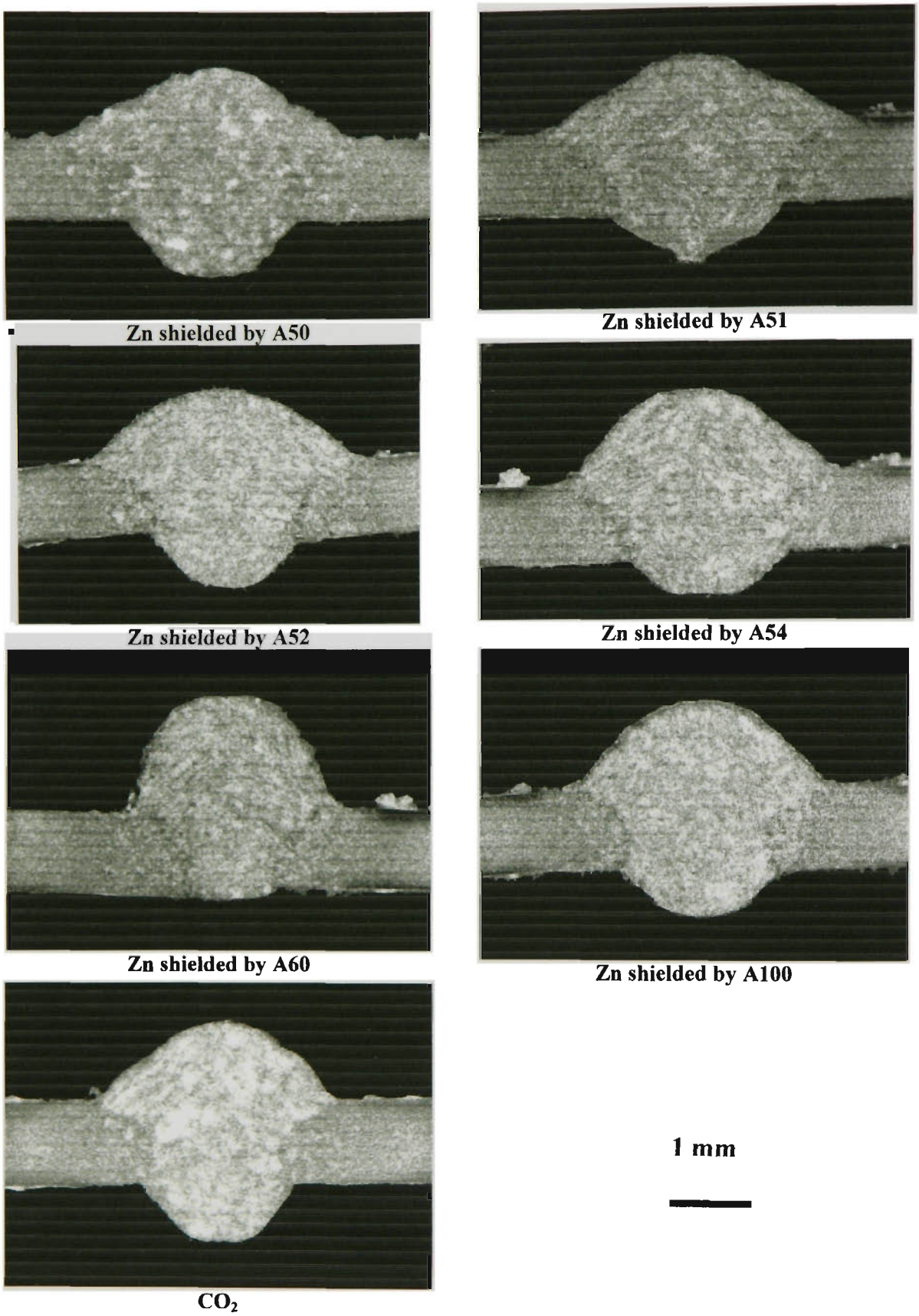

Figure 8.22 Macro-photographs showing the weld metal cross-sections of GMA welded ZINC-HI-TEN™ G550 sheet steels at heat input of 80 J/mm with various shielding gases.

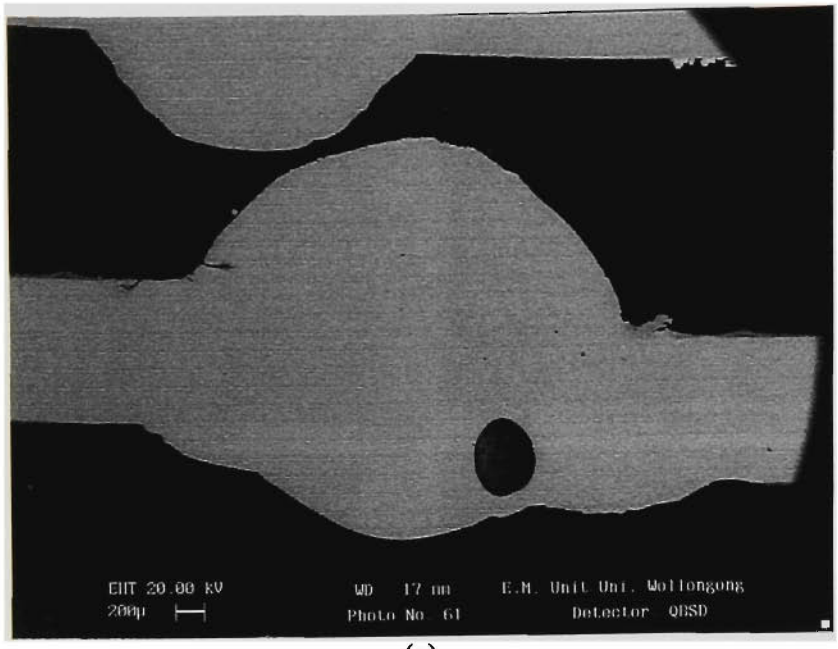

(a)

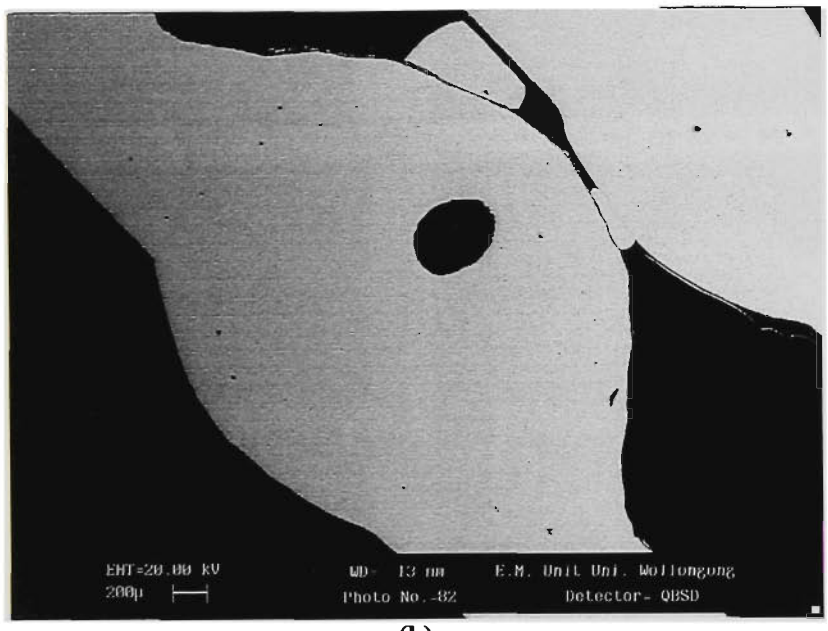

(b)

Figure 8.23 Back scattered electron micrographs showing large pores caused by gas entrapment in the molten weld pool of **(a)** GMA welded ZA sheet steel and **(b)** FCA welded ZHT sheet steel.

(a) 0.85 mm GMA welds at 60 J/mm

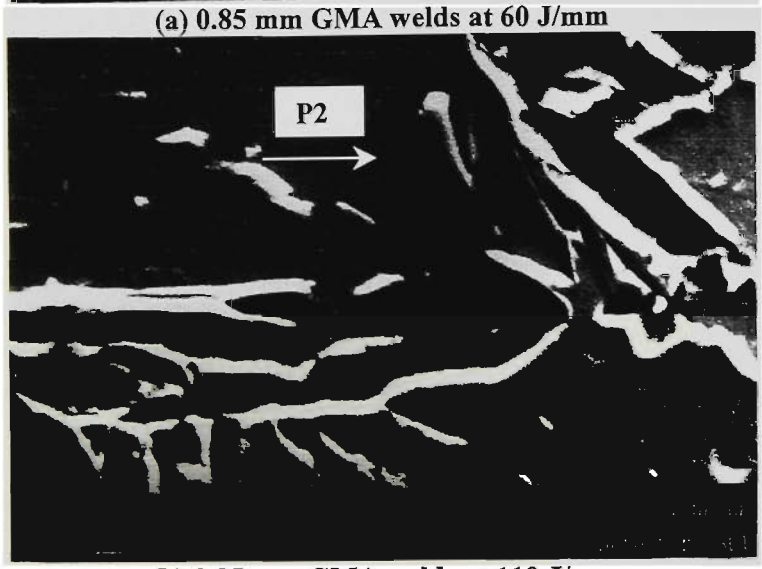

(b) 0.85 mm GMA welds at 110 J/mm

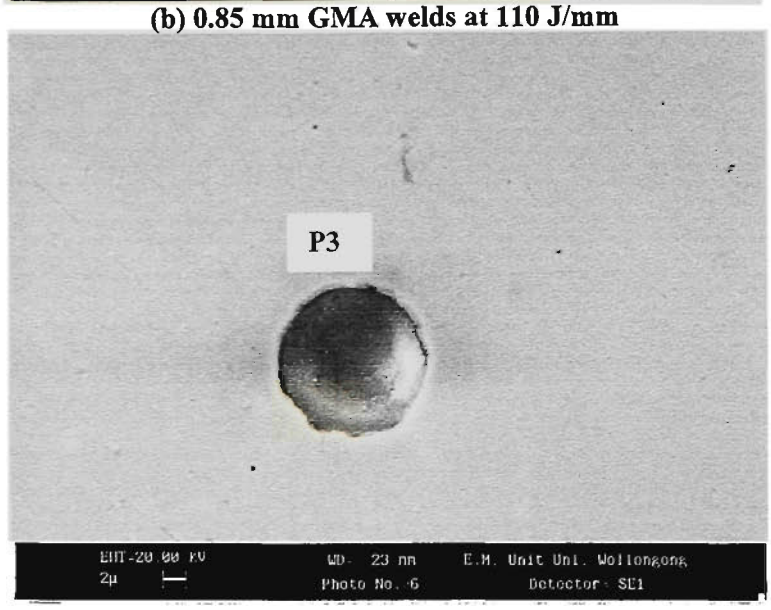

(c) 1.0 mm GMA welds at 80 J/mm

Figure 8.24 SEM micrographs showing Al-rich particles **P1**, **P2** and **P3** in the weld metal of GMA welded ZINCALUME^{TM} G550 sheet steel.

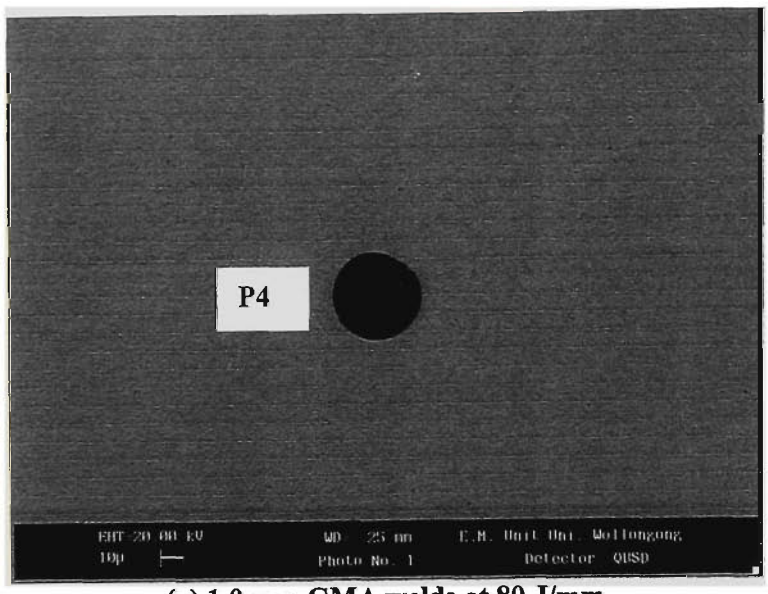

(a) 1.0 mm GMA welds at 80 J/mm

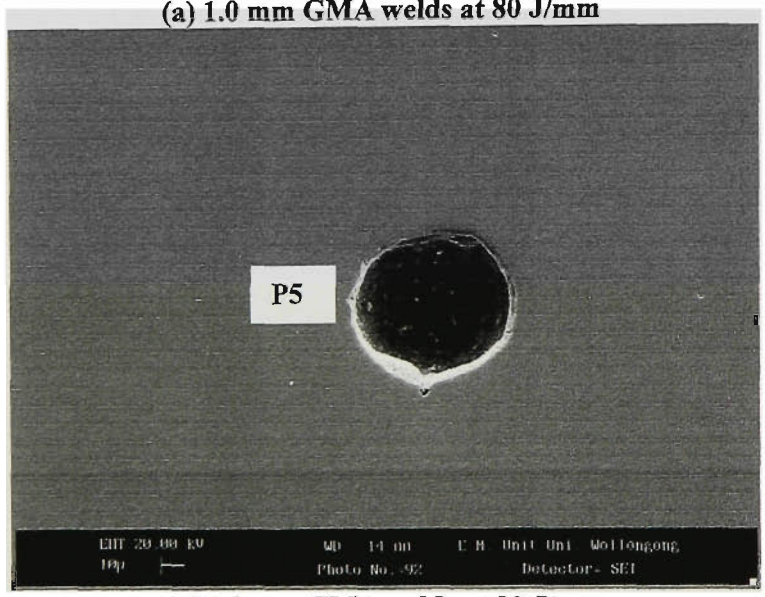

(b) 1.0 mm GMA welds at 80 J/mm

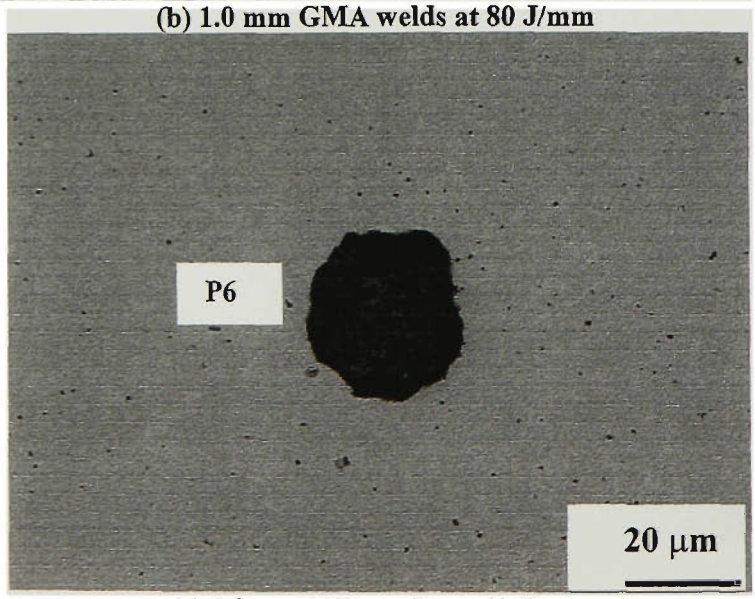

(c) 1.0 mm FCA wells at 60 J/mm

Figure 8.25 SEM micrographs showing the Al-rich particles in ZINCALUME™ GMA weld metal **(a)** and **(b)** and FCA weld metal **(c)**.

Table8.14 Chemical compositions (wt.%) of the weld metals for GMA welded ZA and ZHT G550 sheet steels at heat input of 80 J/mm shielded by various shielding gas.

S.Gas	C	P	Mn	Si	S	Ni	Cr	Cu	Al	Zn	N	O
ZA												
A50	.08	.017	.75	.43	.015	.018	.016	.053	.5	.038	.0049	.0115
A51	.09	.017	.7	.4	.014	.019	.016	.048	.48	.043	.005	.017
A52	.09	.017	.72	.41	.014	.019	.016	.051	.49	.028	.0049	.019
A54	.08	.017	.74	.43	.015	.019	.016	.053	.63	.042	.0047	.011
A60	.08	.017	.73	.42	.015	.019	.016	.05	.57	.025	.0053	.0055
A100	.09	.011	.85	.36	.008	.047	.053	.13	.26	.038	.0056	.034
CO_2	.095	.011	.89	.37	.008	.048	.055	.14	.27	.035	.0064	.047
ZHT												
A50	.05	.017	.56	.3	.016	.016	.016	.041	.024	.03	.0051	.029
A51	.06	.017	.6	.3	.015	.016	.015	.042	.025	.022	.0048	.0315
A52	.07	.017	.67	.36	.015	.016	.016	.048	.022	.042	.0052	.032
A54	.06	.017	.64	.34	.015	.016	.015	.048	.023	.036	.0054	.027
A60	.06	.018	.73	.42	.017	.016	.017	.056	.021	.017	.0076	.013
A100	.065	.018	.73	.41	.017	.016	.016	.052	.02	.027	.0055	.022
CO_2	.075	.012	.78	.3	.009	.043	.053	.14	.015	.054	.0083	.048

The current control mode provides a smoother weld bead than the constant voltage control mode.

8.3.2.5 Effect of welding process

The macro-photographs in **Figure 8.21** illustrate the cross-sections of the weld bead of GMA and FCA welded ZA sheet steels. The chemical compositions of the weld beads are given in **Table 8.13**. It is clearly shown that the flatter and smoother weld beads obtained in the FCAW process have a lower weld metal oxygen concentration, but a much higher nitrogen content than that of the GMAW process.

8.3.2.6 Effect of the shielding gas

Figure 8.22 shows the macro-photographs of the cross-sections of the weld bead of GMA welded ZHT sheet steel obtained using different shielding gases. The chemical compositions of the welds under different shielding gases are given in the **Table 8.14**.

8.3.3 Porosity of the Weld Metal

There was no evidence of a significant number of gas pores in the weld beads of the GMAW Zn-Al coated steel in the present study. However, isolated large spherical pores (up to 500 μm in diameter) were observed in the weld metals of the GAMW and FCAW ZA and ZHT sheet steel as shown in **Figure 8.23**. EDS microanalysis of the surface of the large pore shown in **Figure 8.23** revealed nothing but Fe.

8.3.4 Al-rich Particles in Weld Metal

Al-rich particles observed in the weld metal of the GMA welded ZA sheet steels are shown in **Figures 8.24** and **8.25**. Similar Al-rich particles were also observed in the weld metal of the FCAW ZA steels (**Figure 8.25 (c)**). The composition of the particles was analysed using SEM/ EDS and the microanalysis results are listed in **Table 8.15**.

Table 8.16 Comparison of important characteristics of non-metallic inclusions

HI J/mm	Materials	(Shielding gas) OP%	N	N_a, 1/μm	V_v, %	$\overline{d_a}$, μm	$\overline{d_v}$,	$\overline{A}$, μm^2	$P_{\leq 0.2\ \mu m}$	$P_{\leq 0.4\ \mu m}$	$P_{>0.8\ \mu m}$
80											
GMAW(B)	ZA	(A60) 1.5	1146	0.013	0.0755	0.1850	0.2905	0.0578	53.4	81.4	3.79
		(A54) 5	1123	0.023	0.1837	0.2481	0.3895	0.0736	39.0	88.3	2.06
		(A100) 5	1155	0.020	0.1959	0.2734	0.4292	0.0967	41.1	83.3	3.36
		(A50) 5.6	1218	0.021	0.1082	0.2486	0.3903	0.0640	39.6	84.7	3.51
		(A51) 10.75	1202	0.021	0.1406	0.2391	0.3754	0.0667	48.0	88.0	1.06
		(A52) 11.5	949	0.020	0.1271	0.2202	0.3457	0.0636	36.1	85.3	2.47
		100% CO_2	1331	0.032	0.3040	0.2965	0.4655	0.0955	32.3	82.5	1.69
60											
GMAW(B)	ZA	(A50) 5.6	914	0.017	0.1461	0.2860	0.4490	0.0881	32.9	83.8	2.16
FCAW(B)	ZA		705	0.012	0.4263	0.5154	0.8092	0.3447	21.7	45.0	25.7
80											
GMAW(B)	ZHT	(A50) 5.6	1824	0.030	0.2491	0.2436	0.3825	0.0830	35.1	76.1	4.33
FCAW(B)	ZHT		638	0.009	0.3053	0.4321	0.6784	0.3455	33.8	68.7	14.1
GMAW											
80 (P)	ZA	(A50) 5.6	929	0.016	0.1133	0.2198	0.3451	0.1001	42.5	79.6	7.47
80 (F)	ZA	(A50) 5.6	893	0.017	0.1087	0.2392	0.3755	0.0624	49.0	73.1	0.52

N: the number of particles

N_a: the number per unit area of particles

V_v: the volume fraction

$\overline{d_a}$: the average two dimensional particle diameter

$\overline{d_v}$: the average three dimensional particle diameter

$\overline{A}$: the average area of the particles

Table 8.15 Particle compositions determined by EDS analysis (at.%)

Particles	Heat Input (J/mm)	Size (μm)	Al%	Fe%	O %	Others %
P1	60	3	49.04	49.23	0	Mn
P2	110	10	30.46	66.43	0	Mn
P3	80	13	> 90	0	Detected	Ca
P4	80	40	93.83	6.17	Detected	
P5	80	65	> 90			
P6	80	55	40	60	0	

8.4 NON – METALLIC INCLUSION ANALYSES

The nature and distribution of non-metallic inclusions can strongly influence the microstructure and toughness of the weld metal. The inclusion characteristics are sensitive to the oxygen content and deoxidising element concentrations. The formation of inclusion depends strongly on the concentrations of dissolved oxygen and deoxidising elements, and on the weld cooling rate.

8.4.1 Non-Metallic Inclusion Characteristics

The important inclusion characteristics are the number of particles N; the number of particle per unit volume N_V; the volume fraction V_v; the arithmetic mean two and three dimensional particle diameters $\bar{d}_a$ and $\bar{d}_V$; the mean area of the particles $\bar{A}$. The $\bar{A}$ can be obtained directly by using the combination of SEM and image analysis program Video Pro32 and other characteristics were calculated based on the following basic stereometric relationships and the results are summarised in **Table 8.16** [Underwood 1970; Klulen et al. 1988].

V_V = area of the detected features / field area

$$d_a = 2\left(A/\pi\right)^{1/2}$$

$$\bar{d}_a = \Sigma d_a / N$$

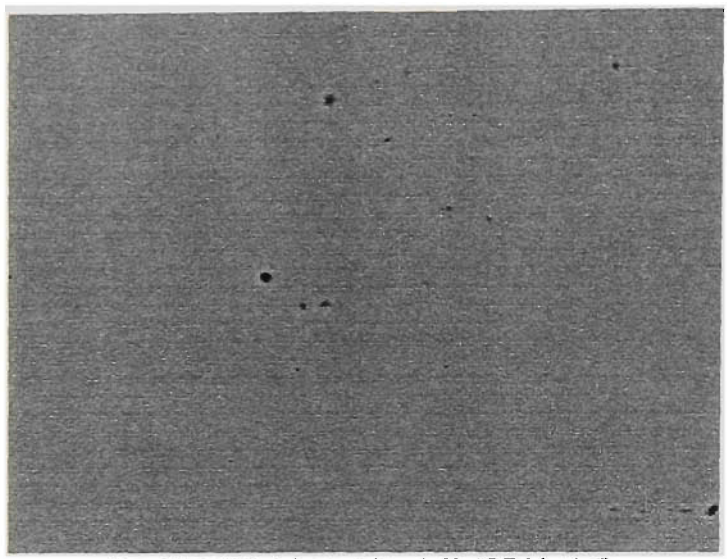

ZA GMAW shielded by A60 (OP%=1.5)

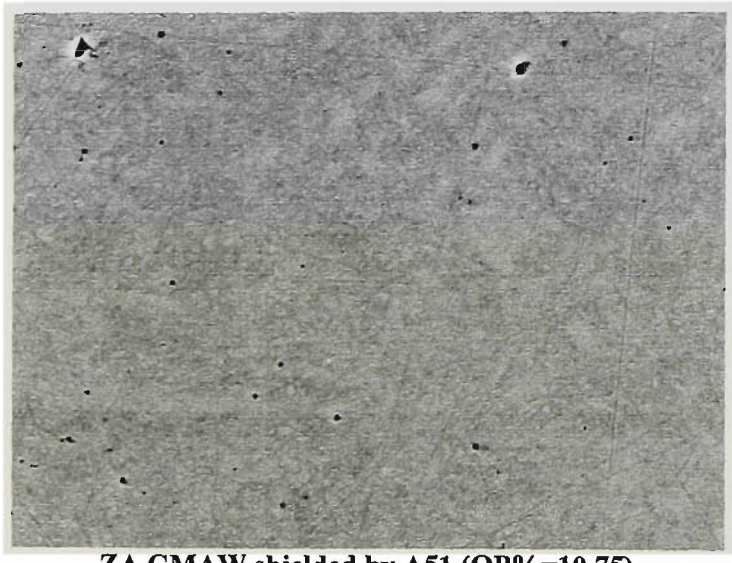

ZA GMAW shielded by A51 (OP%=10.75)

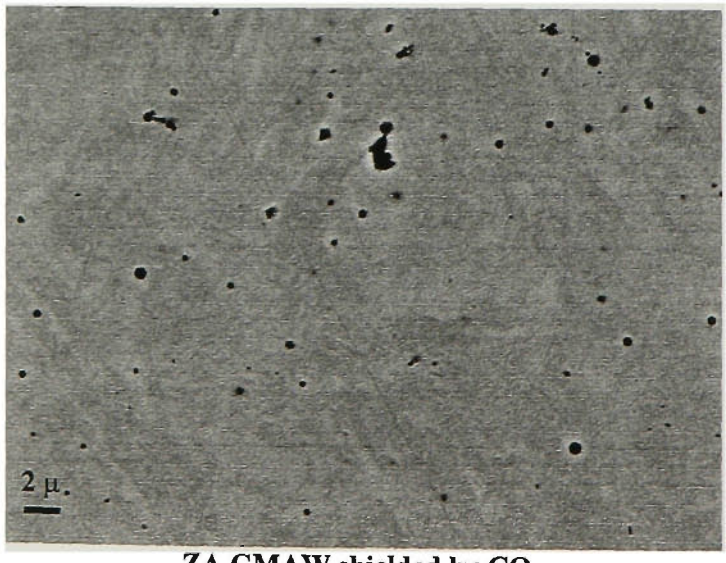

ZA GMAW shielded by CO_2

Figure 8.26 Effect of oxygen potential (**OP%**) of shielding gases on the appearance of non-metallic inclusions for GMA backhand welded ZA G550 1.0 mm sheet steels.

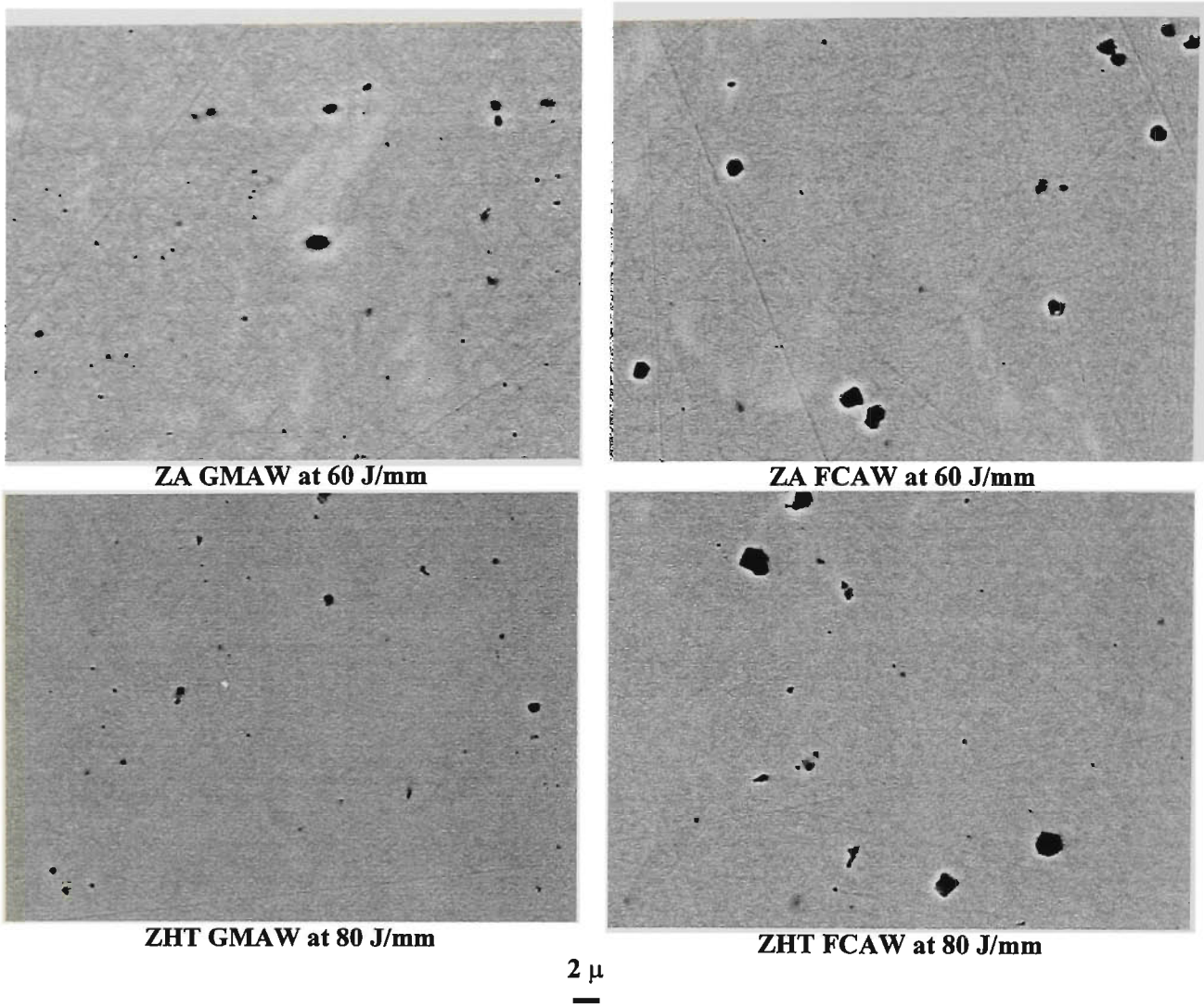

Figure 8.27 Appearance of the non-metallic inclusions of GMA and FCA welded ZA and ZHT welds.

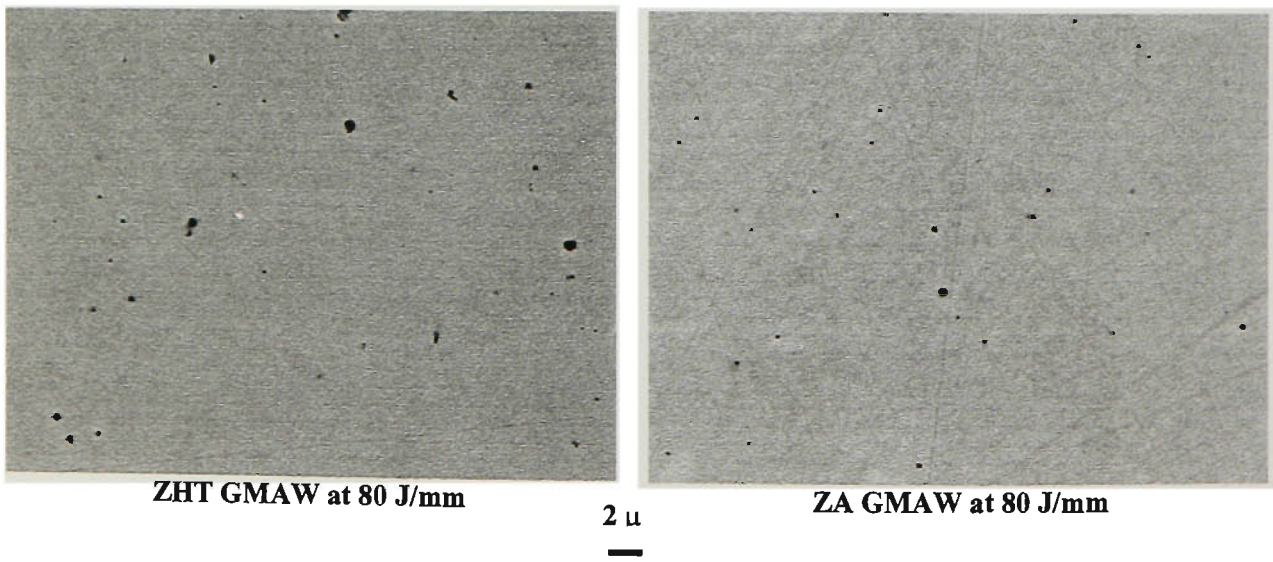

Figure 8.28 Effect of Zn alloy coating on the appearances of non-metallic inclusions of GMA welded ZHT and ZA welds.

$$\bar{d}_V = \pi \left(\bar{d}_a / 2 \right)$$

$$N_v = 6 \left(V_V / \pi \bar{d}_V^{\ 3} \right)$$

$$N_a = N_V \bar{d}_V$$

and

$$\bar{A} = A_A / N_a$$

8.4.1.1 Effect of shielding gas

The volume fractions V_V fall within the range of 0.075 to 0.4263 for the GMA welded Zn-Al steel shielded by A60 and the FCA welds of the same steel. **Figure 8.26** shows SEM images of the non-metallic inclusions in backhand GMA welded metals of the ZA sheet steels under the various shielding gases. It can be seen that the inclusions formed in the weld metal with the shielding gas CO_2 are coarser than those with other shielding gases.

8.4.1.2 Effect of welding process

The effect of the two different welding processes, GMAW and FCAW on non-metallic inclusions is shown in **Figure 8.27**. Clearly, FCAW produced inclusions with larger mean particle sizes ($\bar{d}_a$ = 0.5154 μm and 0.4321 μm in the ZINCALUME™ weld metal and the ZINC-HI-TEN™ weld metal respectively) than those ($\bar{d}_a$ = 0.2860 and 0.2436 μm) produced by GMAW. It was also noted that inclusions produced in the FCAW have irregular shapes. The results are consistent with the fact that the FCAW produced a higher volume fraction of inclusions than the GMAW: the volume fraction of inclusions are 0.4263 and 0.1461 for FCAW and GMAW respectively in the ZA welds and 0.3053 and 0.2491 in the ZHT welds. The oxygen contents of the FCA welds (0.0035 % and 0.006 % for the Zn-Al coated steels welds and the Zn coated welds respectively) are much lower than those of the GMA welds (0.0125 and 0.029 %). On the other hand, the nitrogen contents of the FCA welds are higher (0.055 % and 0.045 % for the Zn-Al

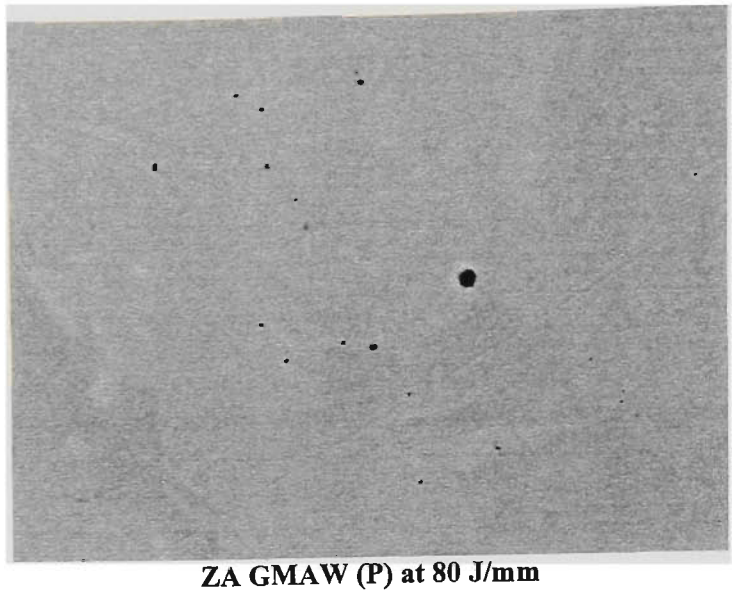

ZA GMAW (P) at 80 J/mm

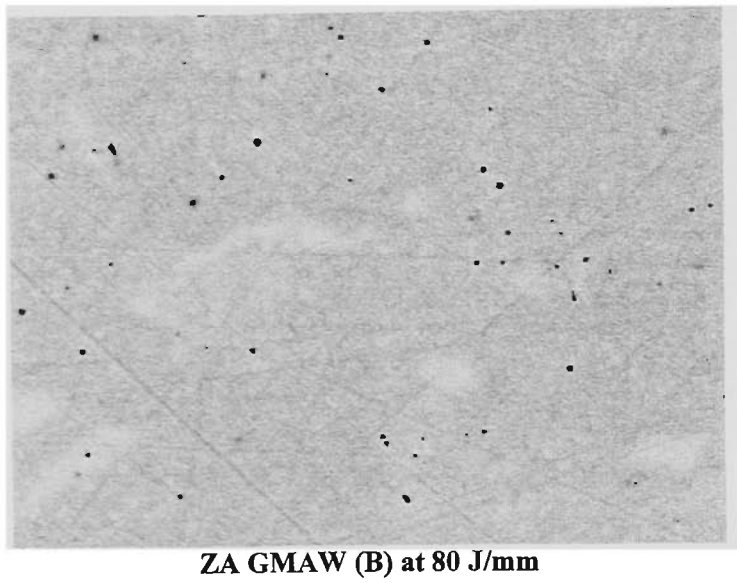

ZA GMAW (B) at 80 J/mm

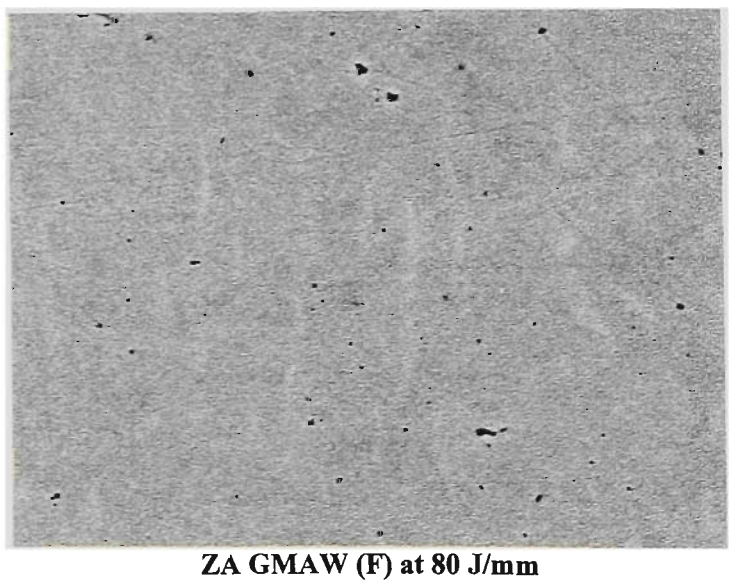

ZA GMAW (F) at 80 J/mm

2μ

Figure 8.29 Effect of the electrode orientation on the appearances of non-metallic inclusions of GMA welded ZA sheet welds.

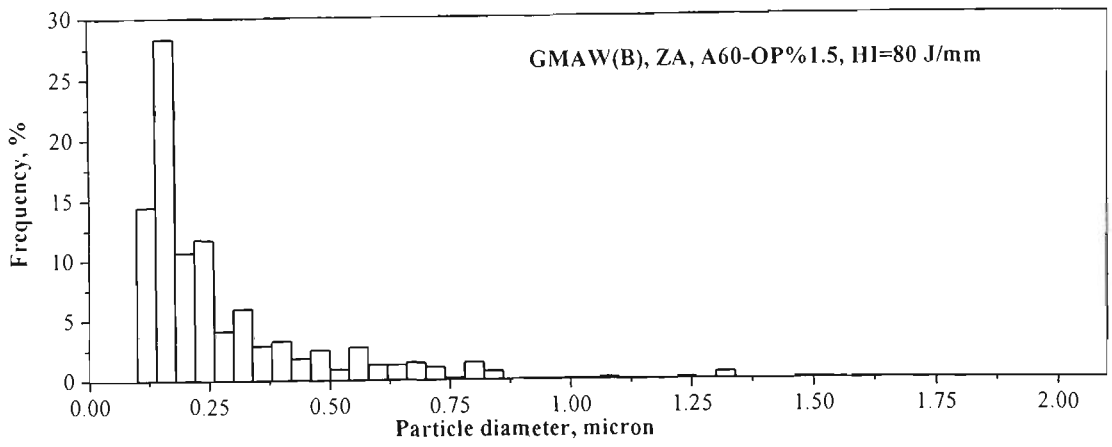

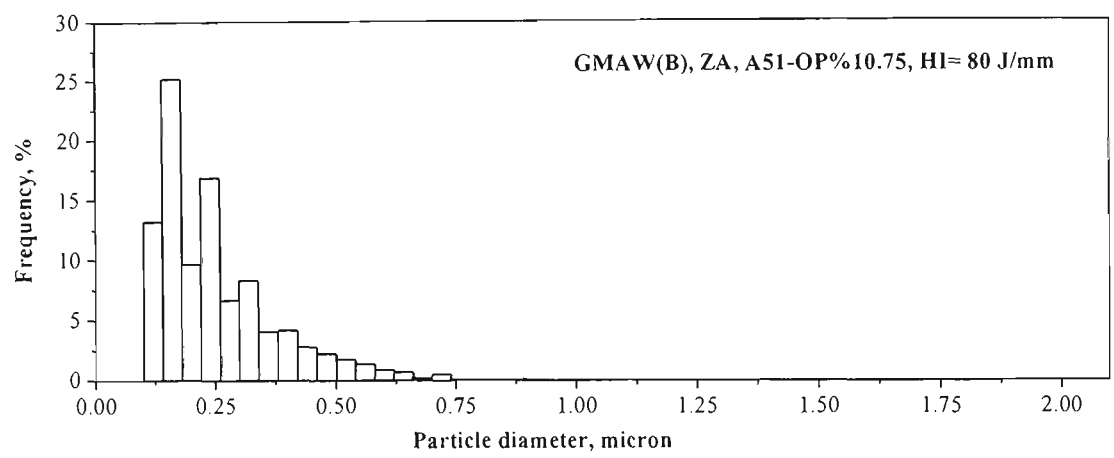

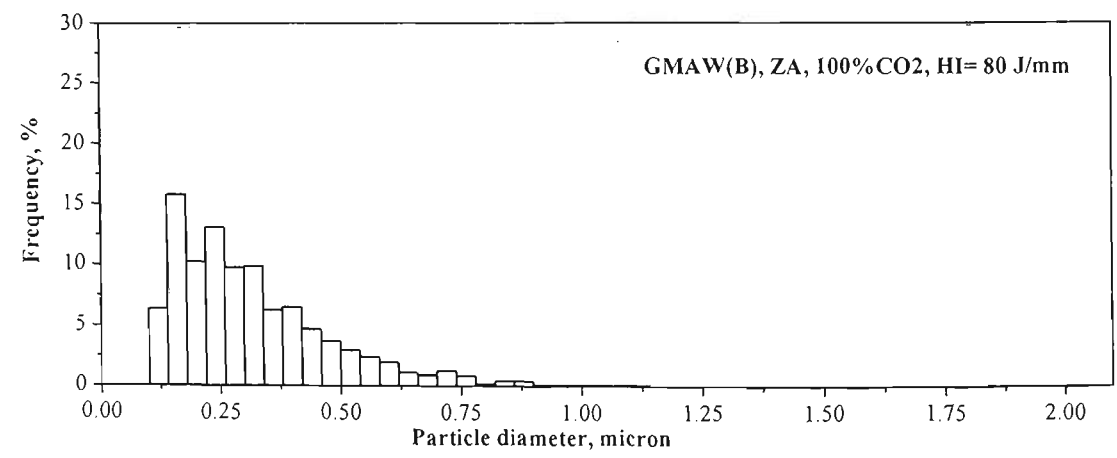

Figure 8.30 The size distribution histograms of inclusions in weld metal of GMA welded ZA sheet steel deposited with different shielding gases (at heat input of 80 J/mm).

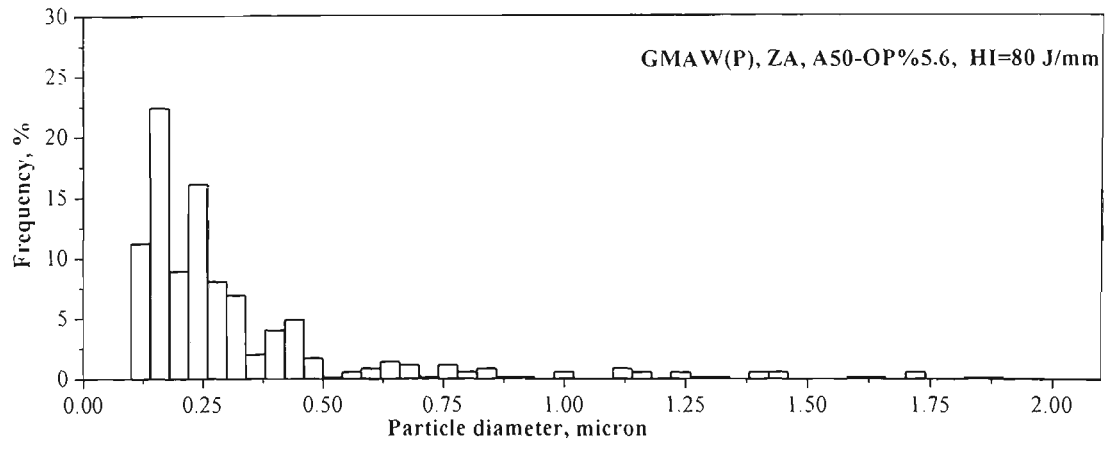

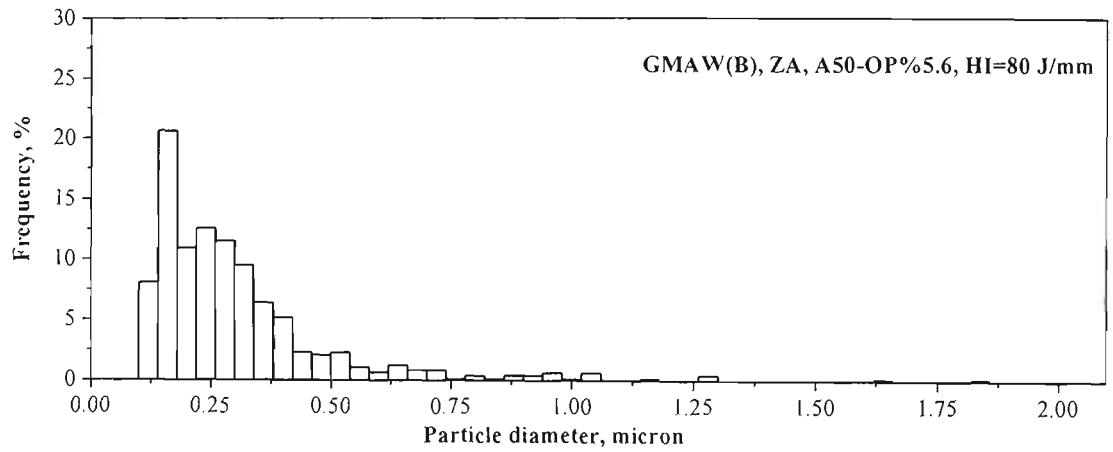

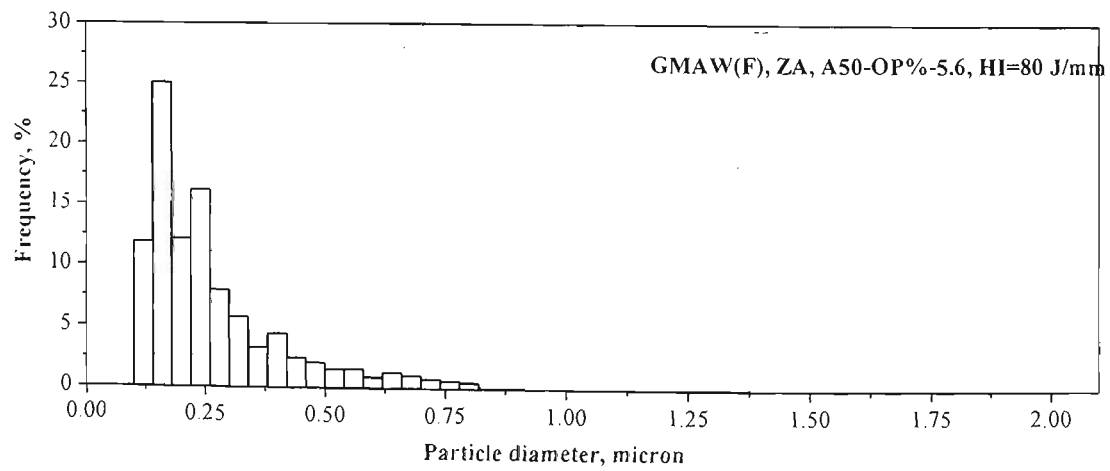

Figure 8.31 Comparison of the size distribution histograms of inclusions in weld metal of GMAW ZA using different electrode orientation.

welds and Zn welds, respectively) than those of the GMA welds (0.0051 % for both steel welds).

8.4.1.3 Effect of Zn alloy coating

It was found that for GMAW the weld metal of the Zn coated sheet had a higher volume fraction (0.2491) of non-metallic inclusions than that of the Zn-Al coated steels welds (0.1082) as shown in **Figure 8.28**. This result is consistent with the oxygen contents of these two weld metals.

8.4.1.4 Effect of electrode orientation

Typical images of non-metallic inclusions observed in the GMA ZA welds using different electrode orientations are shown in **Figure 8.29**. It was found that the perpendicular GMA welds produced a slightly higher volume fraction of inclusions (0.1133) than the backhand (0.1082) and forehand (0.1087) welds. Furthermore, the perpendicular welds had a small mean particle size (0.2198μm) compared with backhand (0.2486μm) and forehand (0.2392μm) welds.

8.4.2 Size Distribution of Non-Metallic Inclusions

To obtain representative average values at least 30 fields of $40\times40\mu m^2$ were randomly selected for the size distribution studies of the non-metallic inclusions. The results are presented in **Figure 8.30**. The 2-D size distributions are roughly the same and non-uniform with the skew towards larger particle sizes for the different shielding gases. The majority of the non-metallic inclusions are in a sub-optical microscopic size range, for example, non-metallic inclusions in the size range of 0.2~0.6μm accounted for about 50% of the total inclusion volume fraction in the GMAW Zn-Al coated steel weld metal.

Figure 8.31 shows the 2-D size distribution histograms of inclusions in the weld metal of the GMAW Zn-Al coated steels welds using different electrode orientations. It is evident that the 2-D inclusion size distribution is not significantly affected by the

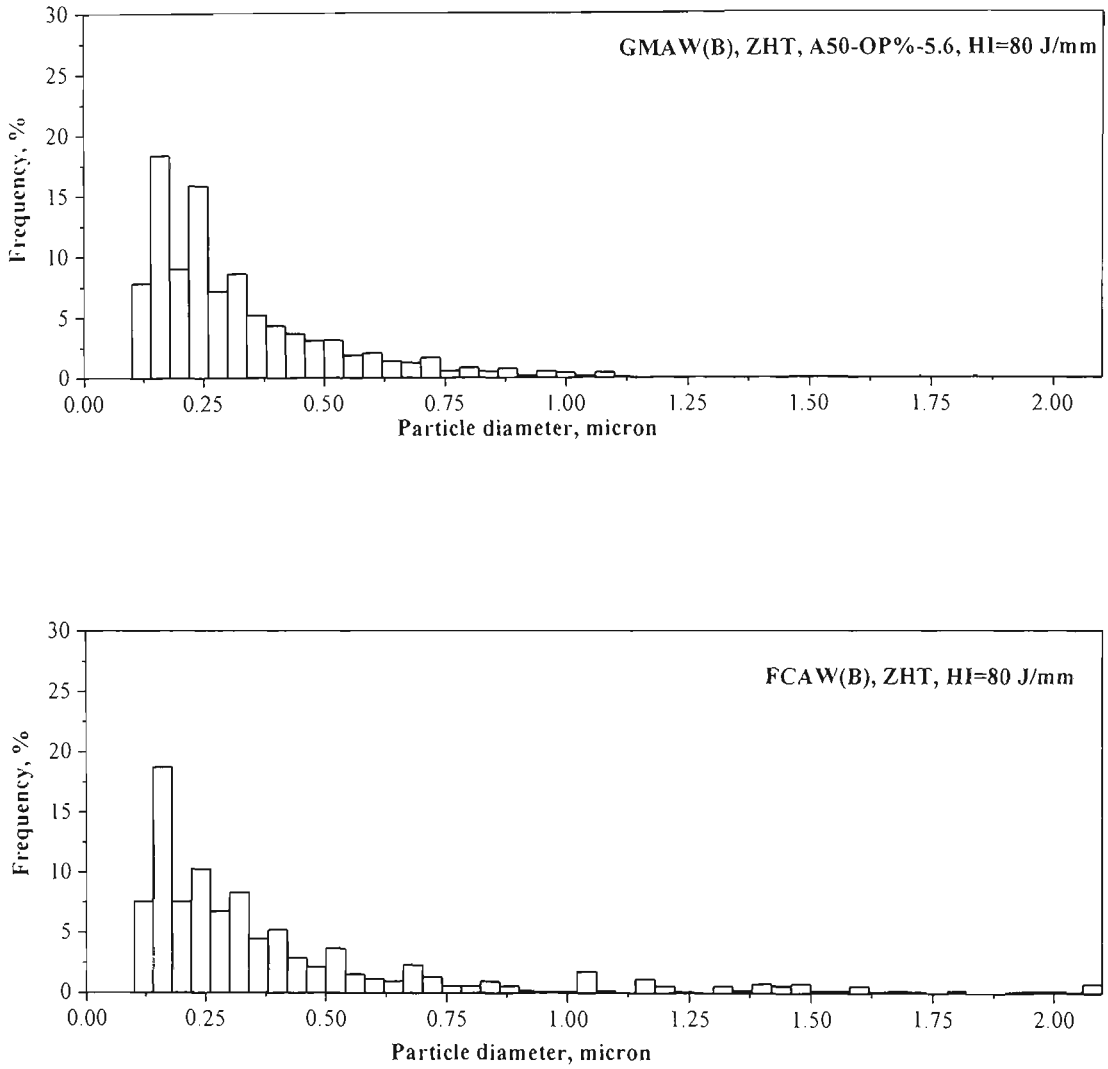

Figure 8.32 Comparison of the size distribution histograms of inclusions in weld metal of GMA and FCA welded ZA welds.

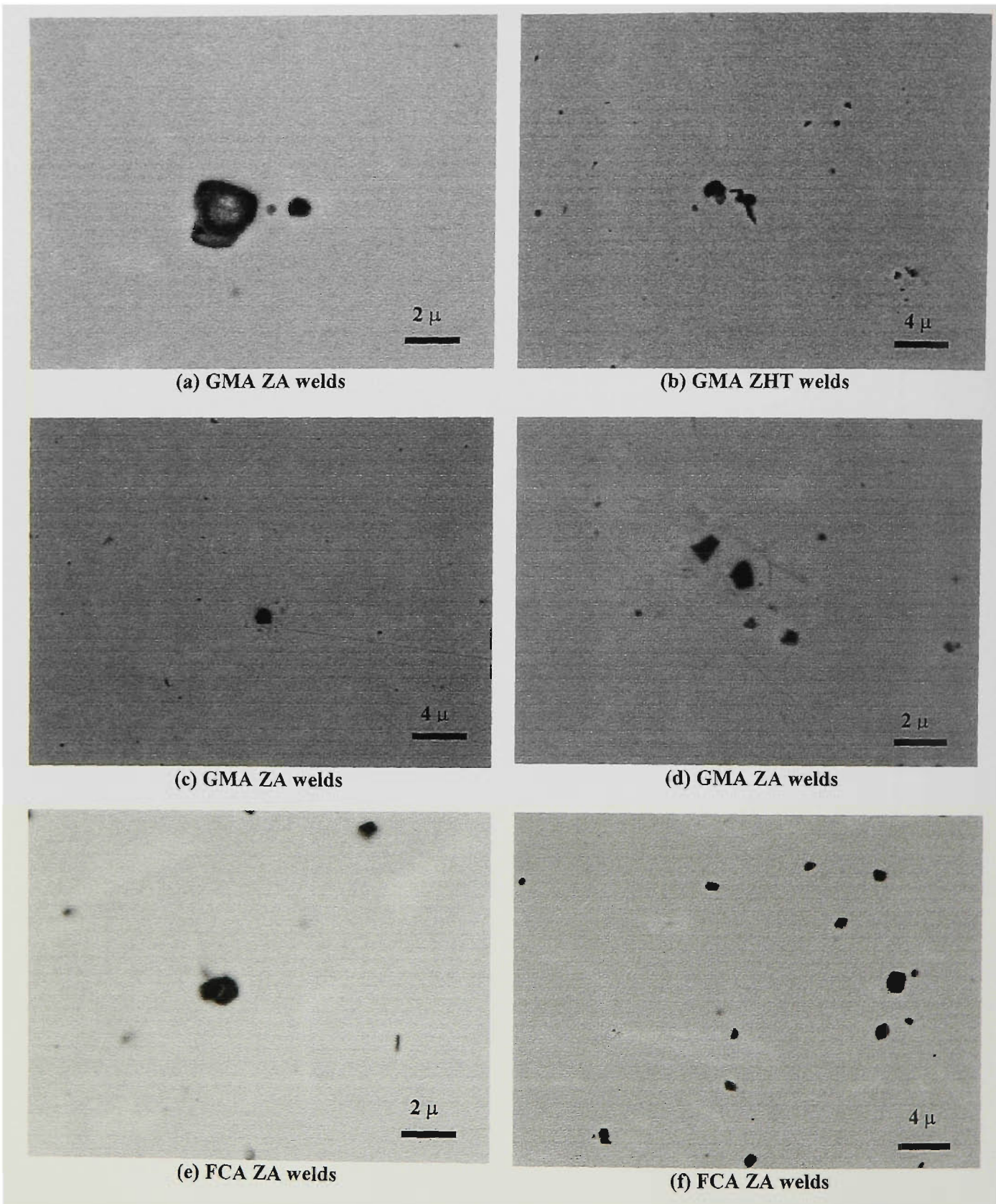

Figure 8.33 Back scattered electron micrographs of inclusions consisting of **(a)** aluminium oxides; **(b)** a manganese sulphide and silica; **(c)** and **(d)** iron carbides; **(e)** and **(f)** aluminium nitride.

Table 8.17 Welding conditions for HAZ thermal cycles measurement

Code No.	Heat Input J/mm	Voltage (Volt)	Current (Ampere)	Travel Speed (mm/min.)	W. Feed Rate (m/min.)	Tensile Strength (MPa)	Deposition Rate (g/hr.)
ZA	**(GMAW)**						
178598B	50	17	63	850	2.1	522	606
1642118B	120	17	70	420	2.6	468	728
165098B	80	16	62	500	2.1	480	597
1674140B	80	16	88	740	3.1	485	855
165092P	80	17	60	500	1.9	501	540
165092F	80	17	60	500	2.0	505	566
ZHT	**(GMAW)**						
165297B	80	17	62	520	2.0	487	567
1652122B	100	16	76	520	2.6	498	730
16104295B	100	16	159	1040	6.5	496	1019
ZA							
GMAW	60	16	43	480	2.16	510	602
FCAW	60	14	52	480	2.16	482	554

Table 8.18 Results of critical cooling times of the HAZ

ode No.	Heat input (J/mm)	T_p (°C)	Dwell 1100°C	Time 800°C	500°C	$\Delta t_{Tp/1100}$	Cooling $\Delta t_{1100/8}$	Time $\Delta t_{8/5}$	$\Delta t_{5/3}$
ZA	**(GMAW)**								
178598B	50	1331	1.04	2.28	6.49	0.48	1.09	4.04	7.46
1642118B	120	1254	1.90	4.75	12.97	1.42	1.94	7.86	13.24
165098B	80	1140	0.96	3.20	10.74	0.60	2.03	7.18	9.89
1674140B	80	1308	0.92	3.06	8.82	0.50	1.85	5.51	8.57
165092P	80	1269	0.92	2.70	8.44	0.57	1.56	5.57	14.36
165092F	80	1150	0.92	2.50	9.84	0.36	1.39	7.06	9.81
ZHT	**(GMAW)**								
165297B	80	1230	0.96	3.41	11.10	0.57	1.78	7.25	10.35
1652122B	100	1284	1.72	4.84	12.97	0.86	2.58	7.89	11.29
16104295B	100	1170	0.70	2.96	10.26	0.39	1.91	6.78	9.30
ZA									
GMAW	60	1178	0.64	1.21	6.84	0.38	1.03	4.64	7.88
FCAW	60	1291	1.0	3.26	9.0	0.50	2.02	5.57	9.18

electrode orientations and the Zn alloy coating. However the welding processes have significant influences on the 2-D inclusion size distributions, as shown in **Figure 8.32**. The FCAW produced larger sizes and higher volume fraction of inclusions than the GMAW in both the ZA and ZHT sheet steels welds (**Table 8.16**).

8.4.3 Alloying Elements in the Non-Metallic Inclusions

In the present study, SEM/EDS was employed for examining the alloying elements in the non-metallic inclusions of the weld metals. Light elements such as, O, C and N were also examined using SEM/EDS fitted with an ultra-thin widow detector. Most inclusions were manganese oxides and aluminum oxides as shown in **Figure 8.33 (a)**. Some inclusions were manganese sulphide and silica (**Figure 8.33 (b)**), iron carbides (**Figure 8.33 (c)** and **(d)**), aluminum nitride (**Figure 8.33 (e)** and **(f)**). Typical EDS spectra of the inclusions are given in **Appendix I (a)** and **(b)**.

8.5 MEASUREMENT OF HAZ THERMAL CYCLES

The microstructures and mechanical properties of the HAZ are strongly dependant on the welding thermal cycle experienced during the welding. Therefore, it is necessary to measure actual welding thermal cycles, particularly the cooling curve with determines the microstructural and its evolution of the HAZ mechanical properties.

8.5.1 Deposition Rate

The welding conditions used for the measurements of the thermal cycles are given in **Table 8.17**. The deposition rates are calculated directly from the measured wire feed rates. The deposition rate increases with increasing heat input.

In order to maintain a constant heat input the current must be increased with increasing travel speed, which in turn requires increased wire feed or deposition rate. Although a high travel speed welding reduces the joint completion time it has little effect on the ultimate tensile strength (**Table 8.17**). It is also noted expectedly that the FCAW has lower deposition rates than the GMAW welds at the same equivalent heat input.

8.5.2 HAZ Thermal Cycles

The measured thermal cycles of the HAZ under various welding conditions are shown in **Appendix II (a)** and **(b)**. Three cooling times $\Delta t_{8/5}$, $\Delta t_{8/3}$ and $\Delta t_{3/1}$ are important as the microstructural evaluation of the HAZ is governed by the $\Delta t_{8/5}$; recrystallisation and recovery of the deformed sheet steel is controlled by the $\Delta t_{8/3}$; and hydrogen effusion depends strongly on the $\Delta t_{8/1}$. However, in this work, only the cooling times $\Delta t_{8/5}$, $\Delta t_{8/3}$ were determined as the hydrogen concatenation is not a concern of this study. **Table 8.18** shows the critical cooling times and the dwell times, the former were determined from the measurements of the actual thermal cycles of each HAZ and the latter were determined from the measurements of the predicted thermal cycles at the peak temperature of 1350°C.

8.5.3 Prediction of Thermal Cycle for 1350 °C Peak Temperature

To compare the thermal responses for different welding conditions, thermal cycle based on the same peak temperature need to be compared. Practical measurements close to the fusion boundary were unsuccessful because of the uncertainties in the weld pool position and shape and the thermocouple position. Consequently, the thermal response at the same peak temperature was obtained by interpolating or extrapolating, assuming a linear relationship existed in the heating curve of the thermal cycles due to the rapid heating rate of the arc welding. The interpolation of the thermal responses are based on the assumption that the peak temperature of 1350°C sits between the two highest temperature readings lower than but close to 1350°C.

Since the responses can be very sharply peaked, the natural logarithms of the readings were extracted [Ahmed and Jarvis 1998]. These were then aligned by offsetting the time base of one with respect to the other until the correlation between them was a maximum. This was determined numerically and the process assuming a linear transformation from one response to the other. The following equation is obtained by linear interpolation:

$$\ln(t_3) = \ln(t_1) + k\,(\ln(t_2) - \ln(t_1))$$

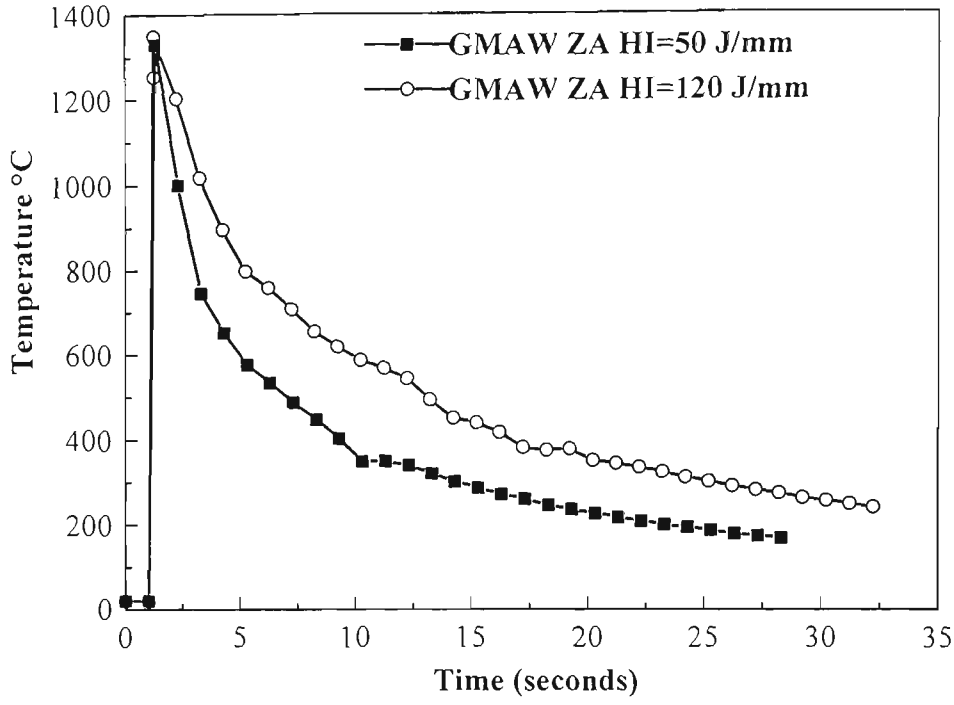

(a)

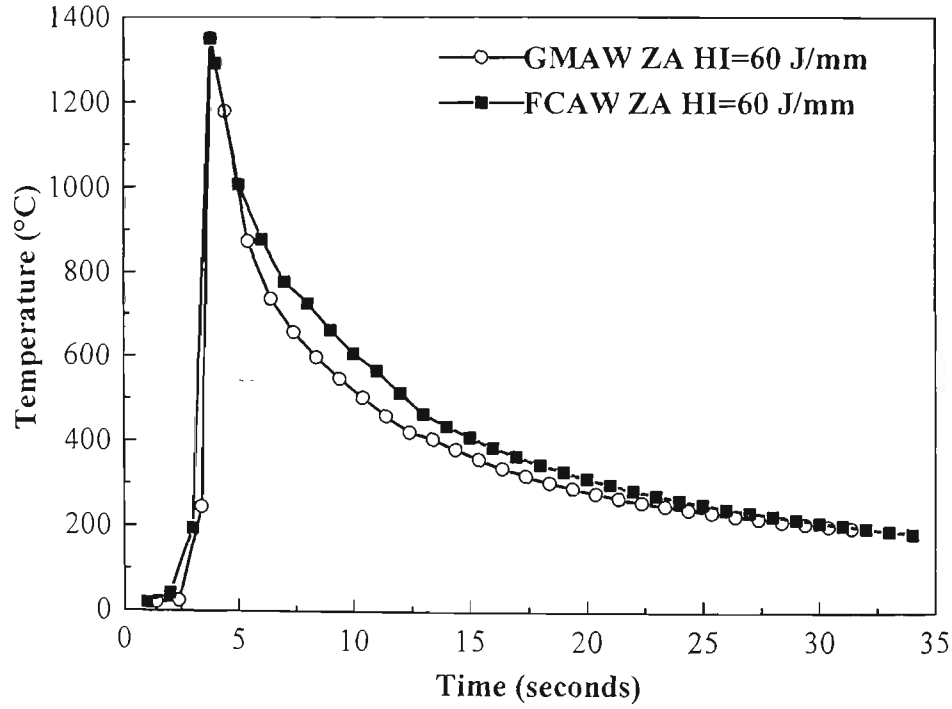

(b)

Figure 8.34 Extrapolated responses to **(a)** GMAW ZA welds at the heat inputs of 50 J/mm and 120 J/mm; **(b)** GMAW and FCAW ZA welds at heat input of 60 J/mm for a peak temperature of 1350 °C.

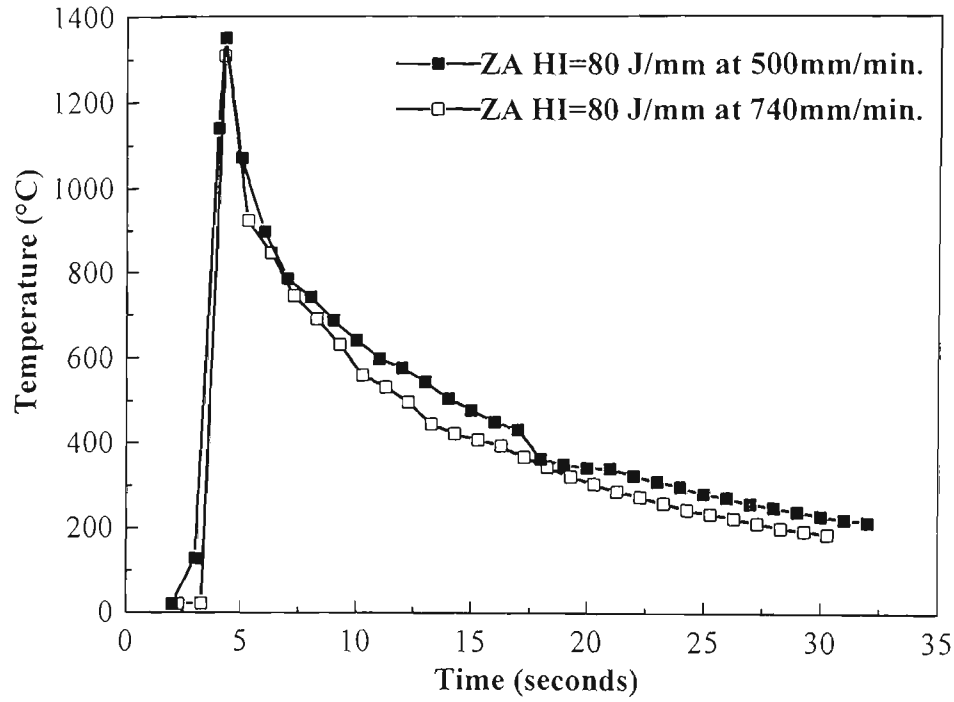

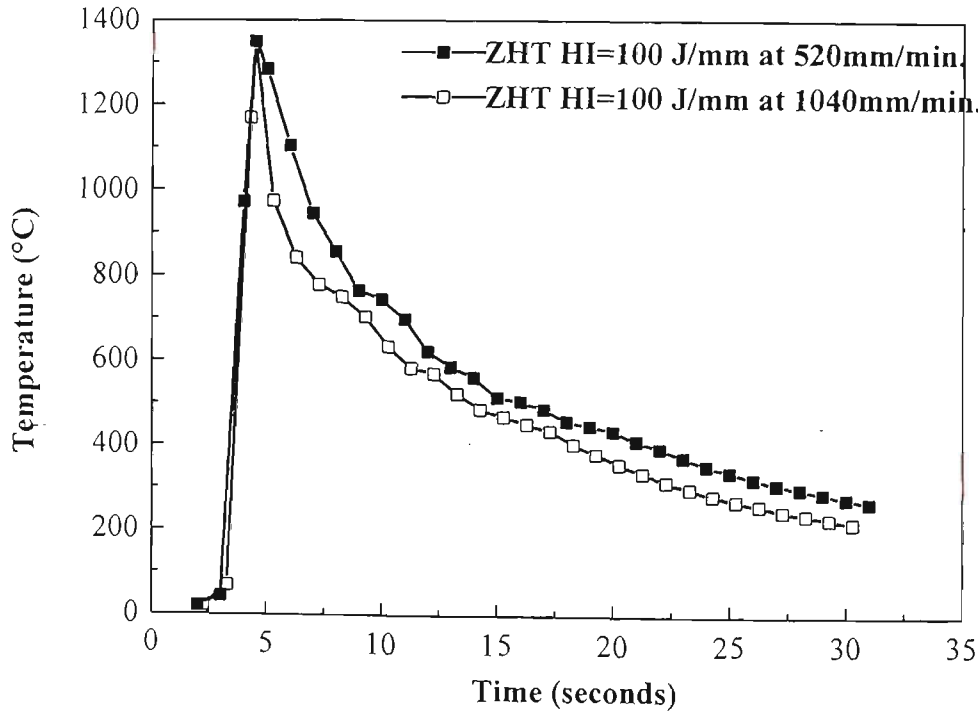

Figure 8.35 Extrapolated responses to GMA welded ZA and ZHT steels at different travel speeds for the peak temperature of 1350 °C.

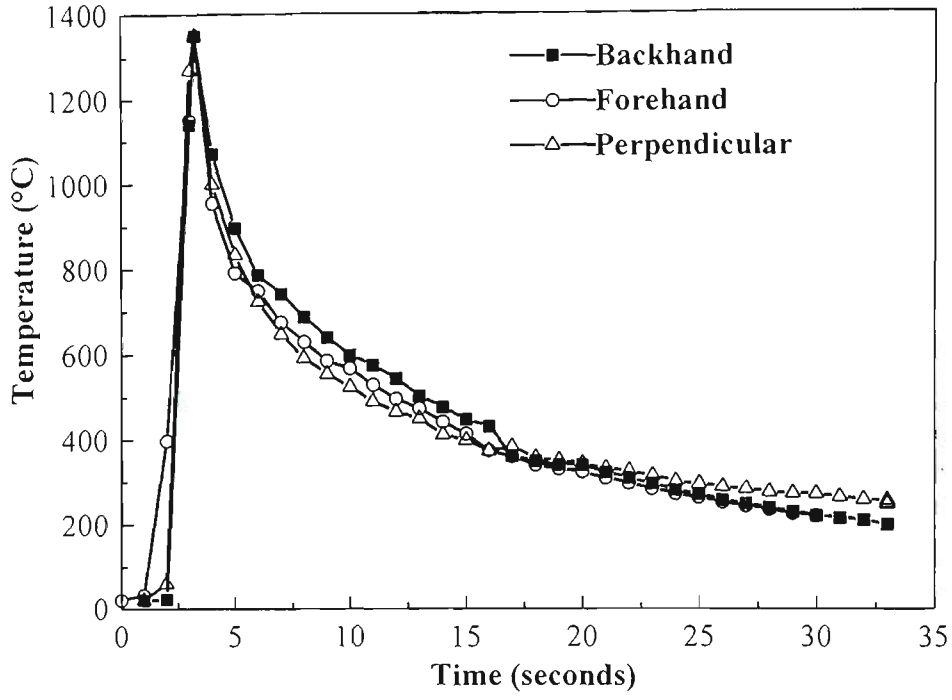

(a)

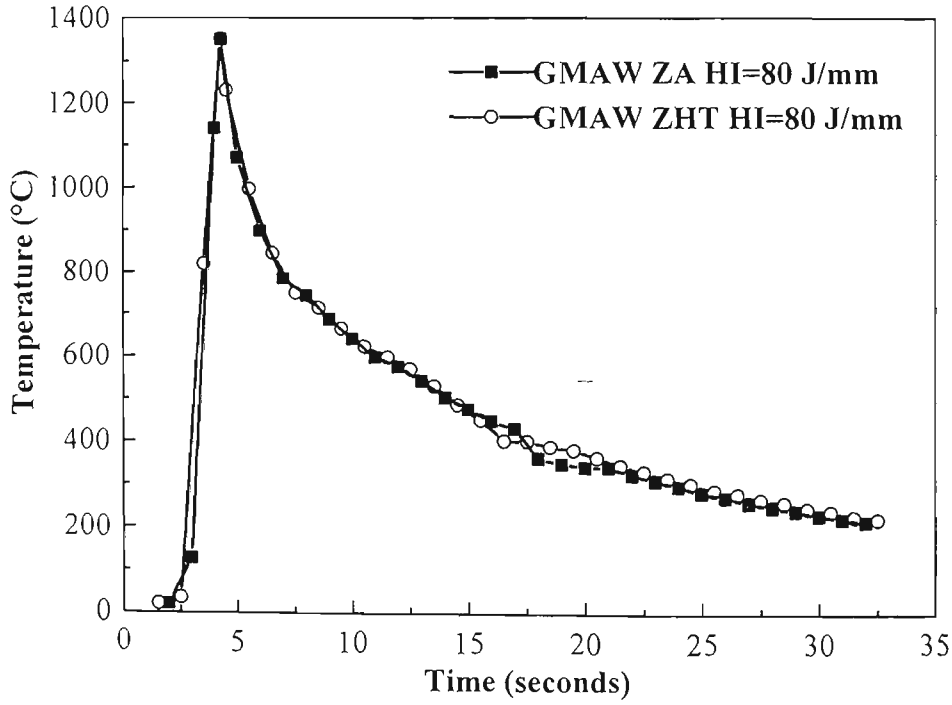

(b)

Figure 8.36 Extrapolated responses to **(a)** the different electrode orientation for GMAW ZA welds at the peak temperature of 1350 °C; **(b)** the GMAW ZA and ZHT welds at the peak temperature of 1350 °C.

where **k** is an arbitrary constant. The t_1, t_2 are the times related the temperatures selected and t_3 is the time related to the peak temperature 1350°C. The actual response is the exponential of this:

$$t_3 = \exp(\ln(t_1) + k\,(\ln(t_2) - \ln(t_1))$$

The value of **k** was obtained by numerical solution for the desired peak temperature of t_3.

The extrapolation method of determining thermal responses at a certain peak temperature T_p uses the extension of a heating curve graphically and estimates the **Tp**-time point. The graphically determined thermal responses are used in this work, and the actual thermal responses closest to the peak temperature of 1350°C were chosen for the prediction of the thermal responses in order to minimize error.

The extrapolated thermal responses to the GMA and FCA welded Zn-Al coated steels at the heat inputs of 50 J/mm, 60 J/mm and 120 J/mm are shown in **Figure 8.34**. It is an evident that the change in the heat input from 50 J/mm to 120 J/mm influences the cooling time $\Delta t_{8/5}$ (from 4.04 to 7.86 seconds) significantly. The cooling time $\Delta t_{8/5}$ is considered directly proportional to heat input [Easterling 1992]. A higher heat input correlates with a larger value of $\Delta t_{8/5}$ and a lower cooling rate. As expected, the heat input of 120 J/mm results in a lower average cooling rate than the 50 J/mm heat input. It also clearly shows that the FCAW produces a longer cooling time ($\Delta t_{8/5}$ =5.57 seconds) than the GMAW welds ($\Delta t_{8/5}$ = 4.64 seconds) at the same nominal heat input of 60 J/mm.

Figure 8.35 shows the extrapolated thermal responses of the ZA and ZHT welds at different travel speeds. The results are consistent with other published work [Ahmed and Jarvis 1998]. At a constant heat input, increasing travel speed reduces the cooling time. For the Zn-Al coated steel welds the increase of speed from 500 to 740 mm/min reduced the cooling time $\Delta t_{8/5}$ from 7.86 to 5.51 seconds. A similar result has also been obtained for the Zn coated steel welds. **Figure 8.36** illustrates the extrapolated thermal

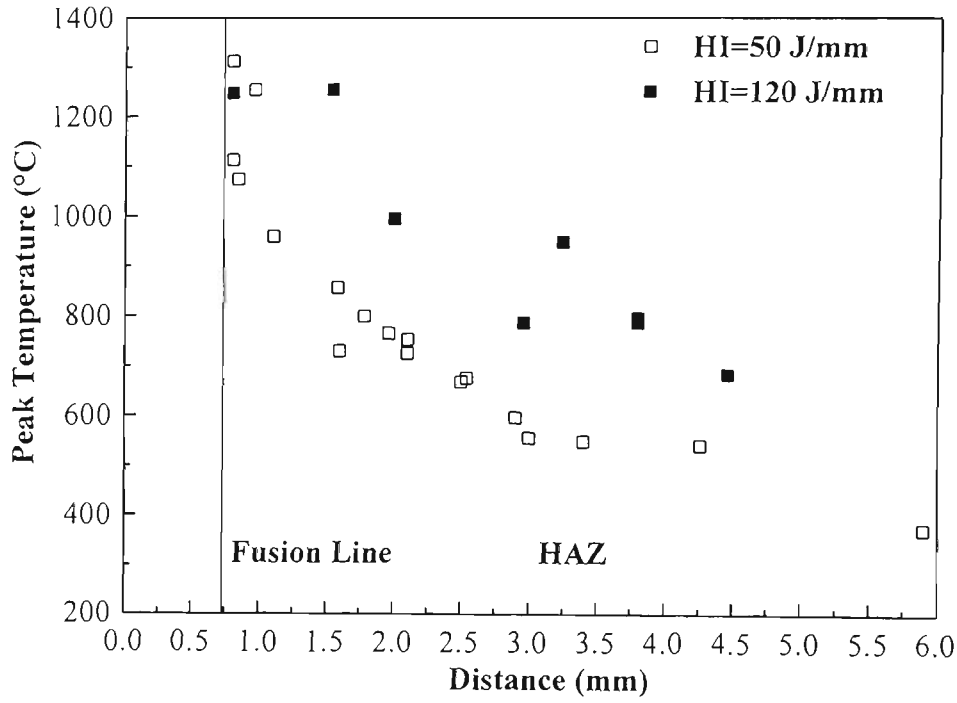

Figure 8.37 Peak temperature as a function of the HAZ depth for GMA welds of ZA steels at different heat input.

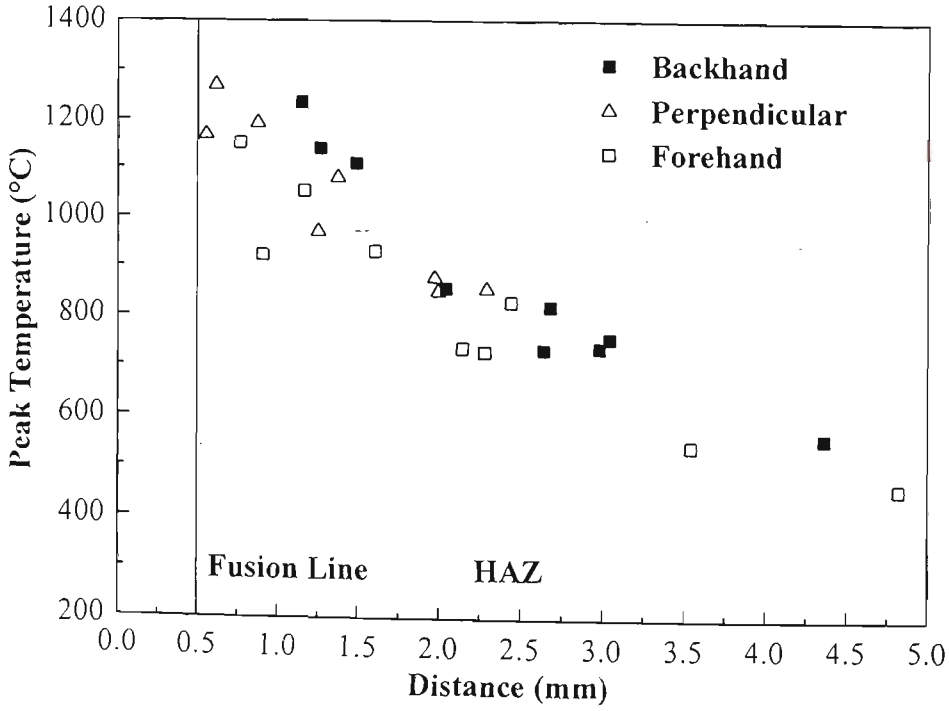

Figure 8.38 Peak temperatures as a function of the HAZ depth for GMAW ZA welds at the heat input of 80 J/mm with different electrode orientation.

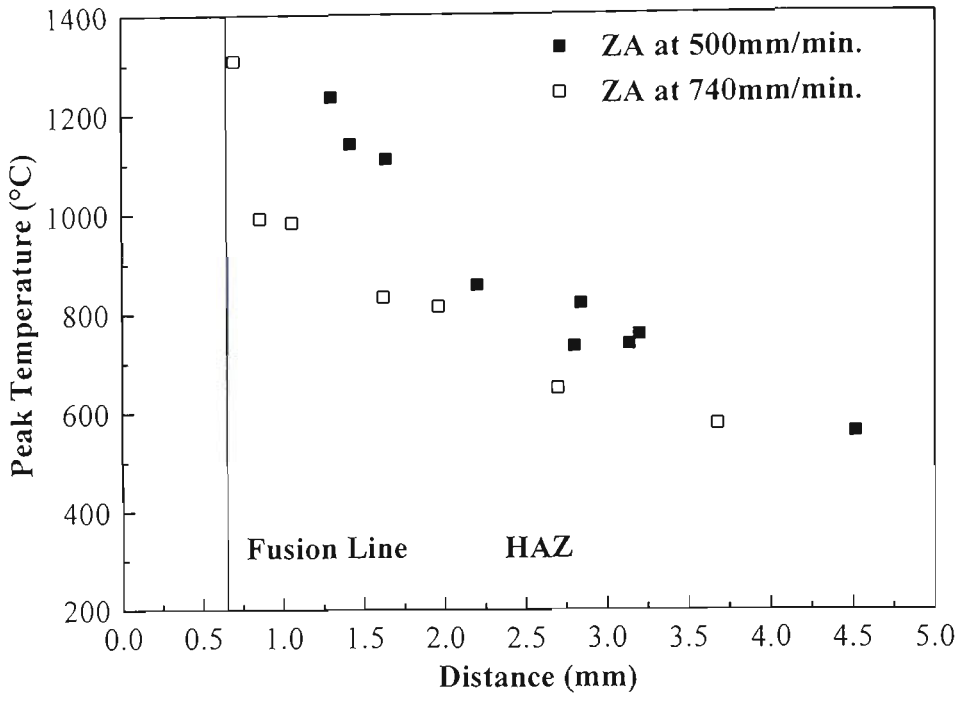

(a)

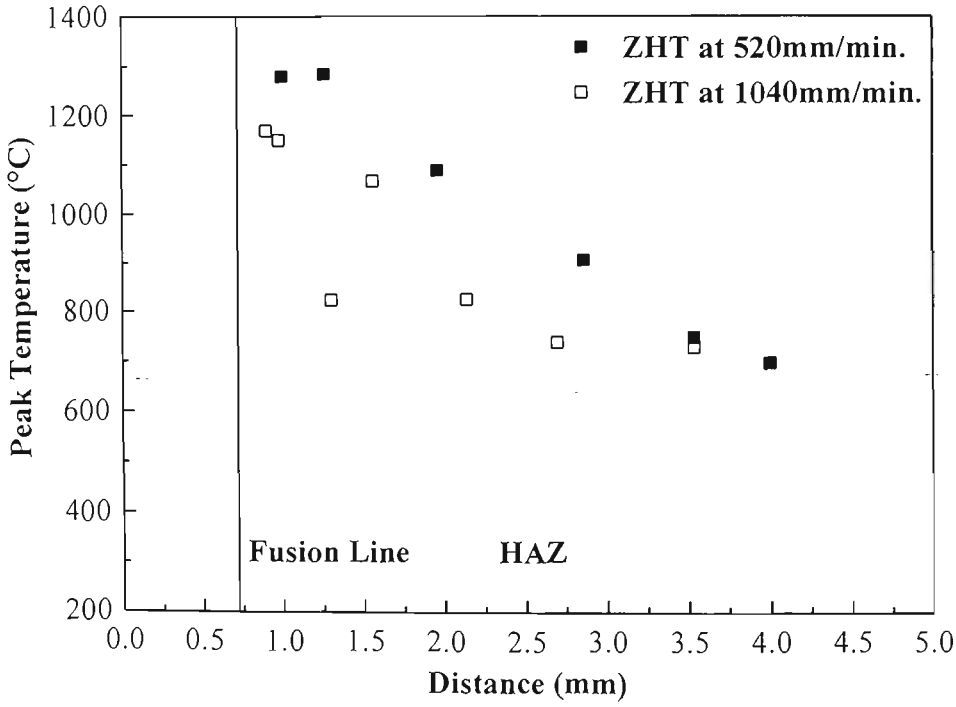

(b)

Figure 8.39 Peak temperature as a function of HAZ depth for GMAW **(a)** ZA welds at the heat input of 80 J/mm at different travel speeds; and **(b)** ZHT welds at the heat input of 100 J/mm at different travel speeds.

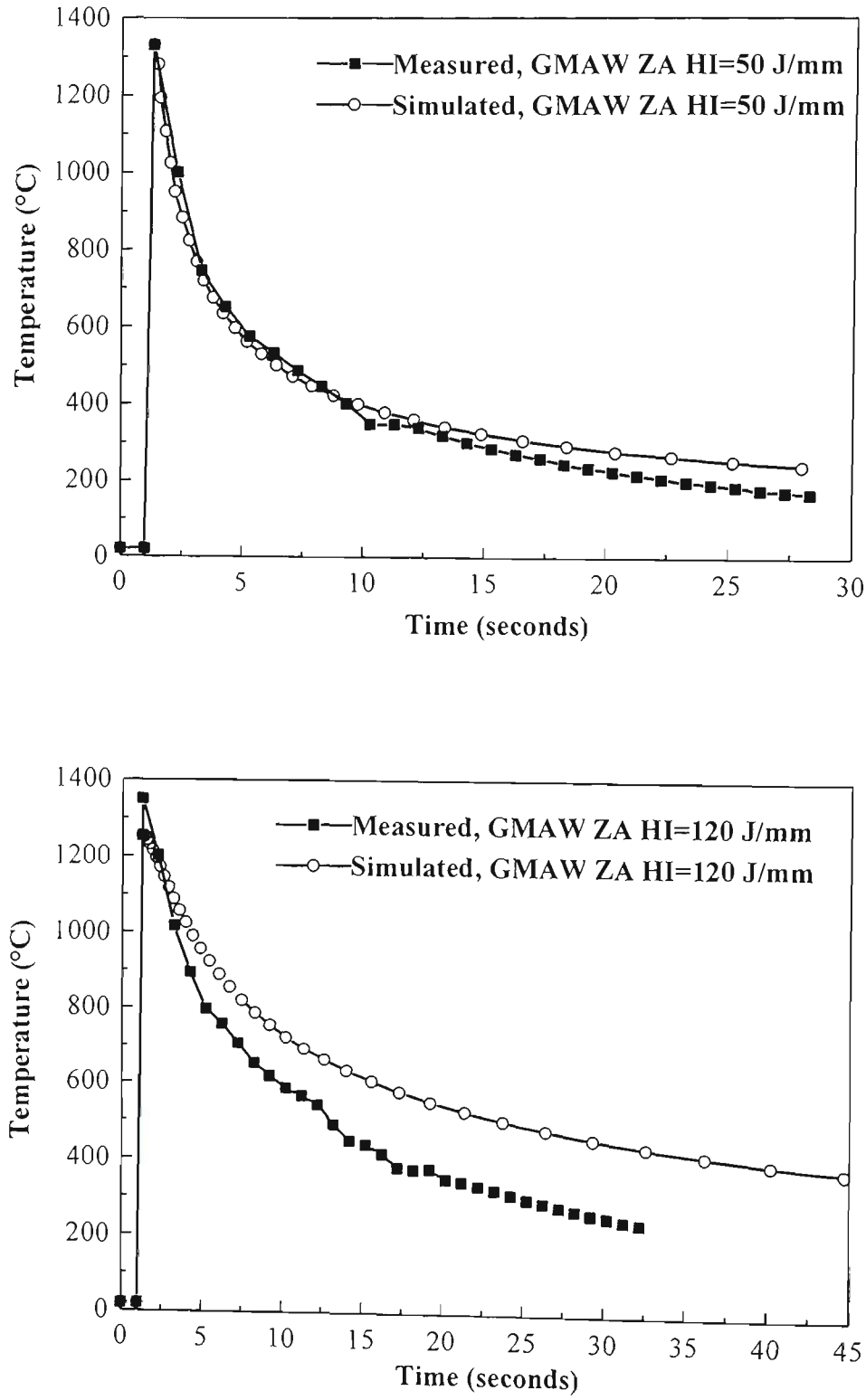

Figure 8.40 Comparison of thermal cycles between the measured real welds and predicted by Rykalin-2D at heat input of 50 J/mm **(a)** and 120 J/mm **(b)**.

responses to the different electrode orientations for the Zn-Al coated steel welds and Zn coated steel welds. It can be seen that the backhand welding gives a longer cooling time than the perpendicular and forehand electrode orientations. However, the Zn or Zn-Al coating has little effect on the thermal cycles and cooling times.

8.5.4 Effect of Welding Conditions on Peak Temperature of Thermal Cycles

From the thermocouple outputs, the peak temperature reacted as a function of distance from the fusion boundary was determined. **Figure 8.37** shows the peak temperature as a function of the HAZ distance for the GMAW Zn-Al coated steel welds at the heat inputs of 50 J/mm and 120 J/mm. It clearly shows that the high heat input pushes the peak temperature curve away from the fusion line. Because of this, a larger HAZ width and a coarser grain size in the grain-coarsened region are expected for the heat input of 120 J/mm GMAW welds.

It was also found that the electrode orientation has little effect on the HAZ peak temperature curve (**Figure 8.38**). However, the HAZ peak temperature with backhand welding is in the top band of peak temperatures. The effect of the travel speed on the HAZ peak temperature is shown in **Figure 8.39**. The high travel speeds of 740 mm/min. and 1040 mm/min. for GMAW of the ZA and the ZHT steels respectively, pushed the peak temperature curve of the HAZ towards to the fusion line. This results in the reduction of the HAZ width (**Table 8.7**).

8.5.5 Comparison of Measured and Predicted Thermal Cycles

Generally, the heat input per unit length is taken as a dominant factor in controlling the cooling rate of a weld. The Rykalin-2D model [Rykalin 1951] from the HAZ Programming software of QuikSim for the Windows Gleeble programming environment was used to predict the thermal cycles for these particular thin sheet steel welds. **Figure 8.40** shows comparisons of the measured and predicted thermal cycles for a HAZ region reaching a peak temperature of 1350°C using the Rykalin-2D model at heat inputs of 50 J/mm and 120 J/mm. It is clearly shown that the calculated thermal cycle at the heat input of 50 J/mm agrees fairly well with the measured thermal cycle.

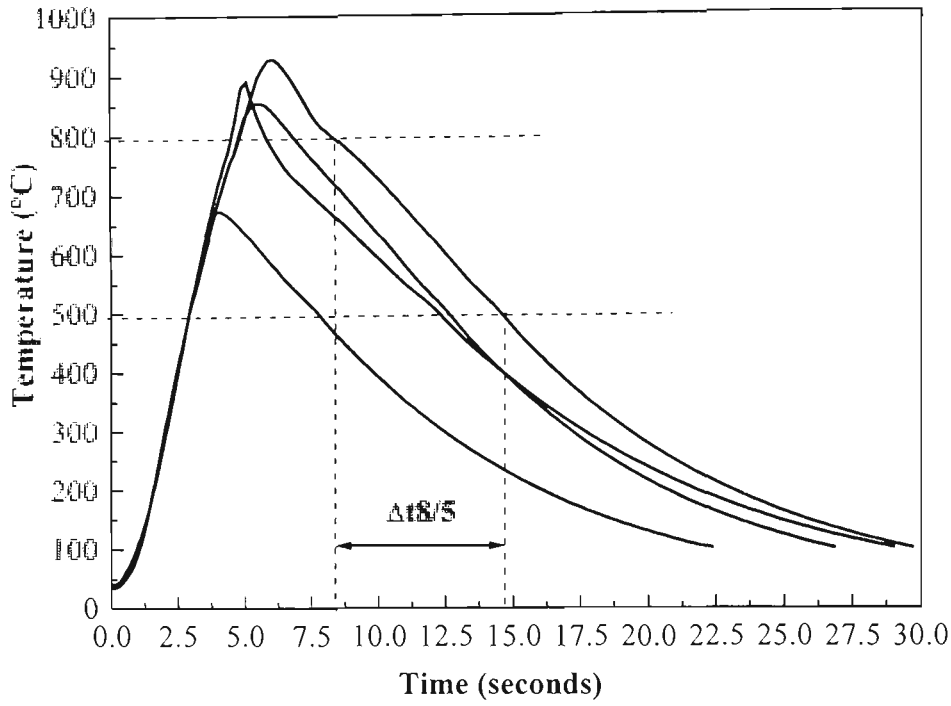

Figure 8.41 Thermal cycles for the simulated samples. The horizontal dashed line is the average $\Delta t_{8/5}$ for the simulated samples.

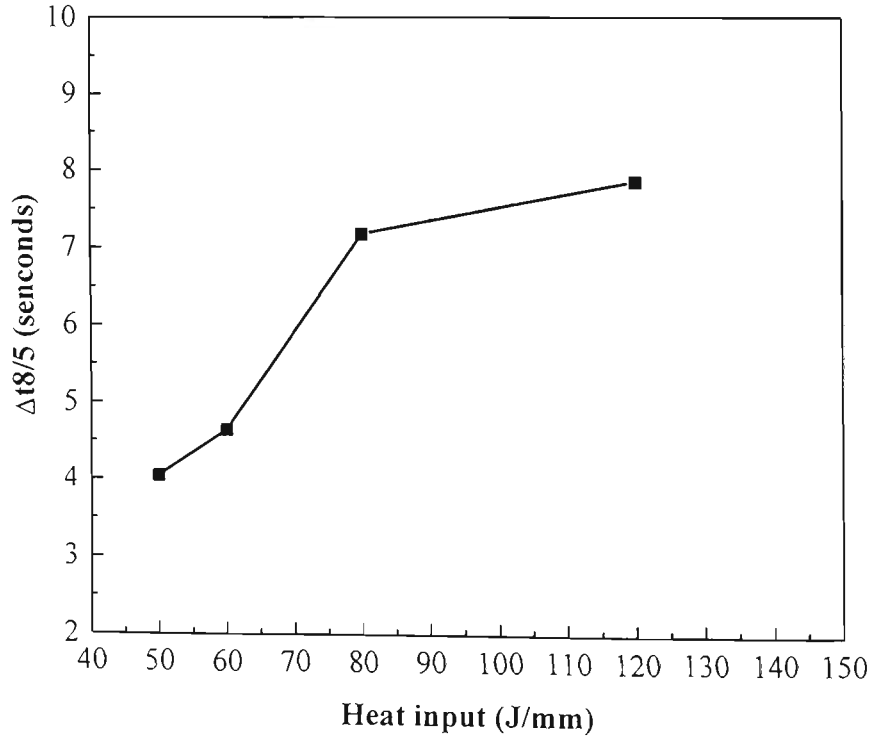

Figure 8.42 Cooling time $\Delta t_{8/5}$ as a function of the heat input for the actual GMAW ZA welds.

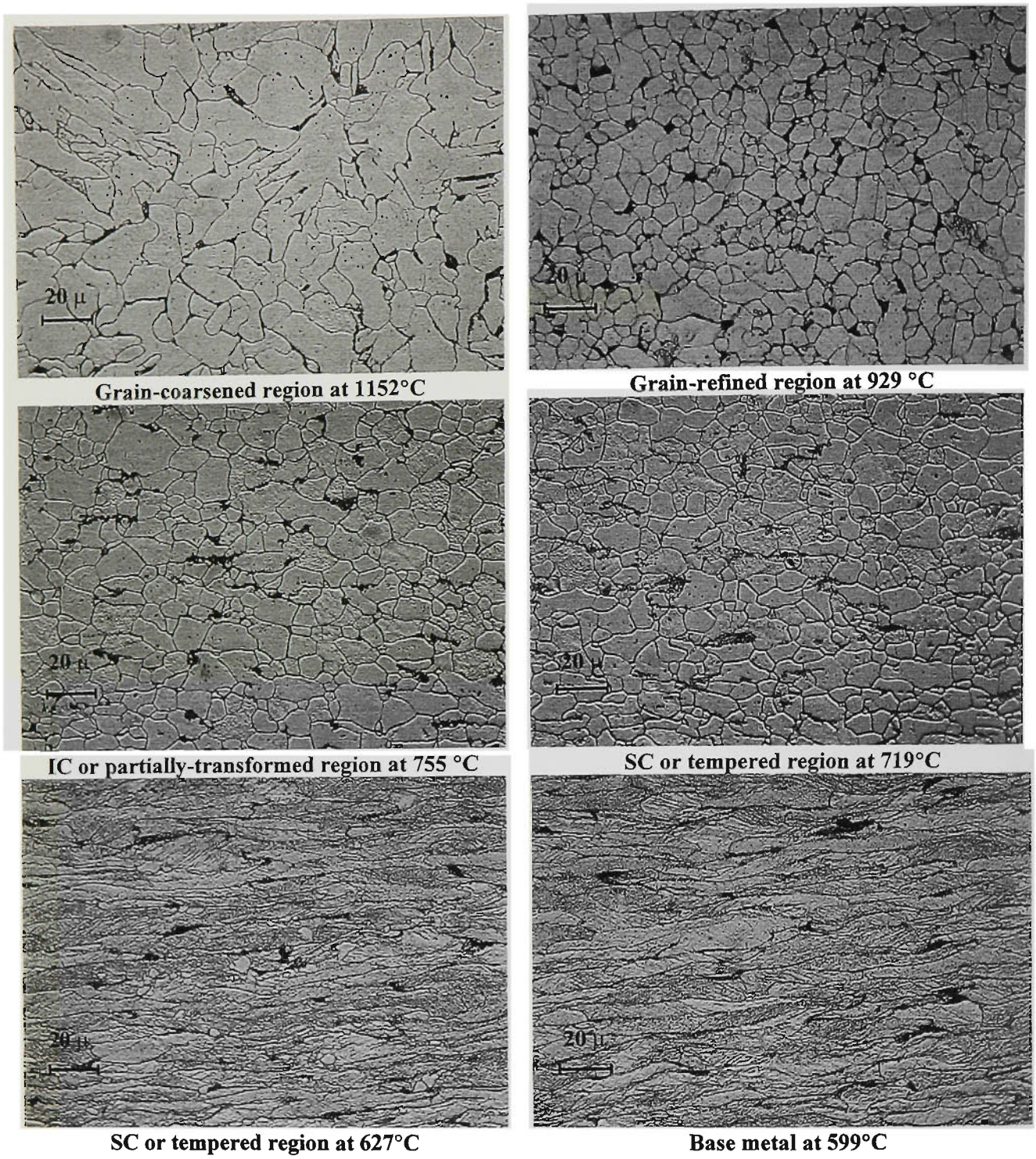

Figure 8.43 Optical micrographs showing the simulated microstructures of sub-zones of HAZ.

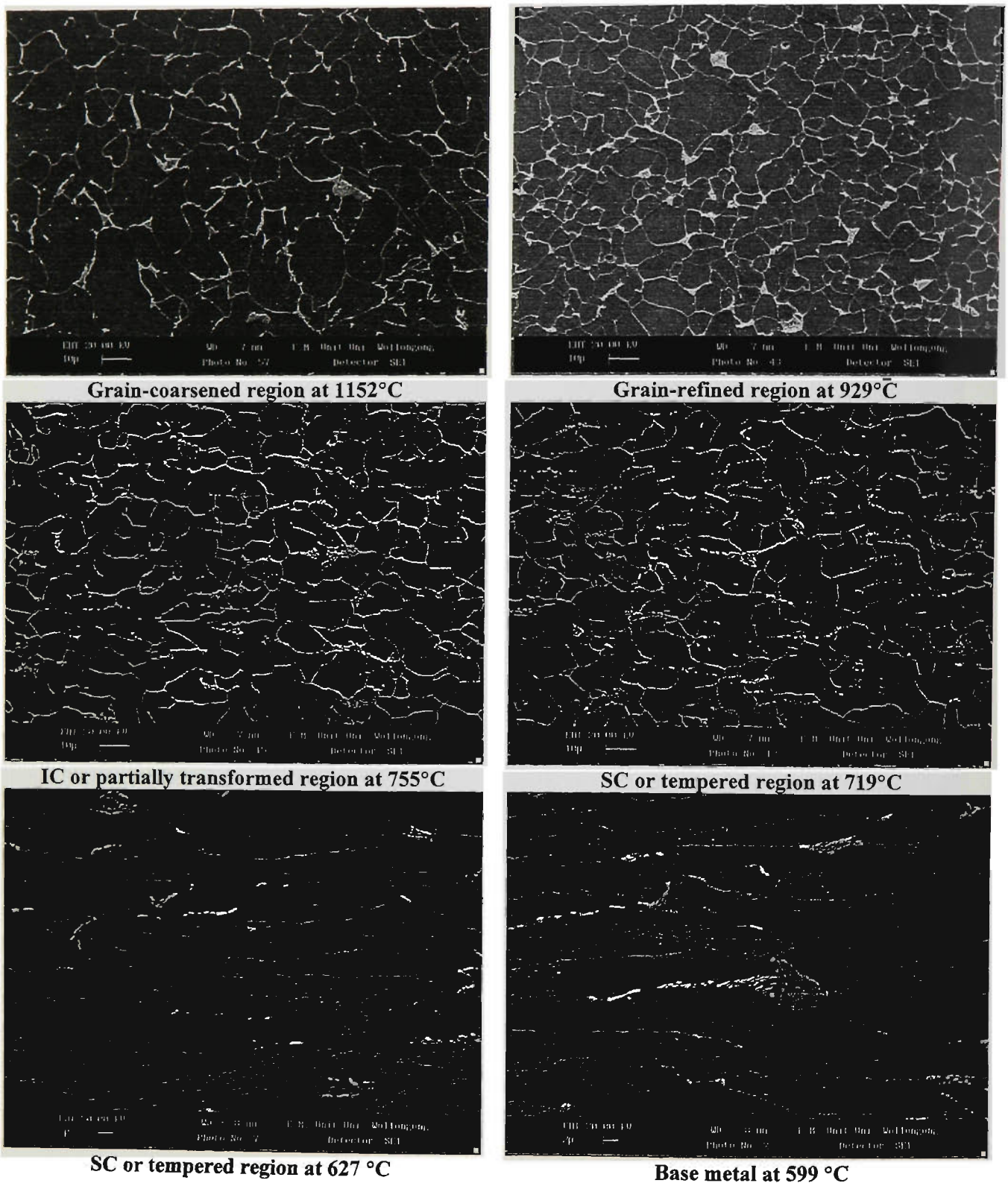

Figure 8.44 SEM micrographs showing the simulated microstructures of sub-zones of HAZ. (Arrow indicates a small recrystallisation grains).

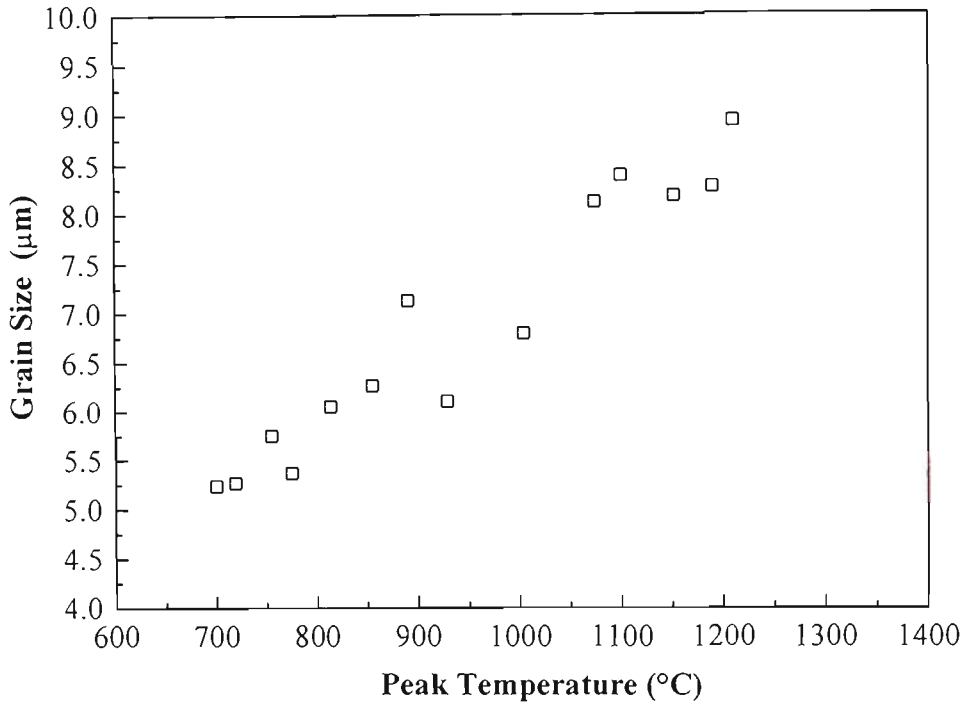

Figure 8.45 Ferrite grain size of the simulated HAZ as a function of the peak temperature

Table 8.19 Results of cooling times of actual measured thermal cycles and predicted thermal cycles by Rykalin-2D calculation

Code No.	HI (kJ/mm)	Tp (°C)	$\Delta t_{P/11}$&(Predicted)	$\Delta t_{11/8}$&(Predicted)	$\Delta t_{8/5}$&(Predicted)	$\Delta t_{5/3}$&(Predicted)
ZA (GMAW)						
178598B	0.05	1331	0.48 (0.36)	1.09 (1.03)	4.04 (3.52)	7.46 (10.98)
1642118B	0.12	1254	1.42 (1.18)	2.25 (4.64)	7.86 (15.92)	13.24 (49.98)
165098B	0.08	1140	0.60 (0.19)	2.03 (2.45)	7.18 (8.40)	9.89 (26.22)
1674140B	0.08	1308	0.50 (0.72)	1.85 (2.22)	5.51 (7.63)	8.57 (23.81)
165092P	0.08	1269	0.57 (0.64)	1.56 (2.34)	5.57 (8.01)	14.36 (25.00)
165092F	0.08	1150	0.36 (0.01)	1.39 (2.39)	7.06 (8.21)	9.81 (25.61)
ZHT (GMAW)						
165297B	0.08	1230	0.57 (0.51)	1.78 (2.28)	7.25 (7.82)	10.35 (24.40)
1652122B	0.10	1284	0.86 (1.00)	2.58 (3.39)	7.89 (11.63)	11.29 (36.29)
16104295B	0.10	1170	0.39 (0.46)	1.91 (3.60)	6.78 (12.34)	9.30 (38.50)
ZA						
GMAW	0.06	1178	0.38 (0.19)	1.03 (1.30)	4.64 (4.47)	7.88 (13.95)
FCAW	0.06	1291	0.50 (0.45)	2.02 (1.48)	5.57 (5.07)	9.18 (15.81)

However, at the higher heat input of 120 J/mm the calculated thermal cycle shows a lower cooling rate than that measured (**Table 8.19**).

8.6 SIMULATED HEAT AFFECTED ZONE

8.6.1 Simulated HAZ Thermal Cycles

HAZ simulations were carried out by using electric resistance heating equipment. The heating rate was about 200°C/S, the maximum heating rate that could be achieved. Compared to the actual arc welding heating rate (in between 500 to 1000°C/S), the simulated heating rate is much slower. Eighteen peak temperatures between 599°C and 1210°C were obtained during the simulation. Some of the thermal cycles of the simulated HAZ samples are shown in **Figure 8.41**. As expected for real welds the cooling time $\Delta t_{8/5}$ is a function of the heat input (**Figure 8.42**). For the peak temperature of 924 °C the $\Delta t_{8/5}$ is about 6.4 seconds, so is the real welds at the heat input of 70 J/mm. The tensile strength of the real welds at the heat input of 70 J/mm was between 490 and 500 MPa (**Figure 8.1**).

8.6.2 Microstructure of the Simulated HAZ

The microstructures of the various HAZ regions were simulated by applying single thermal cycles with different peak temperatures (600-1200°C) to the base steel. Prior to the simulations the Zn-Al coating was taken off using hydrochloric acid to avoid contamination of the furnace. **Figure 8.43** shows the simulated microstructures of the sub-zones of HAZ, which match well with the microstructure of the actual HAZ (**Figure 8.15**). The scanning electron micrographs of the simulated HAZ are shown in **Figure 8.44**. The starting temperature for metallurgically recrystallisation of ZA G550 1.0mm sheet steels was determined to be approximately at 600°C (**Figure 8.44**).

A plot of the average grain size of the simulated HAZ against the peak temperatures is shown in **Figure 8.45**. It is clearly shown that the grain size of the simulated HAZ is proportional to the peak temperature of the thermal cycles. The grain size reduction

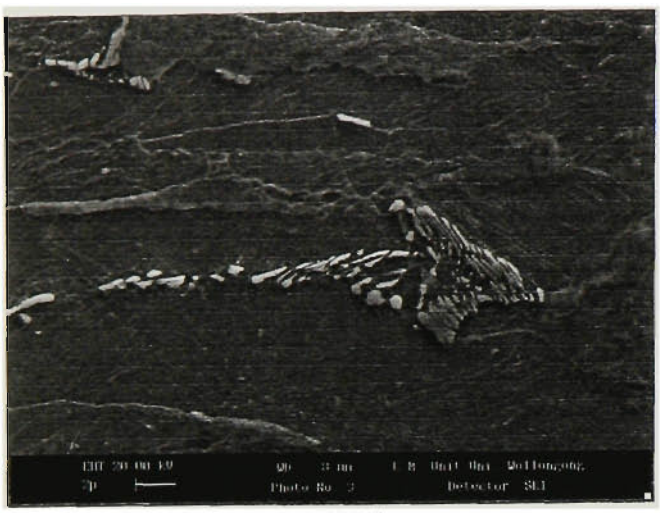

at 599°C

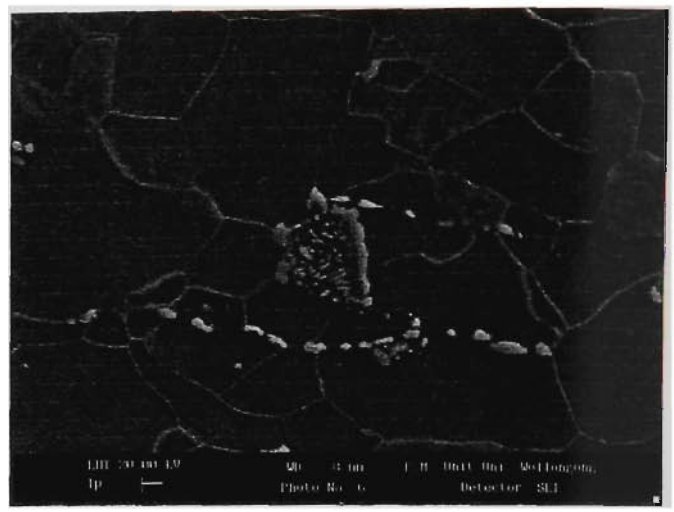

at 700°C

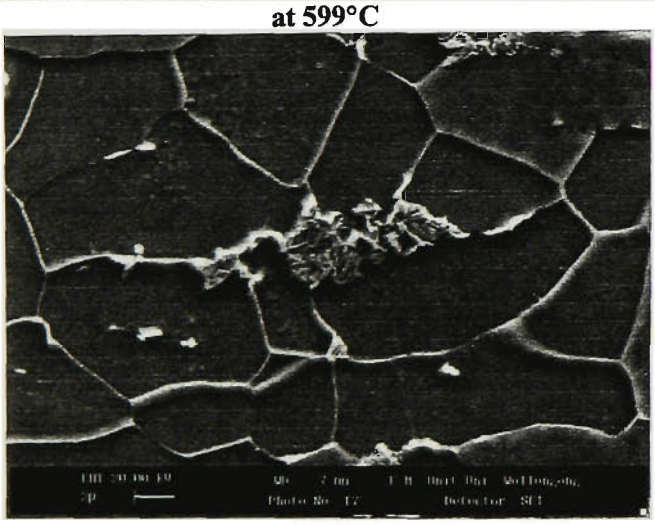

at 755°C

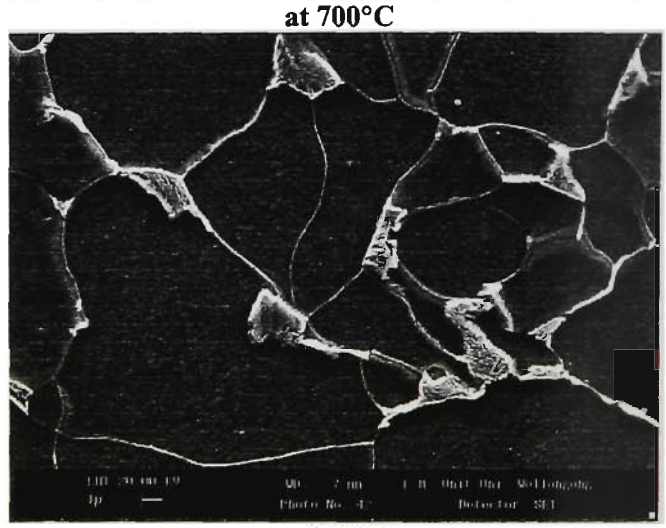

at 890°C

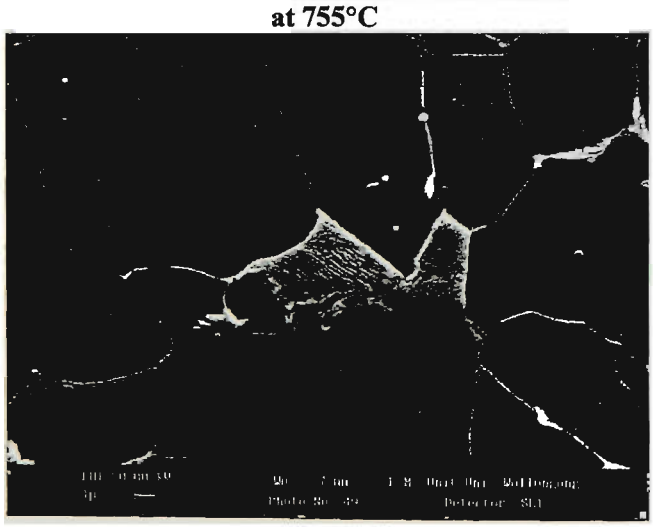

at 1004°C

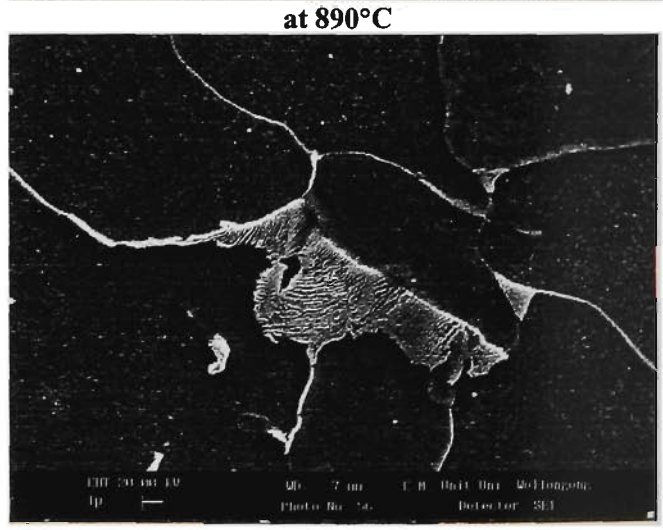

at 1152°C

Figure 8.46 SEM micrographs of pearlite features of simulated samples at temperatures between 599°C and 1152°C.

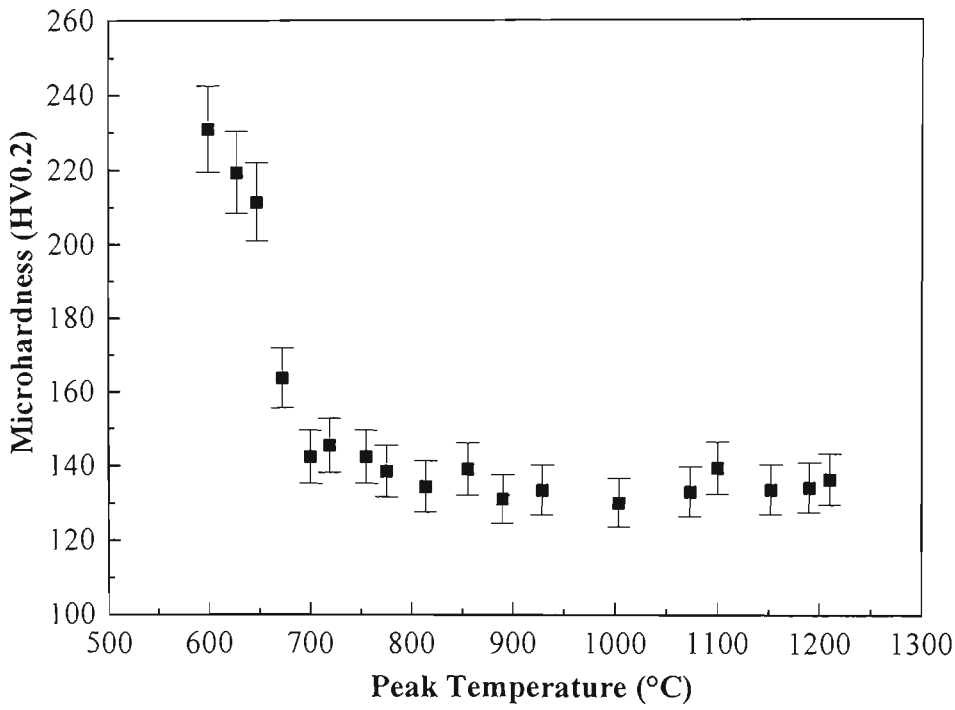

Figure 8.47 Microhardness of the simulated HAZ as a function of peak temperatures.

from 7.12μm to 6.10μm for peak temperatures of 890°C to 929°C is due to complete re-austenisation, then retransformation to ferrite on cooling.

The morphologies of the pearlite of the simulated samples are shown in **Figure 8.46**. It is noticed that at 700°C, the pearlite consists of rods and spheroids of cementite dispersed in the ferrite matrix. The morphology of the pearlite changes from coarse plates or spheroids to fine plates from 599 to 1152°C. The abrupt change of the pearlite morphology occurs at temperature above 755°C and thus the actual start of re-austenisation occur at about 755°C, 32°C higher than the equilibrium $\alpha \rightarrow \gamma$ temperature of 723°C due to the fast heating rates.

8.6.3 Mechanical Properties of Simulated HAZ

Figure 8.47 shows the microhardness of the simulated HAZ as a function of the peak temperature. The value peaks at near 600°C in the **Figure 8.47** is the hardness value of the base metal since any recovery to a polygonised sub-grain structure would not substantially change the dislocation density. In the tempered region of 600°C to 750°C, the hardness value dropped sharply resulting from recrystallisation and grain growth. The minimum hardness ($HV_{0.2} \cong 135$) occurred in the partially transformed region (750°C to 900°C) and in the grain refined region (900°C to 1100°C). The grain size at a peak temperature of 1210 °C was about 8.93μm (**Figure 8.45**), which is larger than the average grain size of the grain-refined region.

Table 8.20 summarises the average tensile strength, yield strength and elongation of grain-refined region of the HAZ simulated samples. The tensile strength and yield strength in the grain-refined region (900°C to 1100°C) are dependant of the microstructure and independent of the peak temperature of the thermal cycles. It is also noticed that the highest elongation of 34.5% was obtained from the sample experiencing a 1020°C peak temperature. Compared to the actual welds, the tensile strength of 410 MPa of the simulated sample is much lower than the actual welds (about 490 to 500 MPa) at the heat input of 70 J/mm (**Figure 8.1**).

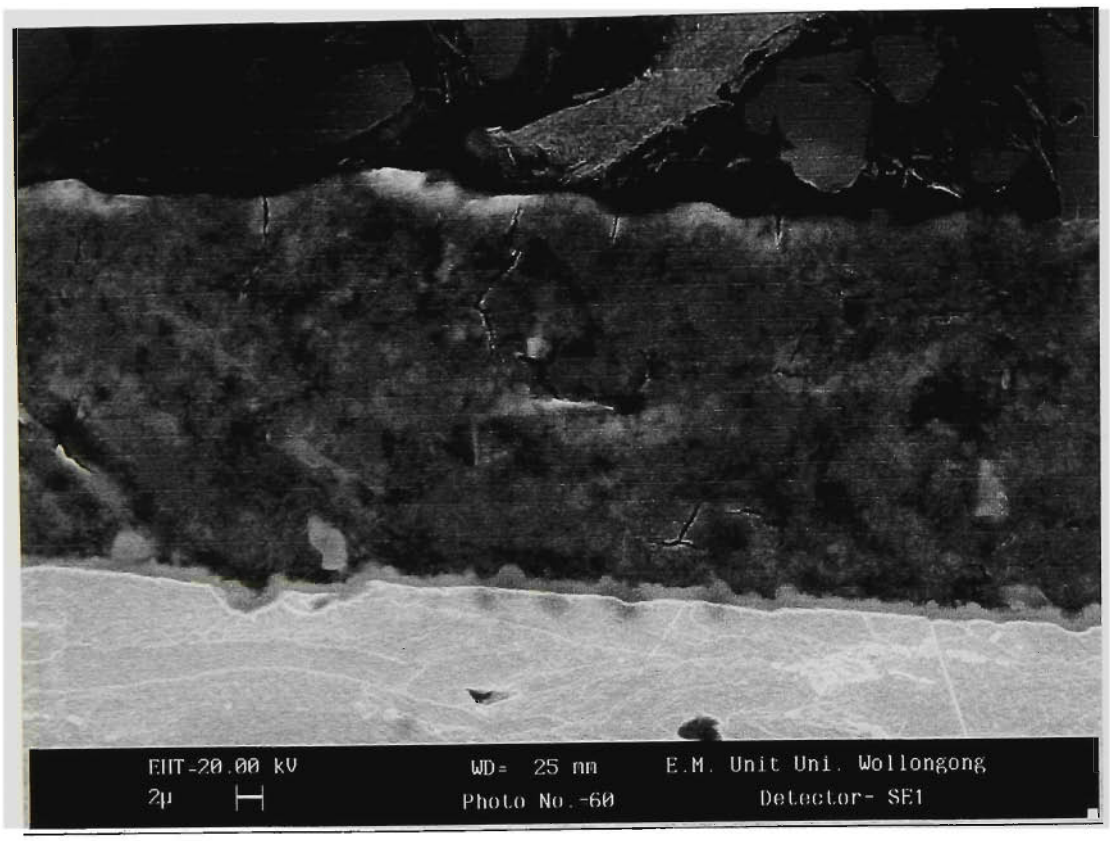

Figure 8.48 SEM micrograph showing the Zn-Al coating of ZINCALUME^{TM} sheet steels.

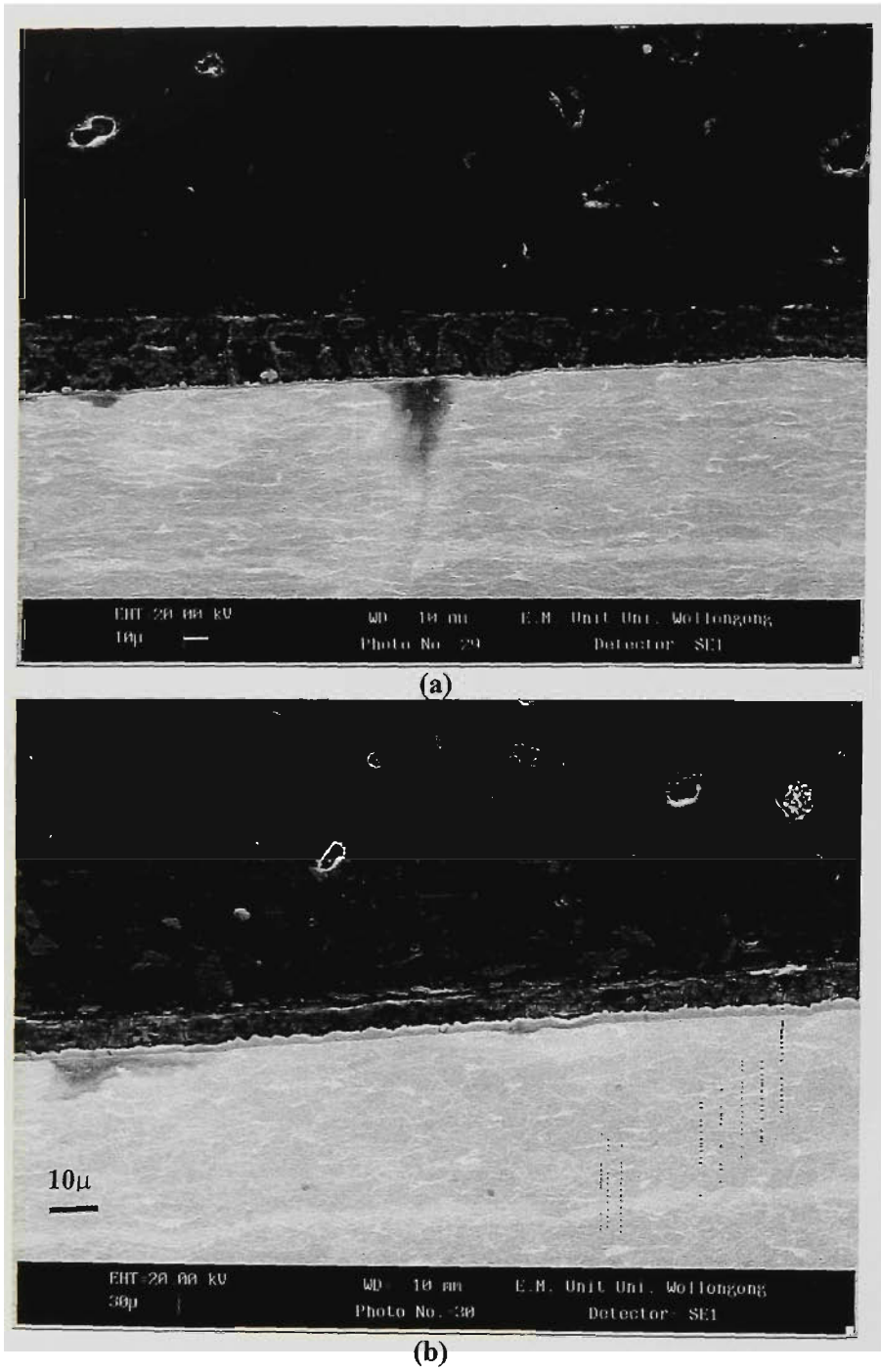

Figure 8. 49 SEM micrographs showing the affected Zn-Al coating in the 'thinned' region'. The thickness of the intermetallic compound gradually increased in the approximate range of 600-700°C from **(a)** 1.26μm to 1.89μm; and **(b)** 2.9μm to 4.08μm with increasing temperature.

Table 8.20 The average tensile strength, yield strength and elongation of grain refined region of the simulated HAZ

PeakTemp. (°C)	Tensile Strength (MPa)	Yield Strength (MPa)	Elongation (%)
910	408±7	346±7	31.5±3.5
1020	410±1	350±4	34.5±0.5
1100	408±2	346±6	31.0±1

8.7 EFFECT OF GMAW ON ZN AND ZN ALLOY COATINGS

8.7.1 Heat Affected Zn-Al Coating

The Zn-Al coating of ZA sheet steel consists of two distinct layers: a wide Zn-Al layer about 25μm and a narrow white intermetallic compound layer about 1.26μm thick, as shown in **Figure 8.48**. In the Zn-Al layer plate-like Si-rich particles were observed and the darker patches are Zn-rich dendrites and the lighter patches are of Al dendrites. The composition of the white compound layer determined by EDS is 55.4%Al, 28.3%Fe, 7.52%Si and 8.7%Zn (at.%).

Appendix III (a) shows a panoramic view of the morphology change of the Zn-Al coating adjacent to the weld toe. It clearly shows that the coating affected length (about 4.60 mm) during GMAW at a heat input of 80 J/mm is well beyond the heat-affected zone (about 3.75mm). The coating was affected by GMAW in two ways: gradual reduction in thickness of the Zn-Al layer and gradual growth of the white intermetallic compound layer, which may contain many sub-layers. Furthermore, there is also a coating 'neck' where the total width of the coating is at the minimum.

The thinning start point may indicate where the coating becomes affected by the welding. **Figure 8.49 (a)** and **(b)** show the morphology of the two layers of the coating at the neck starting point where the reduction of the original Zn-Al layer and growth of the intermetallic compound layer were observed. The reduction of the Zn-Al outstrips the growth of the white compound layer. Towards the weld metal the original Zn-Al coating are gradually thinned and the intermetallic compound layers are expanded (**Figure 8.49 (b)**). Overall, the total width of the coating decreases. The temperature

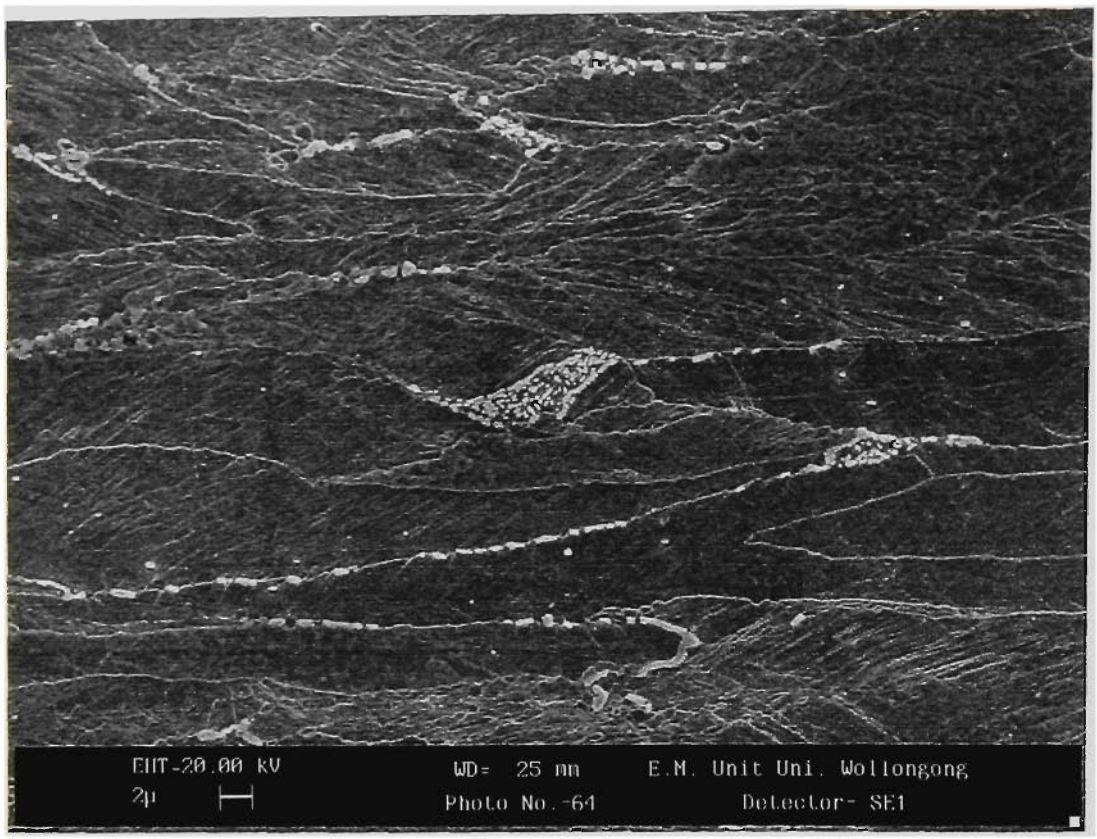

(a) at 599°C

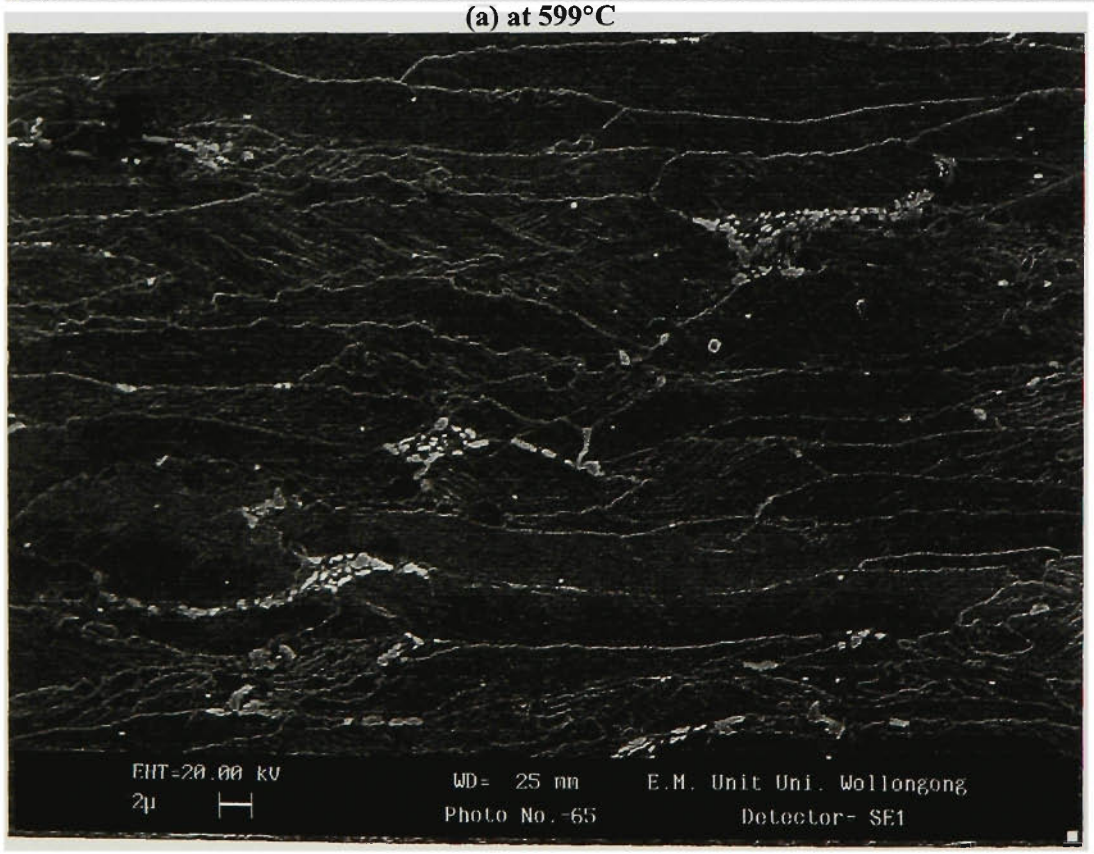

(b) at 627 °C

Figure 8.50 SEM micrographs of HAZ below the thinned Zn-Al coating area showing that recrystallisation started in areas **(a)** and **(b)**.

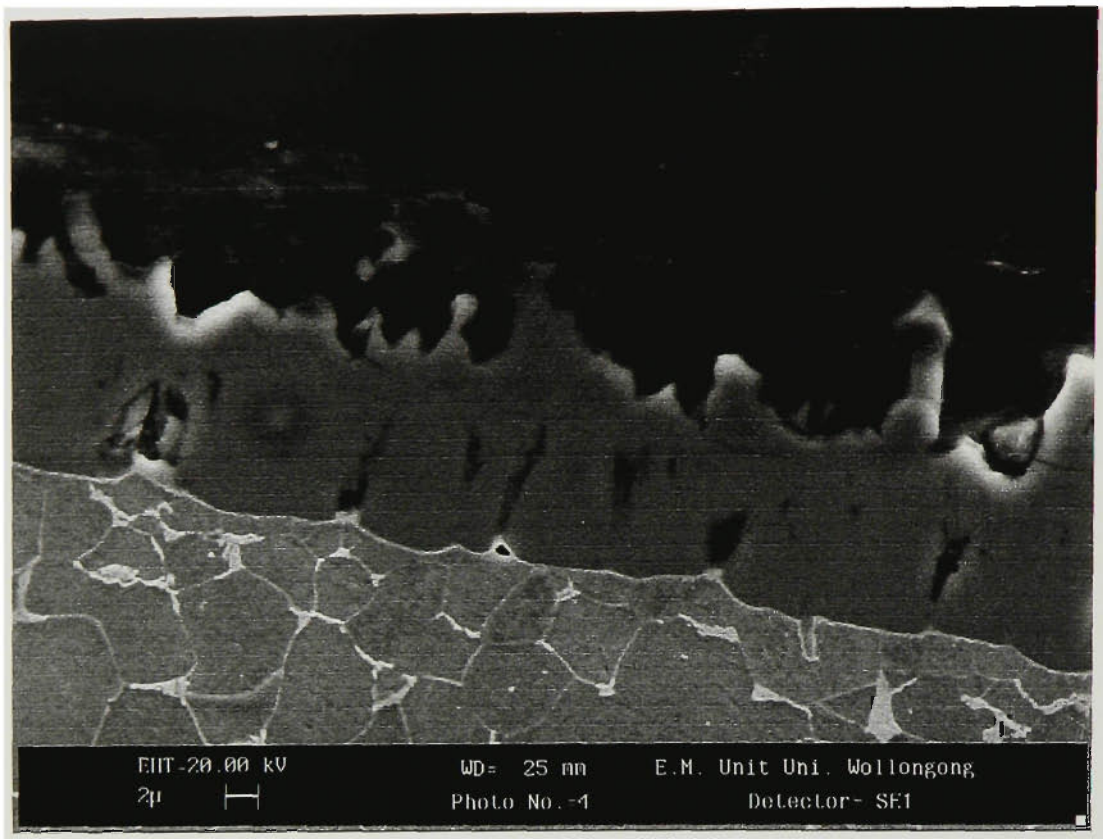

(a) At about 750 to 900 °C

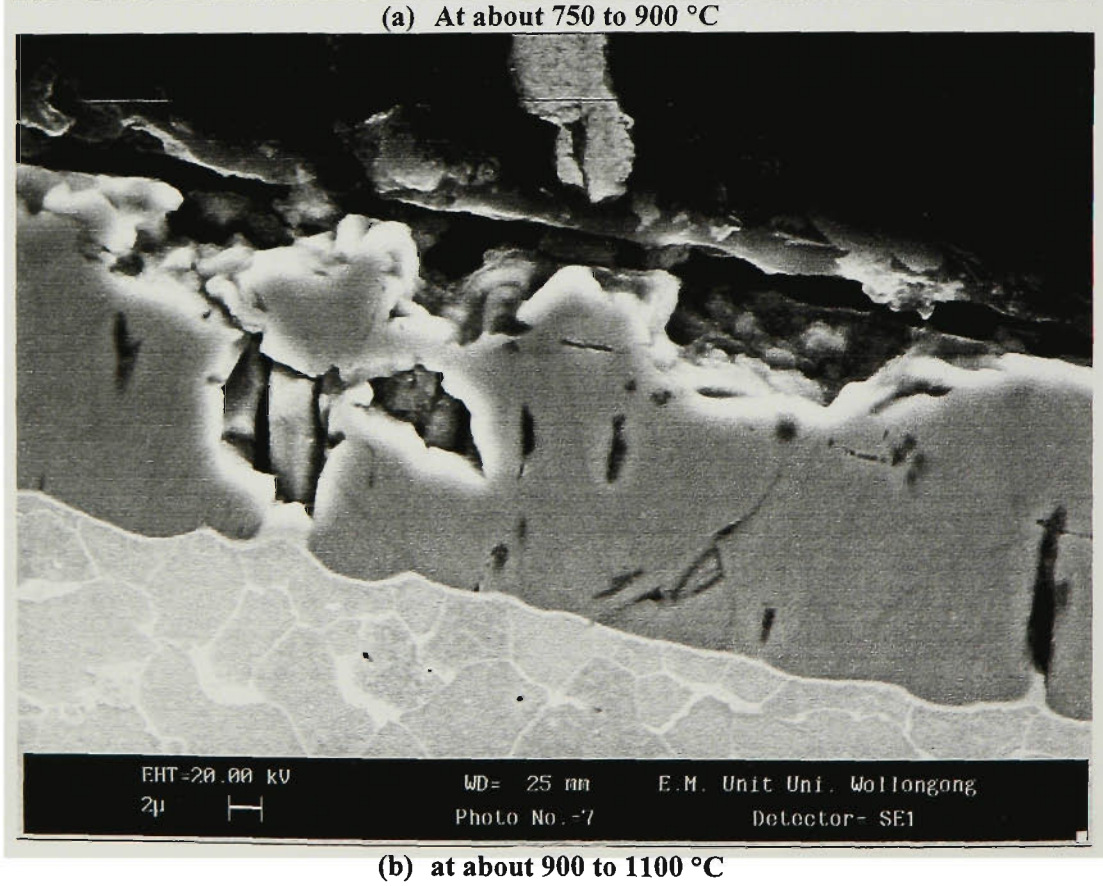

(b) at about 900 to 1100 °C

Figure 8.51 SEM micrographs showing **(a)** the white intermetallic layer increased in thickness in the end of SC and IC regions (750 to 900°C); **(b)** the thickest white layer occurred in the grain refined region (900 to 1100°C).

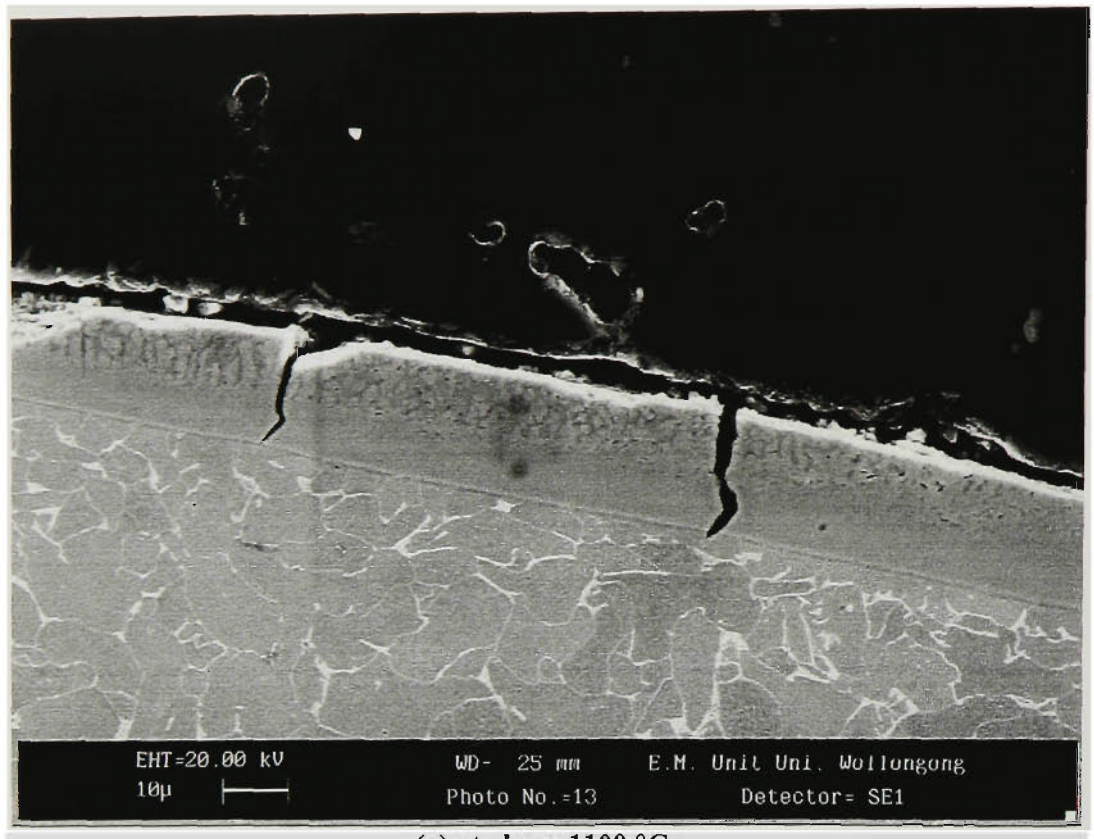

(a) at above 1100 °C

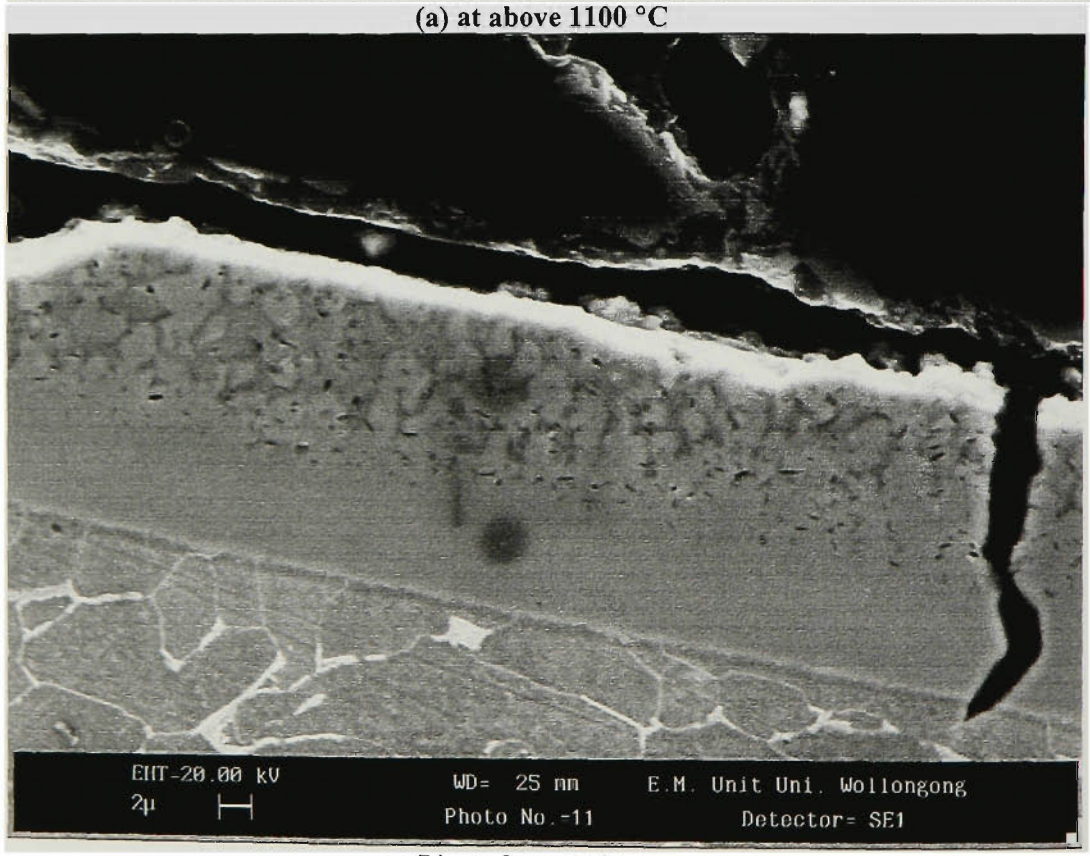

(b) at above 1100 °C

Figure 8.52 SEM micrographs showing cracking of the Zn-Al coating in the grain coarsened region.

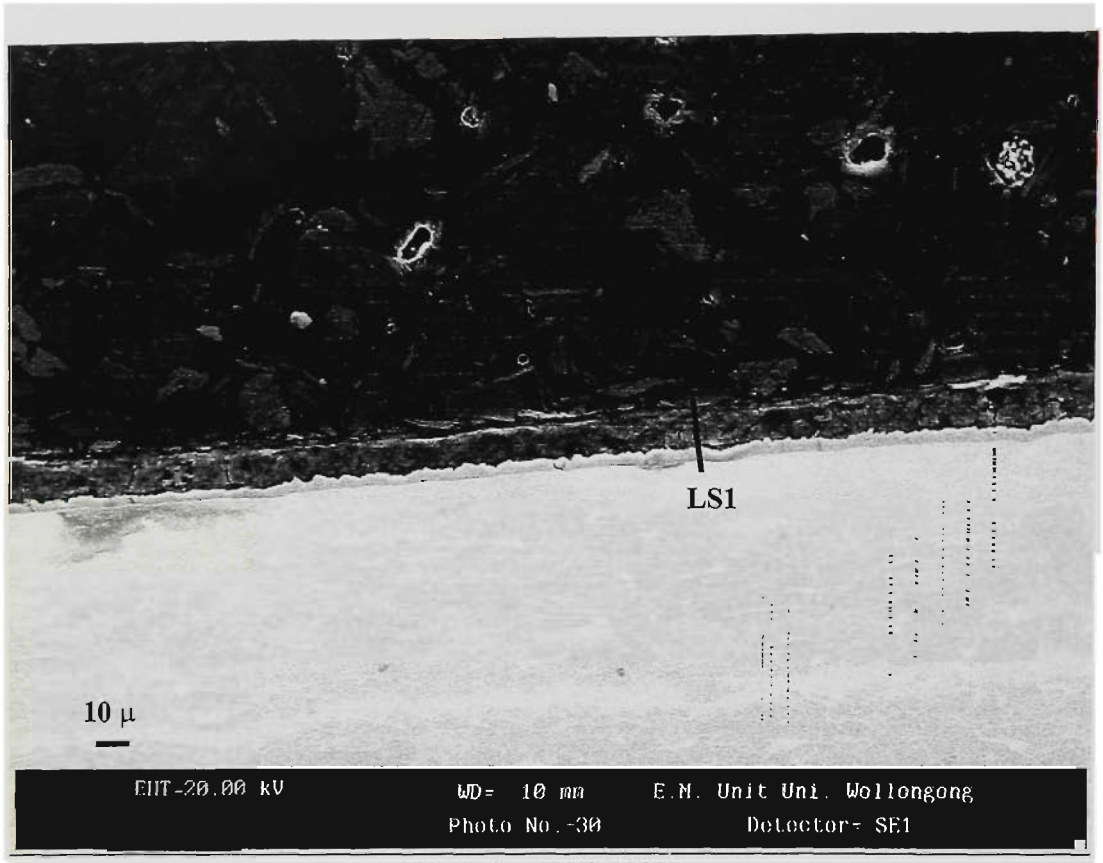

(a) at about 600-700°C

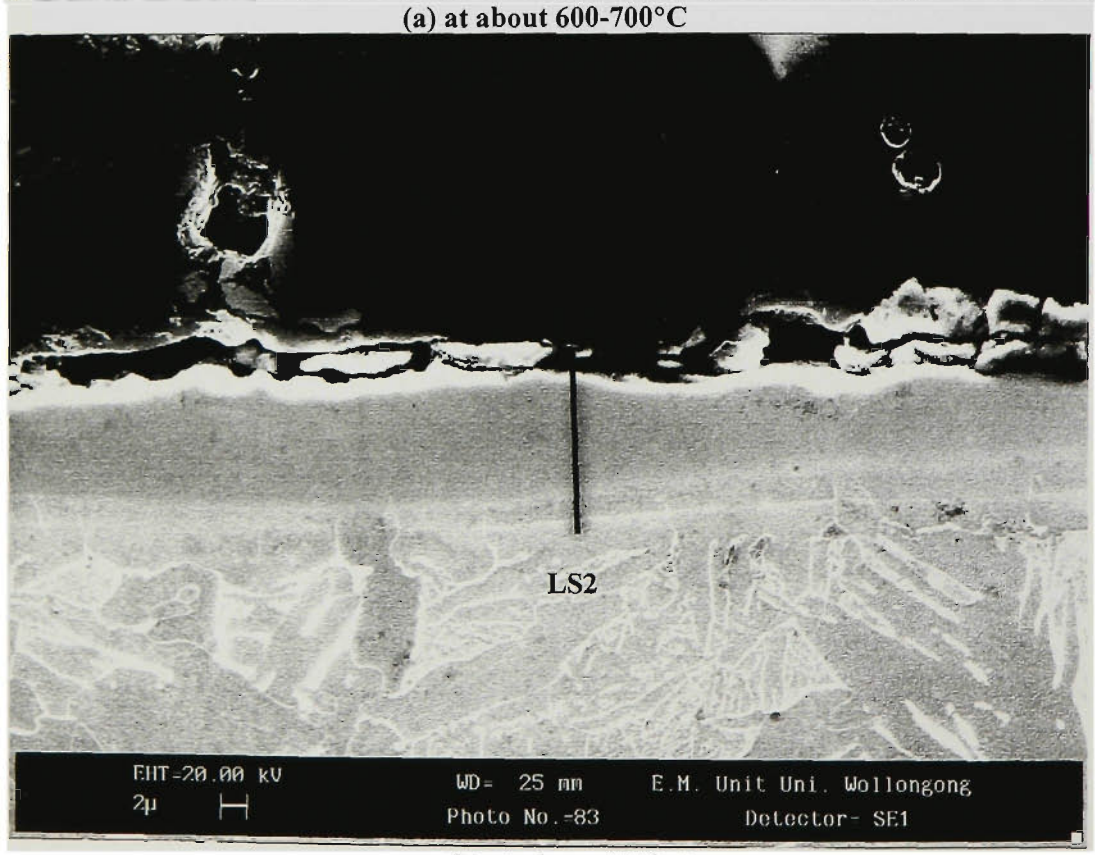

(b) at above 1100°C

Figure 8.53 Positions of EDS line scans of cross sections of the heat affected Zn-Al coating.

corresponding to the thinning start was estimated by examining the microstructure of the steel matrix adjacent to the necking start point. It was estimated that the temperature is about 600°C because of the presence of a small number of polygonal recrystallized grains in the area adjacent to the coating neck (**Figure 8.50 (a)**).

As the temperature increases towards the weld metal the thickness of the Zn-Al layer decreases rapidly and the thickness of the intermetallic compound layer increases only moderately. Within the IC or partially transformed region (between 750 and 900°C) the thickness of the Zn-Al layer is reduced from about 6μm to less than 1μm and the thickness of the white intermetallic compound increases from 8μm to 14μm (**Figure 8.51 (a)**). At a temperature of approximately 900°C the entire coating consists virtually of the intermetallic compound layer and has a composition of 57.6%Al, 40.2%Fe and 2.2%Zn (at.%), as shown in **Figure 8.51 (b)**. The composition of the intermetallic compound layer is close to the composition of FeAl.

As the temperature increase a thin layer appeared in between the white compound layer and the steel matrix as shown in **Figure 8.52 (a)** and **(b)**. The thickness of the new layer formed at about 1100°C was less than 1 μm and had the composition 97.6%Fe and 2.4%Al (at.%) and this is α-Fe with 2.4%Al in solid solution. There is about 5μm thick layer next to the α-Fe had the composition 23.4%Al and 76.6%Fe (at.%). The composition of the new compound is close to Fe_3Al. The layer of the Fe_3Al compound grows rapidly with decreasing distance from the weld metal and the entire coating consists of this layer near the weld metal, as shown in **Figure 8.12**.

EDS line scans as well as spot analysis was carried out on the various parts of the affected coating layers to investigate the compositional change of the coating layers. **Figure 8.53** shows the position of the line scans of the heat affected Zn-Al coating. A typical EDS line scan **LS1** across the coating consisting of $FeAl_2$ and Zn-Al layers is shown in **Appendix IV (a)**. It can be seen that there is a little variation of the Al content across the whole coating. However Zn content increases gradually in the $FeAl_2$ intermetallic compound layer and reaches a maximum at the interface between the $FeAl_2$ and Zn-Al layer, whereas the Fe content decreases gradually in the $FeAl_2$ and reaches to the minimum at the interface of the $FeAl_2$ and Zn-Al layer. It is quite

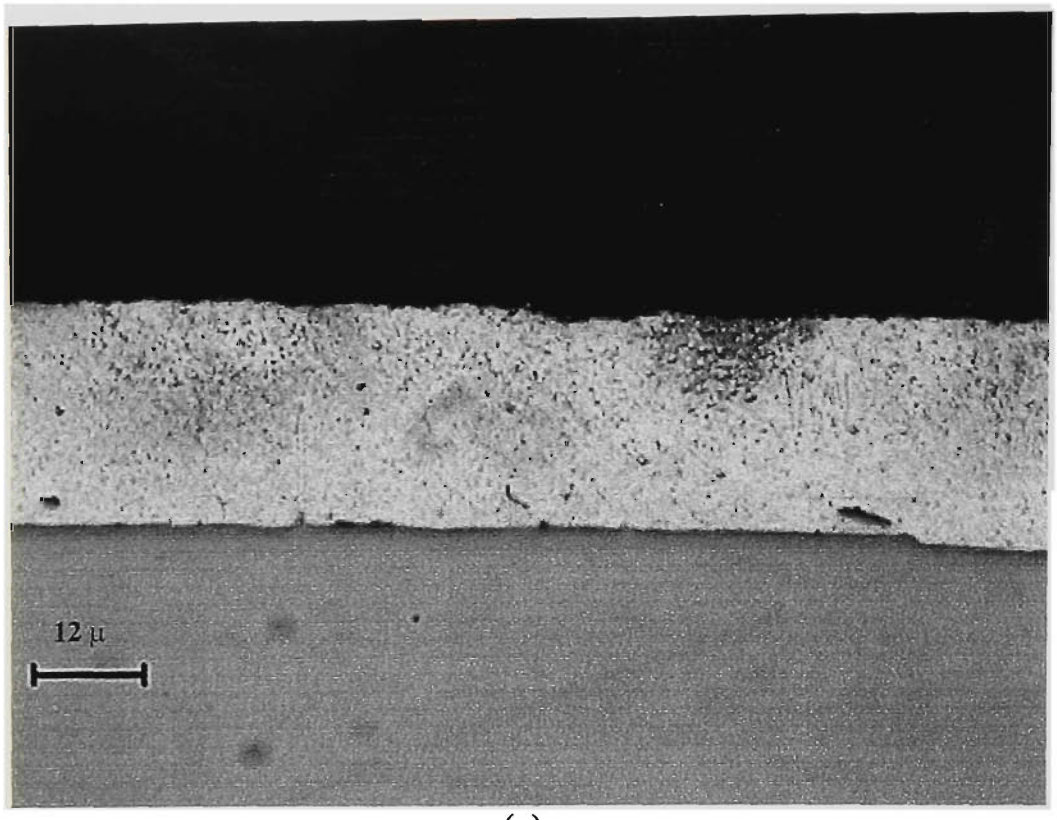

(a)

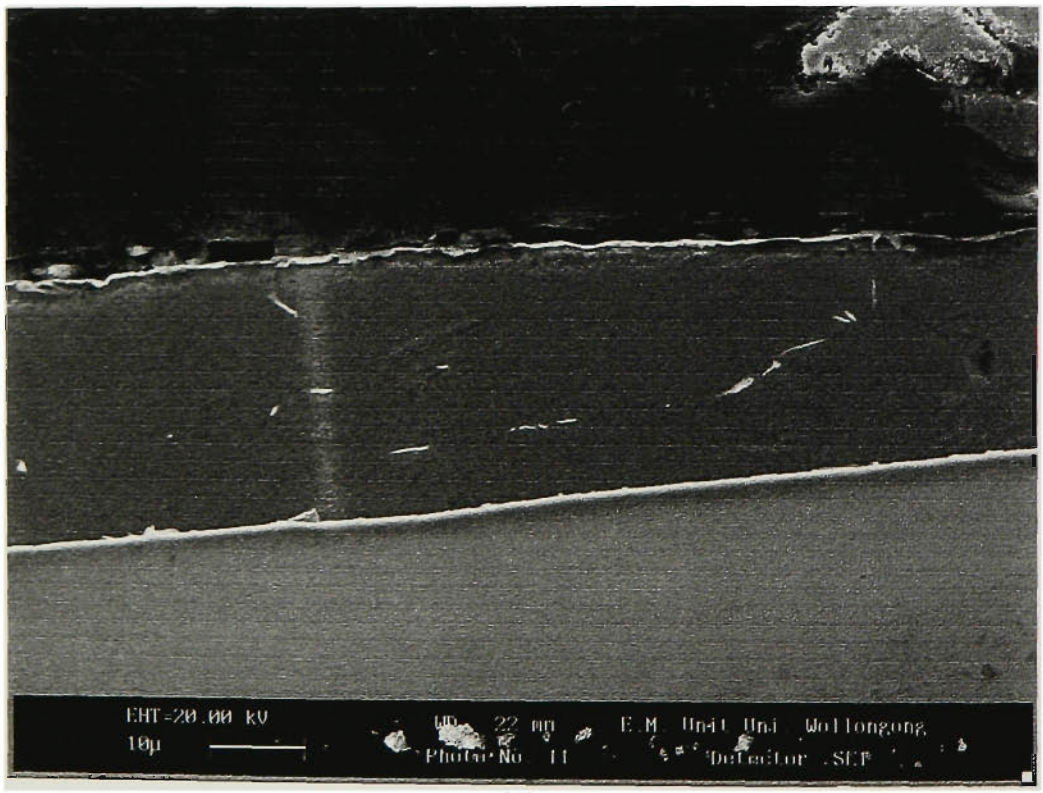

(b)

Figure 8.54 Optical **(a)** and SEM **(b)** micrographs showing the Zn coating morphology.

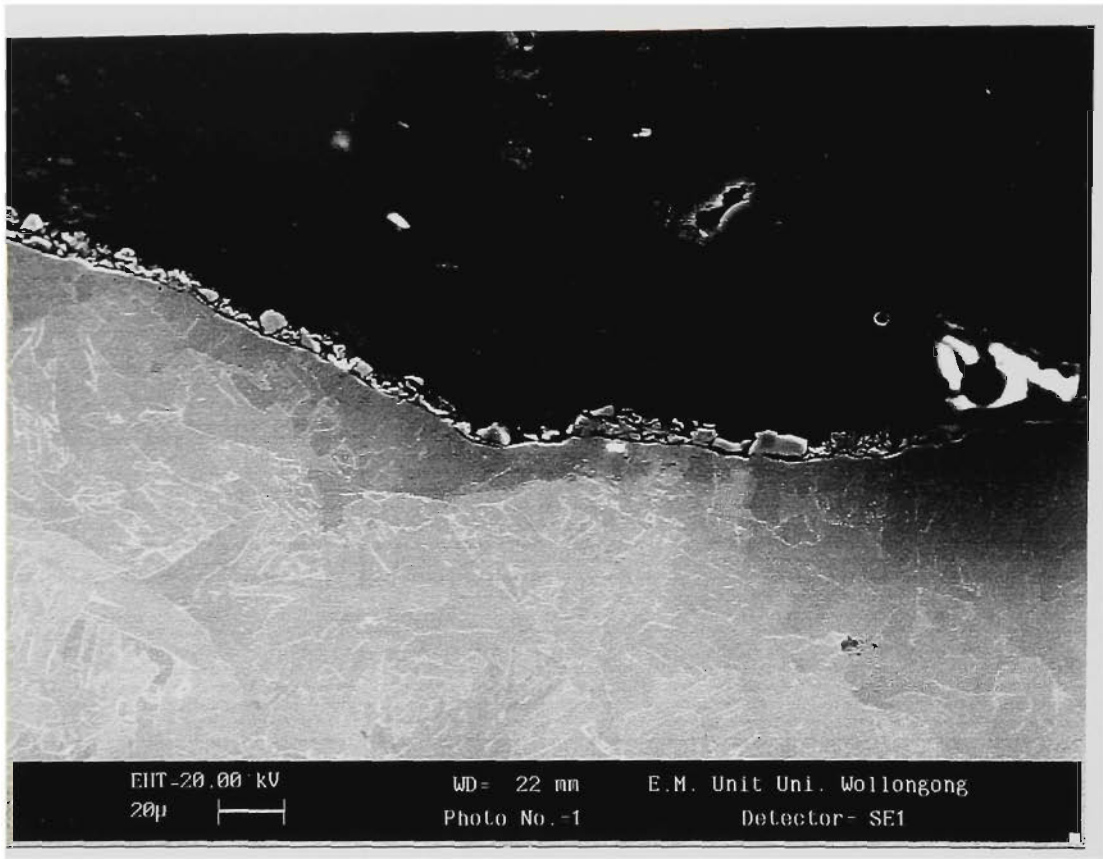

Figure 8.55 SEM micrograph showing the heat affected Zn coating in the area of the weld toe.

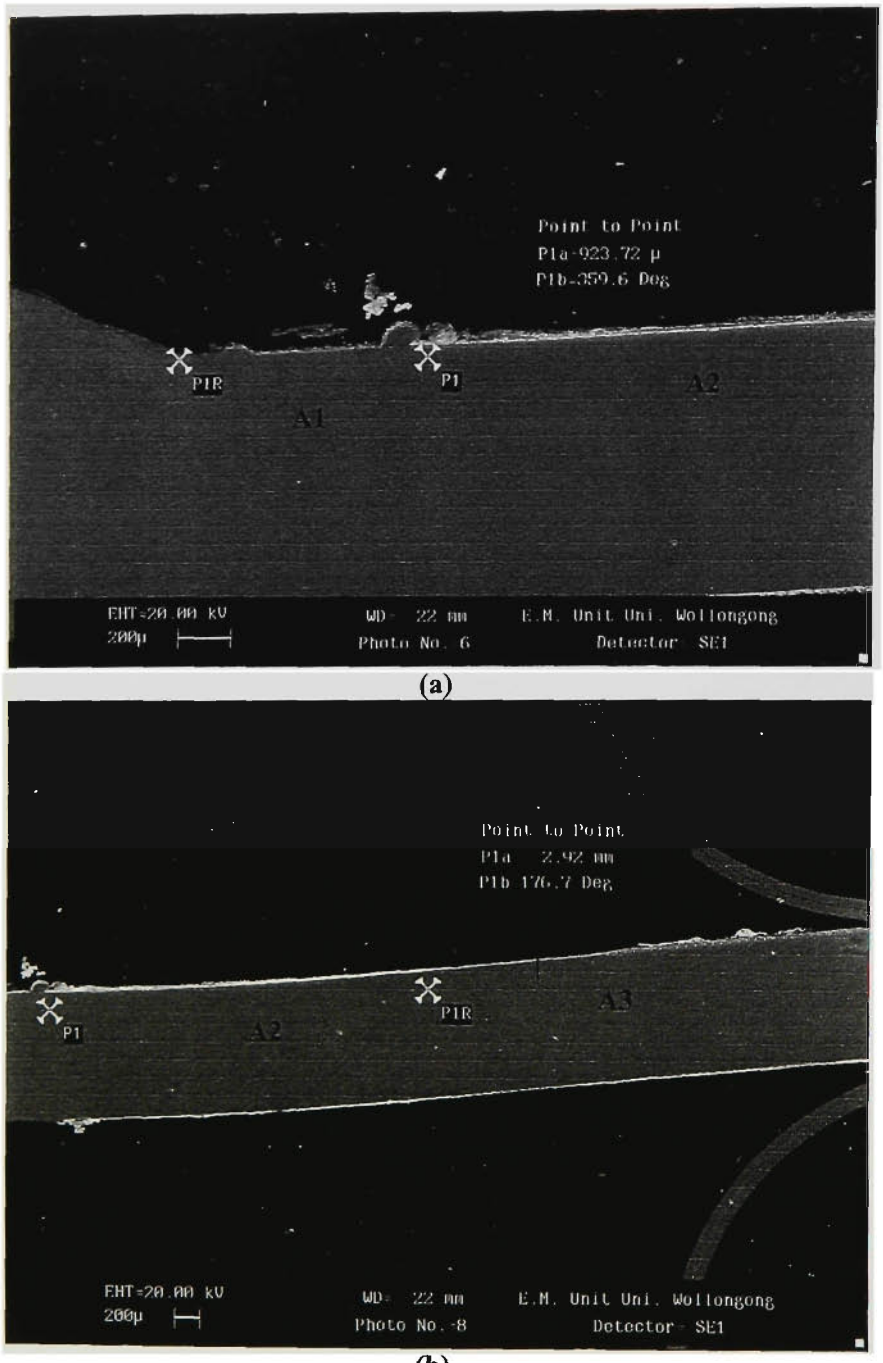

Figure 8.56 Damaged Zn coating away from the weld metal can be divided into three zones, **A1**, **A2** and **A3** according to the thickness of damaged coatings.

interesting to note that the Si content, like Zn, increases slightly but reaches the maximum within the $FeAl_2$ compound layer and drops very quickly to the minimum at the interface of the $FeAl_2$ and Zn-Al layer. A typical EDS line scan **LS2** of the coating consisting of Fe_3Al, $FeAl_2$ and Zn-Al multi-layers is shown in **Appendix IV (b)**. The Al content increases gradually within the Fe_3Al and $FeAl_2$ layers and reaches a maximum within the $FeAl_2$ layer near to the interface between the $FeAl_2$ and Zn-Al layer. In the Zn-Al layer a sharp Al peak accompanied with a very modest Zn peak was also observed. The Si content is constant across the entire coating. The Fe content decreases gradually within the Fe_3Al and $FeAl_2$ layers and drops very sharply at the interface between the $FeAl_2$ and Zn-Al layers.

8.7.2 Heat Affected Zn Coating

The microstructure of the ZHT coating is given in **Figure 8.54** and it contains mainly Zn with small amounts of Fe, Al, Si and Mn. The coating has a uniform thickness of 25 μm (determined using SEM). The panoramic view of the morphology of the coating after the GMAW at a heat input of 80 J/mm is presented in **Appendix III (b)**. The ZHT coating was quite extensively damaged by the GMAW process and the damaged area extended from the fusion line to about 6.1 mm away from the fusion line, which is higher than the 4.6 mm of the ZA coating welded using the same process at the same heat input. It should be noted that in nowhere was the coating completely removed by the GMAW process. In the area of the weld metal adjacent to the base metal a thin layer of particles was observed, as shown in **Figure 8.55**. EDS microanalysis shows that these particle contain either Fe or Si oxides, but no Zn.

Away from the weld metal the damaged coating maybe divided into three zones: **A1**, **A2** and **A3**, according to the thickness of the damaged coatings (**Figure 8.56**). Zone **A1** extends from the weld metal to the grain refined region (T>900°C) and **A2** extends from the grain-refined region to the SC and IC (600°C–900°C) and zone **A3** is in a temperature region lower than 600°C. The respective thickness of the zones **A1**, **A2** and **A3** of the damaged coating are about 2μm, 15μm and 5μm and the zone lengths are about 0.9 mm, 2.9mm and 1.0mm.

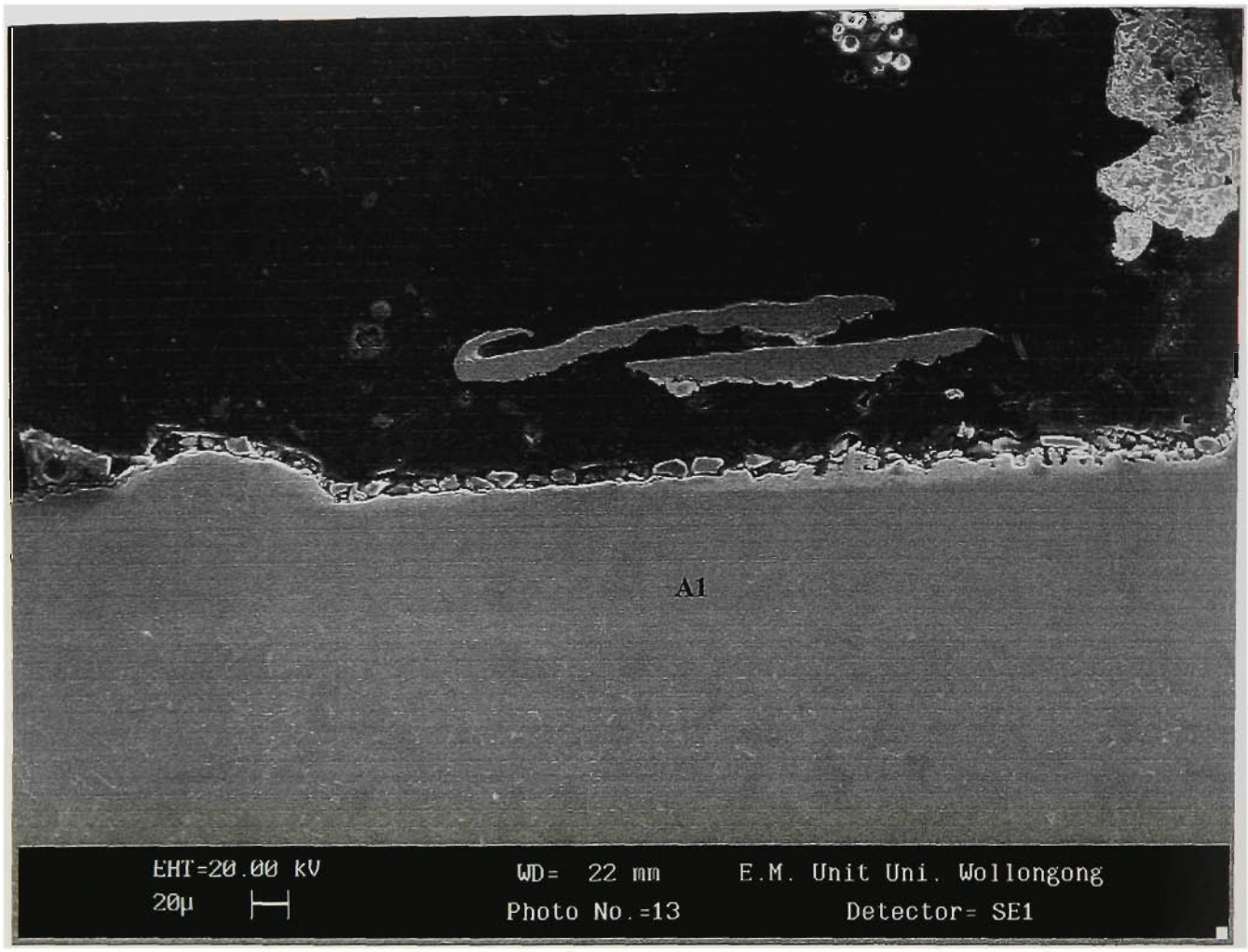

(a)

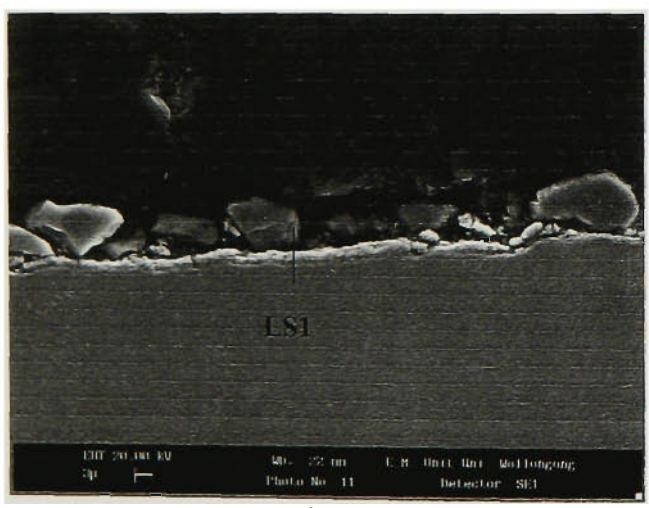

(b)

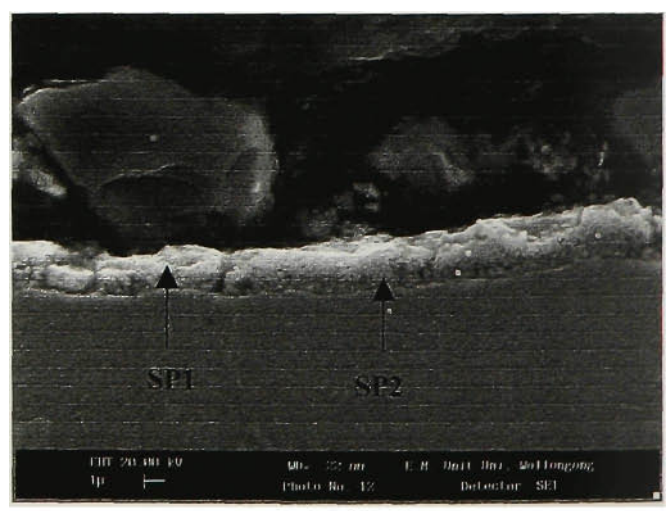

(c)

Figure 8.57 SEM micrographs showing the heat affected Zn coating **(a)** the **A1** zone in the grain coarsened region; local details of the **A1** zone **(b)** and **(c)**. (**LS1**-line scan; **SP1** and **SP2**-EDS spot analysis).

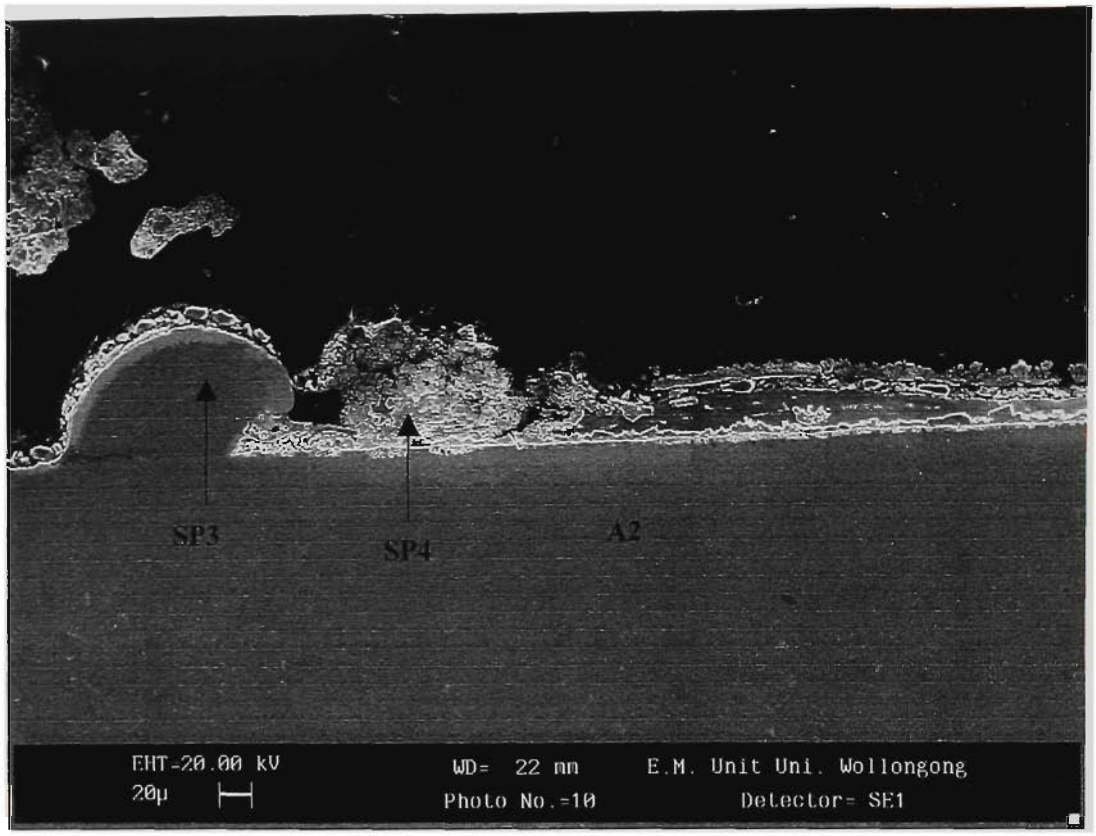

Figure 8.58 SEM micrograph showing the **A2** zone of the heat affected Zn coating.

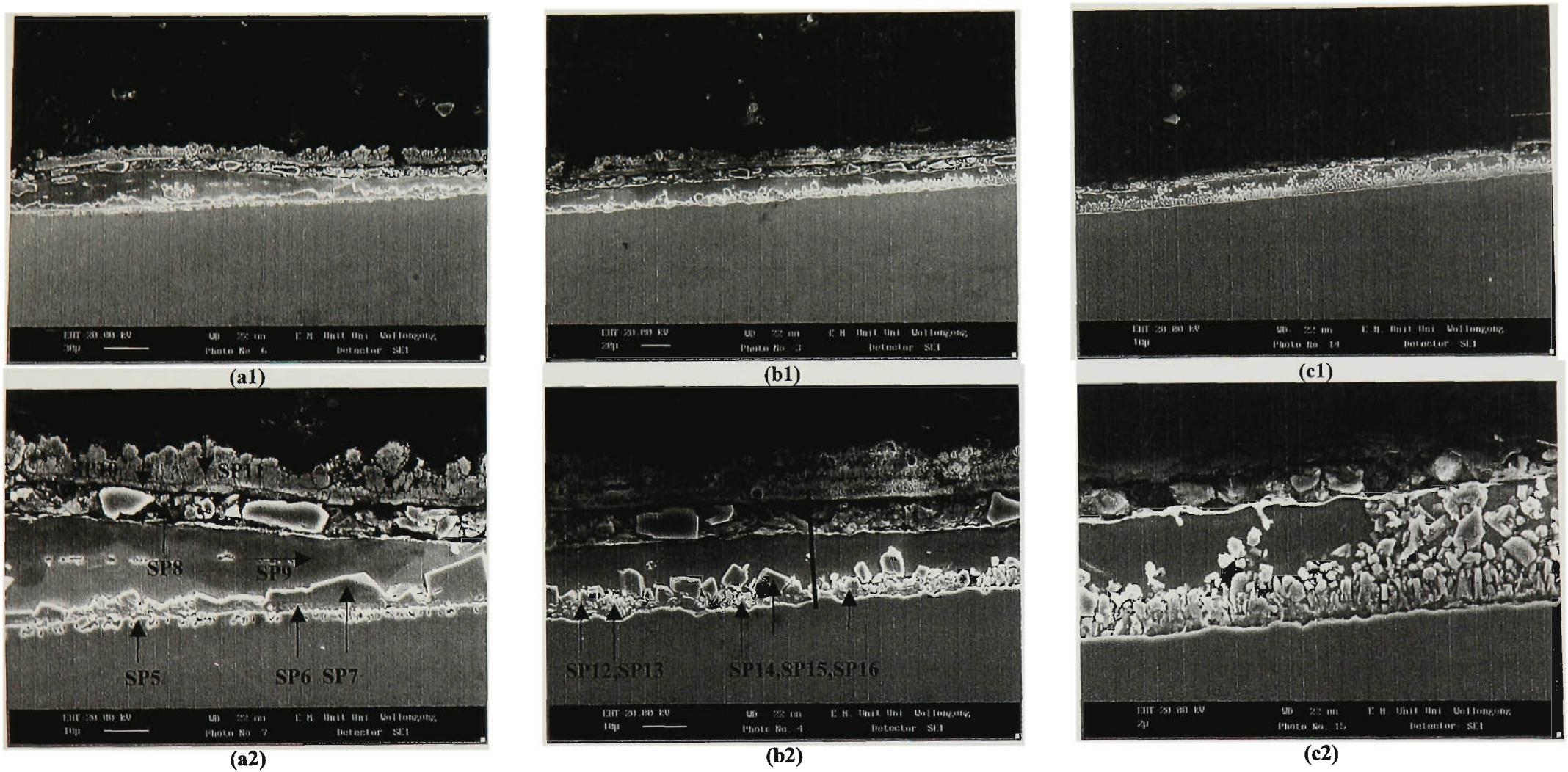

Figure 8.59 SEM micrographs of the heat affected Zn coating showing the coating morphologies in the **A2** zone **(a)** to **(c)** (direction away from weld metal).

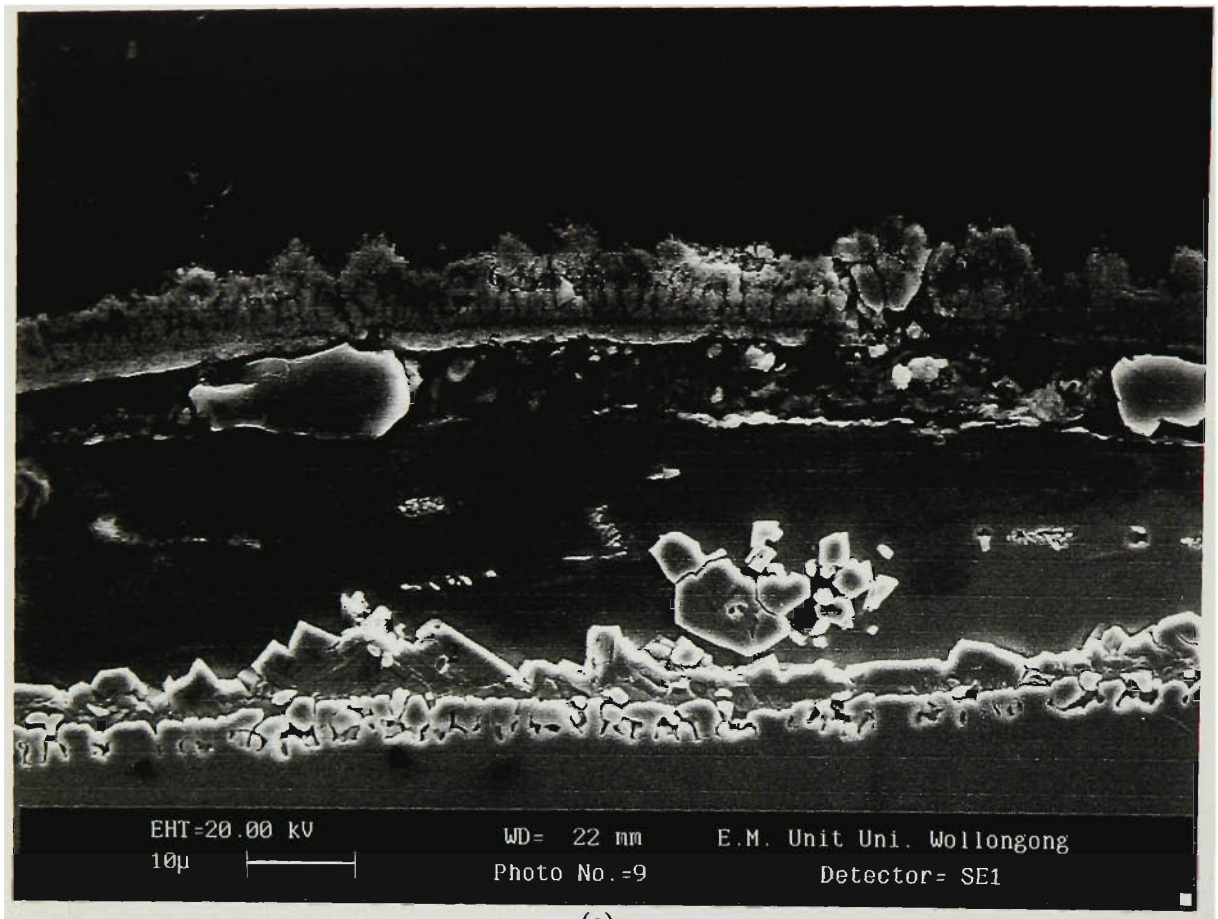

(a)

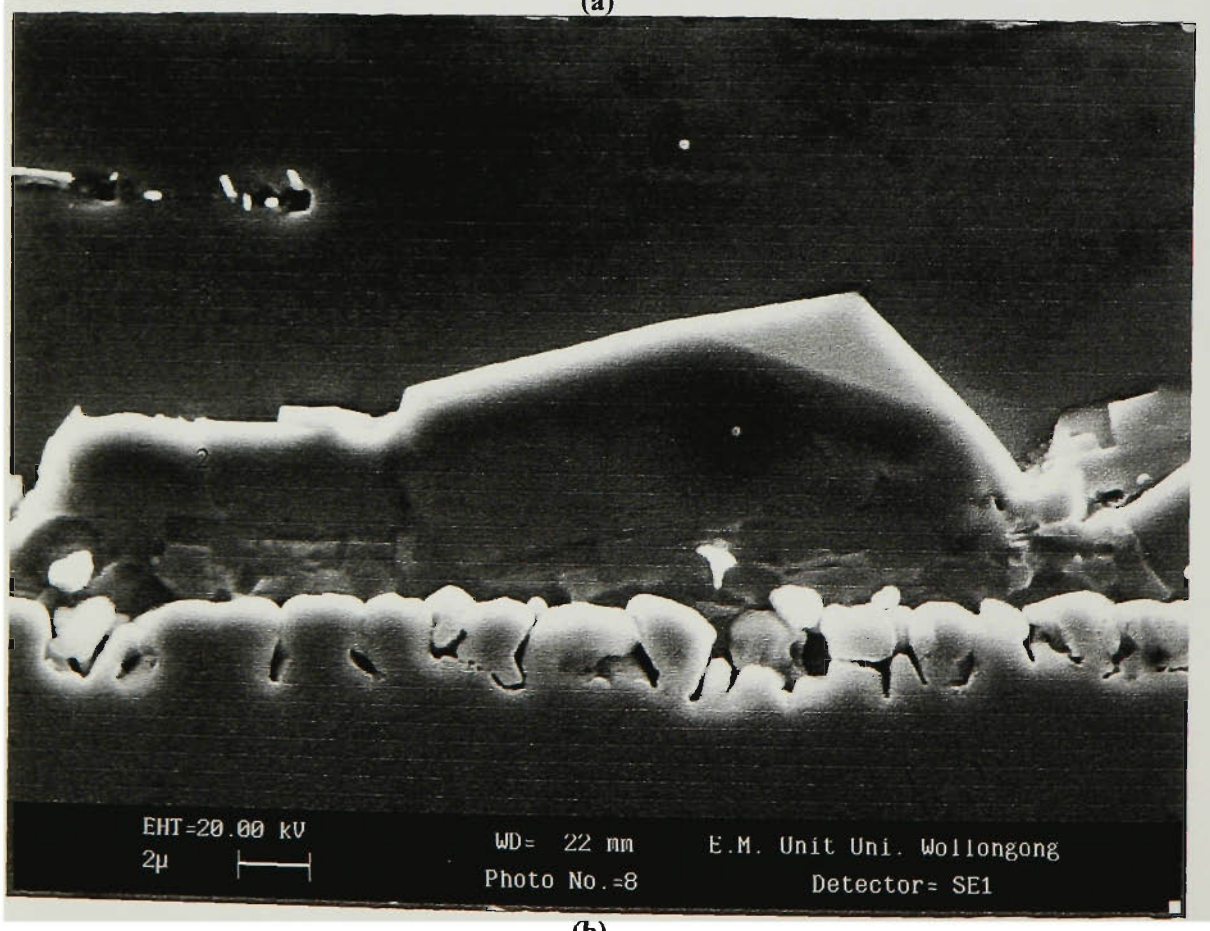

(b)

Figure 8.60 SEM micrographs showing **(a)** the six layers of the heat affected Zn coating; **(b)** the details of the layers 1, 2 and 3.

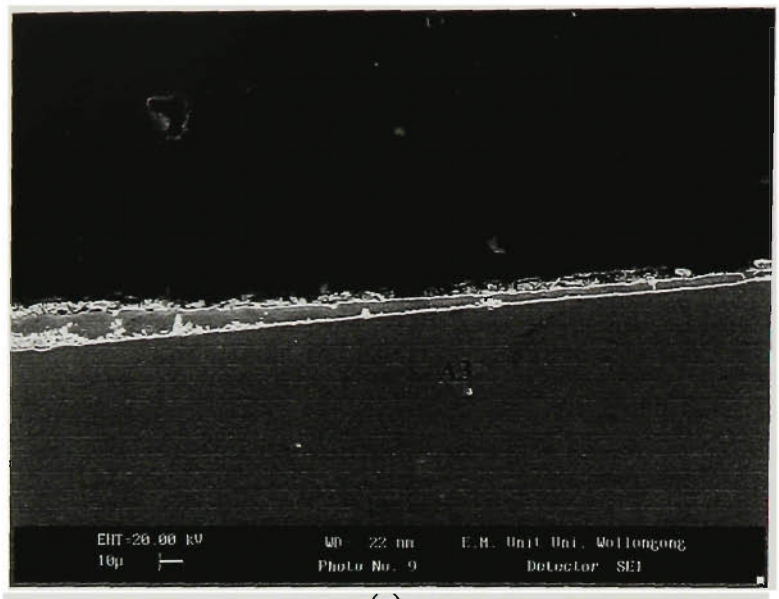

(a)

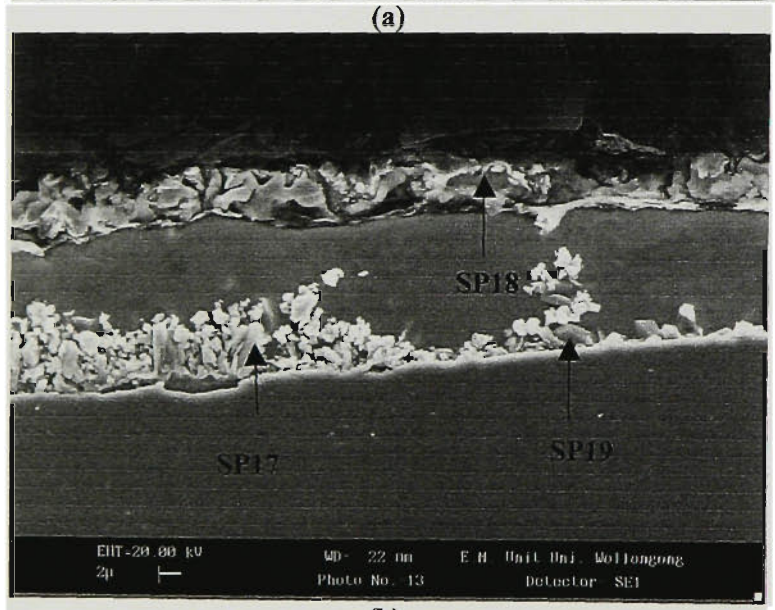

(b)

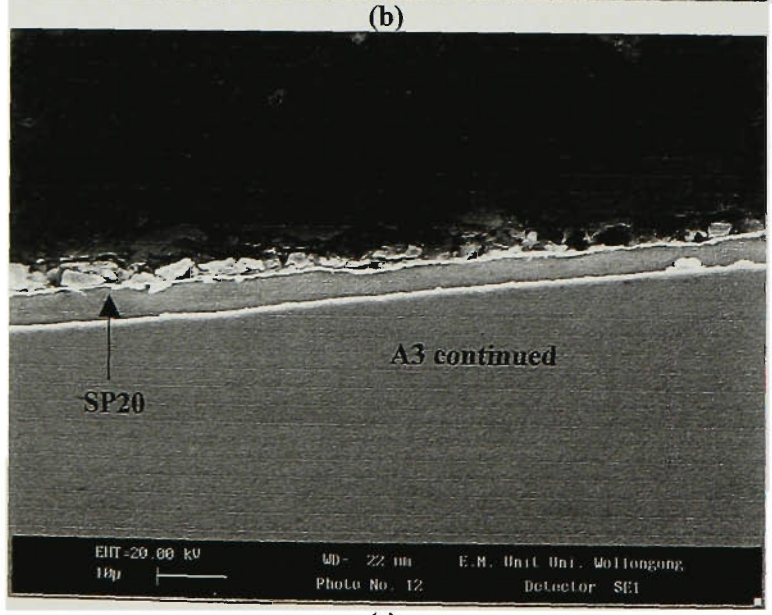

(c)

Figure 8.61 SEM micrographs of the heat affected Zn coating showing **(a)** the coating morphologies in the zone **A3** adjacent to the zone **A2**; **(b)** the details of end of **A2** zone; **(c)** continued **A3** zone.

Table 8.21 Results of EDS analysis of heat affected Zn-coating in the A1, A2 and A3 zone as well as unaffected coating (at.%)

EDS	Zn	Fe	Si	Mn	Cr	Al
SP1	79.95	6.96	13.15			
SP2	56.83	31.94	2.2	9.02		
SP3		100				
SP4	78.75	21.25				
SP5	17.21	82.79				
SP6	79.6	20.4				
SP7	87.4	12.6				
SP8	80.89	19.11				
SP9	98.5	1.5				
SP10	94.81	5.19				
SP11	68.53	22.36	1.63	7.48		
SP12	73.06	26.77				
SP13	69.99	25.56				4.45
SP14	81.1	16.81				2.09
SP15	84.71	14.74				
SP16	77.11	22.89				
SP17	83.55	12				4.45
SP18	98.8	1.14				
SP19	86.41	11.79				1.8
SP20	93.6	4.8			0.3	1.2

The microstructure of the coating zone **A1** is given in **Figure 8.57** and it consists of a rather thick (about 6μm) layer of fragments similar to those observed on the weld metal and a thin (about 2μm) continuous layer. The EDS line scan result (**Appendix V (a)**) shows that the Fe concentration continuously decreases from the steel and coating interface, but Zn is quite constant across the layer. However, Mn concentration has a maximum in the layer close to the steel matrix whereas the Si is concentrated in the outermost region of the layer.

The microstructure of zone **A2** is shown in **Figure 8.58** and **Figure 8.59**. The coating consists of six distinct layers (**Figure 8.60**): the first, a thin out-growing layer (about 2μm) immediately next to the steel matrix; the second, a layer of coarse and faceted particles; the third, a smooth and wide featureless layer; the fourth, was granular layer; the fifth, a thin and continuous layer (about 2μm); and the sixth, an outermost granular layer. EDS microanalysis results for these six layers are summarized in **Table 8.21**. The first, outgrowing, layer has the composition of 83%Fe and 17%Zn (at.%), the second layer has the composition of 20%Fe and 80%Zn (at.%), the third layer is virtually pure Zn, the fourth layer has a composition of 20 %Fe and 80 %Zn, the fifth layer has a composition of 5%Fe and 95%Zn (at.%) and the outermost layer has a composition of 22%Fe, 69%Zn, 7.4%Mn and 1.6%Si (at.%). A typical EDS line scan result is given in **Appendix V (b)** and it is consistent with the results of EDS microanalysis presented above. The coating in zone **A3** has changed little apart from a slight reduction of the thickness. The microstructure of zone **A3** is shown in **Figure 8.61**.

CHAPTER 9

DISCUSSION

In this Chapter, the experimental results presented in Chapter 8 are discussed mainly in terms of the effects of the welding process variables on mechanical properties and microstructure of HAZ of the welds. It explores:

1. the effect of heat input on the properties and microstructures of GMA and FCA welded ZINCALUME^{TM} (ZA) and ZINC-HI-TEN^{TM} (ZHT) G550 1.0 mm sheet steels;

2. the effect of welding conditions, including process, shielding gas, electrode orientation, welding travel speed, control mode and Zn and Zn-Al coating on the properties and microstructure of the HAZ;

3. the relationship between the heat input and the thermal cycle experienced by the base metal;

4. the correlation between the various welding conditions and weld metal characteristics;

5. the effect of welding on the Zn alloy coatings.

9.1 PROPERTIES AND STRUCTURES OF HAZ OF ZA AND ZHT G550 WELDS

9.1.1 Mechanical Properties

ZA and ZHT G550 sheet steels are supplied in the cold rolled condition and have a specified tensile strength not less than 550 MPa (**Table 7.2**). The actual measured tensile strengths for these particular sheet steels were about 645 and 725 MPa for the longitudinal and transverse directions respectively (**Table 7.3**). According to the compositions of the steels, their fully annealed yield strength would be around 250 MPa, and this has been used for design purposes in the past. A large portion of the high tensile strength (>345 MPa) of the commercial sheet steels comes from work hardening. Clearly the welding process thermal cycles will have a significant and detrimental effect

on the tensile strength as the material in the heat affected zone (HAZ). The HAZ will experience rapid heating and cooling thermal cycles which not only recrystallise the cold rolled microstructure but also causes $\alpha \rightarrow \gamma$ phase transformation on heating and the $\gamma \rightarrow \alpha$ phase transformation on cooling. The measured c ross-welded tensile strengths were in the range of 460~520 MPa (**Figure 8.1 (a)** and **Figure 8.2 (a)**). These values lie between the original longitudinal tensile strength of 645 MPa of the as cold rolled sheet steels and 250 MPa for the annealed sheet steels over the range of the nominal heat inputs that were examined. After welding the yield or proof stress lie in the range of 400~500 MPa (**Figure 8.2 (b)** and **Figure 8.2 (b)** and these data should be used for design purpose rather than tensile strength. The mean HAZ microhardness is about 150 $HV_{0.2}$ which is also lower than that of the weld metal and base metal (about 225 $HV_{0.2}$) (**Table 8.4**).

9.1.2 Microstructures

The microstructural changes which result in these property changes have been presented in Chapter 8. The heat affected zone of joints in ZA and ZHT sheet steels consisted of the grain-coarsened (GC), grain-refined (GR), intercritical (IC) or partially transformed and subcritical (SC) or tempered regions. The GC region is adjacent to the fusion line and the SC region is the outermost heat affected region, as shown in **Figure 8.15**. It is clear that grain boundary ferrite and Widmanstatten ferrite side-plates are the dominant structures in the GC region, due to the relative high peak temperature and slow cooling rate after arc welding. The GR region, however, consists of very fine equiaxed grains resulting from the allotropic transformations $\alpha \rightarrow \gamma$ on heating and $\gamma \rightarrow \alpha$ on cooling. In the IC region, pearlite in the base metal transforms on heating to austenite at or above the eutectoid temperature due to its high carbon content and thus low stability. At higher temperatures within the IC region, α transforms allotropically to γ. On cooling α, then pearlite, reforms from the γ phase. Equiaxed ferrite grains are also the dominant constituent in the SC region as a result of recrystallisation, but no $\alpha \rightarrow \gamma$ transformation occurs in this region. The simulated HAZ experiments showed that the grain size of the HAZ up to a peak temperature of 1210°C generally increases with the peak temperature of the thermal cycle (**Figure 8.45**). Recrystallisation of the ZA G550 sheet steels started from a peak temperature of about 600°C and was completed at about 700°C (**Figure**

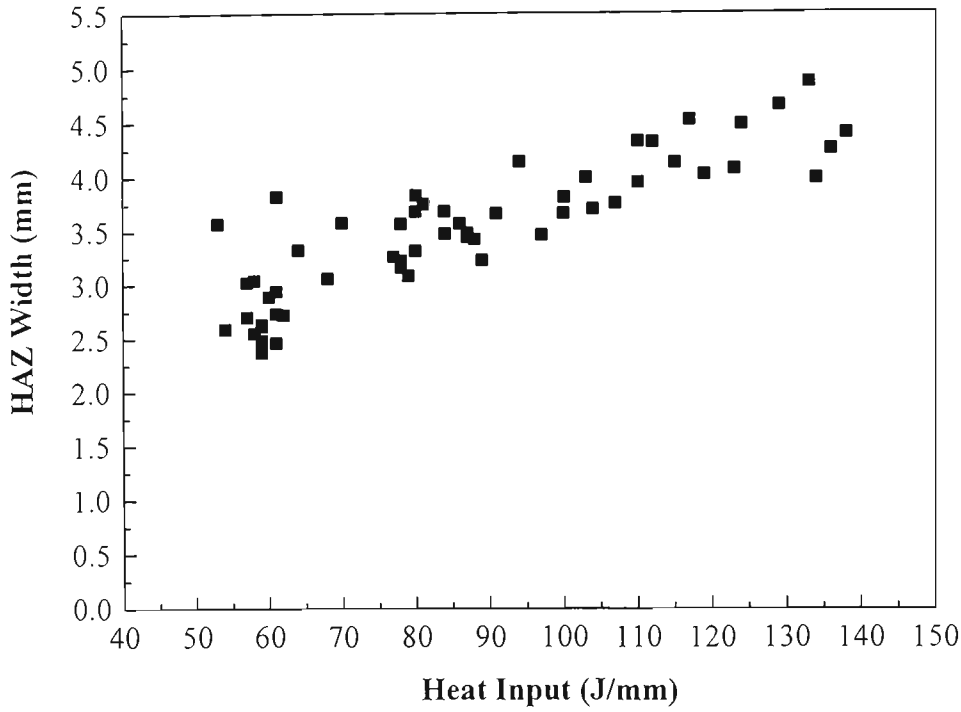

(a)

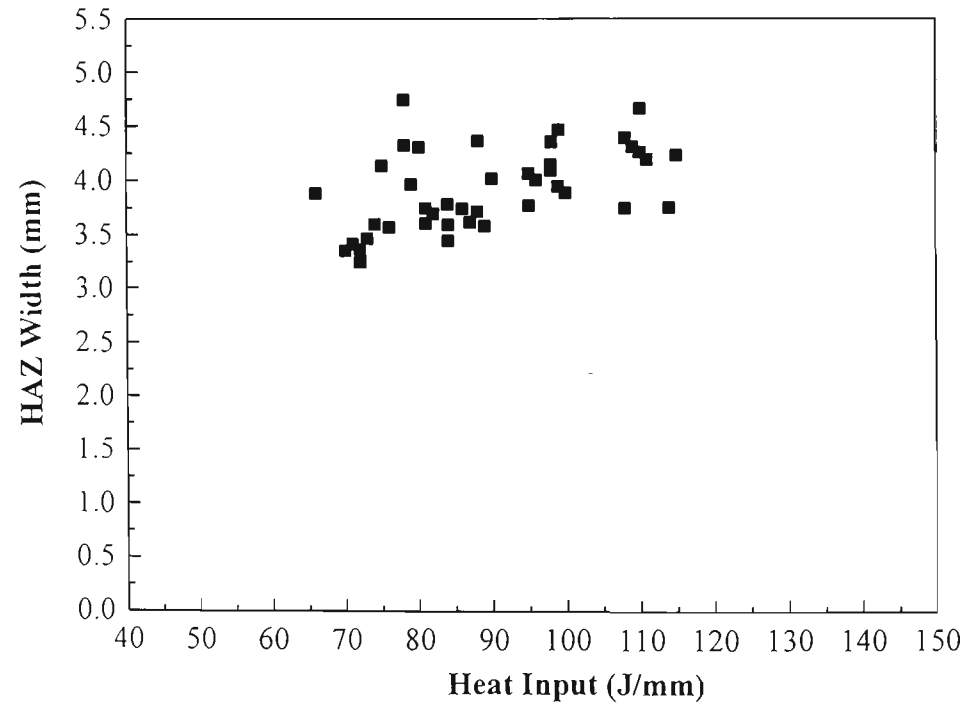

(b)

Figure 9.1 Effect of heat input on HAZ width for **(a)** ZA sheet steels; **(b)** ZHT sheet steel.

8.43, **F igure 8.44** and **F igure 8.46**). Although r ecovery o ccurred b elow 60 0°C, t he tensile strength is not reduced because recovery does not substantially change the dislocation density and only forms a polygonised subgrain structure (**Figure 3.3**). Increasing the peak temperature from 700°C to 900°C increases the grain size as a result of higher temperatures favoring the growth of larger α grains at the expense of the smaller grains. The amount of austenite formed also increases in this temperature range. The α grain size is then determined by untransformed α grains and α reformed from austenite on cooling. At 900°C the grain size decreases significantly due to complete α→γ phase transformation and γ→α transformation of cooling. Beyond 1050°C the γ grain growth is very rapid due to the high peak temperature reached and the longer dwell time at high temperatures. **Figure 8.46** shows the SEM micrographs of pearlite features in simulated samples at various peak temperatures. It is clear that the residual pearlite become partially spherodised o n heating t o a peak t emperature of l ess than 755°C. At peak temperatures 755°C or higher all the residual pearlite was dissolved and new pearlite was formed on cooling. The plate size of the fresh pearlite and grain size depend on the peak temperature. The higher the peak temperature, the coarser the pearlite plate and grain size. Thus, the high peak temperature gives rise to slower cooling rate, and a higher pearlite formation temperature.

The widths of the HAZ is in the range of 2mm to 5mm for both ZA and ZHT sheet steels at the various nominal heat inputs, as shown in **Figure 9.1**. The upward trend in HAZ width with heat input is more obvious for the case of ZA. For the case of ZHT the narrower heat input range makes this trend less evident. The differences in HAZ widths at the same nominal heat input occurred due to the effect of welding conditions and parameters on the effective heat input. The details will be discussed later.

9.1.3 Tensile Fractures

As expected, all tensile test samples fractured in the HAZ, as the HAZ of the cold rolled sheet steel experienced a localized softening [Welding Handbook Vol.1 1989]. Detailed studies of these fractures reveal that the fracture occurred in the grain-refined region (GR region) closed to the grain-coarsened region (GC region) (**Figure 8.9** and **Figure 8.10**). It is believed that the concentration of strain in this region led to the failure at

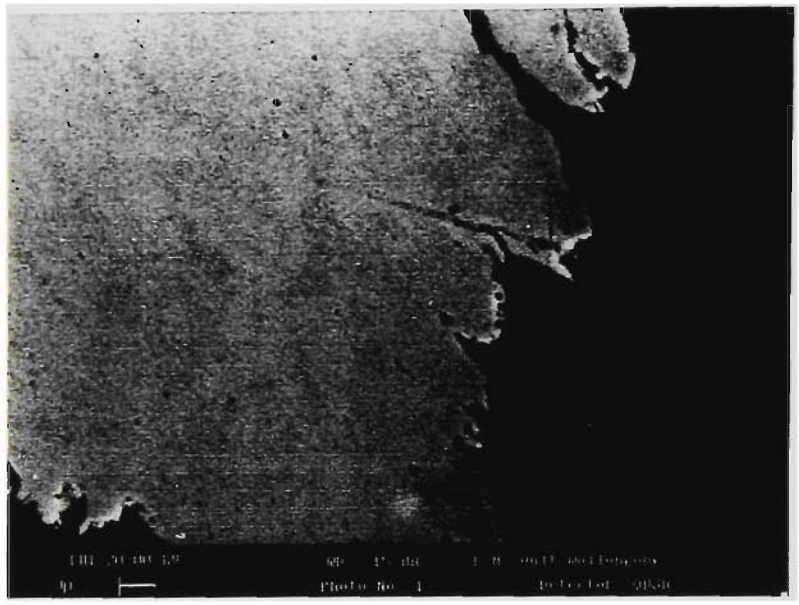

Figure 9.2 (a) SEM micrograph showing the void formation in fracture region.

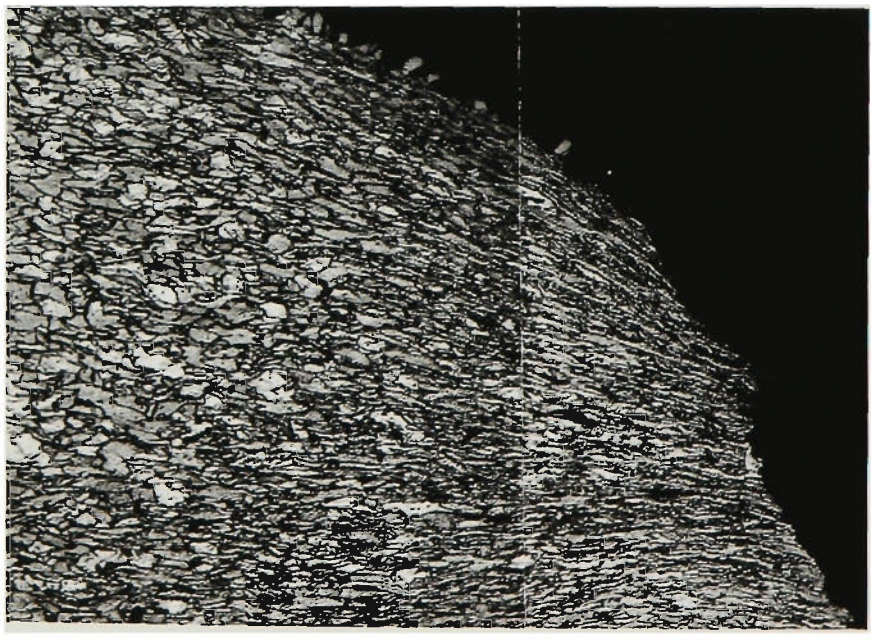

Figure 9.2 (b) Optical micrograph showing the voids formation in fracture region.

both decreasing stress and strain (elongation). Although the tensile elongations (engineering elongations) of the welded samples were low, the strain at the failure site was both locally extensive (**Figure 8.10**), and globally restricted and there was a relatively small volume of ductile metal within the gauge length (**Figure 8.9**). This volume increased with the increase of the heat input (**Figure 9.1**), but the strain during tensile testing always concentrated near the boundary of the GC region and GR region, preventing any substantial increase in fracture strain. However, tensile elongation increased slightly due to an increase of the HAZ volume associated with increased heat input (**Figure 8.3**).

The premature fracture in between the GC and the GR regions can be attributed to this strain concentration arising from discontinuities in hardness and structure in this region. The relatively sharp discontinuity in hardness and structure between the GC region and GR region results in preferential microvoid formation in this region as shown in **Figure 9.2 (a)**. The considerable amount of plastic deformation, including necking, observed in the fractured welds suggested that it is wholly a ductile fracture (**Figure 8.11** and **Figure 9.2 (b)**). It is quite interesting to note that nearly all the fractures occurred in the GR region but near the GC region not the IC region. In other words, the cracks were initiated at the interface between the GR and the GC regions. This maybe interpreted in terms of strain incompatibility between the harder and stronger GC region and softer and more ductile GR region. The strain incompatibility (or strain gradient) leads to the generation of geometrically necessary dislocations in the GR region and thus a concentration of strain in the GR region near the GC region. Necking then concentrates the stress in this region, therefore, this region experiences a higher total strain than other regions. As a result, voids are more likely to nucleate at the interface of the GC and the GR region, probably at micro-discontinuities, such as interfaces between the ferrite matrix and particles, such as pearlite or non-metallic inclusions [Courtney 2000].

It is well known that the strength of the HAZ mainly depends on cooling rate rather than heating rate because the cooling rate in conjunction with the grain size and prior thermal history determine the final microstructure of the HAZ [Easterling 1992]. In the steels investigated, the microstructure of the HAZ is determined by $\Delta t_{8/5}$ and the microstructure will determine the tensile properties. The value of $\Delta t_{8/5}$ is strongly

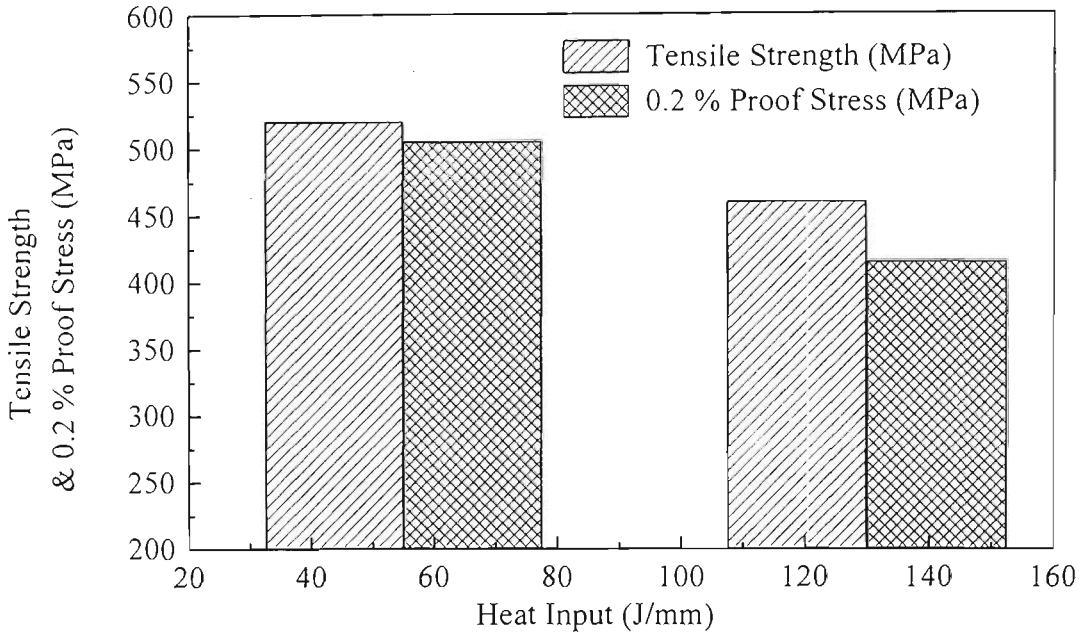

(a)

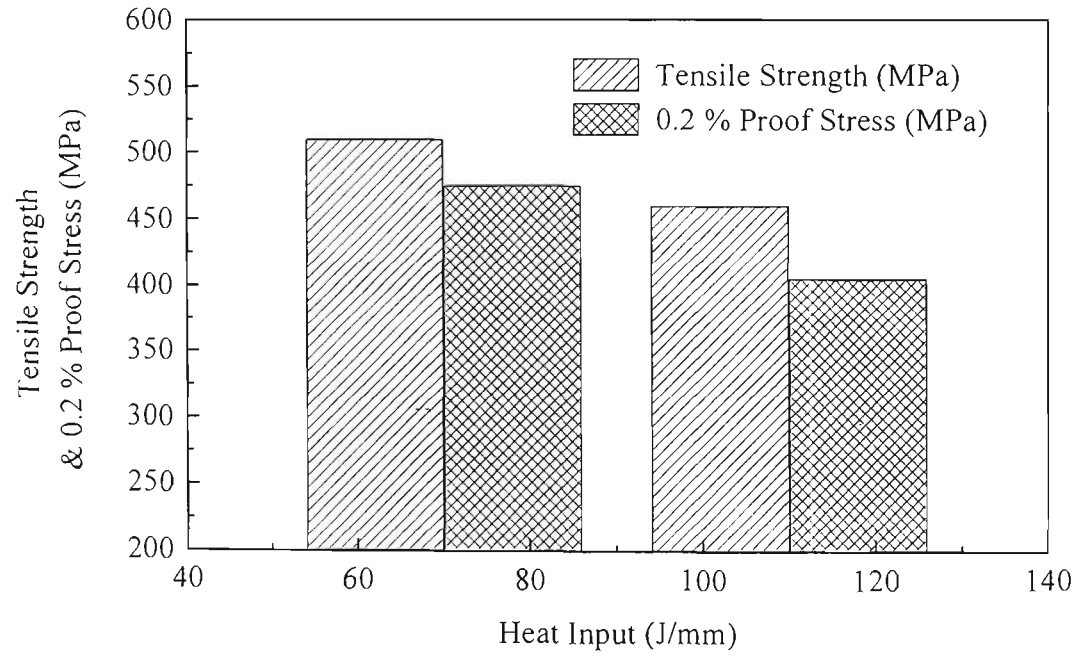

(b)

Figure 9.3 Effect of the heat input on tensile strength and 0.2 % proof stress for **(a)** ZA and **(b)** ZHT GMA welds.

dependent on heat input; the higher the heat input the larger the $\Delta t_{8/5}$ value, the lower the tensile strength and the mean HAZ microhardness (**Figure 4.9**). Any welding conditions and parameters affecting the effective heat input will affect the tensile properties of the HAZ and thus the effects of welding variables on tensile properties of the HAZ will be discussed in terms of their effect on real heat input.

9.1.4 Effect of Heat Input on Properties and Structures

9.1.4.1.1.1 Effect of heat input on properties

After GMA welding the tensile strength of G550 1.0 mm sheet steels decreased by an amount in the range of 125 to 185 MPa for ZA (with 645 MPa original longitudinal tensile strength), and 145 to 195 MPa for the ZHT (with 655 MPa longitudinal tensile strength) (**Figure 8.1**, **Figure 8.2** and **Table 7.3**). The strength loss depends on the heat input. As expected, the higher the heat input the larger the strength loss. Increasing the heat input had a detrimental effect on both tensile strength and proof stress. For GMA welded ZA steel sheet the lowest tensile strength (460 MPa) and proof stress (415 MPa) were obtained for the highest heat input (about 130 J/mm), with the highest strength (520MPa) and proof stress (about 505 MPa) were observed for the lowest heat input (55 J/mm). For GMA welded ZHT sheet steel, the lowest tensile strength of 465 MPa and proof stress of 405 MPa were obtained for the heat input of 110 J/mm and the highest tensile strength of about 510 MPa and proof stress of 475 MPa were achieved for the lowest heat input of 70 J/mm (**Figure 8.1** and **Figure 8.2**). The heat input has a slightly larger effect on the proof stress than the tensile strengths (**Figure 9.3**). The elongations of the GMA welds for both steel welds are in the range of 2.0~3.5% which are much lower than that for cold rolled sheet steels prior to GMAW, 9~12% (**Table 7.3**). The ductility of the GMA welds seemed to show a slight increase with increasing heat input (**Figure 8.3**). The mean microhardness of the HAZ decreased with increasing the heat input (**Table 8.4**).

Higher heat input results in a higher peak temperature (**Figure 8.37**), longer dwell time and a slower cooling rate $\Delta t_{8/5}$ (**Table 8.19** and **Figure 8.34 (a)**). Experiments recording

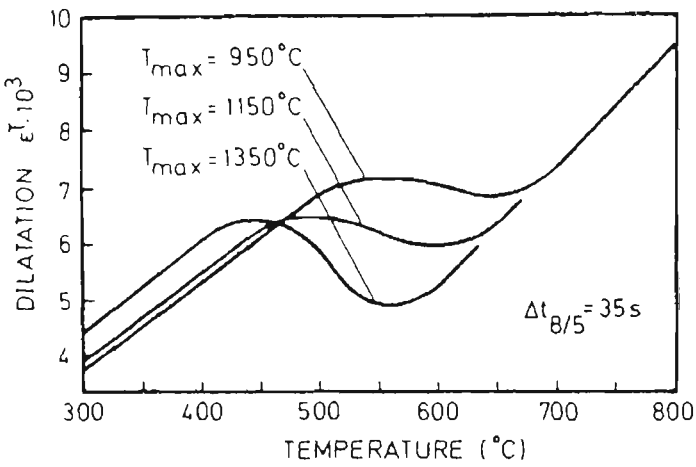

Figure 9.4 Temperature-dilatation curves for quenched and tempered steel showing the effect of peak temperature on $\gamma \rightarrow \alpha$ transformation temperature [After Anderson 1978].

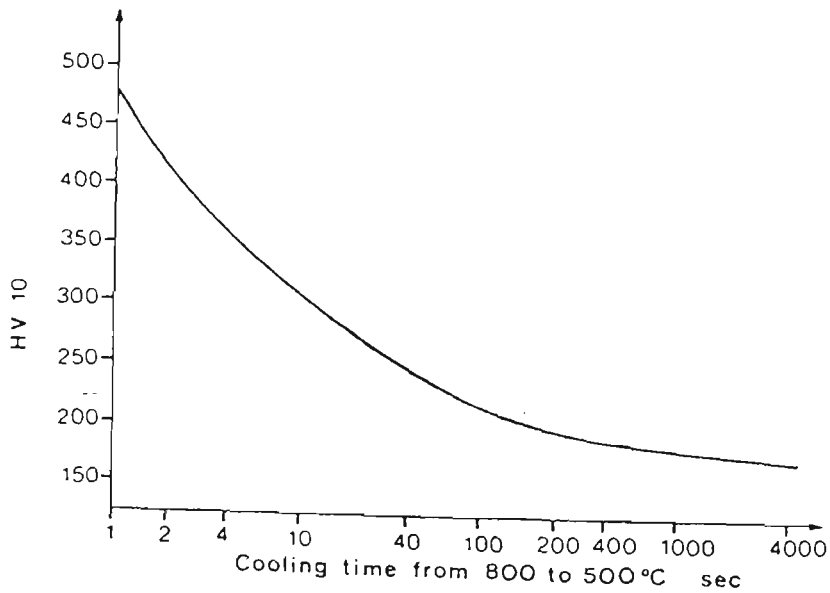

Figure 9.5 Effect of the cooling rate on mean microhardness in HAZ for medium strength 20 mm C-Mn steel [After Inagaki and Sekiguchi 1960-Lin's 74].

the welding thermal cycles indicated that the higher the heat input the longer the cooling time from 800°C to 500°C (**Figure 8.42**), but the relationship is not linear.

At the same distance from the fusion line, the higher the heat input the higher the peak temperature recorded (**Figure 8.37**). The higher the peak temperature and the larger the austenite grain size, the lower the $\gamma \rightarrow \alpha$ transformation temperature on cooling at a constant rate (**Figure 9.4**). Although grain coarsening increases the hardenability, the longer $\Delta t_{8/5}$ values for the higher heat input has a counteractive effect on hardenability, so that no significant hardening of the HAZ is expected with increasing heat input. Moreover, hardness measurement indicated a slight decrease with increasing heat input (**Table 8.4**). This result is supported by the ductility measurement of the welded sheet specimens: the higher the heat input, the larger the elongation at fracture (**Figure 8.3** and **Figure 9.5**). The yield stress of the base metal is much higher (about 625 MPa in the longitudinal direction) (**Table 7.3**) than the yield stress (about 415~505 MPa for ZA and 405~475 MPa for ZHT welds), indicating that the plastic deformation is confined to the HAZ. As a result, the volume of the HAZ will have a significant effect on the engineering tensile elongations. The greater the HAZ volume, the larger the elongation as the tensile fracture in the HAZ is ductile in nature. The volume of the HAZ with a high heat input is larger than that of the HAZ with a low heat input. Thus larger tensile elongations were obtained with the high heat input welds.

Although the engineering tensile elongations are very low, in the range of only 2.0~3.5%, regardless of the heat input, the tensile fractures of the HAZ are ductile in nature as can be seen in **Figure 8.9** in which the plastic deformation is rather uniform over the entire HAZ. **Figure 8.10** shows nearly perfect 45° shearing and **Figure 8.11** shows the ductile dimples. Thus, the apparent low engineering ductility of the HAZ is due to the small deformation volume of the HAZ. The true ductility of the HAZ would be much higher. This conclusion is supported by the tensile testing results of the simulated HAZ samples (**Table 8.20**), which show the elongations of the simulated HAZ samples are as high as 35%. The heat input has a larger effect on the proof stress than the tensile strength as mentioned before (**Figure 9.3**). This effect is again interpreted in terms of the volume of the HAZ. The larger the HAZ volume the more extensive the plastic deformation and the work hardening can occur. As a result, the

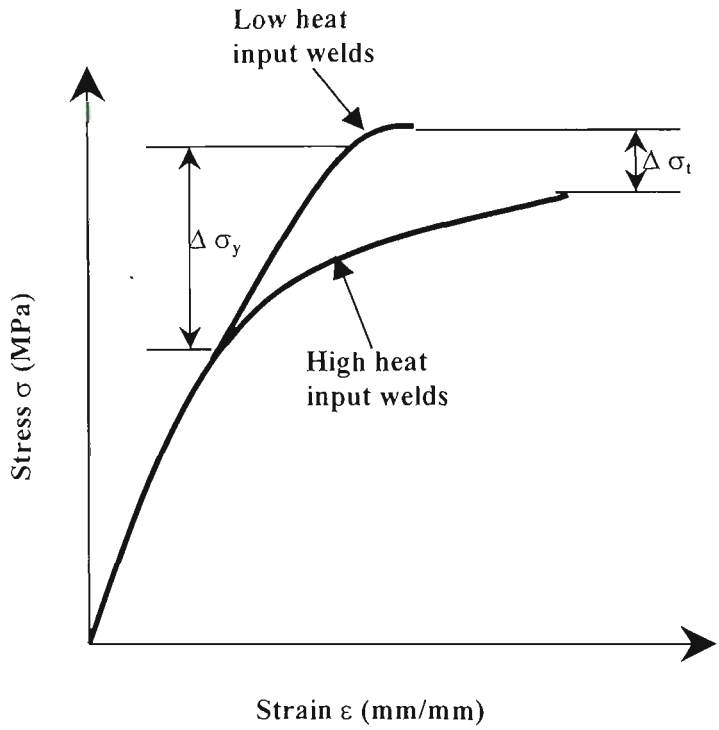

Figure 9.6 Comparison of Stress-Strain curves of tensile test samples of GMA welds at low and high heat input.

Weld metal → Base metal

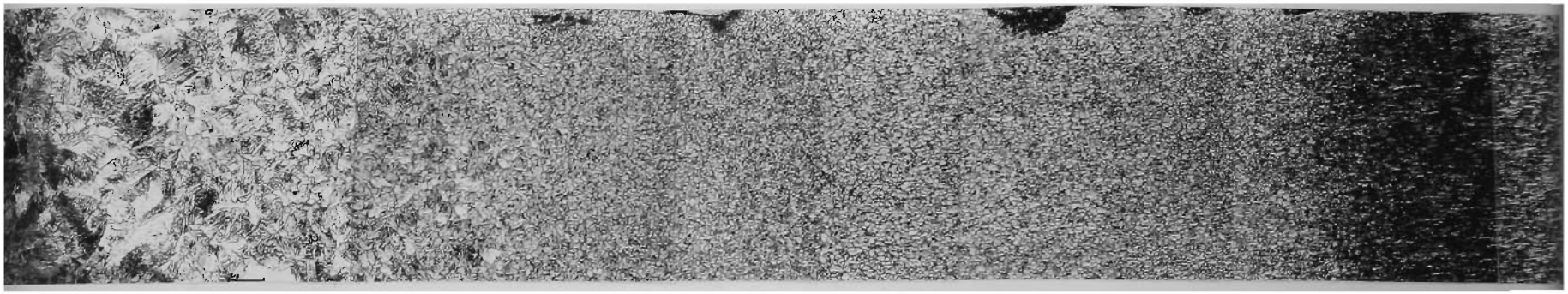

(a) at heat input of 80 J/mm.

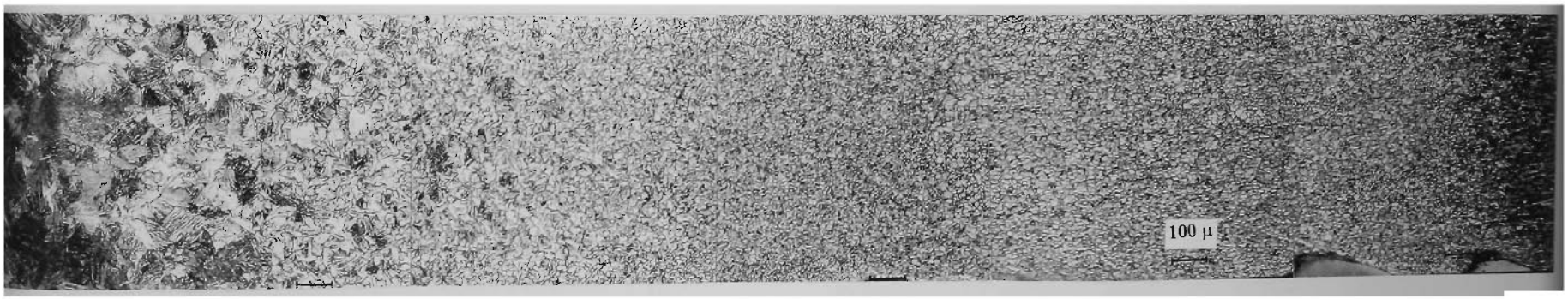

(b)at heat input of 120 J/mm.

Figure 9.8 Panoramic views of microstructures of HAZ for GMA welded ZINCALUME^{TM} sheet steel at different heat inputs.

difference between the high heat input and low heat input welds on the tensile strength will be smaller than its effect on the yield stress (**Figure 9.6**).

As expected, the HAZ mean microhardness decreased with an increase of the heat input as shown in **Table 8.4**. It is evident that the minimum mean microhardness values of the HAZ were obtained in the GR and IC regions. The GC region has the highest mean microhardness in the HAZ because of the coarse prior austenite grain size and therefore a lower temperature of $\gamma \rightarrow \alpha$ phase transformation. The HAZ experiences different rates of expansion and contraction as a result of the changes in temperature, which also changes the mechanical properties (**Figure 4.8**) even at the low temperatures of 500-600°C [Easterling 1992]. The magnitude of the dilatation stress caused by the $\gamma \rightarrow \alpha$ phase transformation on cooling depends on the transformation temperature, which is determined by the austenite grain size, the peak temperature reached and the cooling rate. The higher the peak temperature, the coarser the austenite grain size, the lower the transformation temperature and in turn, the larger the dilatation in transforming from the f.c.c to b.c.c. lattice (**Figure 9.4**). As a result, the dislocation density will be higher due to the lowering of the transformation temperature. The larger the grain size, the lower the transformation temperature will be because of the lack of nucleation sites for b.c.c ferrite. The grain-coarsened region in the HAZ experiences a thermal cycle with peak temperatures in the range of 1100–1500°C, which are beyond the austenite grain coarsening temperature for most steels. Thus extensive grain growth occurs. High heat inputs also result in a longer dwell time above the coarsening temperature (**Figure 8.34 (a)**). A coarser Widmanstatten ferrite side-plate structure was produced in the GC region in the HAZ at high heat input compared with low heat input (**Table 8.5**; **Figure 9.7** and **Figure 9.8**). In addition, the mean grain size in the GR region was higher. An increase in grain size in the GR region for the high heat input welding effectively reduces the yield strength of the HAZ because of the Hall-Petch effect: $\sigma_y = \sigma_i + kd^{-1/2}$, where the σ_i is a constant for a given material, and k represents the slope of σ_y vs $d^{-1/2}$).

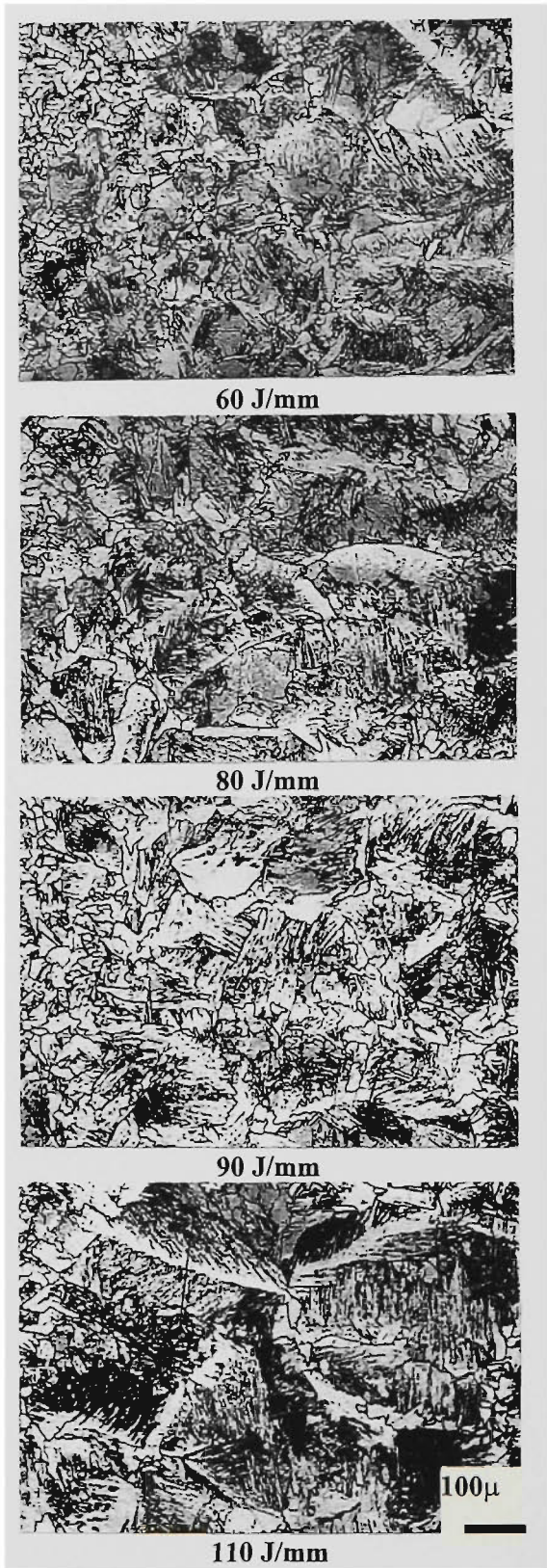

Figure 9.7 Optical micrographs of the grain-coarsened regions obtained with increasing heat input.

9.1.4.2 Effect of heat input on microstructures

Figure 9.7 shows typical optical micrographs of the grain-coarsened regions for the different heat inputs. As expected, a coarser grain size in the GC region was obtained with the higher heat inputs as a result of a high peak temperatures and slow cooling rates. Recorded welding thermal cycles (**Appendix II** and **Figure 8.34 (a)**) clearly show the effect of the heat input and other welding conditions on the temperature profiles. The lower the heat input, the steeper the temperature profile (fast cooling rate). The lower welding current of 63 ampere associated with the 50 J/mm heat input resulted in a relatively short cooling time $\Delta t_{8/5}$ = 4.04 seconds (**Table 8.19**). The higher heat input of 120 J/mm generated a less steep temperature profile (slow cooling rate) as a result of the higher welding current of 70 ampere and the longer cooling time $\Delta t_{8/5}$ = 7.89 seconds. In the GC region of the HAZ, the intragranular transformation of austenite resulted in the formation of bainitic ferrite and the overall structure was dominated by ferrite plates in the form of side-plates and low carbon bainitic ferrite. The width of the HAZ increased from 2.72 to 4.65mm as the heat input increased from 60 to 130 J/mm (**Table 8.5**). Macroscopically, the HAZ of the GMA welded cold rolled sheet steels may be divided into two parts, the GC region plus GR region; and the IC or partially transformed plus SC or tempered region (**Figure 8.16**). The former is about 60% of the total HAZ width (**Table 8.5** to **Table 8.9**). The heat input seems to have little effect on the ratio of these two regions. An increase in heat input increases the width of the (GC+GR) regions, as well as (IC+SC) regions. From panoramic views of the microstructures of the HAZ (**Figure 9.8**) show that the high heat input resulted in a coarser grain size, not only in the GC region but also in the SC regions due to the slower cooling. The increase of the GC region with increasing heat input appeared to accentuate the structural discontinuity between the GC and GR regions, resulting in increased strain partitioning to this site during tensile testing. The enhanced discontinuity in microstructure and hardness in high heat input welds generates a sharper strain gradient in the HAZ, which ultimately results in a lower tensile strength than the low heat input welds.

9.1.4.3 HAZ Simulations

Although the microstructure of HAZ has been successfully simulated (**Figure 8.43**), the tensile strength of the simulated HAZ are about 90 MPa lower than the HAZ of the real welds (**Table 8.20**). The measured cooling time $\Delta t_{8/5}$ (6.4 seconds) of the simulated HAZ thermal cycle is equivalent to real welding at a heat input of 70 J/mm (**Figure 8.42**). However, the GMA welds at a heat input of 70 J/mm have an average tensile strength of 500 MPa and a yield stress of 450 MPa (**Figure 8.1** and **Figure 8.2**) and an average microhardness of 148 $HV_{0.2}$ for the GR, IC and SC sub-regions (**Table 8.4**). In contrast, the tensile strength and yield stress of the simulated grain refined region are about 410 MPa and 350 MPa, respectively (**Table 8.20**), with an average microhardness of 135 $HV_{0.2}$ over the GR, IC and SC regions (**Figure 8.47**). The large discrepancies in the tensile strength, yield stress and microhardness between the real welds and the simulated samples maybe interpreted in terms of the 'brazing effect' or 'two-phase aggregate effect' in which a soft low strength 'braze metal' (the HAZ) is reinforced by the constraints applied by stronger surrounding materials (weld metal and steel base) [Honeycombe & Bhadeshia 1995]. In other words, the deformation of the welded samples is similar to the 'deformation of two-phase aggregates' [Courtney 2000]. The softer HAZ (as the plastic phase) is sandwiched by two harder materials: the weld metal and the cold rolled base metal. The weld metal and base metal ('elastic' phases) are much harder than the entire HAZ and thus they can provide constraints that effectively increase the plastic shear resistance of the HAZ. In effect, the weld metal and base metal restrict the softer HAZ from plastic deformation, and this gives rise to a secondary tensile stress in the HAZ. This secondary stress reduces the shear stress causing plastic flow and increases the yield and tensile strength of the HAZ. The magnitude of the secondary stress increases as the HAZ width decreases. A similar "pinning" effect can also occur in the actual HAZ in which the finer and more ductile GR is sandwiched by the harder and stronger GC and IC and SC regions. The 'pinning effect' causes a grain growth inhibition and dislocation slip pinning during plastic deformation, with an effective increase in tensile strength of whole HAZ. The strength of the HAZ increases as the volume of the softer layer (HAZ or GR region) decreases.

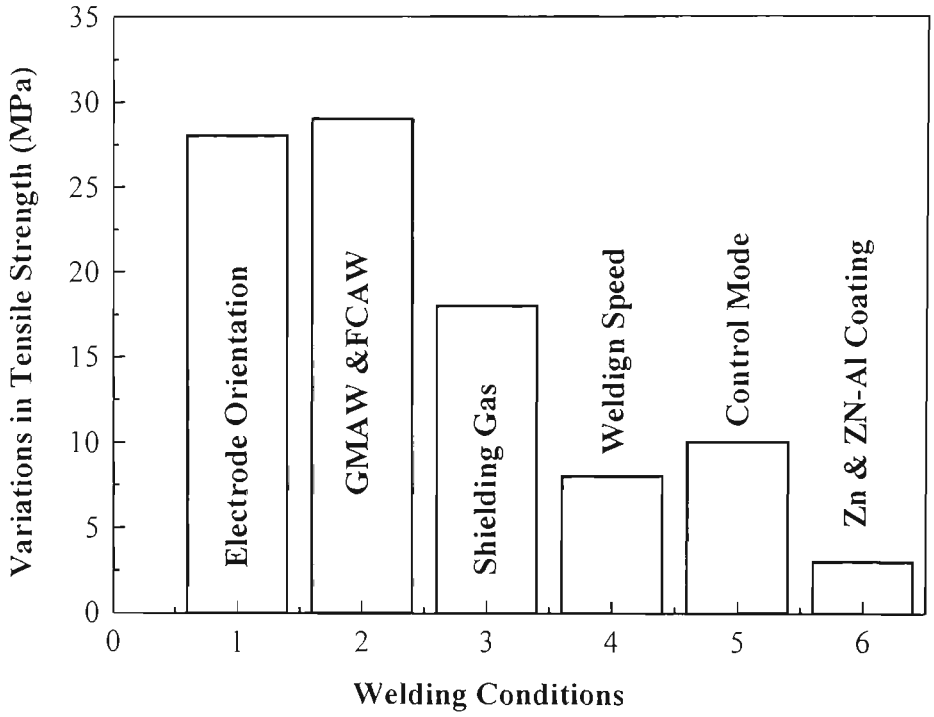

Figure 9.9 Variations in HAZ tensile strengths of ZA sheet steels at the heat input of 80 J/mm.

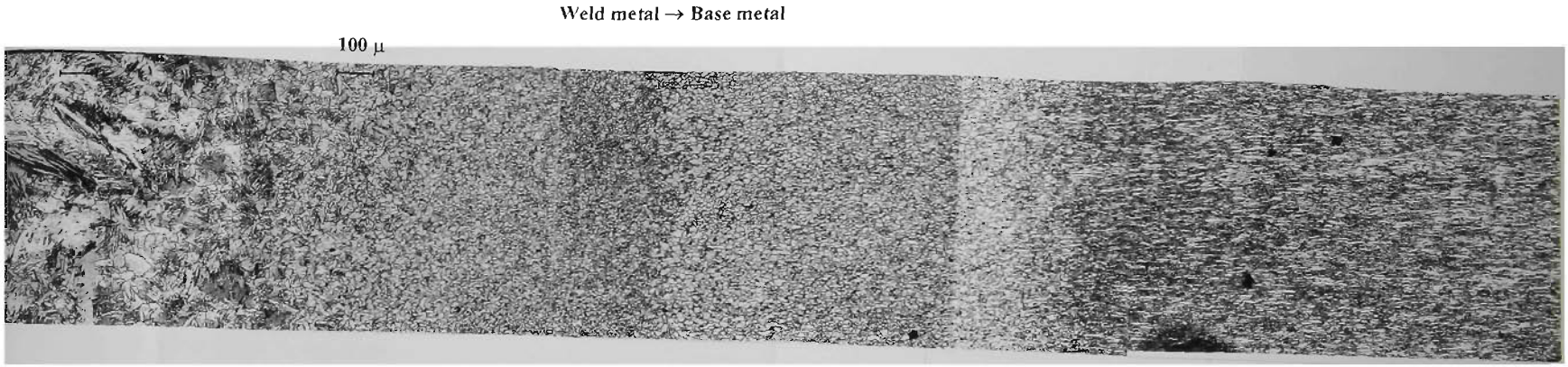

(a) HAZ of GMA weld

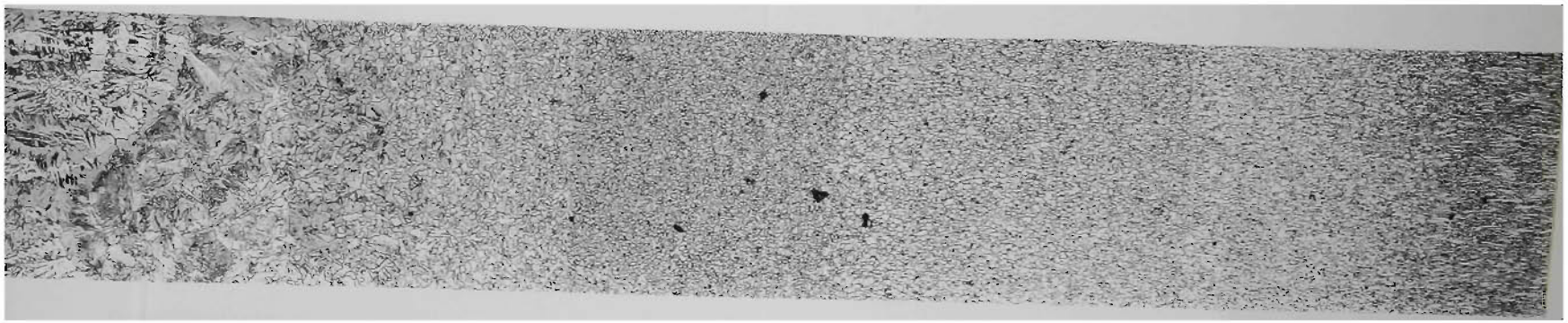

(b) HAZ of FCA weld

Figure 9.10 Panoramic views of microstructures of HAZ for GMA and FCA welded ZINCALUME™ sheet steel at heat input of 60 J/mm.

9.1.5 Effect of Welding Conditions on Properties

The effects of heat input on the tensile properties of the welds have been discussed earlier. It has been shown that the higher the heat input the lower the yield and tensile strengths. However, it was observed that even at the same heat input, different welding conditions resulted in different tensile strengths. This implies that the nominal or calculated heat input does not always reflect the effective heat input. Thus the real heat input is welding conditions dependent and it reflects the arc efficiency. The welding conditions which can affect the arc efficiency are the arc welding process itself, such as GMAW or FCAW, electrode orientation; shielding gases; welding speed; power supply control mode and the surface coatings on steel sheets. The overall effects of these welding conditions on the tensile strength are summarized in **Figure 9.9**, which shows that among the six welding conditions considered, the welding process, electrode orientation and shielding gas have major effects on tensile strength. The welding speed, control mode and surface coating of the steels have minor effects which may ignored. In the following sections, only the effects of the first three welding conditions on the tensile strength are discussed in detail.

9.1.5.1 Effect of GMAW and FCAW on properties

At the same nominal heat input of 50 J/mm (calculated using the heat flow equation: $\mathbf{q = \eta VI/S}$), the GMA welds showed a tensile strength of 520 MPa, which is higher than the tensile strength of 490 MPa for the FCA welds. The difference is about 6 % indicating that the FCAW process must have a higher effective heat input or a higher arc efficiency η than that of the GMAW process.

Figures 9.10 (a) and **(b)** are panoramic views of the microstructures of the HAZ for GMAW and the FCAW. It is clear that the grain size near the fusion line is coarser and the HAZ is wider for FCAW than for GMAW, consistent with the measured thermal cycles. The thermal cycles of the HAZ in the FCAW process exhibited a less steep temperature profile with a longer cooling time ($\Delta t_{8/5}$=5.57 °C/second) than the GMAW process ($\Delta t_{8/5}$=4.64 °C/second) for the same nominal welding conditions (**Table 8.19** and **Figure 8.34 (b)**). The widths of the HAZ of the FCA welded ZA and ZHT materials

(about 3.32mm and 3.88mm respectively), are larger than the GMA welds of the same sheet steels (about 2.72mm and 3.35mm respectively) (**Table 8.9**). The slower cooling rate and the larger HAZ width with FCAW indicate that the actual heat inputs of FCAW are higher than those of GMAW, although the nominal heat inputs have the same value. As a result, the tensile strength of the GMA welds was significantly higher than that of FCA welds at the same nominal heat input (**Figure 8.1** and **Figure 8.2**).

The higher arc efficiency η associated with FCAW could be a result of its self-shielded nature (not using external shielding gas); exothermic reaction in the weld pool driven by the high weld metal Al content; and the extensive slag formed on the surface of weld pool that will 'trap' the thermal energy within the weld pool.

It is well known that the shielding gas and its flow rate have a pronounced effect on the arc characteristics, mode of metal transfer, penetration, weld bead profile a nd weld metal mechanical properties [Welding Handbook, Vol.2, 1991]. The arc characteristics and the mode of metal transfer of GMAW and FCAW would be expected to be different because of the use of the external shielding gas in the former process and self-shielding in the latter process. Although the mechanism of how the shielding gas affects the arc efficiency is complex, the cold external shielding gas used in the GMAW process could absorb some heat and also blow away some arc heat during the welding and effectively reduce the arc energy efficiency. Instead of employing a cold external shielding gas, the self-shielded FCAW process uses the heat of the arc to protect the molten metal through the decomposition and the vaporisation of the flux core. Since the electrode material of the FCAW contains about 1.0% aluminum, the following exothermic reaction will occur and generate increased thermal energy in the weld pool.

$$\mathbf{Al + FeO \rightarrow Al_2O_3 + Fe + Heat}$$

Furthermore, the extensive flux blanket cover on the molten pool during FCAW could result in the reduction of radiation heat loss from the surface of the molten pool and form a relatively thick slag lays on the face of solidified weld bead, enhancing the heat conduction through the work piece. The more heat absorbed by the work piece, the slower the cooling rate.

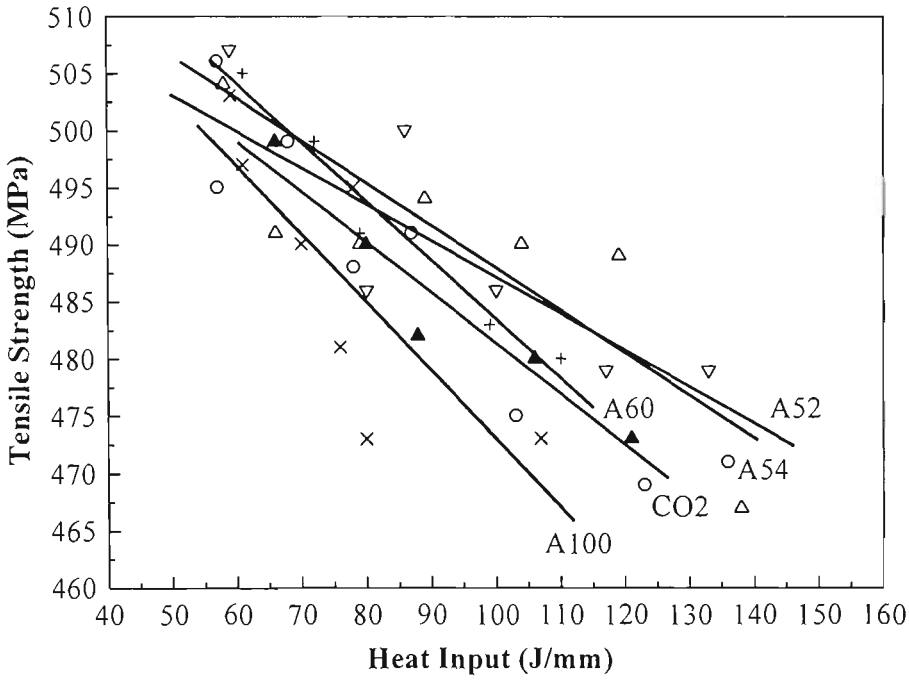

(a)

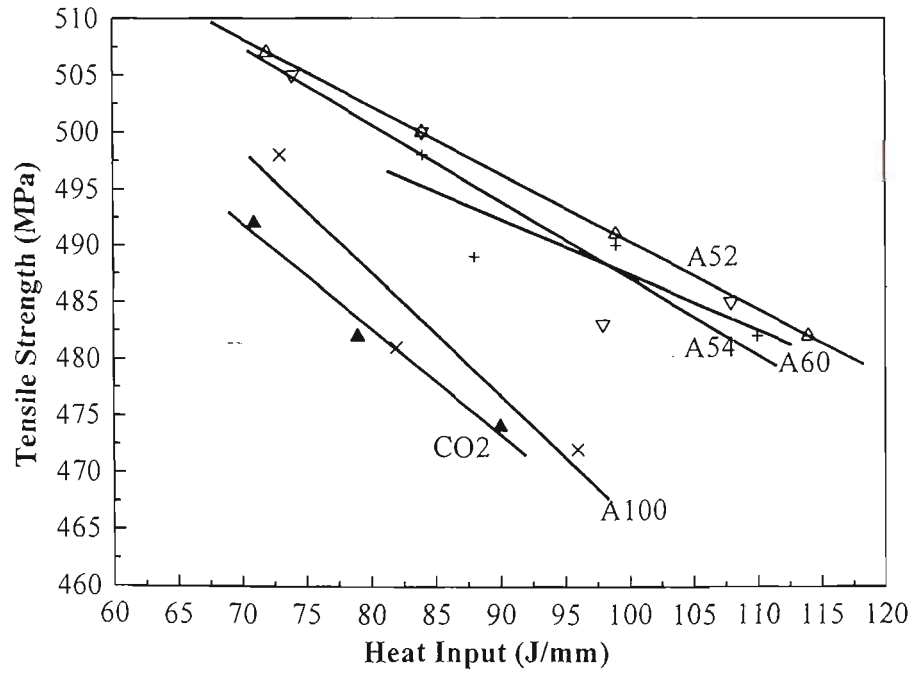

(b)

Figure 9.11 Effect of shielding gas on tensile strength for GMA welded **(a)** ZA sheet steel; **(b)** ZHT sheet steel.

9.1.5.2 Effect of shielding gas on properties

It is well known that the shielding gas plays an important role in arc welding in terms of controlling the mode of metal transfer, the weld bead shape, the penetration and the properties of the weld metal. The effect of shielding gases on tensile strength of the GMA welded of Z A and ZHT sheet steels is given in **Figure 9.11**. The use of the shielding gases A52, A54 and A60 (mixtures of Ar, O_2 and CO_2) have resulted in smaller strength losses than the use of the A100 (mixtures of Ar, CO_2 and He) and pure CO_2. This result maybe interpreted in terms of the thermal conductivities of the shielding gases used in the experiments. The higher thermal conductivity, the higher arc efficiency and thus the higher the strength loss. It is well known that He has a higher thermal conductivity (1.25 kcal/kg) than Ar (0.125 kcal/kg), O_2 (0.128kcal/kg) and CO_2 (0.197kcal/kg) (**Table 2.1**). It is also known that He produces an uniform arc plasma. A gas with a high thermal conductivity can reduce the diameter of the conducting core of the arc and increase the arc voltage and in turn, reduce the arc stability [Norrish 1992]. CO_2 is a chemically active gas and has an exothermic reaction at the work piece resulting in superheating of the molten filler metal and creation of deep penetration and a fluid weld pool. Gas mixtures with a high concentration of CO_2 result in a higher voltage drop for a given wire speed and consequently increase the heat input although this is reflected in the 'nominal' heat input. Thus, as observed, shielding gases containing He and pure CO_2 are expected to generate larger strength losses in the HAZ than other shielding gases.

9.1.5.3 Effect of electrode orientation on properties

As reported in Chapter 8 the backhand technique resulted in a higher tensile strength loss than the perpendicular and forehand techniques. The latter resulted in the lowest tensile strength loss at the same nominal heat input (**Figure 8.4** and **Table 8.1**). This result indicates that the actual heat input of backhand welding is higher than that of the other two orientations. This is consistent with the observation that backhand welding also generated the widest HAZ and largest volume of the weld metal (**Table 8.6**) and the largest $\Delta t_{8/5}$ among these three orientations (**Figure 8.36 (a)** and **Table 8.19**). This trend is also supported by the cross-weld microhardness tests, as shown in **Figure 8.14**

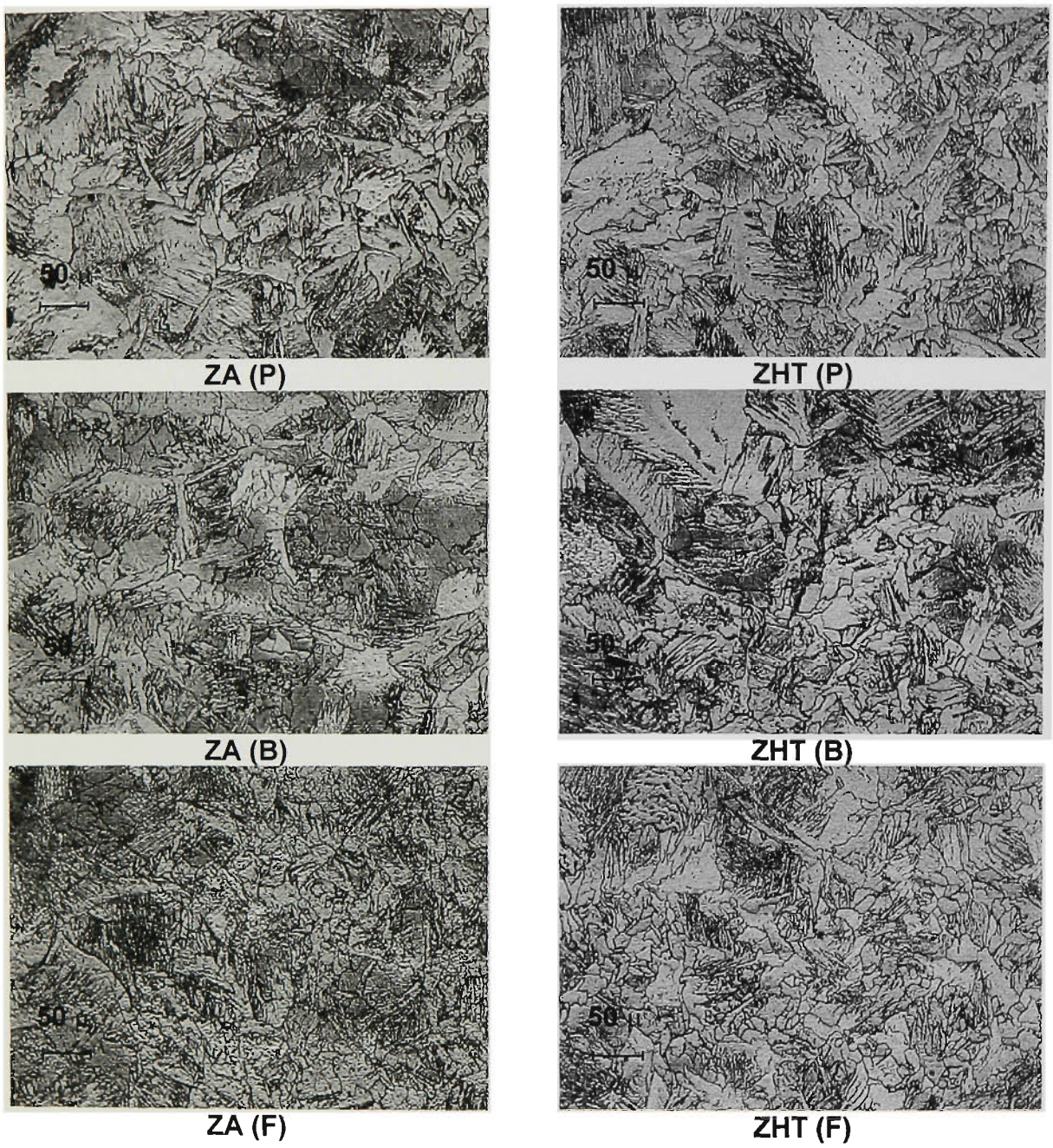

Figure 9.12 Optical micrographs of the grain-coarsened regions obtained for the different electrode orientations for the ZINCALUME and ZINC-HI-TEN sheet steels.

(a) for the ZA welds. The backhand weld shows the largest softened HAZ and the lowest weld bead hardness.

Typical microstructures of the GC region of the HAZ produced using the three welding techniques are shown in **Figure 9.12**. It can be seen that the backhand technique produced the coarsest grains, consistent with the tensile test results. This observation reinforces the conclusion that the backhand technique produces the largest actual heat input of the three welding techniques. This result provides metallographic evidence that backhand GMAW produces a higher effective heat input than perpendicular and forehand welding at the same nominal heat input.

The higher actual heat input produced by the backhand welding technique could be caused by two factors. First, the concentration of the thermal energy back onto the weld bead and deposition of weld metal onto the molten pool result in the enhancement of turbulence in the existing weld pool and increases the melting of the base metal (**Table 8.6**). The concentration of thermal energy into the weld pool and its higher volume are more likely to slow the cooling rate of the weldment and effectively increase the heat input.

From basic welding physics [AWS, Welding Handbook, Vol. 1, 1989]: when using an arc as a welding heat source, two distinct heat transfer processes should be considered: heat is transferred from the source to the surface of the work piece first and then heat is transferred by conduction from the contact area to colder regions of the metal. These two processes are somewhat competitive in terms of the energy density of the heat source. Therefore, there are two efficiencies that should be considered when dealing with the welding heat flow; they are the heat transfer efficiency f_1 (from 0.8 to 1.0 for most consumable electrode arcs) and the melting efficiency f_2. The factor f_1 and f_2 have following relationship:

$$f_2 = \frac{QA_w}{H_{net}} = \frac{QA_w v}{f_1 EI}$$

where Q = specific theoretical quantity of heat.

Table 9.1 Results of the welding parameters recorded during the GMAW of ZA and ZHT sheet steels using three different electrode orientation, perpendicular (P), backhand (B) and forehand (F).

Cide No.	Setting	Heat Input (J/mm)	Welding Voltage (V)	Welding Current (A)	Wire Feed Rate (m/sec.)	Ave. Tensile Strength (MPa)	Ave. Proof Strength (MPa)
ZINCALUME™	1.0 mm						
Y11	164279P	84	16.13	52.37	1.78	499	466
Y36	164279B	78	16.40	47.58	1.78	483	439
Y55	164279F	80	16.07	49.66	1.74	508	473
Y13	164298P	97	16.27	59.65	2.10	493	451
Y37	164298B	94	16.42	57.23	2.22	468	419
Y56	164298F	100	16.18	61.80	2.25	491	446
Y15	1642118P	110	16.25	67.44		490	460
Y38	1642118B	112	16.41	68.08	2.72	469	422
Y57	1642118F	115	16.12	72.02	2.72	483	434
Y17	1642138P	124	16.19	76.35	2.93	476	428
Y39	1642138B	129	16.58	77.80	3.25	460	401
Y58	1642138F	134	16.98	84.10	3.23	479	432
ZINC-HI-TEN™	1.0 mm						
Y27	165298P	86	16.67	63.61		498	458
Y48	165298B	87	16.21	66.17	2.28	488	440
Y62	165298F	81	16.15	62.47	2.26	507	475
Y29	1652118P	96	16.63	71.49		489	441
Y49	1652118B	100	16.20	76.29	2.77	498	457
Y63	1652118F	98	16.39	73.63	2.74	488	432
Y31	1652138P	108	16.58	80.77		481	429
Y50	1652138B	110	16.16	84.41	3.25	466	405
Y64	1652138F	109	16.22	83.10	3.24	491	444

H_{net} = net energy input (J/mm).

A_w = cross section of weld metal area (mm^2).

E = welding voltage (volts).

I = welding current (amperes).

v = travel velocity of heat source (mm/sec).

and $Q = \dfrac{(T_m + 273)}{300000}$

where T_m equals the melting temperature of the metal (°C).

When Q, H_{net} and f_1 are kept constant by using the same welding process, material and energy input, a high melting efficiency f_2 leads to a larger volume of weld metal. Therefore, the backhand welding might be expected to have a higher melting efficiency than the perpendicular and forehand welding, should result in a higher actual heat input than the other two welding techniques.

The change in electrode orientation may also change the arc characteristics. Since the weld volume and the weld thermal cycle have been shown to be a function of the particular values selected for current, voltage and speed, rather than heat input alone [Knhno and Jones 1978; Ahmed and Jarvis 1998; Wingrove, Dunne and Kennon], it is therefore expected that the change in welding orientation could affect the absolute values of welding current and voltage as shown in **Table 9.1**. It is thought that the "drag electrode" (backhand technique) can shorten the arc length [AWS, Welding Handbook, Vol. 2, 1991] as has been observed in the GMA welded ZHT welds. Compared to the perpendicular and forehand welding, the backhand welding of the ZHT sheet results in a shorter arc length and in turn produces a slight decrease in voltage and an increase in current to keep the product of **VI** constant at a given speed, in order to maintain a constant nominal heat input. Conventional theory relates heat input to arc power (i.e. **V**×**I**) but it has been found elsewhere that current alone may have a more significant effect on fusion than power. The increase in arc current may therefore have more effect on actual heat input than the reduction in voltage. For the backhand welding of ZA sheet, however, the opposite results of a longer arc length, higher voltage drop and lower current were obtained. So this factor cannot contribute to the increased effective

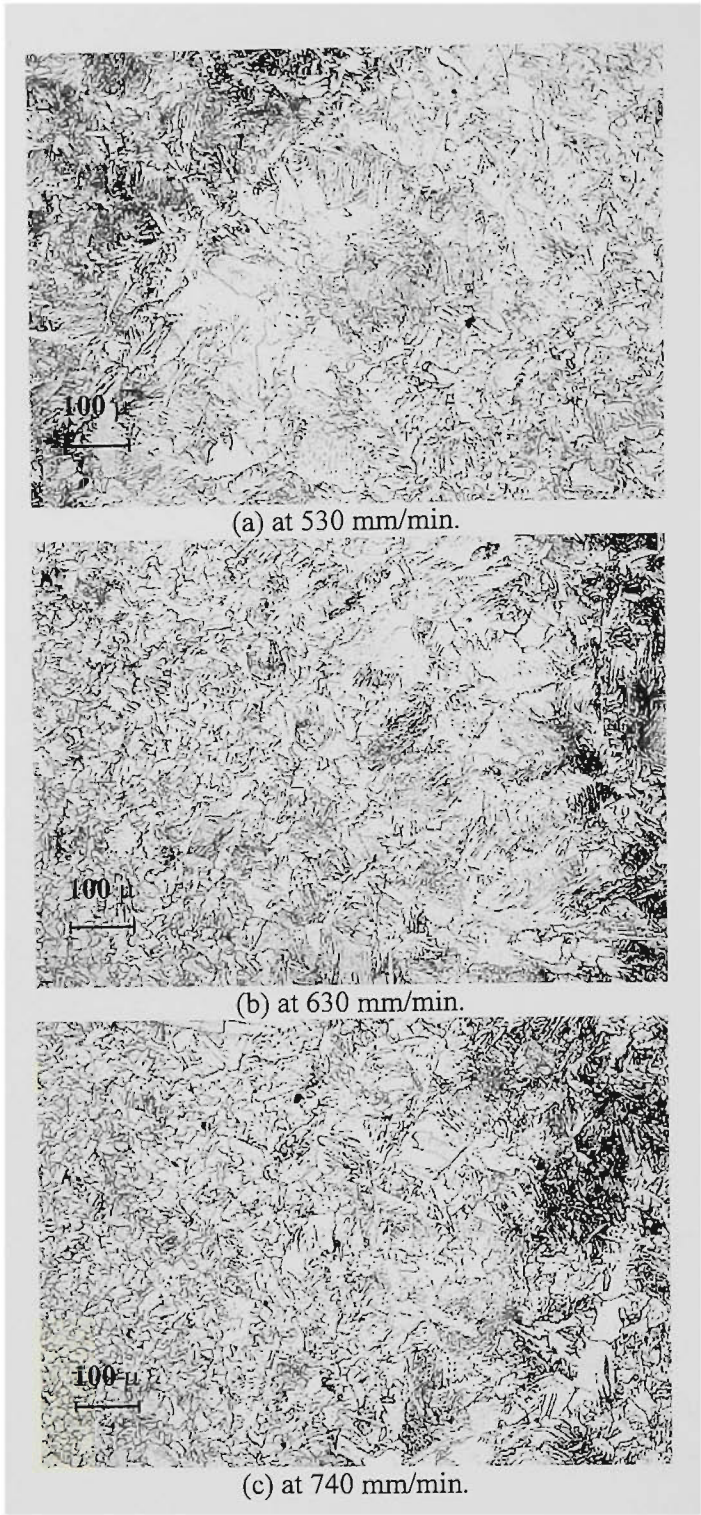

Figure 9.13 Optical micrographs showing the GC regions of GMA welded ZA steel at the heat input of 80 J/mm with various travel speeds.

heat input in this case. Different type of coatings may cause the above unexpected results, as the coating can affect the arc length and the voltage drops by vaporising different elements into the arc column. In the case of Zn coating, only Zn vapour entries the arc column, whereas in the case of a Zn-Al coating both the Zn and Al are vaporised into the arc column. In addition, a higher weld metal area is obtained for the ZHT sheet welds than the ZA welds (**Table 8.6**) when the heat input and welding technique are kept constant which indicated that the melting efficiency f_2 for the ZHT sheet steel welds could be higher than the ZA welds due to its lower thermal conductivity and melting point of the Zn coating than the Zn-Al coating.

9.1.5.4 Effect of Welding Speed on Properties

At a constant nominal heat input, an increase of the travel speed for the GMA welded ZA sheet steels has little effect on tensile strength, even though a reduction in a HAZ width was observed (**Table 8.2** and **Table 8.7**). Furthermore, the microhardness of the HAZ did not seem to be affected significantly by the change in travel speed (**Figure 8.14 (b)**).

To maintain the heat input constant, the welding travel speed and the welding current must be increased simultaneously. As a result, this increases the arc force, and hence displacement of molten metal from the arc impingement zone. Therefore, deeper levels of the sheet are directly exposed to the arc resulting in an increase in both the volume of the crater formed under the arc and the initial cross-sectional area of the weld pool. It is expected that the thermal gradients become steeper and cooling more rapid for higher welding speeds (**Figure 5.9**). Indeed, the recorded thermal cycles show a shorter $\Delta t_{8/5}$ of 5.51 seconds at the travel speed of 740 mm/min compared to 7.18 seconds for a travel speed of 500 mm/min and, in turn a reduction in HAZ width (**Table 8.7**). This result is consistent with a previous study of the effect of welding speed on HAZ dimensions [Ahmed et. al. 1998]. At the same distance from the fusion line, a higher peak temperature was recorded with the higher travel speed than with the lower travel speed (**Figure 8.39**). The higher the peak temperature, the coarser the grain size in GC region, especially close to the fusion line as shown in **Figure 9.13**. However, the change in

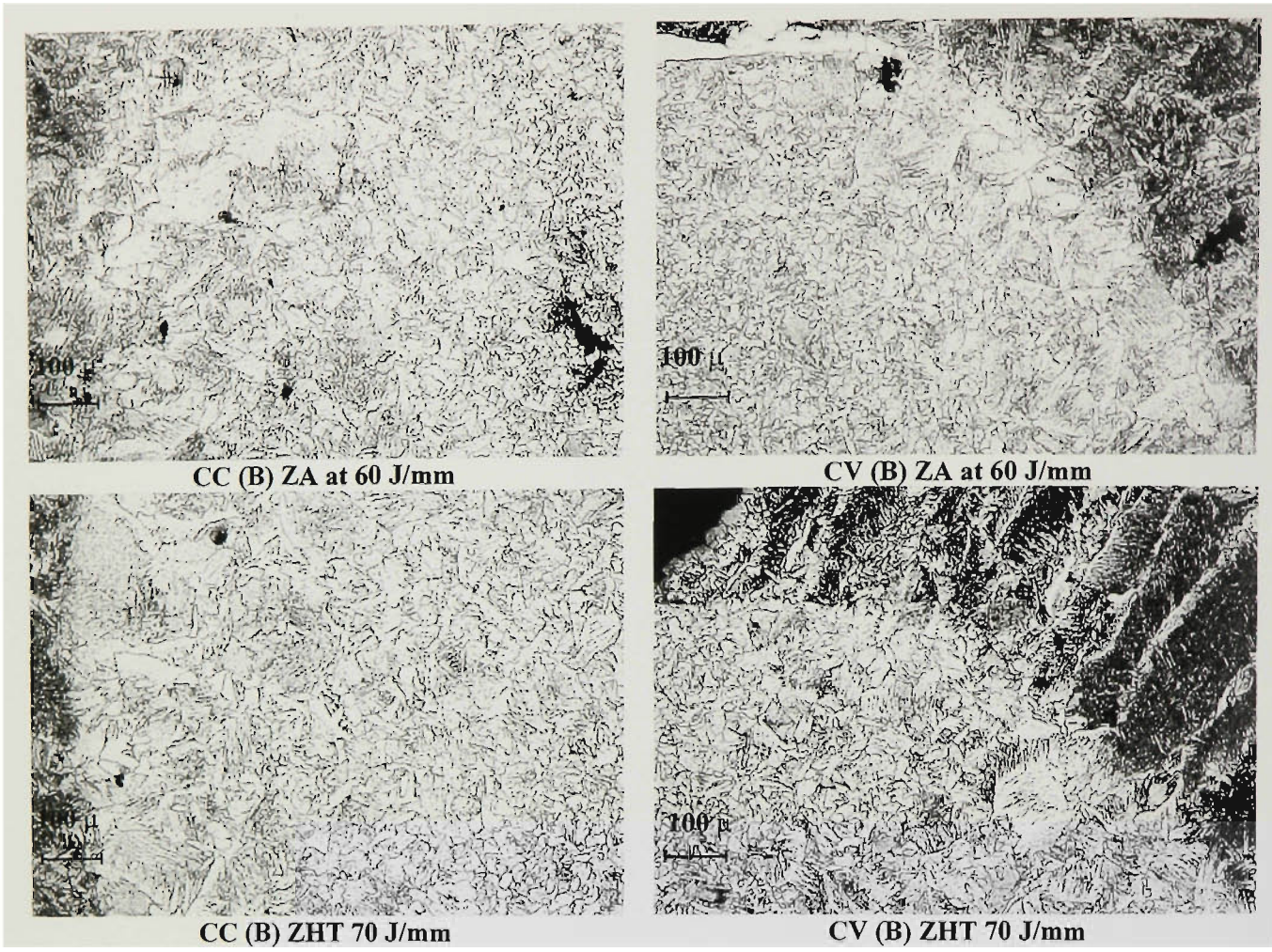

Figure 9.14 Optical micrographs showing the GC regions of GMA welded ZA and ZHT using current control **(CC)** and constant voltage **(CV)** control mode.

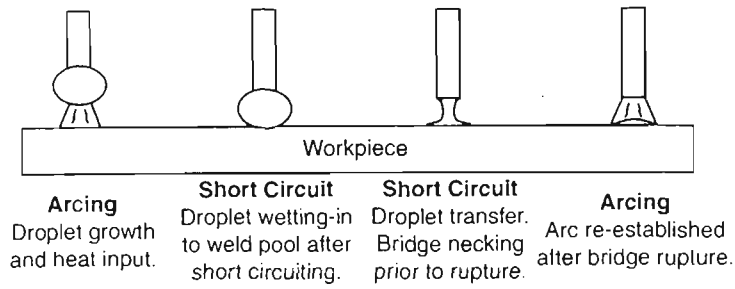

(a)

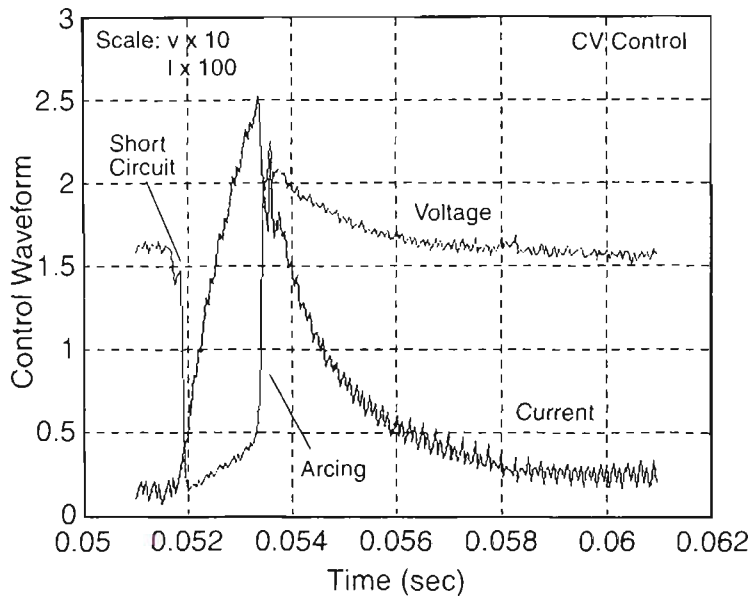

(b) Constant voltage control

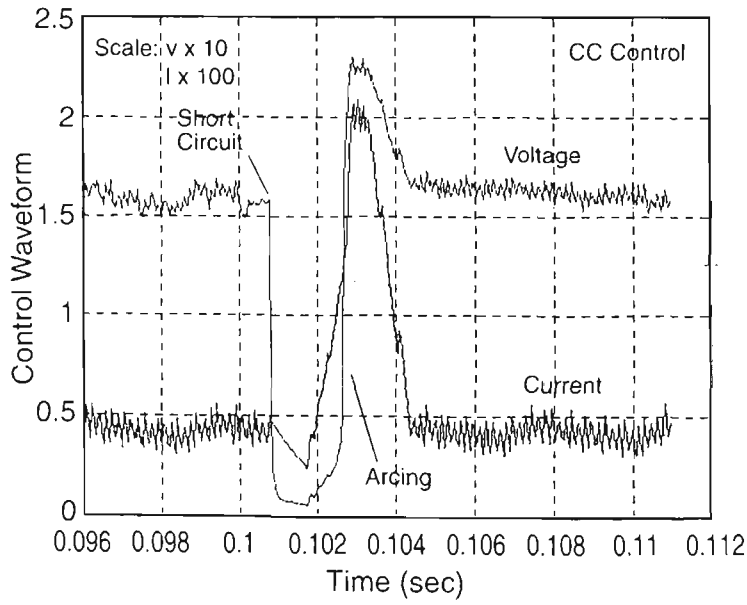

(c) Current control

Figure 9.15 (a) Schematic illustration of the process cycle for dip transfer in GMAW; **(b)** and **(c)** Typical constant voltage control and current control waveforms [After Huang et. al. 2002].

microstructure with the high speed welding has little effect on microhardness and tensile strength.

It can be concluded that a higher welding speed can be used for GMAW of Zn alloy coated sheet steels to increase productivity without any marked changes in the weld metal area, the HAZ width and the mechanical properties of the welded sheet. This conclusion is consistent with result of a previous study of bead-on-plate welding [Ahmed et. al. 1998].

9.1.5.5 Effect of Welding Control Mode on Properties

Of the two control modes: constant voltage mode and current control mode, the current control mode resulted in the larger strength loss, lower microhardness values in the weld metal and HAZ, a wider HAZ and a larger weld metal area than the constant voltage mode, at the same nominal heat input (**Table 8.3** and **Table 8.8**; **Figure 8.14 (c)**). However, the effect of the welding control mode on tensile strength was relatively small (**Figure 9.9**).

Figure 9.14 shows optical micrographs of the GC regions for both the constant voltage and current control modes. It is clear that a coarser grain size was obtained on using the current control mode rather than using constant voltage control mode, indicating a slower cooling rate for the GMA welds using the current control mode at the same nominal heat input. The increase in the HAZ width from 2.9mm to 3.29mm for ZA welds and 3.42mm to 3.68mm for the ZHT welds also confirms that the cooling rate decreased with the use of the current control mode.

The higher actual heat input produced by the current control mode can be interpreted in terms of the electric control waveform. Unlike the constant voltage mode which uses high levels of current during metal droplet transfer and results in low arc heating, the current control mode can control the heat input to the work piece through the arcing current as showing in **Figures 9.15 (a)** and **(b)**. Use of a current control waveform enables decoupling of the short circuit and arcing periods by reducing the current after the initial short circuit to assist the wetting in of the droplet and increasing the current to

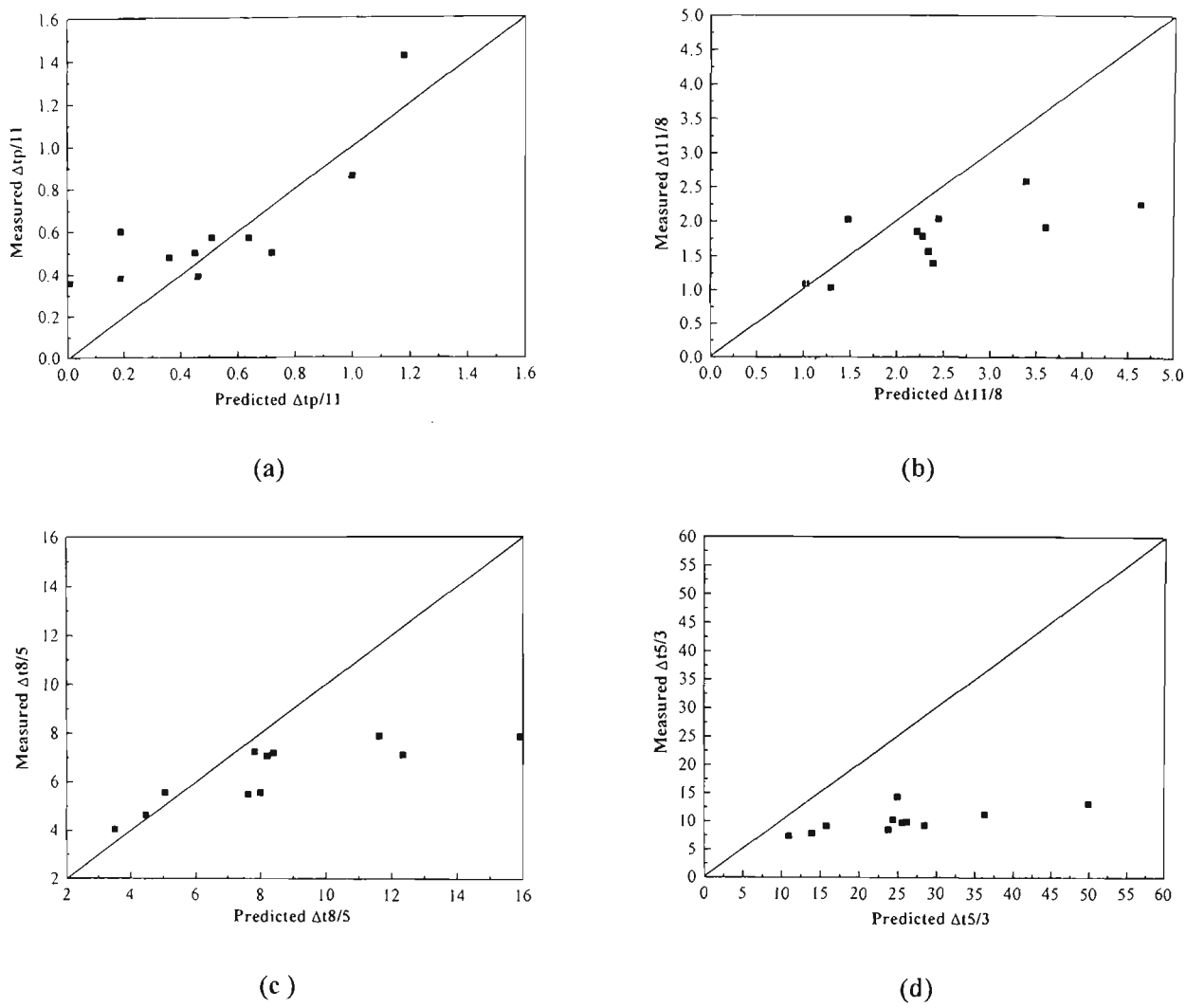

Figure 9.16 Comparison between measured and predicted cooling times using Rykalin-2D calculation for the simulated HAZ; **(a)** from the peak temperature to 1100°C ($\Delta t_{P/11}$); **(b)** from 1100°C to 800°C ($\Delta t_{11/8}$); **(c)** from 800°C to 500°C ($\Delta t_{8/5}$); and **(d)** From 500°C to 300°C ($\Delta t_{5/3}$).

the clamp level until bridge rupture, as well as applying a current pulse to develop the droplet in the arcing period [Huang et. al. 2002]. The more arc energy during the arcing period, the greater the effective heat input.

9.1.5.6 Effect of Zn Alloy Coatings on Properties

Although ZA has a higher thermal conductivity than ZHT, the coating thickness is too small to have a significant effect on properties. In this study, only a minor difference was observed in the $\Delta t_{8/5}$ (7.18 sec for the ZA welds and 7.25 sec for the ZHT welds) with almost the same thermal cycles at a heat input of 80 J/mm (**Table 8.18** and **Figure 8.36**). Although the HAZ width of the ZHT weld was larger and the microhardness was slightly lower than the ZA weld, the tensile strength seems to have been unaffected (**Figure 8.6**). It is likely that the Zn and Zn-Al coatings are not thick enough to influence the critical cooling rate and thus the tensile strength. However, the microhardness of the HAZ and the shape of the weld metal of the ZA and the ZHT GMA welds are affected by the Zn and Zn-Al coatings (**Figure 8.14 (e)** & **Figure 8.23 (a)**). The slightly higher hardness of the weld metal and the HAZ could be caused by the slightly faster cooling rate (**Table 8.19**) and the higher Al content of 0.4 % ~ 0.6 % picked up in the ZA GMA welds compared to 0.02 % ~ 0.04 % in ZHT welds (**Table 8.11**).

9.1.6 Comparison of Measured and Predicted Thermal Cycles

At the low heat inputs the thermal cycles predicted using the Rykalin-2D model agrees fairly well with the measured thermal cycles. However, at high heat input the predicted thermal cycle indicates a much slower cooling rate than that measured (**Table 8.19** and **Figure 8.40**). It was found that the predicted cooling times at high temperatures agree well, but agreement is poor for low temperatures (**Figure 9.16**). This difference is probably the result of the use of a jig to clamp the work piece during the welding process. The steel jig was about 10 mm away from the weld central line and has more effect as a heat sink for the high heat inputs welds than for the low heat input welds. The jig is expected to have a larger effect on low temperature measurements at low

temperatures than at high temperatures, consistent with the increasing difference between predicted and measured temperatures at lower temperatures in the cycle.

9.2 WELDABILITY OF Zn ALLOY COATED SHEET STEEL

9.2.1 Surface Appearance of Zn alloy Coated Steels Welds

The surface appearances of the GMA weld bead on the ZA and ZHT steel sheets are generally satisfactory, as shown in **Figure 8.17**. Although a small amount of spatter was present on the surface of the sheet and the weld bead, there were no obvious macro-defects. The welds appeared to be continuous and the weld bead was sound and smooth. However, welding ZHT sheet steel generates a large amount of Zn oxide 'like parachutes' floating in the air and some of the Zn oxide was redeposited onto the surface of the weld bead and sheet.

There was no Zn penetration cracking observed in the GMA and FCA butt welded ZA and ZHT sheet steels, although the Zn penetration cracking was reported for the GMA welded galvanised steel fillet welds before (**Figure 6.1**). This indicates that the molten Zn penetration cracking is dependent of the welding joint type as mentioned in Chapter 6.

9.2.2 Weld Bead Geometry And Composition

In order to understand the formation of weld metal geometry (profile), the surface tension of the weld pool must be taken into account. If the surface tension is high, the molten metal surface becomes convex. On a flat plate, the liquid pulls away at the edges, and the angle of contact between it and the solid surface approaches 90°. In other words, the molten weld metal does not wet the solid parent metal. If the surface tension is low, the contact angle is small and the molten metal has good wetting characteristics resulting a flatter surface of the weld pool. However, neither of these extremes is desirable in welding practice [Gourd 1980].

The surface tension of the weld pool in arc welding is controlled by the oxygen level of the weld metal, which in turn, is determined by the atmosphere. The relationship between the oxygen content and the surface tension and hence the weld bead geometry is shown in **Table 9. 2.**

Table 9.2 Effect of oxygen content on surface tension of weld bead profile [After Gourd 1980].

Oxygen content	High	Medium	Low
Surface tension	Low	Medium	High
H–V fillet-weld profile	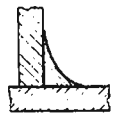	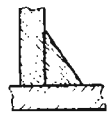	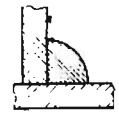

It is observed, however, that only the welding process and shielding gases have a major effect on the oxygen content of weld metal and bead geometry and they are discussed in detail below.

9.2.2.1 Effect of welding process

The weld bead profile of FCA welds was generally flatter and smoother than GMA welds and also contained significantly lower oxygen and higher nitrogen contents (**Figure 8.21** and **Table 8.13**). In this case the flatter and smoother weld beads cannot be a result of oxygen lowering the surface tension of the weld pool because the oxygen level is too low. It seems more likely that the bead shape obtained in the FCAW process is a consequence of the extensive slag cover on the face of the weld bead [AWS, Welding Handbook, Vol. 2, 1991].

The very low oxygen content and high nitrogen content observed in the FCA weld metal are consistent with the findings of Quintana et al [2001]. The low oxygen and high nitrogen concentration in the FCA welds could result from the combination of the relatively high level of carbon (0.25 wt.% residual) and aluminum (1.0 wt.%) in the electrode wire for the FCAW and the contribution from the Zn-Al coating. The high C

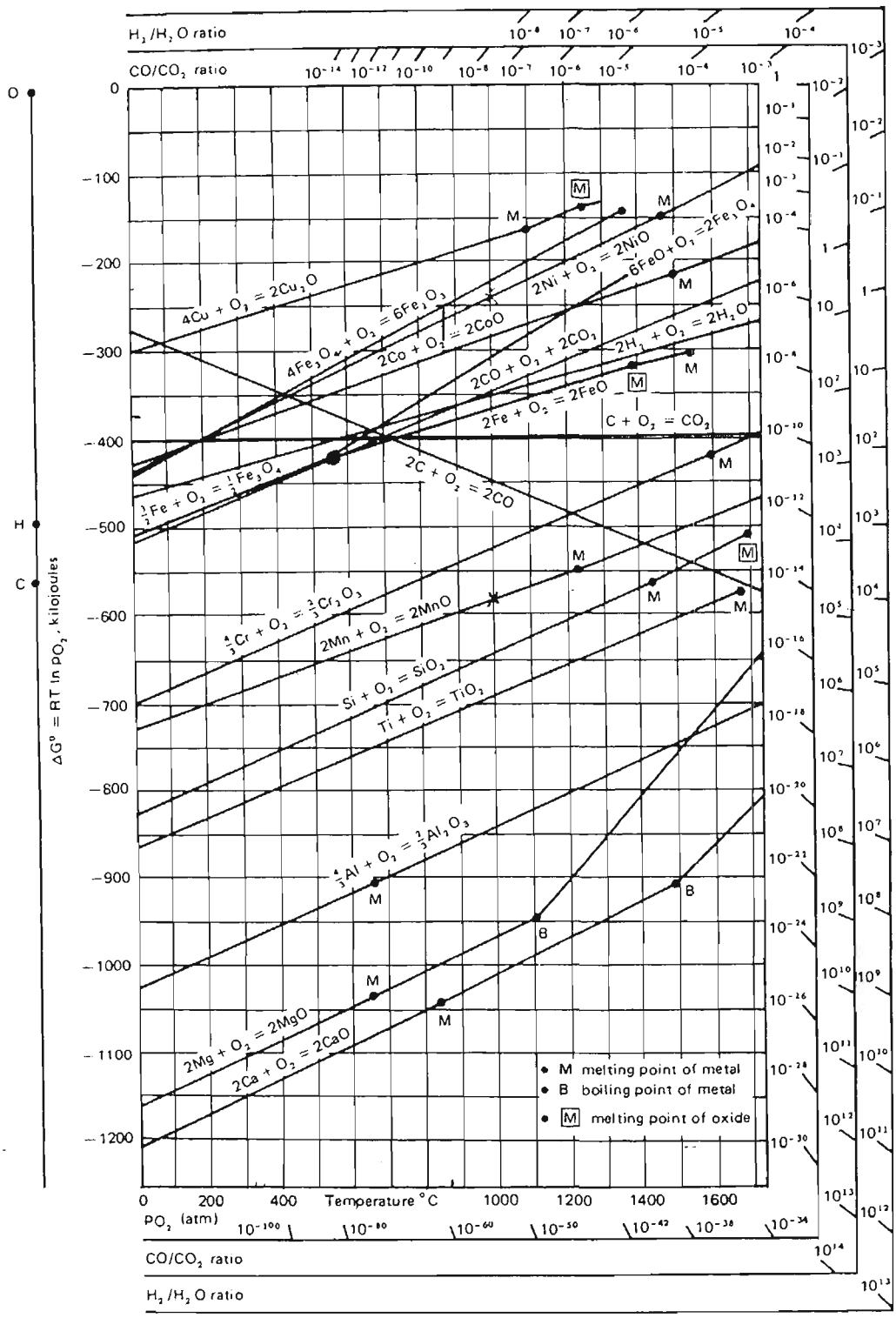

Figure 9.17 The Ellingham diagram for metallurgically important oxides [After Gaskell 1981].

content would be expected reduce oxygen in the melt from forming and evolving CO gas. Furthermore, the high Al content fixes N in the melt by forming AlN.

According to the Ellingham diagram (**Figure 9.19**), the CO has the lowest free energy of formation at temperatures above 2000°C among the potential oxides of aluminum, manganese and silicon [Darken and Gurry 1953]. Thus C has the highest affinity for oxygen in the molten pool at elevated temperature and can form carbon monoxide which escapes from the weld pool during the welding process. The formation and effusion of CO from the molten pool results in significant reductions in the oxygen and carbon contents of the weld metal (**Table 8.13**).

The probability of Al reacting with O_2 to form Al_2O_3 is relatively high at lower temperature as the aluminum oxide has the lowest formation free energy among the potential oxides at temperatures below 2000C. The Al content was high (1.1 wt.%) in the FCAW ZA weld metal because of contribution both from the electrode and from the Zn-Al coating during the welding process. The stability of AlN and Al_2O_3 in high Al weld metal has been studied systematically by Quintana et al. [2001], who presented a calculated stability diagram for AlN and Al_2O_3 in molten iron. Considering the FCA ZA welds, the aluminum content was 1.1 wt.% and the oxygen and nitrogen levels were 35ppm and 550ppm, this diagram predicts the presence of both Al_2O_3 and AlN. However, more AlN was observed than Al_2O_3. A similar result was found for the FCA ZHT weld which had an Al content of 0.55 wt.% and oxygen and nitrogen content of 60 ppm and 450 ppm, respectively.

The nitrogen content of the weld metal comes from two sources: the welding consumables (wire and parent materials) and the air [Evans and Bailey 1997]. Nitrogen can be absorbed as gas or in atomic form through the dissociation of molecular nitrogen. The equilibrium concentration of nitrogen in liquid iron at 1600°C is about 0.0445 wt.% at one atmosphere [Easterling 1992]. Therefore, the measured contents of 0.055% and 0.045% in the ZA and ZHT FCA weld metals just exceed the equilibrium concentration and are much higher than the GMA weld metals (0.0051%) (**Table 8.13**). This non equilibrium solution of nitrogen has been reported by John Norrish before [Norrish IIW Internal Report]. On solidification, the solubility of atomic nitrogen is considerably

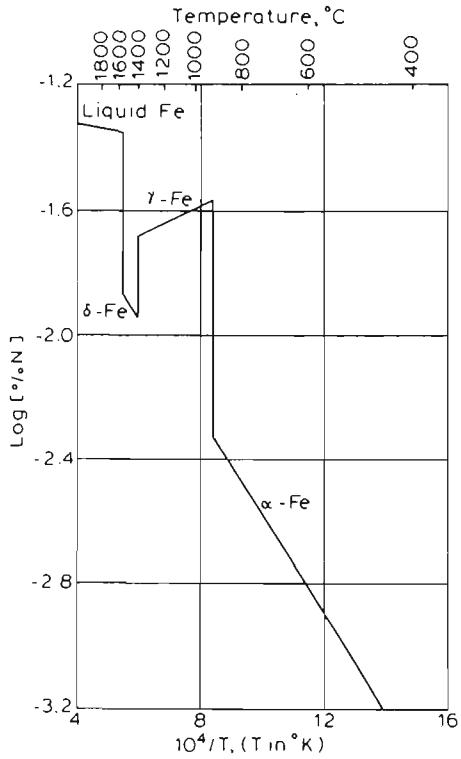

Figure 9.18 The solubility of nitrogen in iron as a function of temperature [After Easterling 1992].

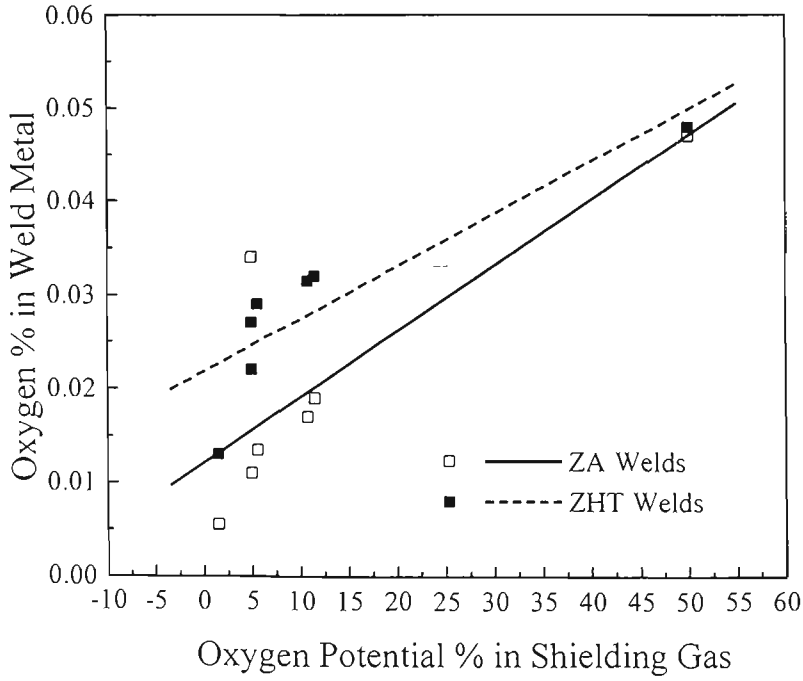

Figure 9.19 Effect of the oxygen potential % in shielding gas on oxygen content of GMA weld metal.

higher in f.c.c. γ–iron than in b.c.c. δ–iron and α–iron (**Figure 9.18**). Since the ambient solubility of atomic **N** in Fe is less than 0.001 wt.%, nitride of Fe and Al are expected to be present. The much lower N content in the GMA weld beads is mainly due to more effective gas shielding and reduction of the solubility of nitrogen in the melt pool as a consequence of high contents of Si and O [Easterling 1992].

9.2.2.2 Effect of shielding gas

It is well known that the shielding gas in arc welding can determine the residual contents of hydrogen, nitrogen and oxygen dissolved in the weld metal and therefore can significantly influence the weld bead profile (**Figure 2.9**) [Welding Handbook Vol.2 1992; Lucas 1997]. As expected, GMA welds shielded by Argoshield 60 (98.5% Ar+1.5% O_2) generated the lowest oxygen weld metal and produced a more convex weld bead profile (**Table 8.14** and **Figure 8.22**), consistent with a higher weld pool surface tension.

The effect of Ar, O_2 and CO_2 mixed shielding gases on the weld metal profile can be assessed using the oxygen potential of the shielding gases consisting of O_2 and CO_2 when the CO_2 is equal or less than 25% [Stenbacka and Perrson 1989]. However, in order to compare the effect of the mixed gases and the pure CO_2 on oxygen content and weld bead profile in the weld metal, the oxygen potential for 100% CO_2 was also calculated using the following formula:

$$\mathbf{OP\% = O_2\% + \frac{1}{2} CO_2\%}$$

It was found that there is a relatively strong correlation between the oxygen potential of the shielding gas and the oxygen concentration in the weld metal. The oxygen content in the weld metal increased with an increase of the oxygen potential of the shielding gas resulting from the increase of the oxygen in the arc atmosphere (**Figure 9.18**).

The ZA weld metal had a lower oxygen content than the ZHT weld metal even though they are shielded by the same shielding gas. This is probably due to the different

coatings. The ZA coated sheet steel contains the active deoxidant aluminum that is likely to react with oxygen in the weld pool producing oxide, at least some of which forms surface slag, thus reducing the oxygen content in the weld metal. On the other hand, the aluminum is also likely to be vaporized into the arc column and react with oxygen resulting the reduction in oxygen content in the atmosphere. The higher the oxygen content in the welding arc column, the greater probability of oxygen contamination in the weld pool.

The oxygen content in the weld metal with the Argoshield 100 is higher (0.034%) than with the Argoshield 54 (0.011%) even though their oxygen potential are exactly at the same level (5%). The helium used for the Argoshield 100 might cause the discrepancy. Gas solution and evolution from the weld pool is a complex dynamic process and among other factors is influenced by the weld pool freezing rate and the surface tension of the weld pool. However, the role played by the helium and its mixture with other gases in dissolving the oxygen potential in weld metal is not clear and a systematic study on this subject needs to be conducted.

Of the shielding gases used, the pure CO_2 has the greater oxidizing potential and results in relatively lower recoveries of the oxidizable elements such as aluminum and silicon in the weld metal (**Table 8.14**). However, the other oxidisable elements such as carbon, manganese and copper etc. tend to be increased with increasing oxygen potential of the shielding gas. According to the Ellingham diagram (**Figure 9.17**), the Al_2O_3 and SiO_2 have lower standard reaction free energies than those other oxidizable elements and thus the aluminum and silicon have the highest affinities for the oxygen at high temperatures [Gaskell 1981]. Consequently, the contents of aluminum and silicon are markedly lower in weld metal shielded by the pure CO_2 shielding gas.

Previous research has shown that the oxygen potential of the shielding gas has a potent effect on the weld pool geometry, increasing the pool depth, width and volume when deposited at the same nominal heat input when arc welding of thick plate [Walsh and Savage 1986; Chen 2000]. The influence of oxygen on the weld pool is due first of all, to its effect on surface tension of the weld metal and secondly, to its effect on the metal or arc energy transfer. The addition of oxygen to the shielding gas can reduce the

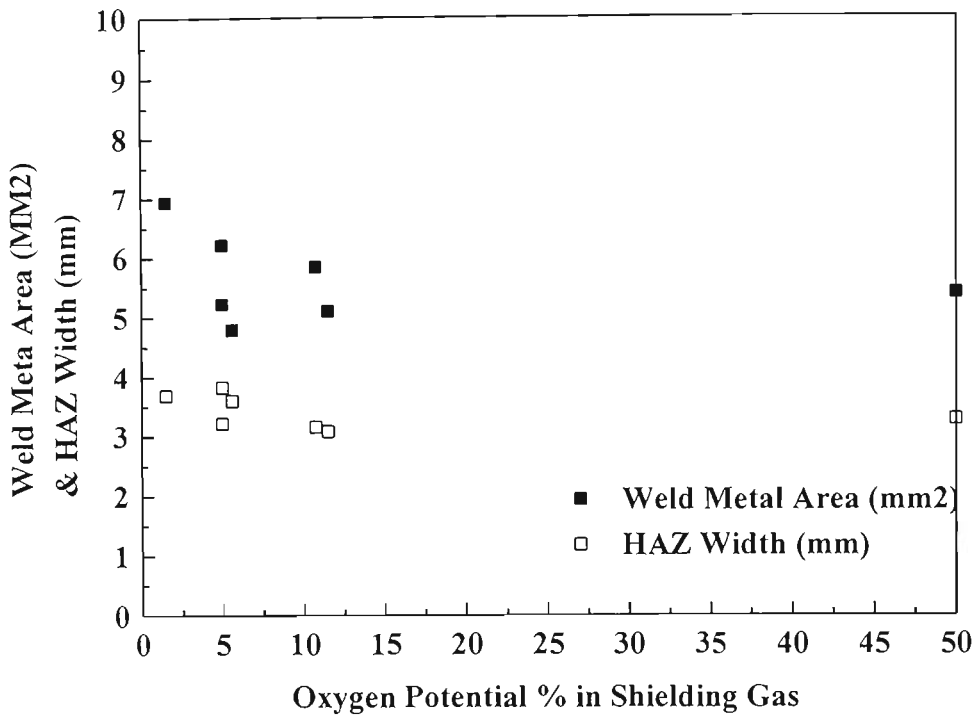

(a)

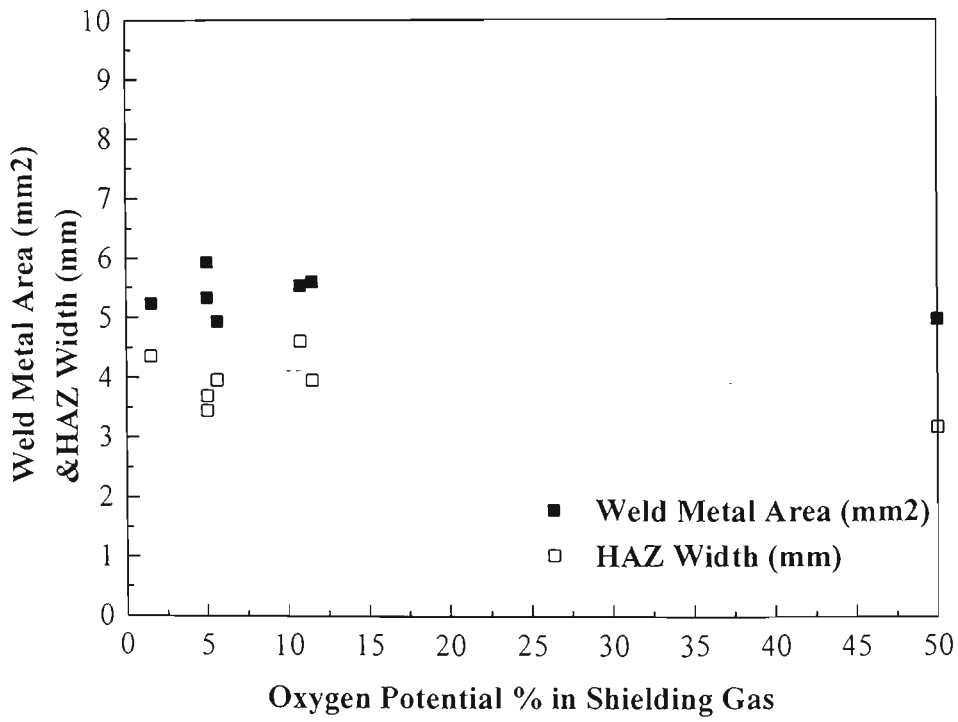

(b)

Figure 9.20 Effect of oxygen potential % in shielding gas on the weld metal area and HAZ width for GMA welded **(a)** ZA sheet steel and **(b)** ZHT sheet steel.

surface tension of the weld metal and thereby improve the wetting condition of the work piece [Jonsson et al. 1995; Lucas 1992]. The addition of carbon dioxide or oxygen to a shielding gas can cause an increase in the anode drop and increase the arc energy transfer to the weld pool. Therefore, the weld metal area and the total fused area can be increased at an equivalent current [Norrish 1992; Walsh and Savage 1986]. However, these effects were not an evident for the GMA welded thin sheet steels (**Figure 9.20**).

9.2.2.3 Effects of heat input and Zn alloy coating

Clearly the weld metal volume increased with an increase in heat input as a result of increased welding current and the wire feed rate at the constant welding voltage and travel speed (**Figure 8.18** and **Table 8.5**). The increase in the welding current results in an increase in depth and width of the weld bead, due to the greater volume of deposited filler and more extensive melting of the base sheet.

Although it may be expected that a relatively high level oxygen content is associated with the high heat input welds due to the smaller wetting contact angle (flatter weld bead profile) than low heat input weld, there is no a strong correlation between the heat input and oxygen content in the weld metal, at least not systematically (**Table 8.10**).

The GMA welds of uncoated sheet steel were flatter and smoother than those of the Zn-Al coated steel (**Figure 8.18**). This again may be due to a lower oxygen content and a higher surface tension in the coated steel welds than in the uncoated steels. The reaction of zinc and aluminum with oxygen in the arc atmosphere will reduce the effective oxygen level. As mentioned before, the low oxygen content in ZA coated steel welds can be interpreted by the deoxidising reaction in which Al in solution in the weld pool reacts with oxygen reducing the oxygen content in weld metal. When the Zn-Al coating vaporizes in the heat of the arc, the weld pool becomes very erratic and unstable resulting in the reduction of the joint penetration, causing spatter and in the worst case, resulting in porosity. Compared to the same settings for GMA welded Zn-Al coated sheet steel, the uncoated sheet steel appears to have a higher heat input with a higher current than the Zn-Al coated sheet welds, even though the wire feed rates were quite similar. This result is consistent with previous work [Huang et al. 2002]. This could be a

result of the presence of Zn-Al coating at the cathode (work piece surface) which affects the cathode voltage drop; and the effect of the Zn-Al coating vaporised into the arc column which influences the arc characteristics, especially its electric conductivity [Gregory 1969; Huang et al. 2002]. For similar heat inputs the uncoated weld metal had a narrower HAZ width and smaller weld metal volume than the coated steel. This may be caused by the different values of the thermal conductivity and diffusivity for the GMAW on the coated and the uncoated steels.

9.2.2.4 Effect of electrode orientation

Figure 8.19 (a) shows macro-photographs of the cross-sections of the weld bead for ZA sheet steel welds obtained using the three different electrode orientations: perpendicular (P), backhand (B) and forehand (F). The backhand technique produced a larger weld bead, even though the nominal heat input was the same (80 J/mm) for all three torch orientations (**Table 8.6**). The weld beads produced by the backhand orientation were also convex and had a deeper penetration with a slightly lower oxygen content in weld metal than using other two orientations (**Figure 8.19 (a)** and **Table 8.11**). As discussed before, in backhand welding the heat source is concentrated back onto the weld bead and metal is deposited onto the existing bead, enhancing the turbulence and accelerating deoxidation in the weld pool and eventually reducing the oxygen content in weld metal.

9.2.2.5 Effect of travel speed

The proportional increase of the welding current and travel speed to maintain the same nominal heat input changes the weld bead geometry significantly, as shown in **Figure 8.19 (b)**. This change is similar to that of the study by Ahmed and Jarvis [1998] in terms of the changes of cooling time and HAZ width. However, bead on plate welding, that they studied, showed that an increase of the travel speed results in the gradual disappearance of the 'crater' and enlargement of the 'finger'. In contrast, the butt welds investigated in the present work show that both the 'crater' and 'finger' were increased with increasing the travel speed. The increase of travel speed had little effect on the oxygen concentration in weld metal (**Table 8.12**), although it would be expected that the high travel speed should produce more closely spaced isotherms in the molten pool

and a narrower weld bead (**Figure 5.9** and **Figure 5.12**). The lack of any significant trends could be the result of limited heat inputs and travel speeds applied to the thin plate in order to achieve quality welds.

9.2.2.6 Effect of control mode

A flatter and smoother weld bead profile and larger weld metal volume were obtained in the current control mode than in the constant voltage mode. This effect could be due to the higher actual heat input in the former control mode than the latter control mode as discussed before (**Figure 8.20** and **Table 8.8**). The actual higher heat input in the current control mode is due to the maintenance of a low current during the short circuit period [Huang et al. 2002].

9.2.3 Porosity of Weld Metal

Previous work on butt joints in GMA joints of galvanised steel indicated that they were relative free from defects and gave clear radiographs. However, gas porosity was reported in arc welding of Zn-Al coated steel [Gregory 1972]. The porosity was considered to be induced by gas pockets of O_2, N_2 and H_2, inclusions and in the worst cases, Zn alloy coating material trapped in the melt. Although there was no evidence of significant macro gas pores in the weld beads of Zn-Al coated steel, a few large spherical pores (up to 500μm) were observed in the weld metals for both GMA and FCA ZA and ZHT welds, as shown in **Figure 8.23**. The spherical pores are caused by entrapped gas, as the EDS microanalysis revealed no significant elements on the surface of the pores other than iron.

9.2.4 Al-rich particles in weld metal

In the arc welding of the Zn-Al coated steel, Zn tends to be volatilized out of the weld bead region due to its lower melting (~420°C) and boiling point (~907°C) than Al. However, Al is easily entrapped in the molten pool since Al has a much higher melting point (~660°C) and boiling point (~2520°C) than Zn. The entrapment of Al-rich particles in the weld metal was revealed by EDS analysis (**Figure 8.24** and **Figure**

8.25). The size of these Al rich particles varied from a few microns to about 65μm and they had both irregular and spherical shapes. The particles analysed by SEM/EDS contained about 30% to 90% aluminum with a balance of iron, plus a little manganese and calcium, as shown in **Table 8.15**.

9.3 NON-METALLIC INCLUSIONS IN WELD METAL OF Zn ALLOY COATED STEEL WELDS

The oxygen content in the weld metal significantly influences the microstructure and properties of the weld metal. Since only minor changes were found in the volume fraction of the non-metallic inclusions for different heat inputs and electrode orientations (**Table 8.16**), the discussion is concentrated on the effects of the oxygen potential of the shielding gases and the GMAW and FCAW processes on the characteristics of the non-metallic inclusions in the weld metal.

9.3.1 Effect of Shielding Gases

Increasing the oxygen potential in the shielding gas provides a significant source of oxygen absorption into the weld pool. Most of the oxygen will dissipate into the surroundings, but some oxygen will combine with alloying elements in the weld pool to form oxides. During solidification, some of the oxides are entrapped as inclusions in the weld metal. The inclusions play an important role in determining the final weld metal microstructure and properties.

Based on the Ellingham diagram (**Figure 9. 17**) aluminum, manganese, silicon and titanium are strong deoxidisers and most likely to react with oxygen during the welding to form MnO, SiO_2 and TiO etc. [Pollard and Milner 1971; Grong and Christensen 1983; Francis et al. 1990]. Some of the oxides are entrapped within the solidified weld pool as finely distributed inclusion particles. A shielding gas with higher oxygen potential is more likely to increases the oxygen content in the weld metal and form oxides during weld metal solidification.

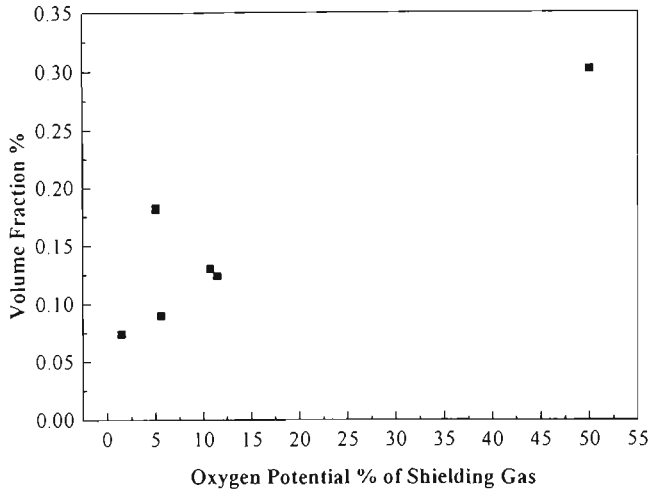

(a)

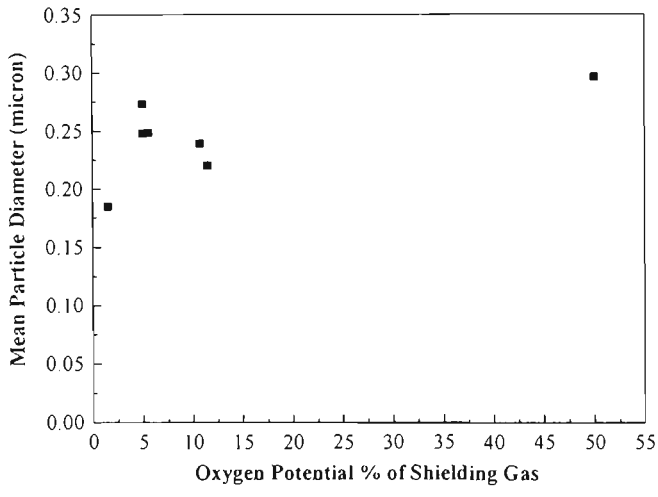

(b)

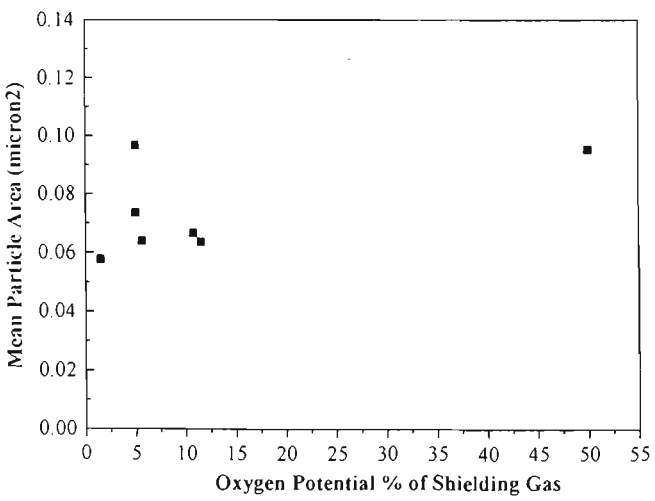

(c)

Figure 9.21 Volume fraction **(a)**, a mean particle diameter (μm) **(b)** and a mean particle area (μm^2) **(c)** as a function of the oxygen potential (%) in shielding gases.

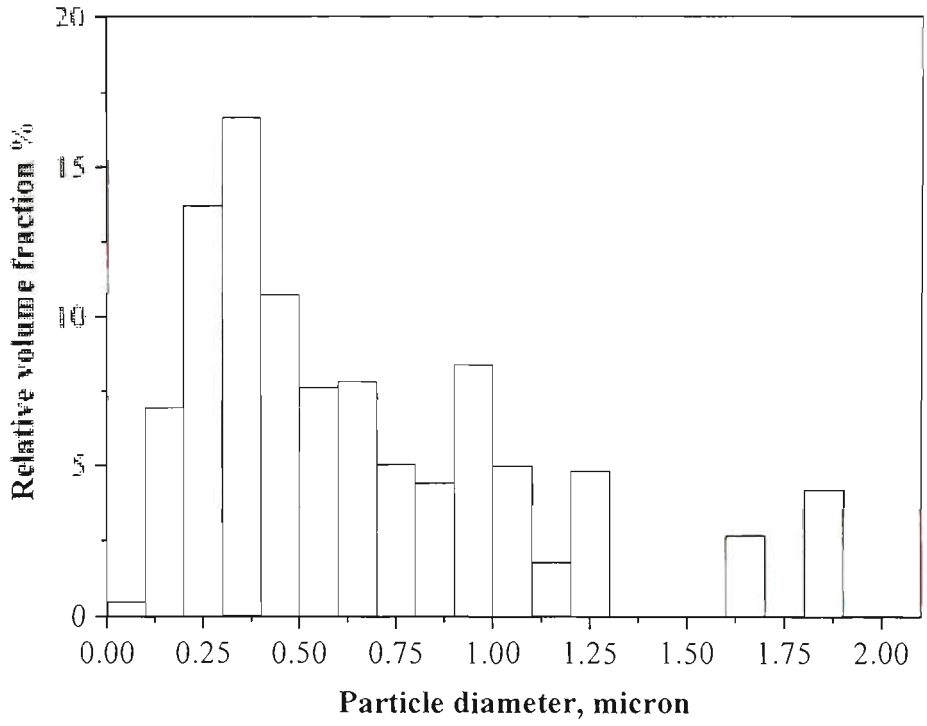

(a)

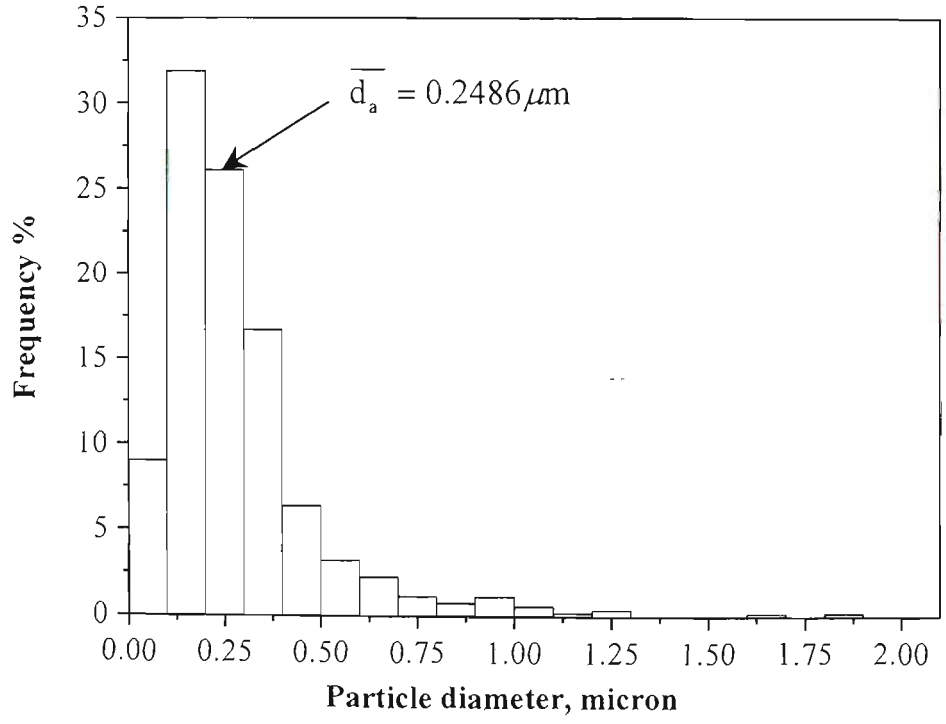

(b)

Figure 9.22 Inclusion data for GMAW ZA welds with heat input at 80 J/mm and shielded by A50, showing **(a)** percentage of contribution of each size class to total inclusions volume fraction; **(b)** 2-D size distribution of inclusions.

The oxygen content in the weld metal increased with increasing oxygen potential of the shielding gases due to the increase of the oxygen in the arc atmosphere (**Figure 9.19**). A lower oxygen content was found in the ZA welds than that in the ZHT welds when shielded by the same shielding gas. This is an effect resulting from the reaction of aluminum from the Zn-Al coating with oxygen and thus reducing the oxygen content in the ZA weld metal.

The inclusion volume fractions (expressed as percentage) of the GMA weld metal produced with different shielding gases fall within the range of 0.0755 to 0.3040 for oxygen potential values of 1.5% (Argoshield 60) to ~50% (100% CO_2), respectively (**Table 8.16**). As expected an increase the oxygen potential increases the volume fraction, 2-D mean particle diameter $\bar{d}_a$ and the mean particle area $\bar{A}$ (**Figure 9.21 (a)**, **(b)** and **(c)**). The non-metallic inclusion characteristics can be affected by cooling rate at high temperatures. Since GMA welding at higher oxygen potential tends to put more heat into the work piece, slower weld pool cooling and a larger dwell time are expected, giving rise to inclusion growth during the weld pool solidification (**Figure 8.26**). However, higher values of volume fraction, 2-D mean diameter $\bar{d}_a$ and the mean particle area $\bar{A}$ were found in the weld metal provided by the Argoshield 100 (mixed gas with helium) than the Argoshield 54 (Ar, CO_2 and O_2 mixed gas). Although the reason for this is not clear, the higher thermal conductivity will certainly result in more heat in the weld pool, resulting in slower weld pool cooling and a larger dwell time, effects similar to those of the high oxygen potential of shielding gases.

The 2-D inclusion diameters for different shielding gases are within the range of 0.1850 to 0.2965μm. Changing the oxygen potential in the shielding gas changes the inclusion distributions, i.e. increasing oxygen potential in shielding gas decreases the percentage of inclusions ≤0.2μm from 53.4% to 32.3% (**Table 8.16** and **Figure 8.30**). The characteristic peak in the inclusion frequency is sited at about 0.1 to 0.25μm as shown in **Figure 9.22**. This result is consistent with the observation that the number of inclusions with diameters ≤0.2μm or >0.8μm decreases with increase of the oxygen potential of the shielding gases whereas the number of percentage of non-metallic inclusions with sizes between 0.2 and 0.8μm increases dramatically (by about 20%)

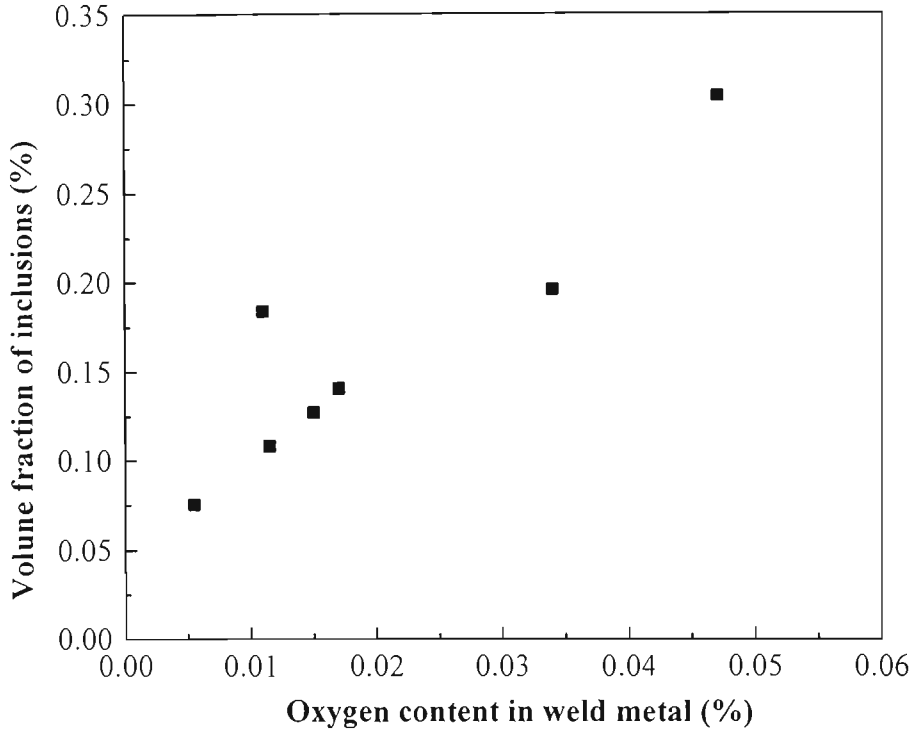

Figure 9.23 Relationship between oxygen content in weld metal and inclusion volume fractions.

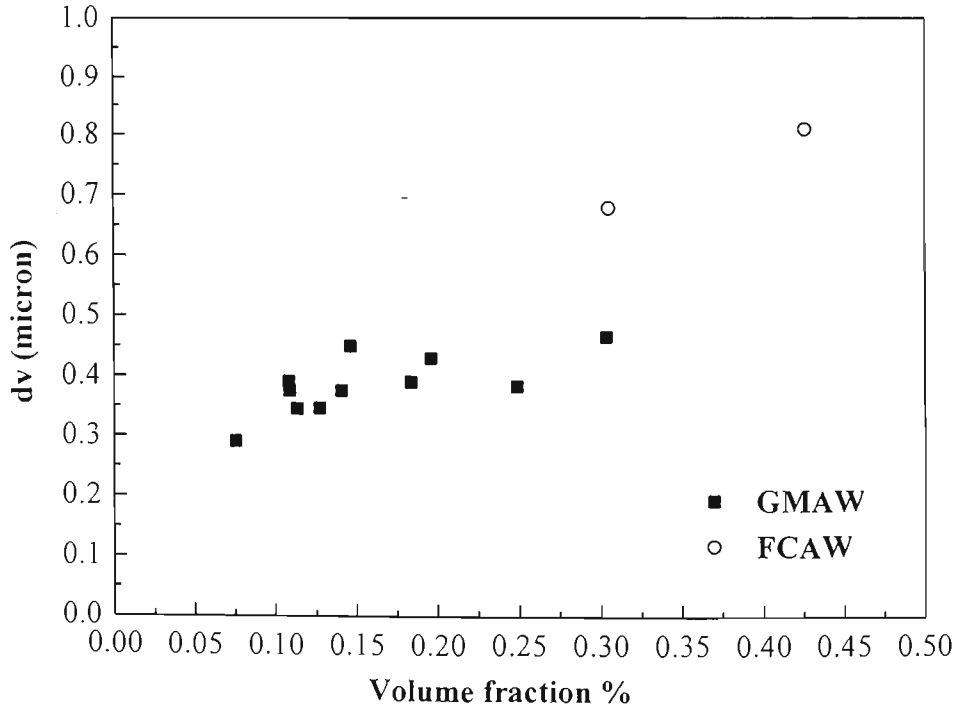

Figure 9.24 Relationship between arithmetic mean three-dimensional (3-D) particle diameter and the inclusion volume fraction.

with an increase in oxygen potential of the shielding gases (**Table 8.16**). The larger number of particles per unit area $\mathbf{N_a}$ for the shielding gas with the high oxygen potential probably contributes to higher transformation temperature during cooling due to a large population of heterogeneous nucleation sites. As expected there was a strong correlation between the oxygen concentration of the weld metal and the inclusion volume fraction (**Figure 9.23**).

9.3.2 Effect of Welding Process

The weld metals produced by FCAW of ZA and ZHT sheet steel appeared to have the higher value of the inclusion volume fraction, the 2-D mean particle diameter $\bar{d}_a$ and mean particle area $\bar{A}$ despite very low oxygen contents compared with those of the weld metal produced by the GMAW welds (**Table 8.16**). However, the nitrogen concentration in the FCA welds is significantly higher (0.055% and 0.045%) than those of GMA welds (0.0051%) for both Zn alloy coated sheet steels. Hence, the increase in inclusion volume fraction, $\bar{d}_a$ and $\bar{A}$ for the FCA welds could be accounted for mainly by the high value of nitrogen content, rather than oxygen content.

Figure 9.24 shows the relationship between the arithmetic mean 3-D diameters and the volume fractions of the inclusions of the GMAW and FCAW weld metals. This figure shows that the 3-D diameters increase with an increase of the inclusion volume fraction in the weld metal. For the same volume fraction, FCAW shows a larger 3-D diameter than the GMAW weld metal. As mentioned in Chapter 7, the electrode wire (FABSHIELD 21B) used for FCAW nominally consists of 1% aluminum that contributes to the high aluminum contents of 1.1% and 0.55% in the FCA welded ZA and ZHT welds. The GMA welds, however, only contained 0.7% and 0.024% Al for the ZA and ZHT sheet steels respectively (**Table 8.13**). It should be noted that a high portion of aluminum in the ZA GMA welds was picked up from the Zn-Al coating during welding. Deoxidation with aluminum induces a high fraction of coarse particles due to the incipient clustering of Al_2O_3 [Coe 1973; Yurioka and Ohshhita 1980]. For the FCA welds the percentages of coarser particles (>0.8μm) were 25.7% for ZA and 14.1% for ZHT. These values are significantly higher than for the GMA welds (2.16% for ZA and 4.33% for ZHT) (**Table 8.16** and **Figure 8.27**). Inclusions consisting of

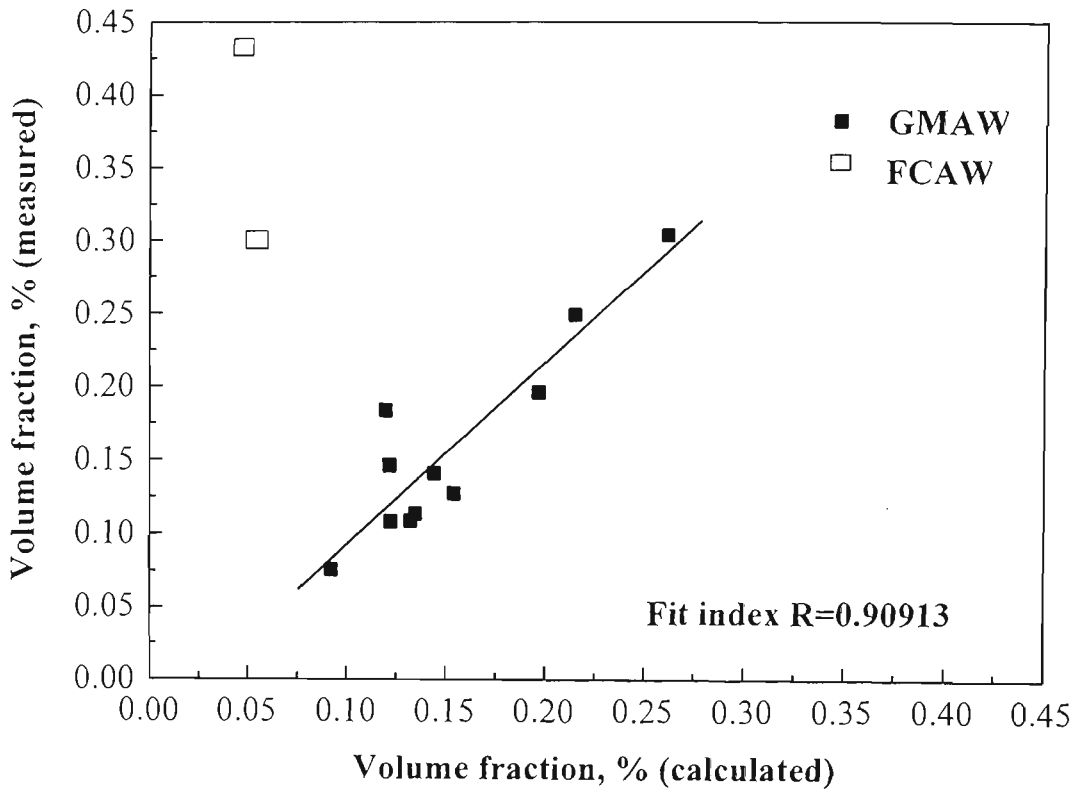

Figure 9.25 Comparison between measured and calculated inclusion volume fractions for GMA and FCA welded ZA and ZHT weld metals.

aluminum and iron nitrides were also present in the FCA welds and characterised by irregular angular shapes (**Figure 8.33 (e)** and **(f)**). A typical spectrum for EDS analysis of the inclusions consisting of oxides and nitrides is given in **Appendix I (a)** and **(b)**. Since the non-metallic inclusions in steel weld metals are very complex and chemically heterogeneous, the existence of several phases within a single inclusion is common as shown in **Figure 8.33** and **Appendix I (a)** and **(b)** [Keville 1983; Dowling et al. 1986; Mills et al. 1987].

9.3.3 Comparison of Calculated and Measured Volume Fraction

The volume fraction of non-metallic inclusions can also be calculated by converting the analytical oxygen and sulphur concentrations to an equivalent inclusion volume using the equation derived by Franklin for Si-Mn de-oxidized steels (Ferrous alloy weldment-R17). In calculation, the solubility of sulphur in solid steel is taken as 0.003 wt%, so that the equation becomes:

$$V_v\,(cal) \approx 10^{-2}\,[5.0\,(wt\%O) + 5.4\,(wt\%S - 0.003)\,]$$

Figure 9.25 shows the comparison between the measured and calculated inclusion volume fraction for the GMAW and FCAW ZA and ZHT sheet steels welds. It is clearly shown that a reasonable agreement between the measured and calculated inclusion volume fraction was obtained for the GMA weld metal, but not for the FCA weld metal due to the very low measured oxygen content in the weld metal (**Table 8.13**). However, the reasonable agreement was obtained for FCAW of Al-Ti-Si-Mn deoxidized steel weld metals by Grong and Kluken [Grong and Kluken 1988]. Since the Franklin equation was derived for Si-Mn deoxidised steels, it seems to be not applicable for the weld metal of FCAW Zn coated steels using a high aluminum content electrode wire. In other wards, the Franklin equation is not applicable to high Al self shielded weld metals.

It is therefore concluded that the Franklin equation can be used for the prediction of the inclusion volume fraction for GMA welded Zn alloy coated sheet steels in practice, but not for the self-shielded FCA welds.

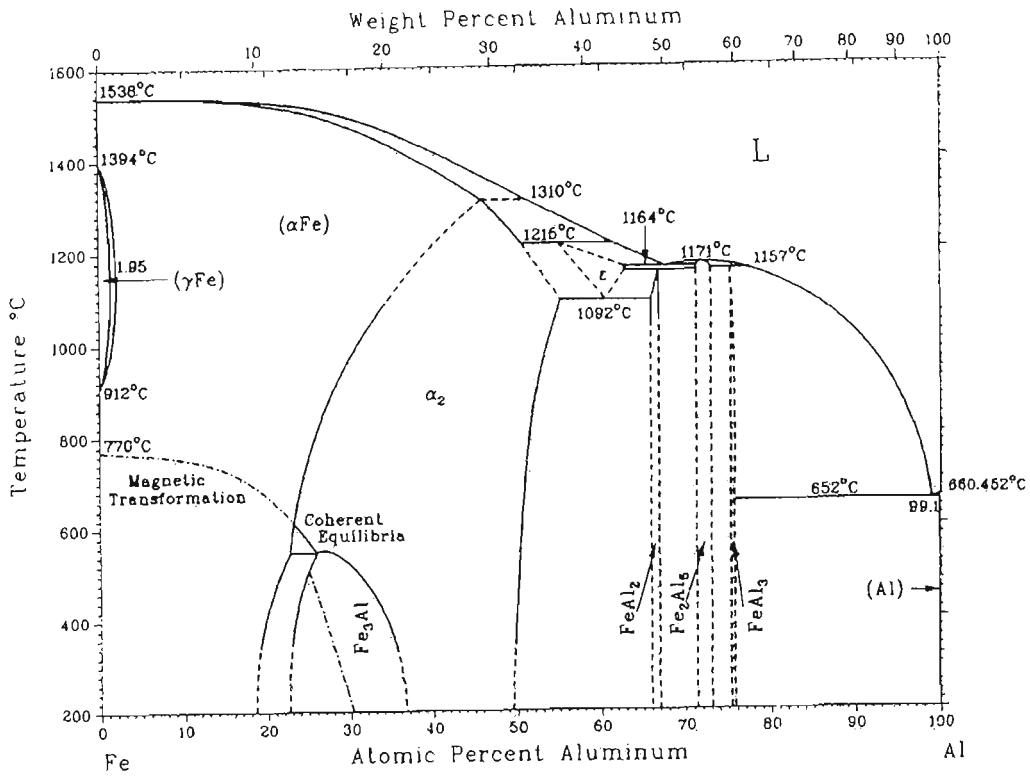

Figure 9.26 Al-Fe phase diagram [After Massslski 1986].

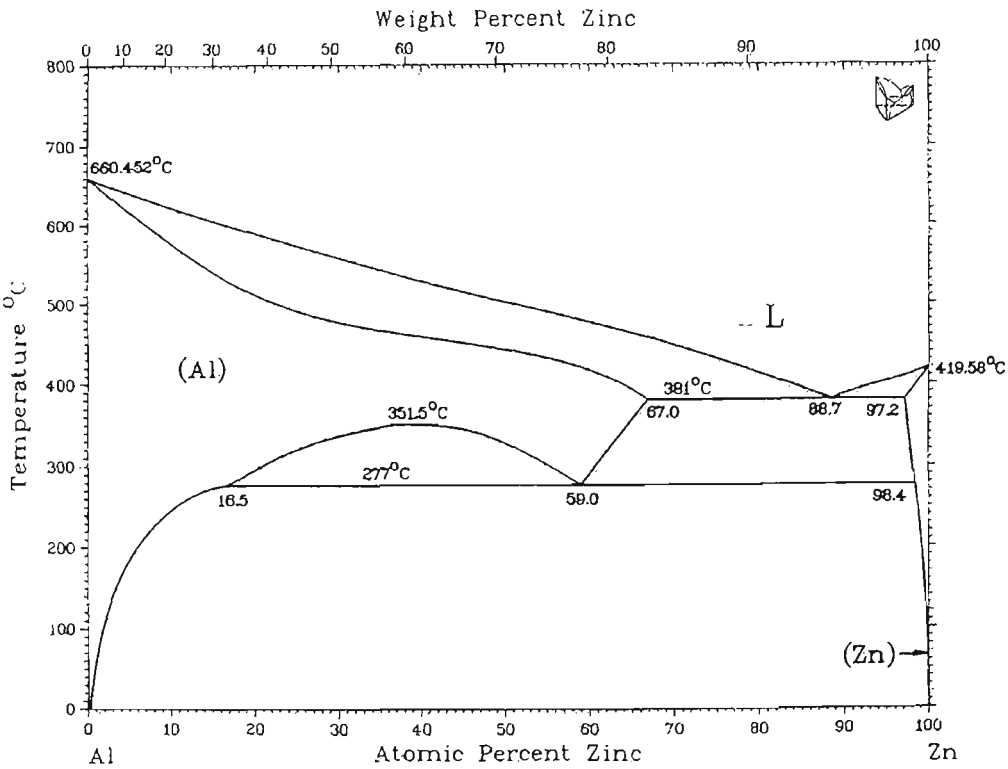

Figure 9.27 Al-Zn phase diagram [After Massslski 1986].

9.4 Zn ALLOY COATING CHANGES AFTER GMAW

9.4.1 Heat Affected Zn-Al Coating

As mentioned in Chapter 3, the ZA coating prior to welding consists of two distinctive layers: a dominant Zn-Al outmost layer about 25μm thick and a narrow intermetallic compound layer about 1μm thick in between the Zn-Al layer and the base metal (**Figure 3.8** and **Figure 8.48**). The measured composition (55.4 at.% Al, 28.3 at.% Fe, 7.5 at.%Si and 8.7 at.% Zn) of the intermetallic compound is very close to $(FeZn)_{37}$ $(AlSi)_{63}$. If the binary Al-Fe diagram is used and the composition is simplified to $Fe_{37}Al_{63}$ (**Figure 9.26**), the compound is closer to $FeAl_2$ than to FeAl (α_2) phase, as supported by a BHP Internal Report. Therefore the $Fe_{37}Al_{63}$ may be assumed to be similar to $FeAl_2$ phase, although the actual compound is quaternary. For this simplifying assumption, any phase changes occurring in between the base metal and the intermetallic phase during welding can be discussed in terms of high temperature heat treatment of a diffusion couple of Fe and $FeAl_2$. The thermal stability of the $FeAl_2$ intermetallic phase is much higher than the Zn-Al coating as the former is stable up to 1150°C and the latter up to about 500°C, according to the binary Fe-Al and Zn-Al phase diagrams (**Figures 9.26** and **9.27**). Consequently the $FeAl_2$ will grow in the heat affected zone, except for regions close to the fusion boundary, where major changes in the coating are to be expected because of the high exposure temperatures.

The thickness of the original Zn-Al alloy coating will be significantly reduced by vaporization and melting during the welding process. The reduction in thickness will depend on the peak temperature reached. The higher the peak temperature, the more Zn is vaporized and thus the larger reduction of the Zn-Al coating (**Appendix III (a)** and **Figure 8.49**) which shows an increase in the $FeAl_2$ layer and a corresponding decrease in the Zn-Al outer layer as the temperature increases from 600°C to 700°C. The growth of the $FeAl_2$ layer thickness accelerates as the temperature increases in the range of 750° to 1100°C. (**Figure 8.51**). The higher the peak temperature, the higher diffusion rate of Fe in the coating and the thicker the $FeAl_2$ phase layer. Furthermore, a new phase layer (α_2) is also expected to form in between the base metal and the $FeAl_2$ intermetallic layer and this new phase is also very stable and will grow rapidly particularly at high

temperatures. The steel substrate will be saturated with Al at the interface with the α_2 phase. As expected the rate of reduction of the Zn-Al layer is much higher than the growth rate of either the $FeAl_2$ phase or the α_2 phase, particularly at high temperatures as the extent of the Zn-Al layer is controlled by the rate of vaporization and the $FeAl_2$ and α_2 by atomic diffusion. As a result, the total thickness of the coating is reduced by the welding process and the coating became thinner towards the fusion line. However, the coating was also necked at a temperature of about 600°C. At this temperature the coating alloy would be expected to melt, but vaporization of Zn would not be expected to be significant (**Figure 8.49 (a)**). However, vaporization could be enhanced and flow of liquid alloy coating away from this region could occur due to the arc force and/or shielding gas flow (**Appendix III (b)**). This hypothesis is supported by the fact that thinning on the underside of the sheet was much less evident.

At temperatures above 1100°C γ phase is present in the steel substrate, but surface enrichment with Al will produce a layer of α phase. The Al-rich coating will become increasingly diluted by Fe with Fe-rich phase being expected to develop. The succession of Fe-enriched phases observed are α with Al in solution, Fe_3Al formed on coating of α_2 phase containing about 25 ~35 at.% Al and α_2 with composition in the range 35 ~ 50 at.% Al. On cooling the Fe-rich regions of α_2 transforms to Fe_3Al (**Figures 8.52** and **8.12**).

The prevalence of thick layer of Fe_3Al in the shoulder regions of weld bead probably developed by partial melting and mixing of Fe and Al, forming a solution that transforms on cooling to the intermetallic Fe_3Al. The α-Fe, intermetallic Fe_3Al and outer α_2 phase are very brittle and they cracked through the entire coating under the influence of thermal stresses.

9.4.2 Heat Affected Zn Coating

The microstructure of the ZINC-HI-TEN^{TM} coating produced by continuous galvanizing deviates from a typical multi-layered coating microstructure produced by a batch Galvanizing process (**Figure 3.6**, **Figure 3.7** and **Figure 8.54**). The coating consists of a predominant Zn-rich phase (98.5%Zn and 1.5%Fe) about 25μm thick and a very thin

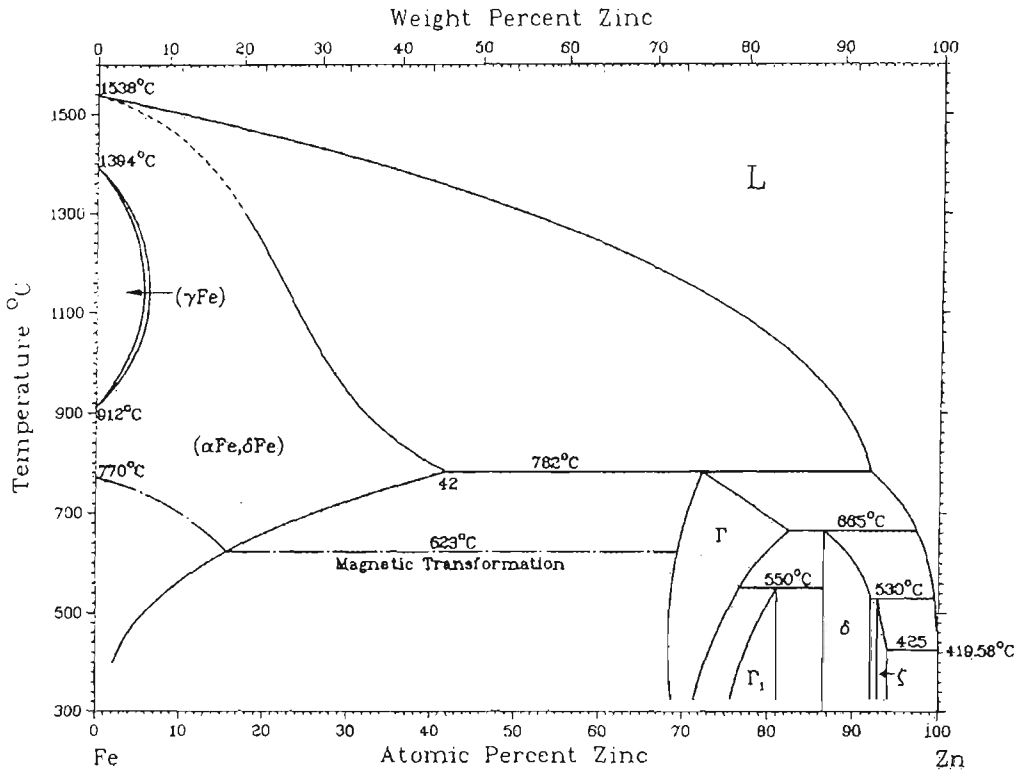

Figure 9.28 Fe-Zn phase diagram [After Massslski 1986].

layer of Γ phase (approximately 75at.%Zn), less than 1μm thick in between the Zn-rich phase and the base metal.

The coating damaged area can be divided into three different zones as described in the results section according to the peak temperatures experienced by the coating (**Appendix III (b)** and **Figure 8.56**). In the zone **A3**, where the peak temperatures were lower than 600°C, there was still macroscopic evidence of the original 'spangle grain' structure, but the total thickness of the coating was substantially reduced from the original 25μm to about 5μm (**Figure 8.61**). The thickness reduction of the coating in this zone is unlikely simply to be caused by heat as the boiling temperature of Zn is about 900°C at one atmosphere which is more than 300°C higher than the peak temperature. However, the shielding gas impinging on surface of the liquid coating alloy could enhance evaporation of the Zn as well as displacing liquid Zn away from the direct gas impingement zone. Interestingly the thickness of the Zn coating in zone **A3** is considerably smaller than in zones **A1**and **A2** which are exposed to higher temperatures.

The coating structure of zone **A2** (**Figure 8.58**) is substantially different from that present prior to GMA welding. In this zone the coating has experienced peak temperatures in the range of 600-900°C. Precipitation and substantial grain growth of precipitates within the coating are very evident. A new phase was formed in between the base metal and the original Zn coating and it has the composition of 83%Fe and 17%Zn (at.%) (**Figure 8.59 (a2)**; **SP5** and **Figure 8.6**). Therefore, the new phase must be a high temperature α phase since at room temperature the solid solubility of Zn in α is less than 1at.% and the solid solubility increases dramatically with temperatures. At 782°C the solid solubility reaches its maximum of 42at.% Zn. At 623°C the solid solubility is about 17at.% Zn which is very close to the composition observed (**Figure 9.28**). Thus the new phase is likely to be high temperature α-Fe, which has been retained by the rapid cooling rate. The angular precipitate particles next to the supersaturated α-Fe phase have the compositions of 70-87at.%Zn and up to 25at.%Fe which are consistent with the composition range of Γ phase (**Figure 8.59 (a2)**, **SP6** and **SP7**; **Figure 3.6**). Thus the precipitates are identified as Γ phase particles, a conclusion that is further supported by the fact that these particles were more extensively precipitated in the lower temperature end of zone **A2** (next to zone **A3**) than the high

temperature end (next to zone **A1**) (**Figure 8.59 (b2) and Figure 8.61 (b), SP12** to **SP17**). According to the binary Fe-Zn phase diagram Γ is stable up to 782°C which explains why fewer Γ precipitates were observed at the higher temperature end (close to 900°C) than the low temperature end which was close to 600°C. Despite its low stability, the Γ phase was observed in zone **A1** where the temperatures were above 900°C (**Figure 8.57**), which is probably a result of formation by eutectic reaction during the cooling cycle. At the high temperature end of zone **A2** the thickness of the Γ layer is reduced and the overlying layer has the composition of 98.5at.%Zn and 1.5at.%Fe which is the same as the composition of the coating prior to the welding process (**Figure 8.59 (a2), SP9**). The thickness of the Zn coating is in the range 15-20μm, compared with 25μm before the welding process. Zone 2 shows three distinct granulated layers along the Zn-rich layer. The layer above the Zn-rich phase has a thickness between 5-10μm and is made of entirely discrete particles, with a metallic element composition of 81%Zn and 19%Fe, similar to that of Γ phase, but it is probably an oxidized compound (**Figure 8.59, SP8**). It seems that this layer and the other outer layers are redeposited oxidized layers caused by the welding process. In fact the Γ-like particle layer extends beyond zone **A2** into zone **A3**. On top of this particle layer there are two more layers, a thin and uniform 95%Zn + 5% Fe layer (1-2μm thick) and an outmost slag-like layer which has the metallic element composition of 69%Zn, 22% Fe, 7.5% Mn and 1.6% Si (**Figure 8.59, SP10** and **SP11**). All three of these outermost layers may be similar to the surface slag formed during welding.

In zone **A1** the uniform Zn-coating was severely damaged by the extreme heat (**Figure 8.57**). The only evidence of the coating left is an continues layer about 2μm thick with a granular outer layer. The 2μm thick continioues layer consists of an inner layer resembling the Γ particle layer observed in zones **A2** and **A3** (**Figure 8.57, SP2**); and an outer layer with a complex ternary composition of about 80%Zn, 7%Fe, 13%Si (**Figure 8.57, SP1**; **Table 8.21**). However, the particles in the outermost granular layer are either silicon oxide or iron oxide although their stoichiometric ratios cannot be determined by EDS/SEM. It is believed that this granular layer was formed by the re-deposition of Si or Fe oxides which were formed by the oxidation of Si and Fe vapour in the arc. The inner layer is relatively thin and continuous but the composition is not uniform across

the layer. The layer near the silicon and iron oxides has a composition close to that of δ phase (approximately 90%Zn, 10%Fe) except for the silicon content (13.2%Si) (**SP1**), which could be artificially affected by adjacent silicon oxides.

The layer near the matrix has very high Fe (32%Fe) and Mn (9%Mn) and a relatively low Zn content (57%Zn) compared to the composition of the Γ phase (**SP2**). Again the microanalysis result could be affected by the adjacent Fe matrix. As discussed before zone **Al** has experienced temperatures higher than 900°C and extensive melting of . coating alloy would be expected. However due to the rapid heating and cooling of the GMAW process, the Γ phase has evidently reformed. Since the Γ phase is a Zn-rich phase it can still provide some protection from corrosion, and so not all of the corrosion protection is lost after the GMA welding process.

CHAPTER 10

CONCLUSIONS

The structural and property changes in the weld zone of the GMA and self-shielded FCA welded cold rolled, Zn alloy coated ZINCALUME™ and ZINC-HI-TEN™ G550 structural sheet steels (0.85 and 1.0mm thick) have been investigated. The present research was focused mainly on the heat affected zone because of the fact that tensile fracture occurred in this area. The strength loss associated with the welding process and welding conditions has also been quantified. The microstructure of the HAZ has been correlated with the strength loss, and HAZ simulation has been used to further elucidate the mechanism of softening. The weldability of the cold rolled, Zn alloy coated steel sheet was also characterised in terms of weld bead appearance and geometry, chemical composition and non-metallic inclusion distributions. Finally, the effect of the welding thermal cycle on the Zn alloy coating has been clarified.

Based on the research carried out in this study the following specific conclusions can be drawn.

1. Under tensile loading, GMA and FCA butt welded 0.85 and 1.0mm thick ZINCALUME™ and ZINC-HI-TEN™ G550 sheet steels fractured in the HAZ away from weld bead. The fracture occurred in the grain refined region closed to the grain coarsened region, probably due to strain concentration caused by the discontinuity in microstructure and hardness between this and the adjacent grain coarsened region.

2. Increased heat input had a detrimental effect on tensile strength because of increase in the width of the softened zone and grain growth in the grain refined region, resulting in a decrease of the yield strength.

3. Tensile elongation increased with an increase of heat input due to the expansion of the localised softened volume of the HAZ rather than an increase in its ductility.

4. The tensile strengths of GMA and FCA welded ZA and ZHT G550 sheet steels fell into a narrow band. Over a range of nominal heat inputs of 50 J/mm to 130 J/mm the tensile strength was 6% to 16% lower than the minimum specified

tensile strength of 550 MPa for the cold rolled sheet prior to welding. The maximum loss in yield strength, at the highest heat input of 130 J/mm, was 150 MPa, suggesting that a minimum yield strength of 400 MPa can be safely used for structural design calculations.

5. For a similar nominal heat input of about 70 J/mm, real welds exhibited a much higher tensile strength (500 MPa) and yield strength (450 MPa) than the simulated HAZ samples (tensile strength of 410 MPa and yield strength of 350 MPa) due to the 'brazing effect' or 'two-phase aggregate effect' in actual welds for which the constraint of stronger material (the weld and the high strength steel) raises the effective strength of the softened HAZ.

6. There was no evidence of 'zinc embrittlement' contributing to the reduction in HAZ strength.

7. At the same nominal heat input, differences in welding conditions can significantly change the effective heat input. From the changes in mechanical properties it was inferred that the welding process, electrode orientation and shielding gas had more significant effects on actual heat input than welding speed, welding control mode and type of Zn alloy coating.

   (a) At the same nominal heat input a higher strength loss was found in FCA welds than GMA welds due to a higher effective heat input arising from the use of 1.0% aluminum in the electrode wire and the formation of an extensive slag layer on the face of the weld bead.

   (b) GMAW using perpendicular and forehand electrode orientations produced a higher tensile strength than backhand welds, for which the thermal energy is concentrated back onto the weld pool with the deposition of weld metal onto the molten pool.

(c) Lower tensile strengths was also found in GMA welds shielded by helium gas mixture and pure CO_2, due to the high thermal conductivity of helium and chemical reactions in the arc column in the case of CO_2.

8. The surface appearance of the GMA and FCA weld beads on ZA and ZHT sheet steels were found generally to be satisfactory, with the welds being continuous and the weld beads sound and smooth. No obvious macro-defects and zinc penetration cracking were found in the butt weld bead and HAZ.

9. The weld bead profile of FCA welds was generally flatter and smoother than GMA welds probably as a consequence of the extensive slag cover on the face of the weld bead. Significantly lower oxygen contents were found in the FCA welds due to the combination of relatively high contents of carbon and aluminum in the FCA electrode wire and Al pick-up from the Zn-Al coating. However, the nitrogen content was much higher in the FCA welds because of pick-up from entrained air.

10. Shielding by Ar goshield 60 (98.5%Ar+1.5%O_2) generated the lowest oxygen weld metal of the GMA welds and produced a more convex weld bead profile, consistent with a higher weld pool surface tension.

11. The oxygen content of GMA weld metal increased with an increase of the oxygen potential of the shielding gas.

12. For the same welding conditions, the ZA weld metal had a lower oxygen content than the ZHT weld metal probably due to the fact that the aluminum in the coating of the ZA sheet is likely to react with oxygen in the weld pool reducing the oxygen content in the weld metal.

13. Although there was no evidence of significant macro-pores in the weld bead of ZA steel, a few large spherical pores were observed in the weld metals for both GMA and FCA welds of ZA and ZHT sheet. Al rich particles were found

entrapped in the weld metal, but there were no Zn rich particles since Zn has a lower melting and boiling point than Al and tends to be volatilized out of the weld bead region. None of these defects resulted in weld metal tensile failure.

14. The volume fraction and mean particle diameter of non-metallic inclusions in the GMA welds increased with increasing oxygen potential of the shielding gas, consistent with the Franklin equation. Increasing oxygen potential increases the effective heat input and produces a higher oxygen level in the weld bead. Slower weld pool cooling and larger dwell time then give a rise to inclusion growth during weld pool solidification.

15. A higher volume fraction and larger mean particle size of the non-metallic inclusions were found in the FCA welds than in GMA welds because of the higher nitrogen, rather than oxygen content in the FCA weld metal. The volume fraction increased with increasing weld metal Al due to increased formation of AlN particles.

16. Although the Zn alloy coating was affected by the welding thermal cycle, it was not completely removed, even close to the weld bead. For GMA welded ZA steel, a white layer formed on the surface of the base metal adjacent to the weld with a composition close to that of the intermetallic compound Fe_3Al.

17. The Zn coating on the ZHT steel was not completely removed during welding. The Γ phase was detected at a high peak temperatures close to the weld bead, because the rapid heating and cooling prevented the complete elimination of Zn rich material. The surviving Γ phase is expected to provide some protection from corrosion.

REFERENCES

- Abson, D. J., Dolby, R. E. and Hart, P. H. M., International conference on Trends in Steels and Consumables for Welding, The Welding Institute, London, 13 – 16 Nov., 1978, p. 75
- Adams, C. M., Welding Joiurnal (AWS), Vol. 37, 1958, p. 210s
- Ahlblom, B., Bergstom, H., Hannerz, N. E. and Werlefors, T., Proceeding International Conference on the Effects of Residual Impurity and Microalloying Elements on Welding and Weld Properties, The Welding Institute, London, England, Paper 38, 1983
- Ahmed, N. U. and Jarvis, B. L., Australasian Welding Journal, Vol. 43, Third Quarter, 1998, p. 40
- Ahmed, N. U. and Javis, B. L., Aus. Weld. Jnl, Vol. 43, Third Quarter, 1998, p. 40
- Aida, Suga and Nakano, Collection of Abstracts from Japan Welding Society, No. 44 series, 1989, p. 216
- Akselsen, O. M. and Simonsen, T., Welding in the World, Vol. 25, (1/2), 1987, p. 26
- Akselsen, O. M., Solberg, J. K. and Grong, F., Scan. J nl. Metall., Vol., 17, 19885, P. 194
- Alberry, P. J. and Jones, W. K. C., Metals Technology, Vol. 9, (10), 1982, p. 421
- Alberry, P. J., Chew, B. and Jones, W. K. C., Metals Tech., June, 1997 p. 317
- Albutt, K. J. and Garber, S., Jnl. Iron Steel Inst., Vol. 204, 1966, p. 1217
- Amano, K., Shiga, C., Kusuhawa, Y., Kamoi, N., Matsumura, H., Muramatsu, S., Tabata, J., Toyasada, M. and Miyazaki, T., Conf. Proc. on 'Fifth International Offshore Mechanics and Arctic Engineering (OMAE) Symposium, Vol. II, Tokyo, 1986, p. 338
- Apps, R. L. and Andrade, A. M. V. P. D., Conf. Proc. on 33ed Annual Conf. of the Australian Welding Institute, Brisbane, Oct., 1985, p. 327
- Arata, Y., Nishiguchi, K., Ohji, T. and Koshai, N., Japan welding Research Institute, Vol. 8, No. 1, 1979, p. 43
- Ardi, Rokujo, Yamada and Suga, Quarterly Journal of Japan Welding Society, Vol. 1, (2), 1983, p. 177

- Asakawa, Ozaki and Yamamoto, welding Technique, Vol. 39, (2), 1991, p. 68
- Ashby, M. F. and Easterling, K. E., Acta Metallurgica, Vol. 30, (11), 1982, p. 1969
- Askeland, D. R., 'The Science and Engineering of Materials', 3rd Edition, Published by Chapman & Hall, 1996, p. 196
- ASM (American Society for Metals), 'Metals Handbook', Vol. 5
- ASM (American Society for Metals), 'Metals Handbook', Vol. 10
- ASM (American Society for Metals), Specialty Handbook, 'Carbon and Alloy Steels', 1996, p. 520-572
- Australian Standard 1544.2, 1989, 'Methods for Impact Tests on Metals, Part 2: Charpy V-notch'.
- Australian Standard, AS 2205.6.1, 'Methods of Destructive Testing of Welds in Metal, Part 6.1, Hardness Test: Weld Joint Hardness Test, Standards Australia, 1988'
- AWRA (Australian Welding Research Association), Technical Note 1, The Weldability of Steels, May, 1982
- AWS (American Welding Society), 'Welding Zinc-Coated Steel', 1983, p21
- AWS (American Welding Society), 'Welding Handbook', Vol. 1, 8th Edition, 1987
- AWS (American Welding Society), 'Welding Handbook', Vol. 4, 1998
- AWS, American Welding Society, 'Welding Handbook', Vol. 2, 1991
- Beck, W., O'M Bockris, J., McBreen, J. and Nanis, L., Proceedings of the Royal Society, Vol. A290, 1966, P. 220
- Beckert, M., Holz, R., Schweisse Technik, Vol. 23, No. 8, 1973, p. 344
- Berkhout, C. F., Seminar Handbook on Welding Thermal Simulation for Research and Problem Solving, London, The Welding Institute, 1972, p. 21
- Bhatti, et al., Welding Journal, Vol. 63, 1984, p. 224
- BHP Steel & Coil Products Division Fastening and Sealing Handbook, Vol. 4, p. 5
- BHP Steel and Coil Products Division, 'Research Internal Report', (based on the privet conversation with a senior stuff who is in charge in coating processing) 2003

- Bibby, M. J., Yurioka., N., Gianetto, J., and Chan, B., 'Awhite Paper Prepared for International Workshop Managing Hydrogen in Welding Applications', Ottawa, Canada, Oct. 6-8, 1998
- Black, N. and Lange, M., technical report on 'Gas Metal Arc Welding Tubemakers Hi-Lite Galvabond Rolled Hollow Section and Duragal Angle Sections', 1993
- Black, N., ' Recommendation for Ga s Metal Arc W elding of D uragal Coated Products', CIGWELD technical report, No. 9216/DGL/01, Sept. 1993
- Boekholt, R., 'The Welding of Galvanized Steel and Zinc Rich Painted Steel', Conf Proc. On 'The 7th International Conference on Hot-Dip Galvanizing, Paris, France, June, 1964 (also on Philips Welding Reporter 66/1)
- Boniszewski, T. and Watkinson, F., Metals and Materials, Feb., 1973, p. 90, and March p. 145
- Boniszewski, T. et al., British Welding Journal, Vol. 12, (7), 1965, P. 14
- Bonomo, F. and Rothwell, A. B., Conf. Proc. on 'International Welding Congress', Bratislava, 1971
- Boothby, P. J., Metal Construction and British Welding Journal, Vol. 17, No. 6, 1985, p. 363
- Bransch, H. N., 'Welding With High Power-Pulsed abd cw Nd: YAG Lasers', Photonics Spectra, Vol. 25, No. 9, 1991, p. 107
- Brisson, J., Maynier, P. H., Dollet, J. and Bastien, P., Weld. Jnl. Res. Suppl., Vol. 51, No. 4, 1972, p. 208
- British Standard 5135, Specification for Metal Arc Welding of Carbon and Carbon-Magnanese Steels, 1974
- British Standard, BS 709 1983-10, 'Test for Hardness Across Welded Joints'
- Bryhan, A. J., Weld. Jnl. Res. Suppl., Vol. 50, (9), 1981, p. 169s
- Cahn, R. W., 'Physical Metallurgy', North-Holland Publ. Co., Amsterdam, 1965
- Chatterjee, K. L. and Waddell, W., Welding and Metal Fabrication, March, 1996, p. 110
- Chen, J. H., Kifuta, y., Araki, M and Matsuda, Y., Acta Metall., Vol. 32, 1984, p. 1779

- Chen, L., 'Characterisation of Transverse Cold Cracking in Weld Metal of a High Strength Quenched and Tempered Steel', A Thesis of Doctor of Philosophy, University of Wollongong, Australia, 2000
- Chen, C.C and Pollack, A., Welding Brazing and Soldering, Vol 6, ASM Handbook, ASM International, 1993, p.416-428
- Chen, Y. W. Dunne, D and Norrish, J., The Eighth East Asia-Pacific Conf. on 'Structural Engineering & Construction', Singapore, 5-7 Dec. 2001
- Chen, Y. W., Dunne, D, Norrish, J and Szalla, J., Australasian Welding Journal, Vol. 45, Fourth Quarter, 2000, p. 39
- Chen, Z., Loretto, M. H. and Cochrane, R. C., Mat., Sci. Tech., Vol. 3, Oct., 1987, p. 836
- Chin, L. L – J., Welding Journal, Vol. 48, 1969, p. 290s
- Chipperfield, C. G. and Williams, J. G., Conf. Proc. on 'HSLA Steels-Metallurgy and Applications', Beijing, China, 1985, p. 535
- Cochrane, R. C. and Kevill, B. R., Welding Institute International Conference, Nov., 1978
- Cochrane, R. C., Ward, J. L. and Keville, B. R., Proceeding International Conference on the Effects of Residual Impurity and Microalloying Elements on Weldability and weld Properties, London, England, The Welding Institute, Paper 16, 1983
- Coe, F. R., 'Welding Steels Without Hydrogen Cracking', Cambridge, Welding Institute, 1973
- Commission of the European Communities, 'Study of the Mechanical Properties of the HAZ in the Weld High Strength Steels', Technical Research Steel Report 5192f, Vol. 2, Dec., 1974
- Cottrell, C. L. M., Metal Construction, Vol. 16, (12), 1984, p. 740
- Courtney, T. H., 'Mechanical Behavior of Materials', McGraw-Hill International Editions, 2000, p. 219
- CSIRO Division of Manufacturing and Technology, Australian Quarterly Progress Report on Productivity Welding: Aug. – Oct., 1989, Generic Technology Grant No. 15020
- Dallam, C. B., Liu, S. and Olson, D. L., Welding Journal, Vol. 64, 1985, p. 140s

- Darken, L. S. and Gurry, R. W., 'Physical Chemistry of Metals', McGraw-Hill Book Company, Inc., 1953, p.349
- David, S. A. and Vitek, J. M., International Metals Review, Vol. 34, 1989, p. 213 – 245
- Davis, G. J. and Garland, J. G., International Metallurgies Reviews, Vol. 20, 1975, P. 83
- Den Ouden, G., Verhagen, J. G. and Tichelgar, G. W., Welding Journal, Vol. 54, (3), 1975, p. 87s
- Dieter, G. E., 'Mechanical Metallurgy', Third Ed., New York McGraw-Hill Book Company, 1986
- Dolby, R. E., Seminar Handbook on Weld Thermal simulation for Research and Problem Solving, London, Welding Institute, April, 1972, M/53/70
- Dolby, R. E., Welding Journal Res. Suppl., Aug., 1979, p. 225s
- Dowling, J. M., Corbett, J. M. and Kerr, H. W., Metallurgical Transactions A, Vol. 17A, 1986, p. 1611
- Drayton, P. A., 'The Welding of Primed Steel Plate', Confidential Report, c178/5/69, The Welding Institute, 1969
- Duren, C., IIW Doc. IX-1365-85, 1985
- Easterling, K. E., 'Advances in Welding Science and Technology', Edited by David, S. A., Proc. of an International conf. On Trends in Welding Research, Gatlinburg, Tennessee, USA, 18 – 22 May, 1986
- Easterling, K. E., 'Introduction to the Physical Metallurgy of Welding', 2nd Edition, Butterworth-Heinemann, 1992
- Eichhorn, F. and Pyrasch, D., Aus. Weld. Jnl., Spring, 1986, p. 39
- Eriguchi, T., Soga, S., Asada, H. and Inoue, S., 'Weldability of Zn, Al and Zn-Al Alloy-coated Steel Sheets', Nisshin Steel Technical Report, No. 72, 1995, p. 35
- Etude, S. S., 'a larc en atmosphere dargon de toles galvanisees de 1.2 mm depaisseur', No. 16964, Institute de Soudure, Nov., 1960
- Evans, G. M., Metal Construction, Vol. 18, 1986, p. 442R and p. 631R
- Evans, G. M, IIW Doc. II-A 546-81, 1981
- Farrar, R. A., Welding and Metal Fabr., Vol. 44, 1974, p. 578
- Fast, J. D., Gases in Metals, Philips Technical Library, 1976

- Ferrante, M. and Farrar, R. A., Journal of Materials Science, Vol. 17, 1982, p. 3293
- Finday, R., Samandi, M. and Howes, S., Australasan Welding Journal, Vol. 2, First Quarter, 1997, p. 39
- Franklin, A. G., J. Iron and Steel Inst., 1969, p. 207
- French Standard, NF A 81-460, 'Method for the Determination of the Underbead Hardness'
- Frewin, M. R., 'Experimental and Theoretical Investigation of Tandem Laser Welding', Thesis for the degree of Doctor of Philosophy, July, 1997
- GAA (Galvanizers Association of Australia), 'Galvanizing', 9th Edition, Pub. By Australian Zinc Development, May, 1981
- Gaskell, D. R., 'Introduction to Metallurgical Thermodynamics', 1981, p. 287
- Gerbase, J., Embury, J. D. and Hobbs, R. M., 'Structure and Properties of Dual-Phase Steels', ed., Kot, R. A. and Morris, J. W., Warrendale, Pa, 1979, The Metallurgical Sociaty of AIME
- German Standard, DIN 50 163 Part 1, 'Testing of Metallic Materials; Hardness Testing on Welding: Joins Welding'
- Granjon, H., 'Fundamental of Welding Metallurgy', English Edition, 1991
- Gregory, E. N., Welding Journal, August, 1968, p. 644
- Gregory, E. N. and Herrschaft, D. C., Welding Journal, June, 1969, p. 463
- Gregory, E. N., 'Welding of Zinc Coated Structures ILZRO Project No. ZM-115', Progress Report, No. 12, Dec., 1968
- Gregory, E. N., Ibid, Vol. 48, (8), Resea. Suppl., 1969, p. 369s
- Gregory, E. N., Welding Journal, Vol. 47, (8), 1968, p. 631 and p. 644
- Grong, O. and Matlock, D. K., International Metals Review, Vol. 31, 1986, p. 27
- Grong, O., Siewert, T. A. and Edwards, G. R., Welding Journal, Vol. 65, 1986, p. 279s
- Grotke, G. E., Weld. Jnl. Res. Suppl., Vol. 43, 1964, p. 265s
- Hancock, G., The WTIA 47th Annual Conf., Queensland, Australia, 18-20 Oct., 1999, p. 19
- Hannerz, N. E. and Holmquist, B. M. J., Met. Source Jnl., Vol. 8, No. 7, 1974, p. 228

- Harrison, P. L. and Farrar, R. A., International Materials Review, Vol. 34, (1), 1989, p. 35
- Hart, P. H. M. and Harrison, P. L., Weld. Jnl. Res. Suppl., Oct., 1987, p. 310s
- He, X. J., Terao, N. and Berghezan, A., Met. Sci., Vol. 18, July, 1984, p. 367
- Heyden, J ., Nil sson, K . a nd Magnusson, C., ' Laser W elding o f Zinc C oated Steel', Conf. Proc. on '5th Int. Conf. of Laser in Manufacturing', Stuttgart, Germany, Sept. 1988, IFS Publications, Bedford, 1988
- Hill, D. C. and Passoja, D. E., Welding Journal, Vol. 53, 1974, p. 481s
- Homma, H., Ohkita, S., Matsuda, S. and Yamamoto, K., Presented at The 67th AWS Convention, Atlanta, U.S.A., April, 1986
- Honeycombe, R. W. K., Conf. Proc. on 'HSLA Stells-Metallurgy and Applications', Beijing, China, 1985, p. 243
- Honeycombe, R. W. K. and Bhadeshia, H. K. D. H., 'Steels Microstructure and Poperties', Second Edition published 1995 by Edward Arnold, a division of Hodder Headline PLC, p. 315
- Hoult, A. P., 'Cutting and Welding With High Power Solid State Lasers', Conf. Proc. on 'Advances in Joining and Cutting Process', Harrogate, Oct/Nov., 1989, p. 17-1, Abington Publishing, Cambridge, 1990
- Howes, S. W., 'The Arc Weldability of Galvanized Steels', BHP Steel Technical Report, No. 1134, August, 1992
- Huang, S. W., Dean, G., Norrish, J. and Nolan, D., Australasian Welding Journal, Vol. 47, First Quarter, 2002, p.33
- Hulka, K. and Heisterkamp, F., Conf. Proc. on 'Technology and Application of HSLA Steels', Philadephia, Oct., American Society for Metals, Oct., 1983, p. 915
- IIW, International Institute for Welding, IIW Doc., IX-537-67, 1967
- IIW, International I nstitute o f Welding, IIW Doc. IIS/IIW-893-86, 198 6, (ex Doc. IX-1309-84), also Weld in the World, Vol. 25, No. ½, 1987, p. 2
- Ikawa, H., Oshige, H. and Hoi, S., Jnl. Weld, (Japan), Vol. 7, 1977, p. 396
- Illin, V. P. and Razikov, M. I., Auto. Weld., Vol. 19, 1966, p. 3
- Inagaki, M. et al., Transactions National Research Institute of Metals (Japan), Vol. 6, (6), 1964, p. 73
- Ito, Y. and Bessyo, K., IIW Doc., IX-576-68, 1968

- Ito, Y. and Nakanishin, M., Journal of Japan Welding Society, Vol. 44 (10), 1975, p. 815
- Jagannathan, V., Conf. Proc. on '2nd Int. Conf. of Zinc and Zinc Alloys Coated Steel Sheet', Verlag Stahleisen, 1992, p. 127
- Jakenouchi, M. and Shimizu, T., Welding International, Vol. 6, (5), 1992, p. 351
- Jonsson, P. G., Muphy, A. B. and Szekly, J., Welding Journal, Vol. 74, 1995, p. 48s
- Jud, R. W., 'Joining Galvanized and Galvannealed Steels', SAE Technical Paper, No. 840285, 1984
- Karppi, R., IIW Doc. IX-1102-78, 1978
- Keville, B. R., Weld. J., Vol. 62, 1983, p. 253s
- Kiessling, R., 'Non – metallic Inclusions in Steel,' Part V, Iron and Steel Instiyute, London, 1989
- Killmore, C. R. et al., Conf. Proc. on Offshore Mechanics Arctic Engineering (OMAE), Hague, Netherlands, March, 1989
- Kilpatrick, I. M., 'The Application of Thermal Simulation Techniques for the Assessment of Mechanical & Metallurgical Properties of the Heat Affected Zone in High Yield Steels', Seminar Handbook, Welding Institute, 1972, p. 25
- Kim, N. J. and Thomas, G., Met. Trans., Vol. 12A, 1981, p. 483
- Kjeld, F., Welding Journal, April, 1991, p. 39-46
- Kluken, A. O., Grong, O., Report No. STF34 F8840, SINTEF, Trondheim, Norway
- Kluken, A. O., Grong, O. and Hijelen, J., Journal Mater. Sci. Tech., Vol. 4, 1988. p. 652
- Kluken, A. O. and Grong, O., Metallurgical Transactions A, Vol. 20A (8), 1989, p. 1335
- Kohno, R. and Jones, S. B., 'An Initial Study of Arc Energy and Thermal Cycles in the Submerged Arc Welding of Steel', Welding Institute Research Report, 81/1978/PE, 1978
- Koukaki, A. H., North, T. H. and Bell, H. B., Metal Construction, Vol. 11, 1979, p. 639

- Kozai Kurabu, 'Welding Guidance for Galvanized Steel Sheet', Committee for Formulation of Guidance for Welding of Galvanized Steel Sheet, 1977
- Kudoh, J. and Pisarski, H. G., Report 294/1986, 7807.01/84/459.3, The Welding Institute, Abington, Cambridge, Jan., 1986
- Lancaster, J. F., 'Metallurgy of Welding', 6th Edition, Abington Publishing, 1999
- Lebedev, Y. M., Letuchi, V. N. and Tsyukh, S., M., Weld. Prod., Vol. 33, No. 12, 1986, p. 24
- Lewis, R. and Wu, K. C., Weld. Jnl. Res. Suppl., Vol. 42, 1963, p. 241s
- Lin, X. and Dunne, D. P., Uni. of Wollongong, Annual Report for Australian Welding Research Association (AWRA), 1988
- Liu, S. and Olson, D. L., Welding Journal, Vol. 65, 1986, p. 139s
- Liu, S., Olson, D. L., Ibbarra, S. and Runnerstam, O., 'Oxygen As a Welding Parameter: the Role of Light Metallography', Proceedings of the 25th Annual Technical Meeting of the International Metallographic Society, Microstructure Science, Vol. 20, 1993, p. 31
- Liu, Y. Q., 'Steels Heat Treatment' Chinese, 1981, p.23
- Lucas, W., welding and Metal Fabrication, Vol. 60, (7), 1992, p. 269
- Lundin, C. D., Conf. Proc. on 'Trends in Welding Research', Gatlinburg, Tennessee, May, 1986, 467s and p. 475
- Lundin, S., 'Arc Welding of Hot-Dip Galvanized Steel Sheet', Svetsaren, Vol. 5, (1-2), 1969, p. 16
- Lyttle, K. A., Stapon, W. F. G., Welding Journal, Nov., 1990, p. 644
- Martyr, D. R, 'Applying High Power Lasers to Shipbuilding', Welding Review, Vol. 6, No. 2, 1987, p. 106
- Massalski, T. B., Murray, J. L., Bennett, L. H., Baker, H. (Editors of ASM), 'Binary Alloy Phase Diagrams', Vol. 1, 1986, p. 112 and p. 185
- Massalski, T. B., Murray, J. L., Bennett, L. H., Baker, H. (Editors of ASM), 'Binary Alloy Phase Diagrams', Vol. 2, 1986, p. 1128
- McCutcheon, D. B., McGrath, J. T., Godden, M. J., Ruddle, G. E. and Embury, J. D., Conf. Proc. on 'Technology and Application of HSLA Steels', Philadephia, 1983, American Society for Materials, p. 881
- McRobie, D. E. and Knott, J. F., IIW Doc, II–A–773–89, 1 (5), 1985, p. 357

- Mills, A. R., Thewlis, G. and Whiteman, J.. A., Mater. Sci. Tech., No. 3, 1987, p. 105
- Mita, Journal of Japan Welding Society, Vol. 59, (8), 1990, p. 12
- Mono, M. and Druce Dunne, Conf. Proc. on 'Recrystallization '90', Edited by T. Chandra, The Minerals, Metales & Materials Sociaty, 1990, p. 827
- Mori, N., et al., IIW Doc, No. 1X-1196-8, International Institute of Welding, 1981
- Mukai, Nishimura, Nakashima and Oku, Quarterly Journal of the Japan Welding Society, Vol. 7, (1), 1989, p. 70
- Nagumo, M., Cof. Proc. on 'Copper in Steel', ATB Metallurgie, XXIII, No. 3, 1983
- Nakanishi, M., Komizo, Y. and Fukada, Y., The Sumitomo Search, No. 33, Nov., 1986, p. 22
- Nakano, N., Bessyo, K., Lida, Y., Seta, I. and Kamada, Y., Conf. Proc. on 'Fifth International Offshore Mechanics and Arctic Engineering (OMAE) Symposium', Vol. II, Tokyo, 1986 p. 354
- Nippes, E. F. and Savage, W. F., Weld. Jnl. Res. Suppl., Vol. 28, (11), 1949, p. 534s
- Nippes, E. F. and Savage, W. F., Weld. Jnl. Res. Suppl., Vol. 28, (12), 1949, p. 599s
- Nippes, E. F., Gerken, J. M. and Schaaf, B. M., Weld. Jnl. Res. Suppl., Vol. 34, 1955, p. 31s
- Nippes, E. F., Savage, W. F. and Owczarski, W. A., Weld. Jnl. Res. Suppl., Vol. 39, 1960, p. 465
- Nippes, E. F., Wawrousek, H. and Fleishchmann, W. L., Weld. Jnl. Res. Suppl., Vol. 34, 1955, p. 169s
- Nishikawa, Y., Suga, T. and Nakano, T., ISIJ International, Vol. 35, No. 10, 1995, p. 1213-1221
- Norris, I. M., 'High Power Laser Welding of Structural Steels-Current Status', Conf. Proc. on 'Advances in Joining and Cutting Processes, Harrogate, Oct./Nov., 1989, p. 55-1, Abington Publishing, Cambridge, 1990
- Norrish, J., 'Advanced Welding Process', IOP Publishing, 1992
- North, T. H., at al., Welding Journal, Vol. 58, 1979, p. 343s

- NZIG Bulletin, 'MIG Welding', Sept. 1980, p. 2
- Ohkita, S. et al., Conference Proceedings on Joint Australian Welding and Testing, Oct./Nov., Perth, Australia, 1984, Paper 27
- Ohkita, S., Homma, H., Tsushima, S. and Mori, N., Australia Welding Journal, Vol. 29, 1984, p. 29
- Pabu, S. S., David J. M., Vitek, J. M., Mundra, K. and DebRon, T., Journal of Materials Science and Technology, Vol. 11, 1995, p. 186
- Pal, T. K. and Majumdar, S. K., Int. J. For the Joining of Materials, Vol. 7, (4), 1995. p. 144
- Palmer, T. J., 'Welding of Hot-Dipped Galvanized Steel', Iron and Coal Trades Review, Vol. 167, (4456), Sep. 4, 1953, p. 533
- Pang, W., Ahmed, N. U. and Dunne, D. P., Conf. Proc. on Material United in the Service of Man, IMMA and WTIA, Perth, Sept. 1990
- Pekoz, T. and McGuire, W., 'Welding of Sheet Steel', American Iron and Steel Institute, 1979
- Porter, F. C., Metal Construction, Oct., 1983, p. 606
- Potapov, N. N., Welding Journal, Vol. 72, 1993, p. 367s
- Powley, C. and Hoskins, C., 'Cut, Drill, Join and Treat-Using Lasers', Machinery and Production Engineering, Vol. 150, No. 3838, 1992, p. 22
- Puech, M., 'Arc Welding Galvanized Steel- Report on Tests and the First Application on Air France Administration Building, Orly. Zinc et Alliags, No. 20, 1959
- Puech, M., 'Arc welding on Galvanized Steel-Reporte on Test and the First Application on Air France Administration Building', Orly Zinc et Alliages, No. 20, 1959
- Quintana, M. A., Mclane, J., Babu, S. S., and David, S. A., Welding Journal, Research Supplement, April, 2001, p. 98-s
- Ramberg, M., Akselsen, O. M. and Grong, F., Conf. Proc. on 'Trends in Welding Research', Datlinburg, Tennessee, USA, May, 1986, p. 679
- Ricks, R. A., Howell, P. R. and Barritte, G. S., Journal of Matterials Science, Vol. 17, 1982, p. 732
- Roberts et al., 'Advances in the Physical Metallurgy and Applications of Steels', The Metal Society, 1982, p. 162

- Rogerson, P. and Jones, C. L., Conf. Proc. on 'Steels for Linepipe and Pipeline Fittings', The Metals Society, London, 1983
- Rudy, F., Welding Journal, Vol. 39, (5), Resear. Suppl., 1960, p. 212s
- Rykalin, N. N., 'The Calculation of Thermal Resistance', Mashgiz, 1951; translated into English by Z. Paley and C. M. Adams, Jr. 1963,
- Salter, G. R., British Welding Journal, Vol. 2, 1964, p. 2
- Savage, W. F. and Aaronson, A. H., Weld Journal, Vol. 45, 1966, p.85
- Savage, W. F., 'Evolution of the Gleeble', Seminar Handbook, Welding Institute, 1972, p.1
- Sawhill, M. et al., Welding Journal, Vol. 53, (12), 1974, p. 544s
- Sekino, S. and Mori, N., Conf. Proc. on 'The Scienceand Technology of Iron and Steel', Part I, Tokyo, Iron and Steel Institute of Japan, 1970
- Seyffarth, P., Schw. Tech., Vol. 27, No 2, 1979, p. 58
- Shackleton, D. N. and Luca, W., Weld. Jnl. Resear. Suppl., Dec., 1974, p. 537s
- Shinoda, T., Sugiura, S., Takeuchi, Y., Nagata, M. and Shimizu, T., The 5th Int. Symp. Of the Japan Welding Society, Tokyo, April, 1990, p. 791
- Stenbacka and Perrson, Welding Journal, Vol.68, 1989, p. 41
- Stevenson, R., 'Formable HSLA and Dual-Phase Steel', ed., A. T. Davenport, Warrendale, Pa, The Metallurgical Sociaty of AIME, 1979
- Suga, T., Canadian Metallurgical Quarterly 34, 1994, p. 301-908
- Surian, E., Trotti, J., Herrera, R. and de Vedia, L. A., Welding Journal, June, 1991, p. 133s
- Suzuki, H. and Tamura, H., Trans. Nation. Res. Inst. Metal, (Japan), Vol. 3, 1961, p. 47
- Suzuki, H. and Tamura, H., Trans. Nation. Res. Inst. Metals, (Japan), Vol. 1, 1959, p. 119
- Suzuki, H., IIW Doc. IX-1351-85, 1985
- Suzuki, H., IIW Doc., IX-1279-83, 1983
- Suzuki, H., IIW Doc., IX-1306-84, 1984
- Svelto, O., 'Principles of Lasers', 2nd Edition, Plenum Press, New York, 1982
- Takenouchi, M and Shimizu, T., Welding International, Vol. 6, (5), 1992, p. 351
- Tanaka, J and Kitada, T., IIW Doc. IX-959-76, 1976

- Taylor, L. G. and Farrar, R. A., Weld Metal Fabrication, Vol. 43, 1975, p. 305
- Teh, L. H. and Hancock, G. J., 'Strength of Fillet Welded Connections in G450 Sheet Steels', Research Report No. R802, Dept. of Civil Eng., The University of Sydney, July 2000
- Teresaki, T., Japanese Journal of Welding, Vol. 67, 1981, p. 145
- Tomita, Y. et al., ' conf. Proc. on HSLA steels-Metallurgy and Applications', Beijing, China, 1985, p. 641
- Uchino, K. et al., Conf. Proc. on 'Fifth International Offshore Mechanical and Arctic Engineering (OMAE) Symposium, Vol. II, Tokyo, 1986, p. 373
- Underwood, E. E., 'Quantitive Stereology' ASTM, Addison-Wesley, London, 1970
- Van Adrichem, Th., J., Kas, J., Smit-Weld N. V. Nijmegn, Holectecniek, Netherlands, Vol. 1, No.1, 1971, p. 2
- Van Eijnssbergen, J. F. H., 'The New Campina Dairy Plant: A Welded Pre-Galvanized Structure', Conf. Proc. On 8th International Conf. On Hot-Dip Galvanizing, London, June, 1967
- Van Stone, R. H., Cox, T. B., Low, J. R., Jr. and Psioda, J. A., International Materials Reviews, Vol. 31, 1986, p. 141
- Verburg, S. J., Philips welding Reporter, the Netherlands, 1974/3-4
- Vitek, J . M. a nd D avid, S . A., M etallurgical Transactions A, Vo l. 21A, (7), 1990, p. 2021
- Walsh, D. W. and Savage, W. F., 'Advances in Welding Science and Technology', ASM International, Metals Park, Ohio, 1986, p. 59
- Wang, G. R., Lau, T. W., Weatherly, G. C. and North, T. H., Met. Trans. A, Vol. 20A, Oct., 1989, p. 2093
- Watanabe, I., Susuki, M., Tagawa, H., Kunisada, Y., Yamazaki, Y. and Iwasaki, N., Nikkon Kokan Tech. Report, Overseas No. 47, 1986
- Welding D esign and Fabrication, ' Welding Better With Pulsed Power', Oct., 1984, p. 57
- Welland, W. G., Weld. Jnl., March, 1989, p. 55
- Widgery, D. J., 'Weld Thermal Simulation for Research and Problem Solving', Seminar Handbook, London, The Welding Inst., April, 1972

- Widgery, D. J., Conf. Proc. on Weld Thermal Simulation for Research and Problem solving, 'Weld thrmal Simulators: a Review', London, Welding Institue, April, 1972
- Wingrove, A. L., Scan Jnl. Met., Vol. 16, 1987, p. 174
- Wingrove, A. L., Dunne, D. P. and Kennon, N. F., Australian Welding Research Journal, Vol. 14, No. 12, 1985, p. 8
- Wirth, P., Conf. Proc. on 'The Laser VS the Electron Beam in Welding, Cutting and Surface Treatment', Reno, Nevada, 1985, Bakish Materials Corp., Egnlewood, New Jersey, 1985
- Wyatt, D. J., 'The Structure and Properties of Laser Welding Zinc-Coated Sheet Steels', Thesis of Bachelor of Engineering, Uni. of Wollongong, Australia, 1993
- Yamamoto, Harada and Yasuda, Welding Technique, Vol. 37, (2), 1989, p. 67
- Yasuda, N akano, Komatsu a nd N akashima, w elding Technique, Vo l. 37, (2), 1989, p. 94
- Yurioka, N., Ohsita, S., IIW Doc. IX-1161-80, 1980
- Yurioka, N., Ohsita, S., Tamehiro, H., Cof. Proc. on the Specialist Symposium on Pipeline Welding in the 80s, 1981,
- Yurioka, N., Okumura, M., Kasuya, T. and Cotton, H. J. U., Metal Construction, Vol. 19, No. 4, 1987, p. 217R
- Yurioka, N., Oshita, S. and Tamehiro, H., Proc. on Symp. Of Australian Welding Research Association, Melbourne, 1981; also Welding Research Supplement, Vol. 62, (6), 1983, p. 147s
- Yurioka, N., Proc. on First United States-Japan Symp. On Advanced in Welding Metallurgy, Florida, American Welding Society, 1990, p. 79
- Zacharia, T., David, S. A., Vitek, J. M. and Kraus, H. G., Metall. Transactions, Vol. 22B, 1991, p. 243 – 257

APPENDICES

Appendix I (a) Typical EDS spectra of non-metallic inclusions consisted of (a) aluminium and manganese sulphides; (b) aluminium oxides

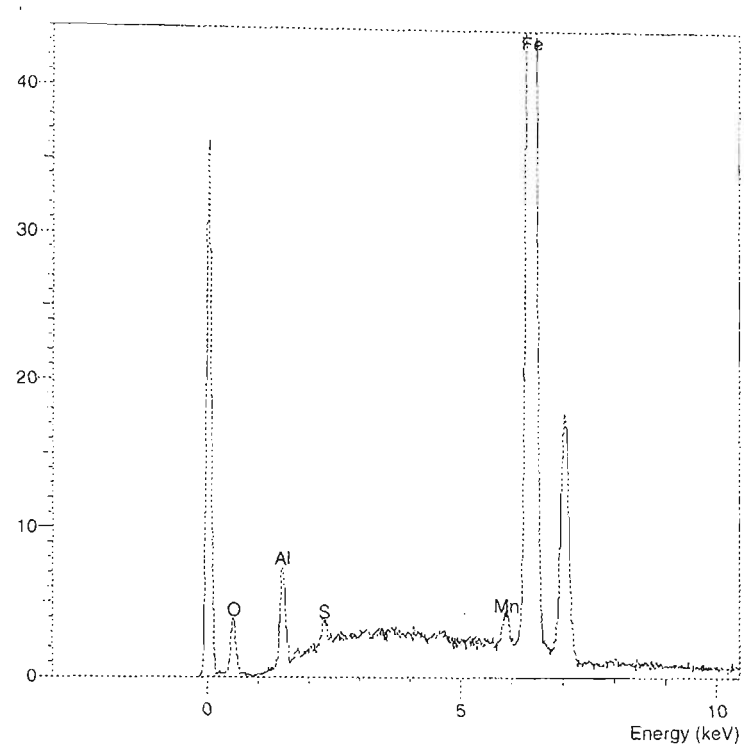

(a)

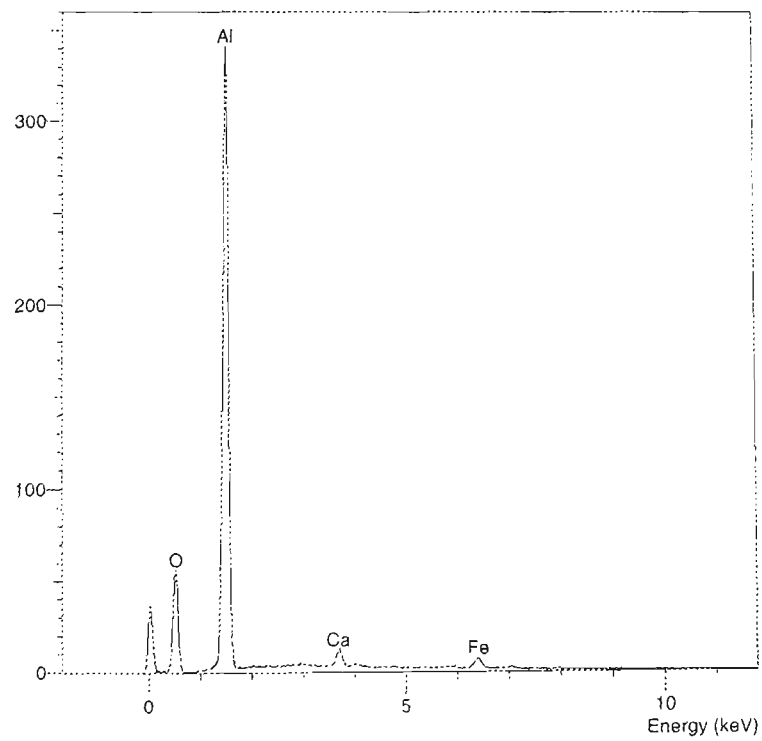

(b)

Appendix I (b) Typical EDS spectra of non-metallic inclusions consisted of aluminum nitride

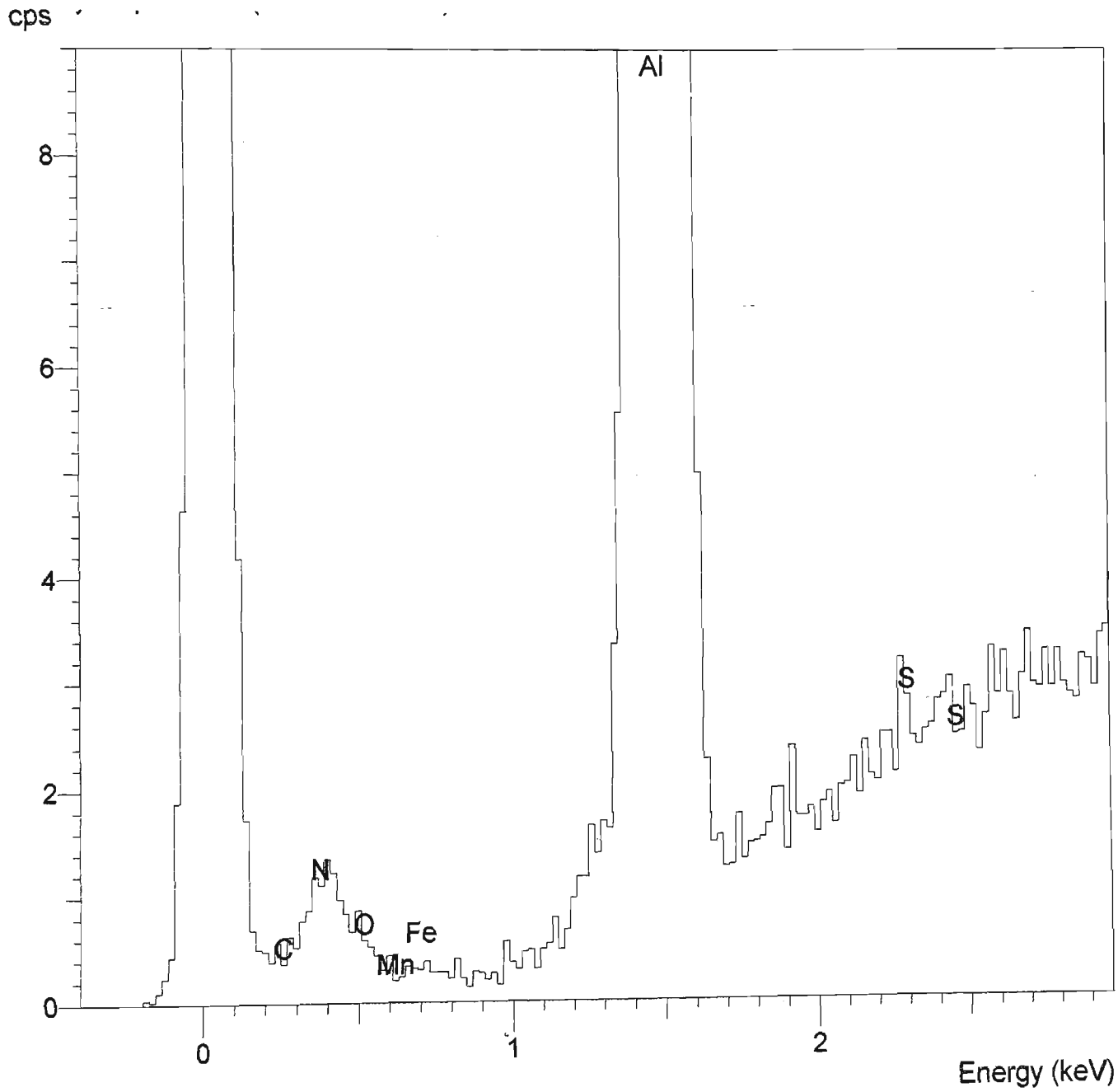

Appendix II (a) Thermal responses to GMAW of Zn and Zn-Al coated steels welds under different welding conditions from (a) to (f)

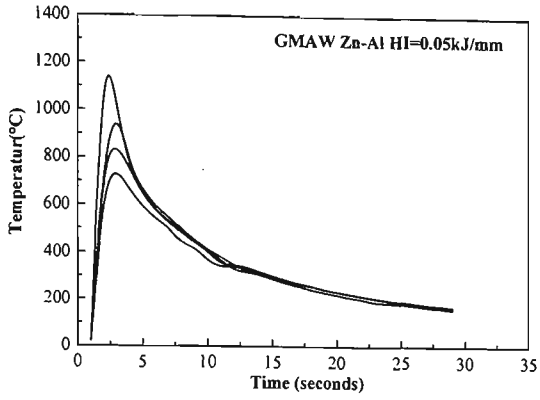

(a)

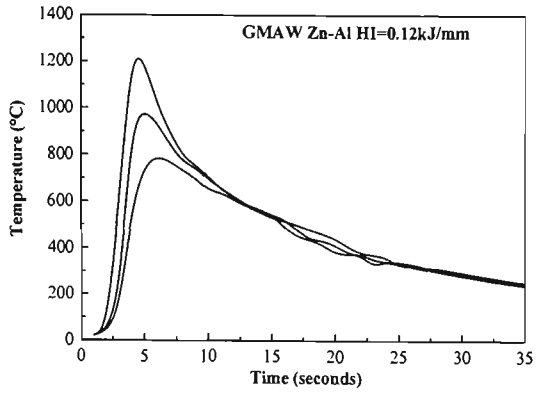

(b)

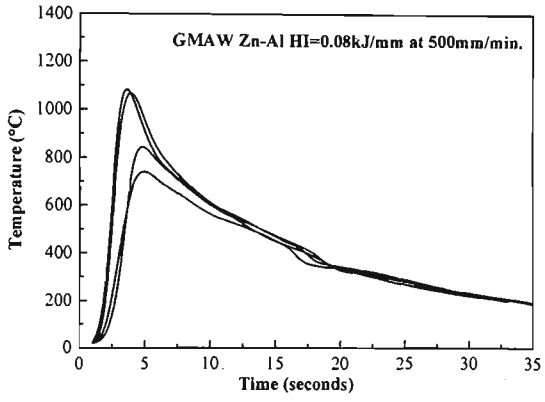

(c)

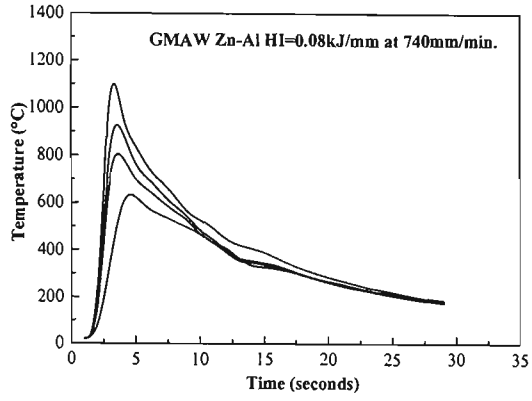

(d)

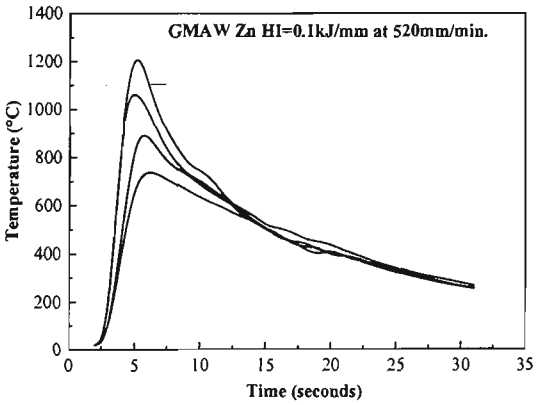

(e)

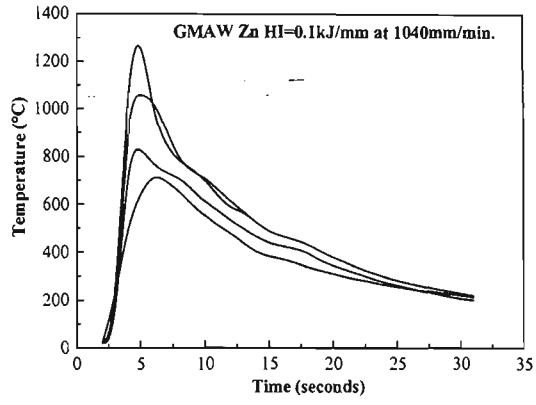

(f)

Appendix II (b) Thermal responses to GMAW and FCAW of Zn and Zn-Al coated steel welds under different welding conditions from (g) to (i)

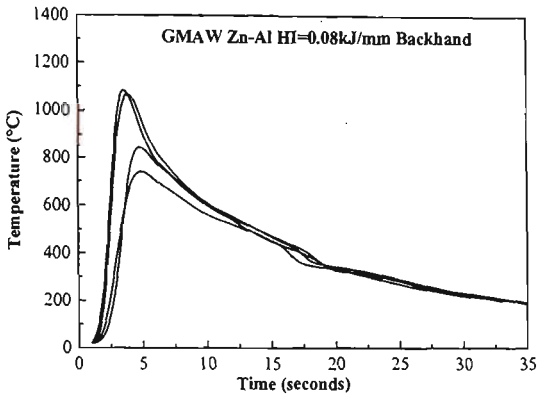

(g)

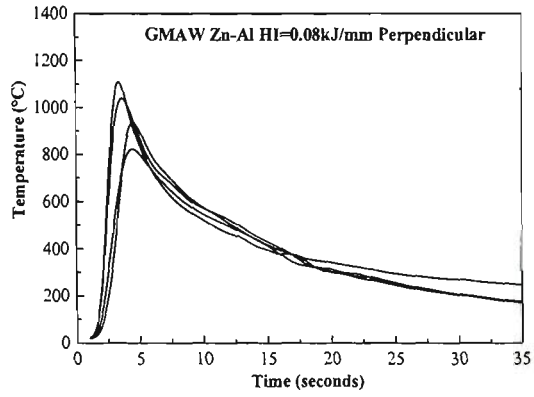

(h)

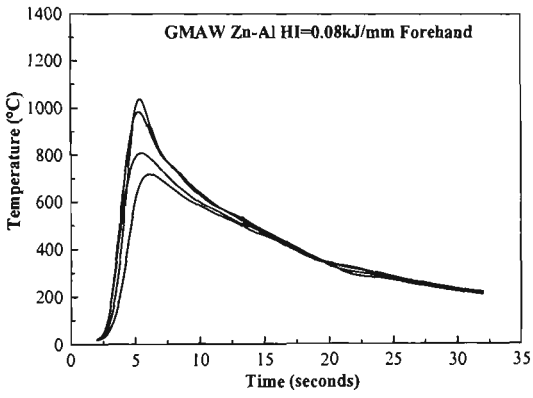

(i)

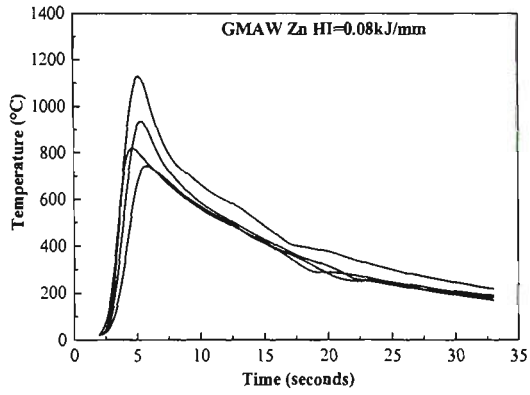

(j)

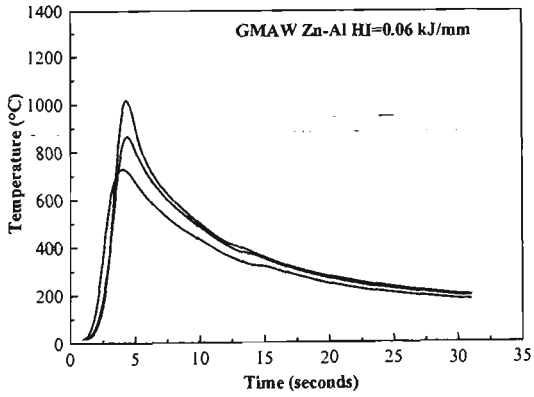

(k)

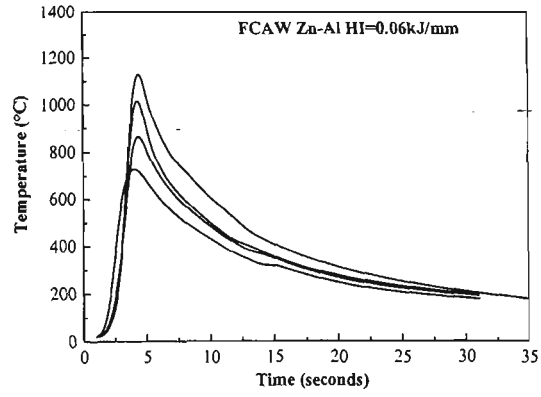

(l)

APPENDIX III Panoramic views of the morphology changes for: (a) the ZINCALUME^{TM} coating; and (b) the ZINC-HI-TEN^{TM} coating after GMA welding at the heat input of 80 J/mm

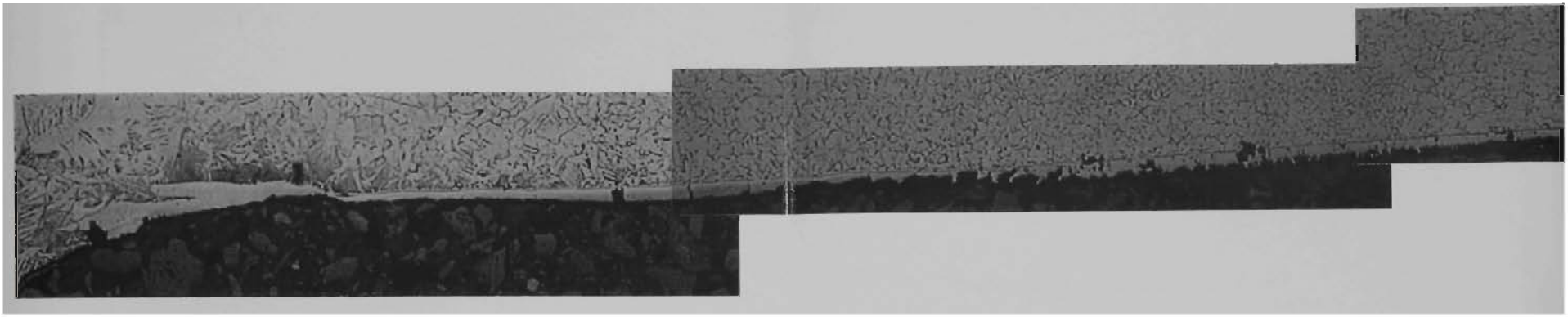

Weld metal →Base metal

(a) damaged Zn-Al coating after GMA welding

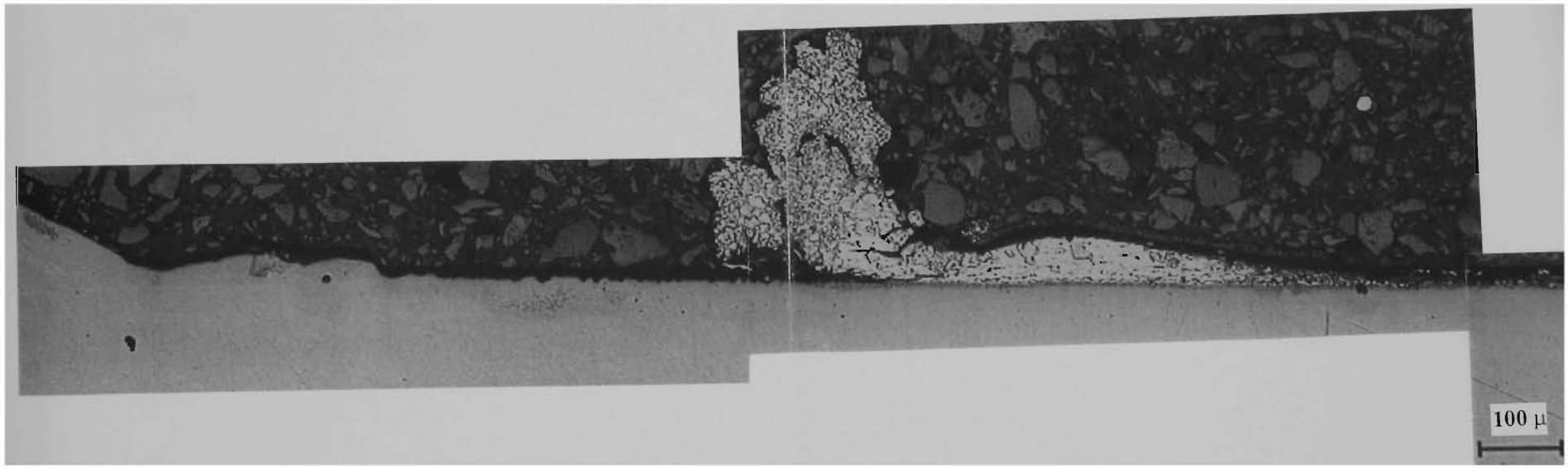

(b) damaged Zn coating after GMA welding

Appendix IV (a) Results of EDS line scan across coating consists of FeAl and Zn-Al layers (Figure 8.53 LS1)

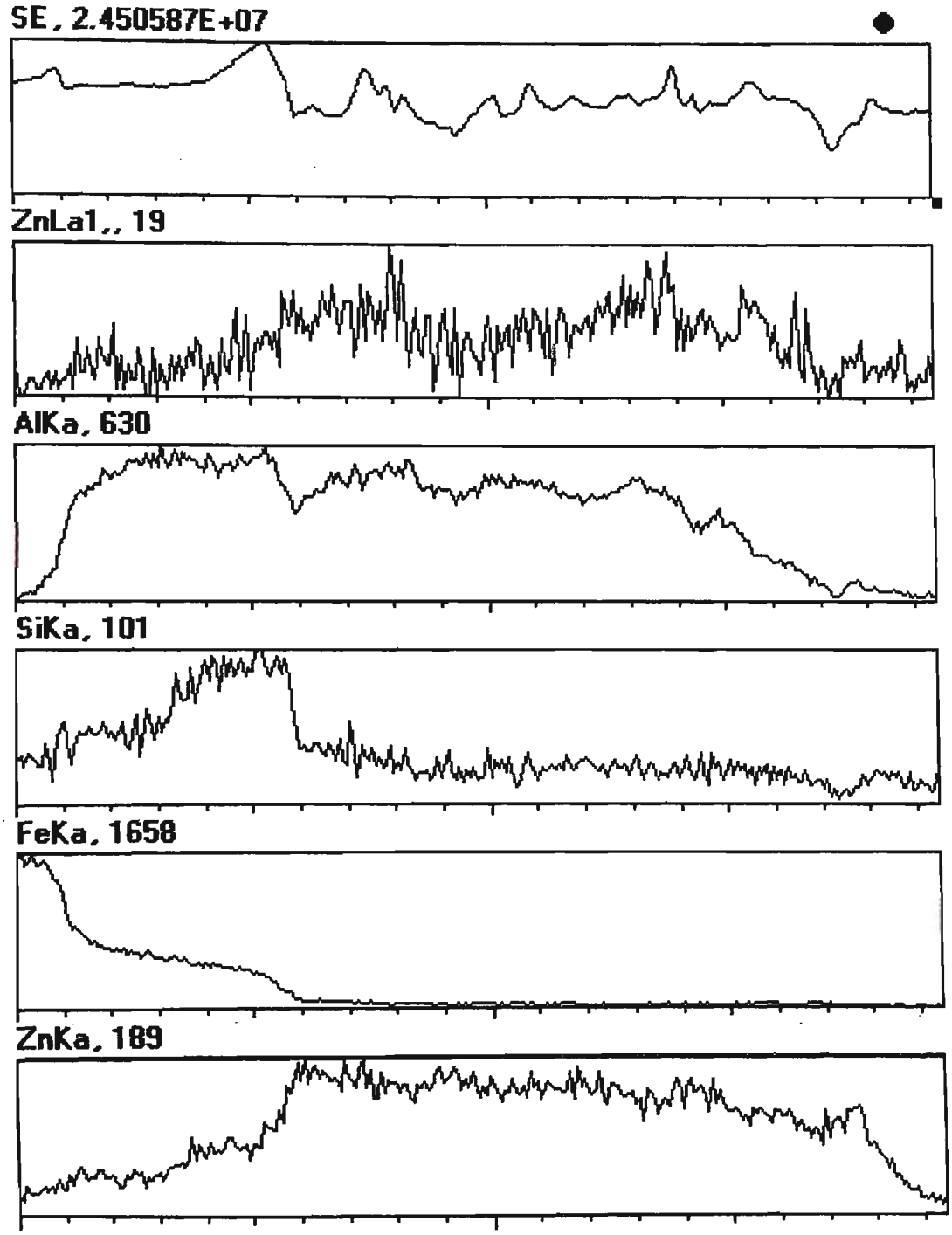

Appendix IV (b) Results of EDS line scan across coating consisting of Fe_3Al, FeAl and Zn-Al and Zn-Al multi layers (Figure 8.53 LS2)

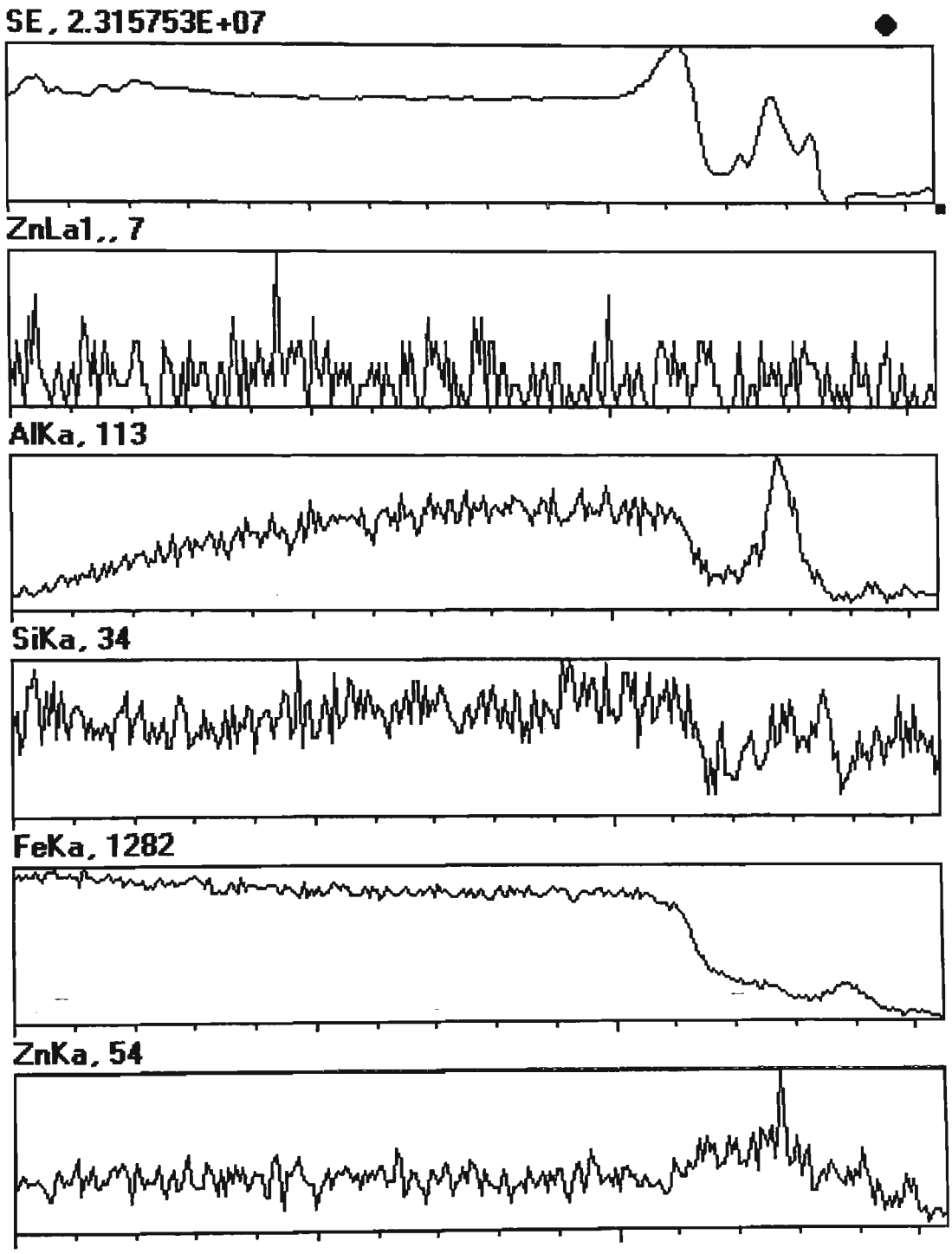

Appendix V (a) Results of EDS line scan cross Zn damaged coating

(Figure 8.57 LS1)

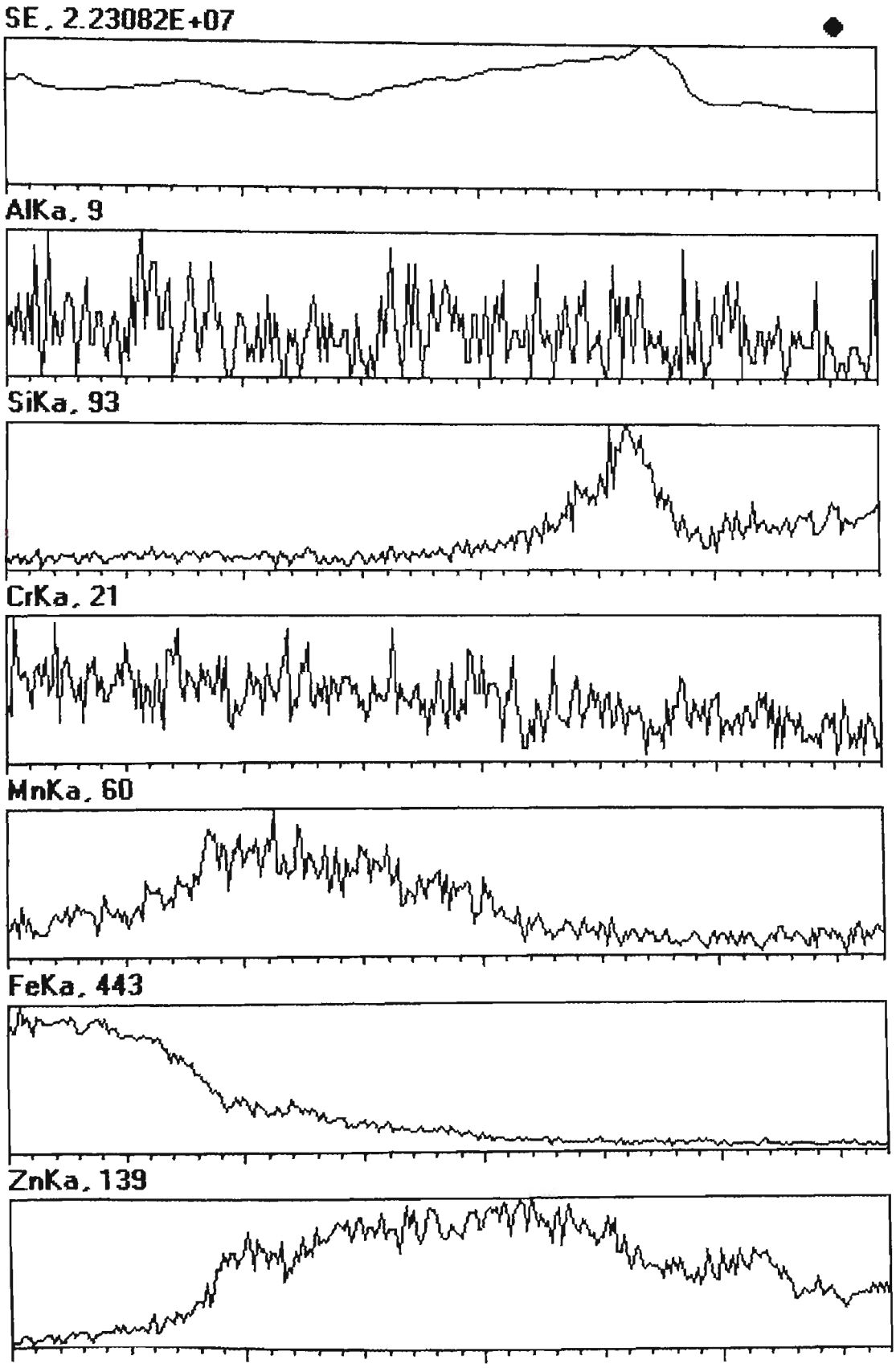

Appendix V (b) Results of EDS line scan cross Zn damaged coating in A3 zone (Figure 8.59 LS2)

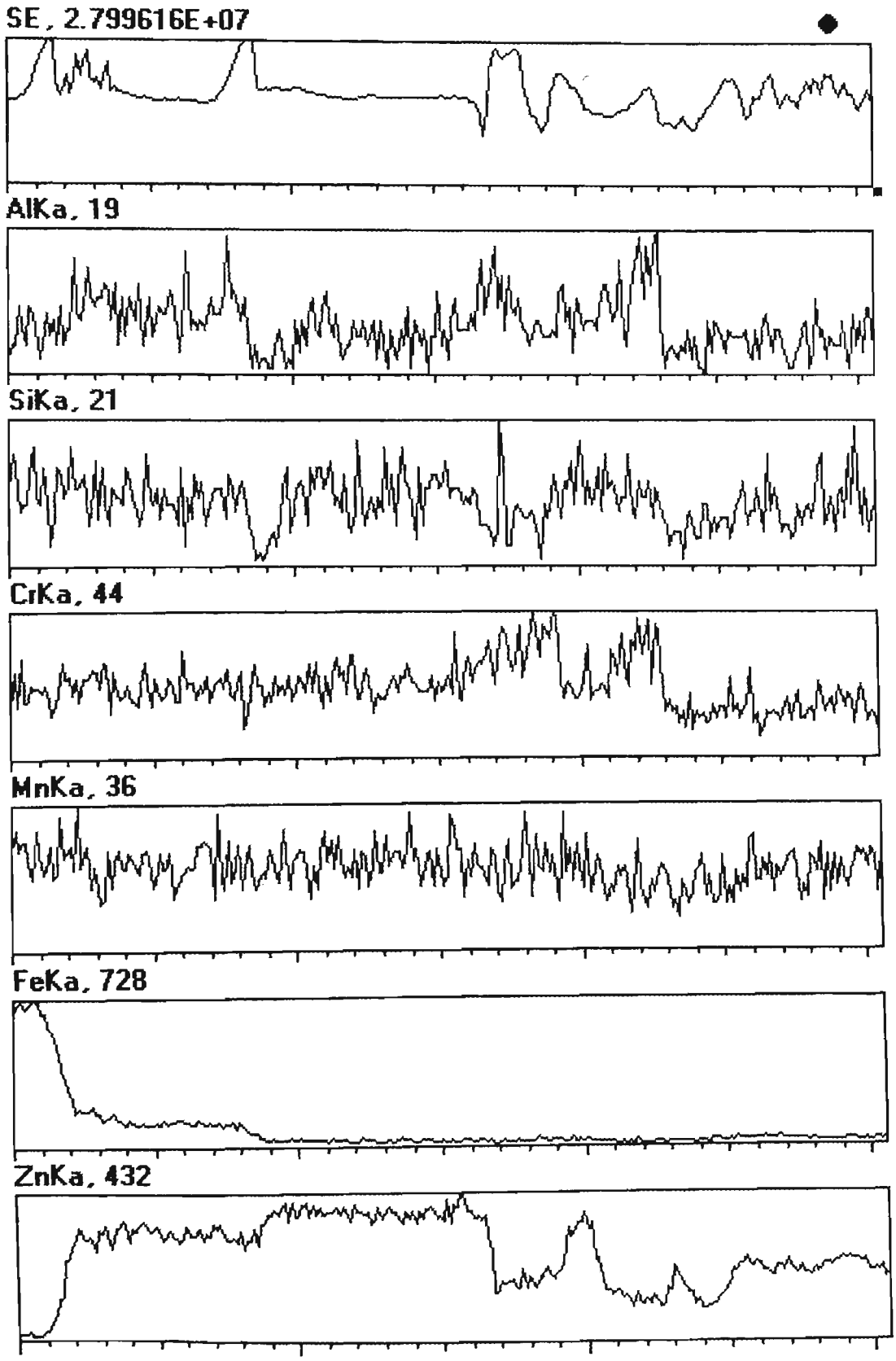

PUBLICATIONS

1) Yan Wang, 'Recent Development of the Electric Furnaces in the World, Xian Institute of Electric Furnace Internal Report', 1985, 30 pp.

2) Y. W. Chen, 'Cathode Materials for Lithium rocking Chair Batteries' Univ. of Wollongong Internal report, 1996, 22 pp.

3) Y. W. Chen, 'Carbon as Anode Materials for Lithium Rocking Chair Batteries', Univ. of Wollongong Internal Report, 1996, 15 pp.

4) Y. W. Chen, ' The Development of the Thin Film Lithium Rechargeable Batteries', Univ. of Wollongong Internal Report, 1996, 20 pp.

5) Y. W. Chen, ' The Development of Lithium Polymer Rechargeable Batteries', Univ. of Wollongong Internal Report, 1996, 15 pp.

6) Z. Chen and Y. Wang, ' The Effect of Ru on Microstructure of TMP Treated Gamma Titanium Aluminide', Proc. Thermec' 97, Int. Conf. On TMP of Steels and Other Materials, Eds T Chandra and T Sakai, TMS, 1997, 1449-1455.

7) K. Ng, Y. Wang, Z. Chen and M. Samandi, ' Deposition and Characterisation of Titanium Aluminide Thin Films Produced by a Filtered Arc Evaporation System', Proc. Thermac' 97, Int. Conf. On TMP of Steels and other Materials, Eds T Chandra and T Sakai, TMS, 1997, 1397-1403.

8) Z. Chen, Y Wang, K. Ng and M. Samandi, ' Titanium Aluminides Coatings Produced by a Filtered Arc Evaporation System', Proc. ICSE Shanghai' 97 Ed Xu Binshi, 1997, China Machine Press, 287-290.

9) Z. Chen and Y. Wang, ' Microstructure and Properties of Some TMP Treated Gamma Titanium Aluminides', Conf. Proc. Processing and Fabrication of

Advanced Materials IV, 1997 Singapore, Eds K. A. Khor et al. The Institute of Materials 1998, 1945-1956.

10) Y. W. Chen, ' Influence of GMA Welding Conditions on Microstructure and Mechanical Properties of G550 Recovery Annealed Sheet Steel', Technical Report to BHP, March 1999, pp23.

11) Y. W. Chen, D. Dunne, J. Norrish and J. Szalla, ' Effect of GMA Welding on Microstructure and Mechanical Properties of G550 Sheet Steel', The WTIA 47th Annual Conference, Australia, 1999, Paper 22, 15 pp.

12) Y. W. Chen ' Influence of Welding Conditions on the Thermal Cycles and Weld Bead Geometry in GMAW and FCAW of G550 Zn Alloy Coated Cold Rolled Structural Steels', Technical Report, University of Wollongong, June 2000, pp28.

13) Y. W. Chen, D. Dunne, J. Norrish and J. Szalla, 'Microstructure and Mechanical Properties of GMAW Welded G550 ZINCALUME Sheet Steel', Australasian Welding Journal, Volume 45, Fourth Quarter, 2000, 39-47.

14) Y. W. Chen, Druce Dunne and John Norrish, 'Effect of Electrode Orientation of GMA Welding on Microstructure and Mechanical Properties of G550 Structural Steel', EASEC-8 Conference (The Eighth East Asia-Pacific Conference of Structural Engineering & Construction 5-7 December 2001, Singapore) Paper No. 1417, 6 pp.

15) Y. W. Chen, Druce Dunne and John Norrish, 'Effect of Electrode Orientation on Structure and Properties of GMA Butt Welds of High Strength Zinc Alloy Coated Sheet Steel', The WTIA 50th Annual Conference, Australia, 2002, Paper 33, 9 pp.